Isogeometric Analysis and Shape Optimization in Fluid Mechanics

Nørtoft, Peter; Gravesen, Jens; Gersborg, Allan Roulund; Pedersen, Niels Leergaard

Publication date:
2012

Document Version
Publisher's PDF, also known as Version of record

Technical University of Denmark

Isogeometric Analysis and Shape Optimization in Fluid Mechanics

Ph.D. Thesis

Peter Nørtoft Nielsen

DTU Mathematics
Technical University of Denmark
Matematiktorvet 303S
DK-2800 Kgs. Lyngby
Denmark
Phone +45 4525 3031
Fax +45 4588 1399
www.mat.dtu.dk

DTU Mechanical Engineering
Technical University of Denmark
Nils Koppels Allé 404
DK-2800 Kgs. Lyngby
Denmark
Phone +45 4525 1960
Fax +45 4593 1475
www.mek.dtu.dk

Title of Thesis:

Isogeometric Analysis and Shape Optimization in Fluid Mechanics

Ph.D. Student:

Peter Nørtoft Nielsen
DTU Mathematics & DTU Mechanical Engineering
Technical University of Denmark
Matematiktorvet 303S
DK-2800 Kgs. Lyngby
Denmark
p.n.nielsen@mat.dtu.dk

Supervisors:

Jens Gravesen
DTU Mathematics
Technical University of Denmark
Matematiktorvet 303S
DK-2800 Kgs. Lyngby
j.gravesen@mat.dtu.dk

Allan Roulund Gersborg[1]
DTU Mechanical Engineering
Technical University of Denmark
Nils Koppels Allé 404
DK-2800 Kgs. Lyngby
agersborg.hansen@gmail.com

Niels Leergaaard Pedersen
DTU Mechanical Engineering
Technical University of Denmark
Nils Koppels Allé 404
DK-2800 Kgs. Lyngby
nlp@mek.dtu.dk

Examiners:

Mathias Stolpe, Technical University of Denmark, Denmark
Yuri Bazilevs, University of California, San Diego, USA
Bert Jüttler, Johannes Kepler University Linz, Austria

[1]Present address: Burmeister & Wain Energy A/S, Lundtoftegårdsvej 93A, DK-2800 Kgs. Lyngby, Denmark

Summary

This thesis brings together the fields of *fluid mechanics*, as the study of fluids and flows, *isogeometric analysis*, as a numerical method to solve engineering problems using computers, and *shape optimization*, as the art of finding "best" shapes of objects based on some notion of goodness. The flow problems considered in the thesis are governed by the 2-dimensional, steady-state, incompressible Navier-Stokes equations at low to moderate Reynolds numbers. We use isogeometric analysis both to solve the governing equations, and as framework for the shape optimization procedure. Isogeometric analysis unites the power to solve complex engineering problems from finite element analysis (FEA) with the ability to effectively represent complex shapes from computer aided design (CAD). The methodology is appealing for flow modeling purposes also due to the inherent high regularity of velocity and pressure approximations, and for shape optimization purposes also due to its tight connection between the analysis and geometry models. The thesis is initiated by short introductions to fluid mechanics, and to the building blocks of isogeometric analysis. As the first contribution of the thesis, a detailed description is given of how isogeometric analysis is applied to flow problems. We present several new discretizations of the velocity and pressure spaces, we investigate these in terms of stability and error convergence properties, and a benchmark flow problem is analyzed. As the second contribution, we show how isogeometric analysis may serve as a natural framework for shape optimization within fluid mechanics. We construct an efficient regularization measure for avoiding inappropriate parametrizations during optimization, and various numerical examples of shape optimization for fluids are considered, serving to demonstrate the robustness of the method. As the third contribution, the methodology is extended to acoustics. We establish a coupled flow-acoustic model of sound propagation through flow in ducts based on isogeometric analysis. Validations using known acoustic duct modes demonstrate the powers of the methodology. Based on the model, we identify distinct geometric effects that enhance the sensitivity of the acoustic signal to the background flow. The thesis is concluded by suggestions for future studies within the field.

Resumé (in Danish)

Denne afhandling omhandler *fluidmekanik*, som er studiet af fluider og væskestrømninger, *isogeometrisk analyse*, som er en numerisk metode til vha. computere at løse problemer indenfor ingeniørvidenskaben, og *formoptimering*, som er kunsten at finde den "bedste" form af et objekt ud fra et givent mål for kvalitet. Strømningsproblemerne, som behandles i denne afhandling, er styret af den 2-dimensionale, stationære, inkompressible Navier-Stokes-ligning ved lave til moderate Reynoldstal. Vi anvender isogeometrisk analyse både til at løse de styrende ligninger og som fundament for formoptimeringen. Isogeometrisk analyse kombinerer evnen til at analysere komplekse ingeniørmæssige problemer fra *finite element*-metoden (FEM) med evnen til på en effektiv måde at repræsentere komplekse former fra *computer aided design* (CAD). Metoden er attraktiv indenfor modellering af væskestrømninger også pga. den indbyggede regularitet af approksimationen af hastigheds- og trykfelterne, og ligeledes indenfor formoptimering også pga. den tætte forbindelse mellem analysemodellen og den geometriske model. Afhandlingen indledes med en kort introduktion til fluidmekanik og til den isogeometriske analyses grundelementer. Som det første bidrag gives en detaljeret beskrivelse af anvendelsen af isogeometrisk analyse på strømningsproblemer. Vi præsentere en række nye diskretiseringer af approksimationsrummene for hastighed- og trykfelterne, vi undersøger disse mht. stabilitet og fejl-konvergens, og vi analyserer et standard-problem indenfor væskestrømninger. Som det andet bidrag vises det, hvorledes isogeometrisk analyse kan anvendes som fundament for formoptimering indenfor fluidmekanik. Vi konstruere et effektivt mål for regularisering, hvilket tjener til at undgå uhensigtsmæssige parametriseringer under optimeringen, og for at demonstrere metodens robusthed løser vi en række numeriske eksempler på formoptimeringsproblemer for fluider. Som det tredje bidrag udvides metoden til akustik. Vi fremsætter en koblet model for lydudbredelsen i væskestrømninger gennem rør baseret på isogeometrisk analyse. Validering af metoden ud fra kendte akustiske *modes* demonstrerer dens potentiale, og med udgangspunkt i modellen identificeres en tydelig geometrisk forstærkning af sensitiviteten af det akustiske signal overfor baggrunds-strømningen. Afhandlingen afsluttes med forslag til fremtidige studier indenfor emnet.

Preface

This thesis is submitted partial fulfillment of the requirements for obtaining the degree of Ph.D. at the Technical University of Denmark (DTU). The Ph.D. project was funded by DTU and carried out as a collaboration between DTU Mathematics and DTU Mechanical Engineering from February 2009 to February 2012. The Ph.D. project was supervised by Jens Gravesen (DTU Mathematics, main supervisor), Allan Roulund Gersborg (DTU Mechanical Engineering, co-superviser from February 2009 to June 2010), and Niels Leergaard Pedersen (DTU Mechanical Engineering, co-supervisor from July 2010 to February 2012). A three months external research stay was conducted at Boeing Research and Technology at The Boeing Company in Washington, USA, with Thomas A. Grandine as supervisor.

The main content of the thesis rests on three research papers written as a part of PhD work and included as appendices. The thesis aims at collecting these and putting them into a broader perspective, with some additional work also included, thereby forming a single, self-contained entity with repetitions kept at a minimum. Many text parts and illustrations in the thesis are taken directly from these papers.

The intended reader of the thesis has a background in engineering with a basic understanding of physics and applied mathematics.

Many persons have contributed actively to the Ph.D. project, and supported me in my work. I would like to thank in particular my supervisors at DTU Jens Gravesen, Allan Roulund Gersborg and Niels Leergaard Pedersen, my supervisors and mentors at Boeing Thomas A. Grandine and Thomas A. Hogan, and my collaborator at University of Southern Denmark Morten Willatzen, for their wisdom and their will to share it with me. Also, I thank my Ph.D. colleague Dang Manh Nguyen, and associate professor at DTU Anton Evgrafov for fruitful discussions. In addition, I thank all my colleagues at DTU Mathematics and DTU Mechanical Engineering, people at the Applied Math group at Boeing Research and Technology, and members of the TopOpt group at DTU, for creating an inspiring scientific and social environment. Last, but not least, I thank my future wife Pia for loving support.

Kgs. Lyngby, February 15, 2012

Peter Nørtoft Nielsen

Contents

Chapter 1

Introduction

The subject of this thesis is isogeometric analysis and shape optimization in fluid mechanics. This chapter gives an account of its motivation, goals, and outline.

1.1 Motivation

Fluid mechanics is the study of fluids and flows, i.e., how gases and liquids behave under the influence of forces. The water running through the plumbing pipes, and the air moving in the atmosphere, are just two out of numerous examples we are all very familiar with. These phenomena are governed by a set of coupled partial differential equations, and the solution of these often rely on computer methods, see e.g. [Durran, 1999; Donea and Huerta, 2003; Mohammadi and Pironneau, 2010]

Shape optimization is the art of determining the best shape of an object in a given situation based on some notion of goodness. Examples of shape optimization problems in fluid mechanics are numerous, see e.g. [Mohammadi and Pironneau, 2004]. They range from the design of microfluidic protein-folding devices [Ivorra et al., 2006], to the design of airplane wings [Painchaud-Oullet et al., 2006], just to mention a few. Again, computer methods are most often employed [Mohammadi and Pironneau, 2010]

Isogeometric analysis is a recently proposed computational method for solving engineering problems [Hughes et al., 2005; Cottrell et al., 2009]. The method unites the powers of finite element analysis (FEA) to solve partial differential equations with the powers of computer aided design (CAD) to represent complex shapes. As such, it provides a natural framework for both analysis and shape optimization in fluid mechanics.

In isogeometric analysis, the geometry representation builds on the methodologies from CAD, where B-splines and NURBS (Non-Uniform Rational B-splines) are standard mathematical tools [Piegl and Tiller, 1995]. Complex domains can be represented exactly, and this is particularly interesting for problems in fluid mechanics, since curvature and cusps are critically important. In isogeometric analysis, the analysis model used to solve the governing equations is tightly connected to the geometric model, using the same type of basis functions. This means that high degrees of continuity for the state variables may

be achieved as well. This is again of extreme importance in flow modeling. Several studies have demonstrated the applicability of isogeometric analysis to problems in fluid mechanics, see e.g. [Bazilevs et al., 2006b; 2007a; Akkerman et al., 2010; Bazilevs and Hughes, 2008; Bazilevs and Akkerman, 2010; Bazilevs et al., 2010b; Akkerman et al., 2011; Hsu et al., 2011].

The mathematical structure of the geometry representation is fixed in isogeometric analysis, and typically only a few design variables are needed to control even quite complex shapes. This means that the geometry can be changed quite easily, and usually without need for heavy re-meshing procedures. In addition, the tight connection between geometry and analysis models alleviates the need for communication between FEA models for the analysis and CAD models for the geometry. All this make isogeometric analysis an ideal tool for shape optimization. The applicability of isogeometric analysis to shape optimization has been demonstrated in several studies, see e.g. [Wall et al., 2008; Cho and Ha, 2009; Qian, 2010; Nagy et al., 2011; Nguyen et al., 2011; Li and Qian, 2011; Qian and Sigmund, 2011].

1.2 Goals

The aim of this thesis is to bring together the fields of fluid mechanics, shape optimization, and isogeometric analysis: *fluid mechanics* as the nature of the problems considered, *shape optimization* as an extension, or add-on, to the flow problems considered, and *isogeometric analysis* as the computational method.

We will firstly study isogeometric analysis of flows. Here, we will investigate various discretizations for the pressure and velocity fields in the mixed formulation of the Navier-Stokes equations that govern flow problems, and we will compare these in terms of error convergence for a problem with a known solution, and apply them to a standard flow problem for benchmarking. Secondly, we will study isogeometric shape optimization of flows. Here, we will investigate a new regularization technique to ensure good parametrizations during the optimization, and we will demonstrate the power of the methodology by applying it to various design problems. Thirdly, applications of isogeometric analysis within flow acoustics will be studied. Here, we will set up a model of sound propagation through flows in ducts with non-trivial geometry. The model will be validated against known acoustic modes in ducts, and based on the model, we will investigate the effects of the duct geometry and flow speed on the sound signal. Finally, we will present some initial investigations of methods for construction of domain parametrizations in isogeometric analysis, and preliminary results for design of idealized airfoils using isogeometric analysis will be presented.

The flow problems considered in the thesis are governed by the steady-state, incompressible Navier-Stokes equations in the laminar regime, i.e., at low to moderate Reynolds numbers. The sound signal in the coupled flow-acoustics problems considered is governed by a linear, time-harmonic, background flow-dependent acoustic equation in the low Mach number regime. As the aim of the thesis is a proof-of-concept, rather than a construction of a full-blown modelling and optimization framework, all studies are for simplicity conducted in two spatial dimensions. For most cases, generalizations to three dimensions are trivial in theory, but cumbersome to implement. We have developed a numerical

framework for doing isogeometric analysis and shape optimization on problems in fluid mechanics. All routines are implemented in MATLAB® [`http://www.mathworks.com`]. The optimization is based on SNOPT [Gill et al., 2008]. All numerical results presented in the thesis are based on this framework.

1.3 Outline

The thesis is organized as follows: In Chapter 2, we introduce the fundamentals of fluid mechanics and the building blocks of isogeometric analysis. In Chapter 3, isogeometric analysis of flows are studied. In Chapter 4, we study isogeometric shape optimization of flows. In Chapter 5, isogeometric analysis of sound propagation through flows are studied. In Chapter 6, we present brief studies on parametrizations and on design of idealized airfoils, along with an outlook on the subject. Finally, conclusions are summarized in Chapter 7.

Chapter 2

Preliminaries

This chapter gives brief introductions to fluid mechanics, and to B-splines and NURBS (Non-Uniform Rational B-Splines) as the building blocks of isogeometric analysis. The introductions are in no way exhaustive, and are merely included to set the scene for the subsequent chapters.

2.1 Fluid Mechanics

Fluid mechanics is the study of fluids and flows, i.e., how gases and liquids behaves under the influence of forces, be it the blood in our veins, the water in our plumbing pipes, or the air in the atmosphere around us. These phenomena are all governed by the same partial differential equations. In the following, we give a short introduction to these, and refer the reader to, e.g., [Donea and Huerta, 2003; Durran, 1999; Reddy and Gartling, 2001; Frisch, 1995; White, 1974] for further reading.

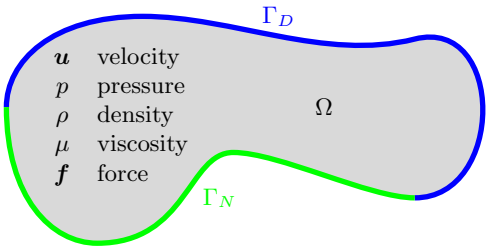

Figure 2.1: *A fluid contained in a flow domain.*

To set the scene, we consider a fluid in a 2-dimensional domain Ω as depicted in Figure 2.1. Assuming the fluid is isothermal, i.e., at constant temperature, the state of the fluid is given by the velocity $\boldsymbol{u} = (u, v)$, the pressure p, and the density ρ. These so-called primitive state variables are governed by the

Navier-Stokes and mass continuity equations:

$$\rho\frac{\partial \boldsymbol{u}}{\partial t} + \rho\,\boldsymbol{u}\cdot\nabla\boldsymbol{u} - \nabla\cdot\boldsymbol{\sigma} - \rho\boldsymbol{f} = \boldsymbol{0} \qquad \text{in } \Omega, \tag{2.1a}$$

$$\frac{\partial \rho}{\partial t} + \nabla\cdot(\rho\boldsymbol{u}) = 0 \qquad \text{in } \Omega, \tag{2.1b}$$

expressing conservation of momentum and mass for the fluid, respectively. Here, t denotes time, $\boldsymbol{\sigma}$ the shear stress tensor, and $\boldsymbol{f}$ additional body forces (such as gravity) acting on the fluid.

The fluids considered in this thesis are assumed to be *incompressible*, i.e., the density ρ is constant, and *Newtonian*, i.e., the stress and the strain rate are linearly related. This gives the following constitutive relation between the stress $\boldsymbol{\sigma}$ and the pressure p and velocity $\boldsymbol{u}$:

$$\boldsymbol{\sigma} = -p\,\mathbb{I} + \mu\left(\nabla\boldsymbol{u} + (\nabla\boldsymbol{u})^T\right), \tag{2.2}$$

where $\mathbb{I}$ is the identity matrix, and μ is the viscosity, which is assumed to be constant. Furthermore, we assume that the flow is *stationary*, i.e., time-independent, and we employ the *convective* formulation for the non-linear inertial term, i.e., $\boldsymbol{u}\cdot\nabla\boldsymbol{u} = (\boldsymbol{u}\cdot\nabla)\boldsymbol{u}$.

With the above assumptions, Equations (2.1) may then be rewritten as the following steady-state, incompressible Navier-Stokes equations:

$$\rho\,(\boldsymbol{u}\cdot\nabla)\boldsymbol{u} + \nabla p - \mu\nabla\cdot\left(\nabla\boldsymbol{u} + (\nabla\boldsymbol{u})^T\right) - \rho\boldsymbol{f} = \boldsymbol{0} \qquad \text{in } \Omega, \tag{2.3a}$$

$$\nabla\cdot\boldsymbol{u} = 0 \qquad \text{in } \Omega. \tag{2.3b}$$

By use of the incompressibility condition (2.3b) in (2.3a), this system may be further reduced to:

$$\rho\,(\boldsymbol{u}\cdot\nabla)\boldsymbol{u} + \nabla p - \mu\nabla^2\boldsymbol{u} - \rho\boldsymbol{f} = \boldsymbol{0} \qquad \text{in } \Omega, \tag{2.4a}$$

$$\nabla\cdot\boldsymbol{u} = 0 \qquad \text{in } \Omega. \tag{2.4b}$$

The equations above govern the flow in the interior of the domain Ω, and they must be augmented by suitable boundary conditions on the boundary $\Gamma \equiv \partial\Omega$. Here, we assume that the velocity is given as $\boldsymbol{u}^*$ along the Dirichlet part Γ_D, and that a condition on the pressure and the normal derivative of the velocity applies along the Neumann part Γ_N:

$$u_i = u_i^* \qquad \text{on } \Gamma_D, \tag{2.5a}$$

$$(\,\mu\nabla u_i - p\,\boldsymbol{e}_i\,)\cdot\boldsymbol{n} = 0 \qquad \text{on } \Gamma_N, \tag{2.5b}$$

where $i = 1, 2$, $\boldsymbol{e}_i$ is the i^{th} unit basis vector, $\Gamma = \Gamma_D \cup \Gamma_N$, and $\Gamma_N \cap \Gamma_N = \emptyset$. Typically, Dirichlet boundary conditions (2.5a) are used at inlets and fixed boundaries, while Neumann boundary conditions (2.5b) are used at outlets [Rannacher, 1995].[1] At symmetry boundaries, the two conditions are combined. When full Dirichlet boundary conditions are employed, i.e., $\Gamma_N = \emptyset$ and $\Gamma = \Gamma_D$, a condition on the pressure, such as $\iint_\Omega p\,\mathrm{d}A = 0$, must be included, as the pressure is otherwise only determined up to an additive constant.

[1] The expression $(\,\mu\nabla u_i - p\,\boldsymbol{e}_i\,)\cdot\boldsymbol{n} = 0$ is the "natural" open boundary conditions for Equations (2.4). For Equations (2.3), the "natural" open boundary condition is $\sigma\cdot\boldsymbol{n} = \boldsymbol{0}$.

Flows may crudely be separated into two very different regimes: *laminar* flows are characterized by smooth and ordered fluid motion, whereas *turbulent* flows exhibit random and fluctuating fluid motion. The *Reynolds* number provides a useful measure of how laminar or turbulent a given flow is:

$$\mathrm{Re} = \frac{\rho U L}{\mu}, \tag{2.6}$$

where U is a characteristic flow speed and L is a characteristic length scale of the problem. The Reynolds number measures the importance of (non-linear) inertial forces to viscous forces in the Navier-Stokes equation (2.4a). The higher the Re, the more non-linear the equation, and the more turbulent the flow. For turbulent flows, spatial and temporal (stationarity) symmetries are broken.

Equations (2.4)–(2.5) constitute a boundary value problem based on a non-linear second order partial differential equation system. Only few formulations of this problem are known to have an analytical solution, and numerical methods are most often the only strategy to solve it. From a theoretical point of view, there are no guarantees for neither existence nor uniqueness of a solution. From a practical point of view, solutions may often be found numerically, provided the problem is sufficiently well behaved. The flow problems considered in this thesis are all at low to moderate Reynolds numbers. Such conditions may be found for sufficiently high (kinematic) viscosities $\nu = \mu/\rho$, low flow speeds U, and small scales L. Moreover, stability of solutions are for simplicity not considered.

2.2 B-splines and NURBS

The building blocks of the isogeometric method are B-splines and NURBS (Non-Uniform Rational B-splines), which are widely used in Computer Aided Design (CAD) systems. In isogeometric analysis, they are used both as basis for describing the geometry, and as basis for approximating the state variables in the governing equations. In the following, we briefly revise the basic concepts of these functions, in their "original" geometric setting, and some often used algorithms are outlined. The concepts are introduced in the plane, but they may be generalized to higher dimensions in a straightforward way. The reader is referred to, e.g., [Piegl and Tiller, 1995; Cottrell et al., 2009; Gravesen, 2002] for more thorough introductions to the subject.

Univariate B-splines: Curves

Referring to Figure 2.2a, we consider a parametrization of a curve $\gamma : \mathbb{R} \to \mathbb{R}^2$ of the following form:

$$\boldsymbol{\gamma}(\xi) = \big(x(\xi)\,,\, y(\xi) \big) = \sum_{i=1}^{n} \boldsymbol{x}_i \mathcal{N}_i(\xi), \tag{2.7}$$

where the basis functions $\mathcal{N}_i : \mathbb{R} \to \mathbb{R}$ are univariate B-splines, $\boldsymbol{x}_i \in \mathbb{R}^2$ are *control points*[2], and n is the number of basis functions and control points. We refer to the curve itself as a *spline curve*, or simply just a *spline*.

[2] Although similar letters are used to denote control points $\boldsymbol{x}_i = (x_i, y_i)$ and spatial coordinates $\boldsymbol{X} = (x, y)$, we emphasize that these should not be confused.

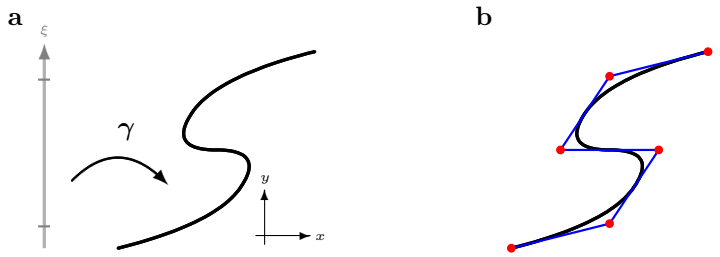

Figure 2.2: **a**: *A parametrization of a curve in* $\mathbb{R}^2$. **b**: *A spline curve (black line) and the corresponding control points (red markers) for the polynomial degree* $q = 2$ *and the knot vector* $\Xi = \{0, 0, 0, 1/4, 1/2, 3/4, 1, 1, 1\}$.

To define the univariate B-splines entering the parametrization above, we firstly define a *knot vector*:

Definition 1. A knot vector, or knot sequence, is a non-decreasing sequence $\Xi = \{\xi_1, \ldots, \xi_{n+q+1}\}$, where $\xi_i \in \mathbb{R}$ is the i^{th} knot, and $n + q + 1$ is the number of knots, where n is the number of basis functions of polynomial degree q on the knot vector.

The knots partition the parameter domain into *knot spans*. A knot vector is called *uniform* if the knots are equidistant, i.e., all non-vanishing knot spans have the same size, and *non-uniform*, otherwise. If $\xi_\ell < \xi_{\ell+1} = \ldots = \xi_{\ell+\nu} < \xi_{\ell+\nu+1}$, we say that the knot $\xi_{\ell+1} = \ldots = \xi_{\ell+\nu}$ has *multiplicity* ν. Knots with $\nu = 1$ are called *simple*, while knots with $\nu = q$ are said to have *full* multiplicity. Finally, a knot vector is said to be *open* if the boundary knots have multiplicity $\nu = q + 1$.

With the knot vector defined, univariate B-splines are piecewise polonymials over the spans of the knot vector, as expressed in the following definition:

Definition 2 (Cox–de Boor recursion formula)**.** Univariate B-splines $\mathcal{N}^q_\Xi : \mathbb{R} \to \mathbb{R}$ are defined recursively from a polynomial degree $q \in \mathbb{N}$ and a knot vector Ξ:

$$\mathcal{N}^j_{\Xi,i}(\xi) = \begin{cases} 1 & \text{if } \xi_i \leq \xi < \xi_{i+1} \\ 0 & \text{otherwise} \end{cases} \tag{2.8a}$$

for $j = 0$ and $i = n + q$, and

$$\mathcal{N}^j_{\Xi,i}(\xi) = \frac{\xi - \xi_i}{\xi_{i+j} - \xi_i}\mathcal{N}^{j-1}_{\Xi,i}(\xi) + \frac{\xi_{i+j+1} - \xi}{\xi_{i+j+1} - \xi_{i+1}}\mathcal{N}^{j-1}_{\Xi,i+1}(\xi) \tag{2.8b}$$

for $j = 1, 2, \ldots, q$ and $i = 1, \ldots, n + q - j$, and where we define $1/(\xi_k - \xi_\ell) \equiv 0$ if $\xi_k = \xi_\ell$.

Univariate B-splines are thus determined by the polynomial degree and the knot vector. Examples of B-splines from different polynomial degrees and knot vectors are shown in Figure 2.3.

Some important properties of B-splines are contained in the following:

Theorem 1. *B-splines with knot vector* Ξ *and polynomial degree* q *fulfill:*

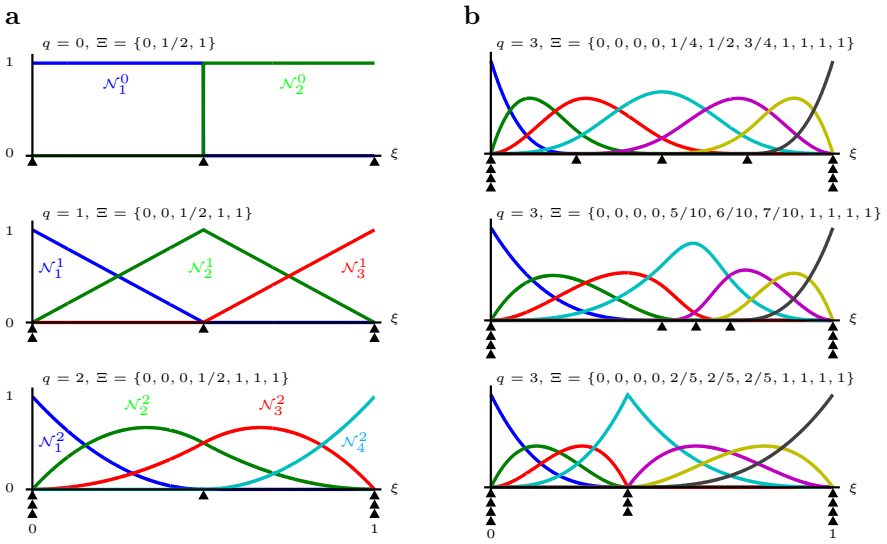

Figure 2.3: **a**: *B-splines for polynomial degrees $q \in \{0, 1, 2\}$ and corresponding open knot vectors with a simple interior knot.* **b**: *B-splines for polynomial degree $q = 3$ and open knot vectors with different simple and full interior knots.*

1. *B-splines are non-negative, i.e., $\mathcal{N}_i(\xi) \geq 0$ for all ξ.*
2. *The support of $\mathcal{N}_i$ is $[\xi_i, \xi_{i+q+1}]$, i.e., B-splines have compact support.*
3. *The restriction of the B-spline $\mathcal{N}_i(\xi)$ to the open knot interval $]\xi_i, \xi_{i+1}[$ is a polynomial of degree q.*
4. *B-splines form a partition of unity, i.e., $\sum_{i=1}^{n} \mathcal{N}(\xi) = 1$ for all $\xi \in [\xi_{q+1}, \xi_{n+1}]$.*
5. *The continuity of $\mathcal{N}_i$ across a knot with multiplicity ν is $q - \nu$.*

The derivative of a B-spline of polynomial degree q is itself a B-spline of polynomial degree $q - 1$. The derivative may be computed recursively from the following theorem, from which also formulae for higher order derivative may be derived:

Theorem 2. *The derivative of the i^{th} B-spline with polynomial degree q and knot vector Ξ is given by:*

$$\frac{\mathrm{d}\mathcal{N}^q_{\Xi,i}}{\mathrm{d}\xi}(\xi) = \frac{q}{\xi_{i+q} - \xi_i}\mathcal{N}^{q-1}_{\Xi,i}(\xi) - \frac{q}{\xi_{i+q+1} - \xi_{i+1}}\mathcal{N}^{q-1}_{\Xi,i+1}(\xi). \tag{2.9}$$

With the B-splines in place, we see that a spline curve, as given in Equation (2.7), is defined from a polynomial degree, a knot vector, and a set of control points. Figure 2.2b shows an example of a spline curve in the plane.

A spline curve inherits many of the properties of its generating B-splines, as stated in Theorem 1. In particular, we mention the property of *locality*, meaning that moving the i^{th} control point of a curve of degree q only affects the image of the parameter values $\xi \in [\xi_i, \xi_{i+q+1}]$. Additional properties worth mentioning

include the *affine covariance* property, meaning that any affine transformation of the spline, i.e. a translation and a linear mapping, may be obtained by applying it directly to the control points, and the *convex hull* property, meaning that a spline of degree q is contained in the polygon obtained by connecting each control point of the spline to the q consecutive control points.

A spline curve may be refined, without changing the parametrization, by inserting more knots in the knot vector, by elevating the polynomial degree, or by a combination of the two. These methods are referred to as h, p, and k refinement, respectively [Cottrell et al., 2009]. The often used knot insertion process is described in the following:

Theorem 3 (Knot insertion)**.** *Let $\gamma(\xi)$ be a spline curve with polynomial degree q, knot vector $\Xi = \{\xi, \ldots, \xi_{n+q+1}\}$ and control points $\mathcal{X} = \{\boldsymbol{x}_1, \ldots, \boldsymbol{x}_n\}^T$. By inserting m knots, γ may be represented identically by the same polynomial degree q, the extended knot vector $\widetilde{\Xi} = \{\tilde{\xi} = \xi_1, \ldots, \tilde{\xi}_{n+q+1+m} = \xi_{n+q+1}\} \supset \Xi$, and the extended control points $\widetilde{\mathcal{X}} = \{\tilde{\boldsymbol{x}}_1, \ldots, \tilde{\boldsymbol{x}}_{n+m}\}^T$, where:*

$$\widetilde{\mathcal{X}} = \boldsymbol{T}^q \mathcal{X}, \tag{2.10a}$$

$$\boldsymbol{T}^0_{i,j} = \begin{cases} 1 & \text{if} \quad \tilde{\xi}_i \in [\xi_j, \xi_{j+1}) \\ 0 & \text{otherwise} \end{cases}, \tag{2.10b}$$

$$\boldsymbol{T}^{r+1}_{i,j} = \frac{\tilde{\xi}_{i+r} - \xi_j}{\xi_{j+r} - \xi_j} \boldsymbol{T}^r_{i,j} + \frac{\xi_{j+r+1} - \tilde{\xi}_{i+r}}{\xi_{j+r+1} - \xi_{j+1}} \boldsymbol{T}^r_{i,j+1}, \tag{2.10c}$$

for $r = 1, \ldots, q-1$ in Equation (2.10c)*.*

Bivariate Tensor Product B-splines: Surfaces

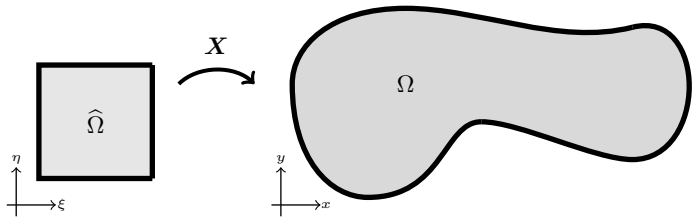

Figure 2.4: *A parametrization of a domain in $\mathbb{R}^2$.*

Referring to Figure 2.4, surfaces may be parametrized analogously to Equation (2.7) through tensor product structures:

$$\boldsymbol{X}(\xi, \eta) = \big(x(\xi, \eta),\, y(\xi, \eta) \big) = \sum_i^n \sum_j^m \boldsymbol{x}_{i,j}\, \mathcal{N}^q_{\Xi,i}(\xi)\, \mathcal{M}^r_{\Psi,j}(\eta), \tag{2.11}$$

where $\mathcal{N}^q_{\Xi,i}$ are the n univariate B-splines with polynomial degree q and knot vector Ξ in the parametric ξ-dimension, $\mathcal{M}^r_{\Psi,j}$ are the m univariate B-splines with polynomial degree r and knot vector Ψ in the parametric η-dimension, and $\boldsymbol{x}_{i,j} \in \mathbb{R}^2$ is the *control net*. We refer to the domain itself as a *spline surface*, or again simply just a *spline*.

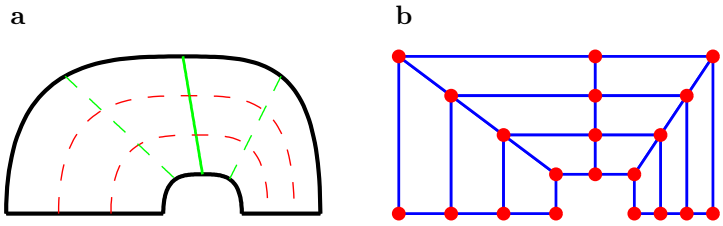

Figure 2.5: *A spline domain in* $\mathbb{R}^2$ (**a**) *and its corresponding control net* (**b**) *for polynomial degrees* $q = r = 3$ *and knot vectors* $\Xi = \{0,0,0,0,1,1,1,1\}$ *and* $\Psi = \{0,0,0,0,1/2,1,1,1,1\}$.

We see that a spline surface is determined by two polynomial degrees, two knot vectors, and a control net. An example is depicted in Figure 2.5.

By a simple reordering, and a slight change of notation in Equation (2.11), we may write the parametrization as:

$$\boldsymbol{X}(\xi,\eta) = \sum_{k=1}^{N} \boldsymbol{x}_k \, \mathcal{P}_k^g(\xi,\eta), \tag{2.12}$$

where $\boldsymbol{x}_k$ are still the control points, and $\mathcal{P}_k^g : \widehat{\Omega} \to \mathbb{R}^2$ are the $N = n\,m$ *bivariate tensor product B-splines*:

$$\mathcal{P}_k^g(\xi,\eta) = \mathcal{N}_{\Xi,i}^q(\xi)\, \mathcal{M}_{\Psi,j}^r(\eta), \tag{2.13}$$

where $k = (j-1)n+i$ for $i = 1,\ldots,n$ and $j = 1,\ldots,m$. The superscript g indicates that the functions refer to specific knot vectors, Ξ and Ψ, and polynomial degrees, q and r, for the geometry.

The construction of a bivariate tensor product B-spline from two univariate B-splines, associated to each their polynomial degree and knots vector, is illustrated in Figure 2.6a. The basis functions $\mathcal{P}_i$ are functions on parameter space $\widehat{\Omega}$. We may consider them as functions on physical space Ω as well through the composition $\mathcal{P}_i \circ \boldsymbol{X}^{-1}$, as shown in Figure 2.6b.

NURBS Parametrizations

The class of geometries that can be parametrized may be enlarged by the use of NURBS, which are rational B-splines on non-uniform knot vectors. We mention, in particular, that geometric objects such as circles and spheres may be described exactly by the use of NURBS. Although most of the subsequent studies are based on B-splines, we briefly touch upon NURBS below.

A NURBS curve is parametrized as in Equation (2.7), but with the basis functions $\mathcal{N}$ replaced by univariate NURBS $\mathcal{B}$. We may define univariate NURBS $\mathcal{B}_{\Xi,W,i}^q : \mathbb{R} \to \mathbb{R}$ from the univariate B-splines in Definition 2 and a set of weights $W = \{w_1,\ldots,w_n\}$, where $w_i \in \mathbb{R}$:

$$\mathcal{B}_{\Xi,W,i}^q(\xi) = \frac{w_i\, \mathcal{N}_{\Xi,i}^q(\xi)}{\sum_{j=1}^{n} w_j \mathcal{N}_j^q(\xi)}. \tag{2.14}$$

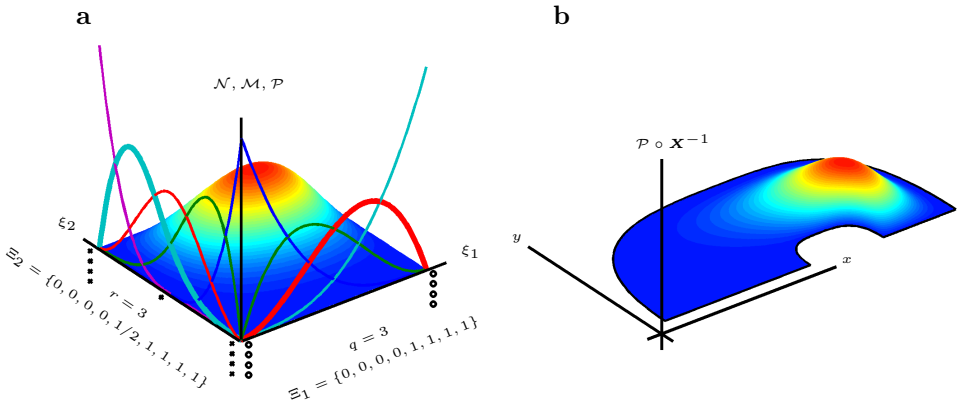

Figure 2.6: **a***: Construction in parameter space of a bivariate tensor product B-spline (surface) from two univariate B-splines (lines in bold) of given polynomial degrees and knot vectors (crosses and circles).* **b***: The bivariate tensor product B-spline over the physical space, using the geometry from Figure 2.5.*

A NURBS surface is parametrized as in Equation (2.12), but with the basis functions $\mathcal{P}$ replaced by bivariate tensor product NURBS $\mathcal{R}$. We may define bivariate NURBS $\mathcal{R}_k^g : \widehat{\Omega} \to \mathbb{R}$ from the bivariate B-splines in Equation (2.13) and the weights $W = \{w_1, \ldots, w_N\}$ with $w_k \in \mathbb{R}$ for $k = 1, \ldots, N = n\,m$:

$$\mathcal{R}_k^g(\xi, \eta) = \frac{w_k\, \mathcal{P}_k^g(\xi, \eta)}{\sum_{k=1}^{N} w_k\, \mathcal{P}_k^g(\xi, \eta)}. \tag{2.15}$$

Many of the properties of B-splines naturally carry over to NURBS, e.g. partition of unity, continuity, support, and affine covariance. Owing to the partition of unity property of B-splines in Theorem 2, NURBS reduce to B-splines when all weights are 1. Formulae for the derivatives of NURBS may be found in e.g. [Piegl and Tiller, 1995].

Multiple Patches

The parametrization in Equation (2.12) covers a single patch. Often, a geometry cannot be parametrized by a single patch. Multiple patches must then be employed, cf. Figure 2.7.

C^0 continuity of the geometry across patches with identical polynomial degrees and knot vectors is trivially achieved be equating the outer row/column of control points of the joining patches. C^1 and higher continuities across patches put requirements on two or more rows/columns of the control net.

Patches with different refinement levels, i.e., different knot vectors, may be stitched together by use of the knot insertion relation in Equation (2.10). This applies both to the control net, and to the basis functions.

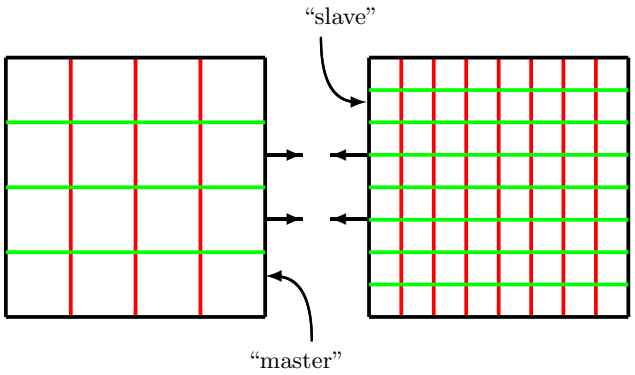

Figure 2.7: *Stitching of two patches.*

Chapter 3

Isogeometric Analysis of Flows

In this chapter, we study how B-splines and NURBS may be used to solve engineering problems within fluid mechanics. More specifically, we apply isogeometric analysis to the 2-dimensional, steady state, incompressible Navier-Stokes equation with Dirichlet boundary conditions, and we investigate such things as stability, error convergence and benchmark comparisons of the method. The chapter summarizes the findings in [Nielsen et al., 2011a] included in Appendix B.

3.1 Introduction

Since the introduction of isogeometric analysis in [Hughes et al., 2005], the methodology has been applied to various flow problems and proved its value within the field of fluid mechanics. Some of the first studies were on steady-state incompressible Stokes flow in the benchmarking lid-driven square cavity [Bazilevs et al., 2006b]. Subsequent analysis of the full time dependent Navier-Stokes equations using the isogeometric method has shown its advantages both in terms of continuity of state variables [Akkerman et al., 2010] and the ability to accurately represent complicated dynamic flow domains [Bazilevs and Hughes, 2008]. Benchmarking of the method for turbulent flows has shown very nice performance of the method [Bazilevs and Akkerman, 2010; Bazilevs et al., 2010b]. Applications to free-surface flows [Akkerman et al., 2011], and to modelling of wind-turbine aerodynamics [Hsu et al., 2011] have also been made.

An important issue in the analysis of the mixed formulation of the governing equations for fluids is the stability of the element, or discretization, used to approximate the state variables. The first stable B-spline discretization for the Stokes problem was proposed in [Bazilevs et al., 2006b]. Recently, two more families of stable B-spline discretizations were identified in [Buffa et al., 2011], thereby further emphasizing how easily high degrees of continuity may be achieved in isogeometric analysis. Mathematical proofs of the stability of a range of discretizations have very recently been made [Bressan, 2010; Personal communication].

Below, we firstly outline how flow problems may be solved using isogeometric

analysis. Secondly, we extend the list of stable B-spline discretizations for the 2D steady state, incompressible Stokes problem. Thirdly, we apply the method to the non-linear 2D steady state, incompressible Navier-Stokes problem and examine how these discretizations perform in terms of error convergence based on a flow problem with an analytical solution. Finally, the benchmarking lid-driven square cavity is analyzed and the results of the discretizations compared to data from the literature.

To set the scene, we consider a viscous, incompressible, isothermal, Newtonian fluid in a steady-state flow through a domain Ω. We assume full Dirichlet boundary conditions along the boundary Γ, and vanishing mean pressure over the domain. The governing equations read, cf. Chapter 2.1:

$$\rho\,(\boldsymbol{u}\cdot\nabla)\boldsymbol{u} + \nabla p - \mu\nabla^2\boldsymbol{u} - \rho\boldsymbol{f} = \boldsymbol{0} \qquad \text{in } \Omega, \tag{3.1a}$$

$$\nabla\cdot\boldsymbol{u} = 0 \qquad \text{in } \Omega. \tag{3.1b}$$

$$\boldsymbol{u} = \boldsymbol{u}_D \qquad \text{on } \Gamma, \tag{3.1c}$$

$$\iint_{\Omega} p\,\mathrm{d}A = 0, \tag{3.1d}$$

where p, $\boldsymbol{u}$, ρ, μ, and $\boldsymbol{f}$ denote pressure, velocity, density, viscosity, and body forces, respectively.

3.2 Isogeometric Method

In the following, we outline how B-splines- and NURBS-based isogeometric analysis may be used to solve the flow problem (3.1) numerically. The method builds on Galerkin's method, known from traditional finite element methods, in which the weak form of the governing partial differential equations is discretized to form a simpler system of algebraic equations. In addition, we parametrize the physical domain, where the equations are formulated, and pull these back to solve them on the parameter domain, equivalent to the isoparametric concept in finite element methods. B-splines and NURBS are used as basis functions both for the geometry and the flow variables. More details may be found in [Cottrell et al., 2009; Reddy and Gartling, 2001; Donea and Huerta, 2003].

Flow Domain Parametrization

We firstly parametrize the physical flow domain by a single patch, see Figure 3.1. We take the parameter domain $\widehat{\Omega}$ as the unit square, i.e. $\widehat{\Omega} = [0,1]^2$, and use the bivariate NURBS defined in Equation (2.15). The parametrization $\boldsymbol{X}:\ [0,1]^2 \to \mathbb{R}^2$ reads:

$$\boldsymbol{X}(\xi,\eta) = \sum_{i=1}^{N^g_{\text{var}}} \boldsymbol{x}_i \mathcal{R}^g_i(\xi,\eta), \tag{3.2}$$

where $\boldsymbol{x}_i$ are the control points, $\mathcal{R}^g_i$ are the NURBS, N^g_{var} is the number of NURBS and control points, and the superscript g indicates that the NURBS functions refer to polynomial degrees, open knots vectors and weights that are specific for the geometry representation, cf. Equation (2.12).

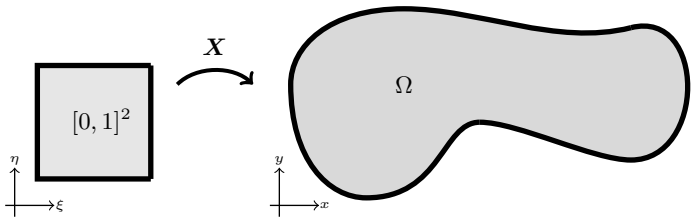

Figure 3.1: *A parametrization of the flow domain* Ω.

For any scalar variable, we will consider it both as a function $\overline{h}$ on physical space Ω, and as a function h on parameter space $[0,1]^2$. For later reference, the gradient $\overline{\nabla}$ and the Hessian matrix $\overline{\boldsymbol{H}}$ in physical space Ω of $\overline{h}$ are related to their counterparts ∇, $\boldsymbol{H}$, and h in parameter space $[0,1]^2$ by the following relations:

$$\nabla h = \boldsymbol{J}^T \, \overline{\nabla h}, \tag{3.3a}$$

$$\boldsymbol{H}(h) = \boldsymbol{J}^T \, \overline{\boldsymbol{H}}(\overline{h}) \, \boldsymbol{J} + \sum_{m=1}^{2} \boldsymbol{H}(x_m) \, \boldsymbol{e}_m^T \, \overline{\nabla h}, \tag{3.3b}$$

where

$$\boldsymbol{J} \equiv \begin{bmatrix} \frac{\partial x}{\partial \xi} & \frac{\partial x}{\partial \eta} \\ \frac{\partial y}{\partial \xi} & \frac{\partial y}{\partial \eta} \end{bmatrix} \tag{3.4}$$

is the Jacobian matrix of the parametrization, and $\boldsymbol{e}_1 = (1\ 0)^T$ and $\boldsymbol{e}_2 = (0\ 1)^T$ are the standard unit vectors.

Field Approximations

In a similar fashion as for the geometry representation in Equation (3.2) above, we seek approximations of the velocity $\boldsymbol{u} : [0,1]^2 \to \mathbb{R}^2$ and pressure $p : [0,1]^2 \to \mathbb{R}$ as linear combinations of the basis functions defined above. Since NURBS are only needed to represent the geometry, and not the velocity and pressure, we will for simplicity use B-splines to approximate the state variables:

$$u_k(\xi,\eta) = \sum_{i=1}^{N_{\text{var}}^{u_k}} \underline{u}_{k,i} \mathcal{P}_i^{u_k}(\xi,\eta), \tag{3.5a}$$

$$p(\xi,\eta) = \sum_{i=1}^{N_{\text{var}}^{p}} \underline{p}_i \mathcal{P}_i^{p}(\xi,\eta), \tag{3.5b}$$

where $k = 1, 2$ in (3.5a) refers to the two components of the velocity field, $\mathcal{P}_i^{u_k}$ denote the B-spline basis functions for the k^{th} component of the velocity field, while $\mathcal{P}_i^p$ similarly denote the B-spline basis functions for the pressure field, as defined in Equation (2.13). They refer to separate sets of polynomial degrees and knot vectors that are in general not the same. $N_{\text{var}}^{u_k}$ and N_{var}^{p} are the number of velocity and pressure basis functions, while $\underline{u}_k$ and $\underline{p}$ are the unknown control variables for the velocity and pressure that are to be determined.

The velocity and pressure fields in Equations (3.5) are defined in parameter space, while the governing equations (3.1) are formulated in physical space. To evaluate the fields in physical space, the inverse of the geometry parametrization $\boldsymbol{X}$ is used; the pressure $p : \Omega \to \mathbb{R}$ over the physical domain is computed as $p \circ \boldsymbol{X}^{-1}$, and the velocity $\boldsymbol{u} : \Omega \to \mathbb{R}^2$ over the physical domain as $\boldsymbol{u} \circ \boldsymbol{X}^{-1}$, mapping each velocity component as a scalar field. With abuse of notation, we here use the same symbol for the state variables both in parameter space and in physical space. To evaluate gradients and Hessians of the fields in physical space, the relations in Equation (3.3) may be used.

Boundary Conditions

For simplicity we impose the Dirichlet boundary conditions in (3.1c) *strongly* as opposed to the weak enforcement suggested in [Bazilevs and Hughes, 2007; Bazilevs et al., 2007b]. Hereby, we avoid the need for definition of penalization parameters.

B-splines have compact support, as stressed in Theorem 1. This means that only a few of the velocity basis functions $\mathcal{P}^{u_k}$ in Equation (3.5a) have support on Γ. We can simply arrange the functions $\mathcal{P}^{u_k}$ so that the first $N_{\text{dof}}^{u_k}$ of these do *not* have support on the boundary, and the corresponding control variables of these are thus "degrees of freedom", while the last $N_{\text{fix}}^{u_k} = N_{\text{var}}^{u_k} - N_{\text{dof}}^{u_k}$ *have* support on Γ, and the corresponding control variables are thus "fixed":

$$u_k = \sum_{i=1}^{N_{\text{dof}}^{u_k}} \underline{u}_{k,i} \mathcal{P}_i^{u_k} + \sum_{i=N_{\text{dof}}^{u_k}+1}^{N_{\text{var}}^{u_k}} \underline{u}_{k,i} \mathcal{P}_i^{u_k}. \tag{3.6}$$

The strong imposition is done by directly specifying suitable values for these last $N_{\text{fix}}^{u_k}$ velocity control variables $\underline{u}_{k,i}$, so that the sum in Equation (3.5a) approximates the specified value $\boldsymbol{u}_D$ in (3.1c). If $\boldsymbol{u}_D$ lies within the function space spanned by $\mathcal{P}_i^{u_k}$, the conditions are satisfied exactly; otherwise they are only satisfied in a least square sense.

For the pressure, we note that only the pressure *gradient* appears in the governing equations (3.1). The pressure is thus only determined up to an arbitrary constant, which is dealt with by the specification of the mean pressure in Equation (3.1d). By inserting the image in physical space of the pressure approximation in Equation (3.5b) into Equation (3.1d), interchanging the order of summation and integration, and finally pulling the integrals back to parameter space, we arrive at the following equation:

$$\boldsymbol{P}\,\underline{\boldsymbol{p}} = 0, \tag{3.7}$$

where $\underline{\boldsymbol{p}}$ is the column vector of pressure control variables, and $\boldsymbol{P}$ is the row vector of pressure basis function integrals:

$$\boldsymbol{P}_i = \iint_{[0,1]^2} \mathcal{P}_i^p \det\left(\boldsymbol{J}\right) \mathrm{d}\xi\, \mathrm{d}\eta. \tag{3.8}$$

Since no pressure control variables needs to be fixed, we have $N_{\text{dof}}^p = N_{\text{var}}^p$ and $N_{\text{fix}}^p = 0$.

Weak Form of the Governing Equations

The governing equations (3.1) are cast into their *weak*, or *variational*, form. For this we use the image in physical space of the B-spline introduced above as *weight functions* for the governing equations. We will use only the first $N_{\text{dof}}^{u_k}$ velocity basis functions, since these have no support on the fixed boundary. We multiply the k^{th} component of the Navier-Stokes equation (3.1a) by an arbitrary weight function $\mathcal{P}_i^{u_k}$ among these velocity basis functions, and the incompressibility equation (3.1b) by an arbitrary weight function $\mathcal{P}_j^p$ among the pressure basis functions, integrate the resulting equations over Ω, and then simplify using integration by parts. After some manipulations, we find the following weak form of the governing equations:

$$0 = \iint_{\Omega} \Big((\mu \nabla \mathcal{P}_i^{u_k} + \rho \mathcal{P}_i^{u_k} \boldsymbol{u}) \cdot \nabla u_k - (p \nabla \mathcal{P}_i^{u_k} + \rho \mathcal{P}_i^{u_k} \boldsymbol{f}) \cdot \boldsymbol{e}_k \Big) \, \mathrm{d}x \, \mathrm{d}y \tag{3.9a}$$

$$0 = \iint_{\Omega} \mathcal{P}_j^p \, (\nabla \cdot \boldsymbol{u}) \, \mathrm{d}x \, \mathrm{d}y \tag{3.9b}$$

for $k = 1, 2$, $i = 1, \ldots, N_{\text{dof}}^{u_k}$ and $j = 1, \ldots, N_{\text{dof}}^{p}$.

Matrix Equation

Finally, we insert the image in physical space of the approximations of the velocity and pressure fields (3.5) into the weak form (3.9) of the governing equations, split the superpositions of $\boldsymbol{u}$ into parts with support on the fixed boundary and parts without as in Equation (3.6), interchange the order of summation and integration, rearrange to get the unknown terms on the LHS and the known terms on the RHS, and pull the integration back to parameter space, using Equation (3.3). This gives:

$$\overbrace{\begin{bmatrix} \mu \boldsymbol{K}_1 + \rho \boldsymbol{C}_1(\bar{\boldsymbol{u}}) & \boldsymbol{0} & -\boldsymbol{G}_1^T \\ \boldsymbol{0} & \mu \boldsymbol{K}_2 + \rho \boldsymbol{C}_2(\bar{\boldsymbol{u}}) & -\boldsymbol{G}_2^T \\ \boldsymbol{G}_1 & \boldsymbol{G}_2 & \boldsymbol{0} \end{bmatrix}}^{\boldsymbol{\mathcal{K}}(\boldsymbol{U})} \overbrace{\begin{bmatrix} \bar{\boldsymbol{u}}_1 \\ \bar{\boldsymbol{u}}_2 \\ \bar{\boldsymbol{p}} \end{bmatrix}}^{\boldsymbol{U}}$$
$$= \underbrace{\rho \begin{bmatrix} \boldsymbol{f}_1 \\ \boldsymbol{f}_2 \\ \boldsymbol{0} \end{bmatrix} - \begin{bmatrix} \mu \boldsymbol{K}_1^\star + \rho \boldsymbol{C}_1^\star(\bar{\boldsymbol{u}}) & \boldsymbol{0} \\ \boldsymbol{0} & \mu \boldsymbol{K}_2^\star + \rho \boldsymbol{C}_2^\star(\bar{\boldsymbol{u}}) \\ \boldsymbol{G}_1^\star & \boldsymbol{G}_2^\star \end{bmatrix} \begin{bmatrix} \bar{\boldsymbol{u}}_1^\star \\ \bar{\boldsymbol{u}}_2^\star \end{bmatrix}}_{\boldsymbol{\mathcal{F}}}, \tag{3.10}$$

or simply $\boldsymbol{\mathcal{K}}(\boldsymbol{U})\,\boldsymbol{U} = \boldsymbol{\mathcal{F}}$, with

$$\underline{\boldsymbol{K}}_{k_{i,j}} = \iint_{[0,1]^2} \nabla^T \mathcal{P}_i^{u_k} \, \boldsymbol{J}^{-1} \, \boldsymbol{J}^{-T} \, \nabla \mathcal{P}_j^{u_k} \, \det\big(\boldsymbol{J}\big) \, \mathrm{d}\xi \, \mathrm{d}\eta, \tag{3.11a}$$

$$\underline{\boldsymbol{C}}_{k_{i,j}} = \iint_{[0,1]^2} \mathcal{P}_i^{u_k} \, \boldsymbol{u}^T(\underline{\boldsymbol{u}}) \, \boldsymbol{J}^{-T} \, \nabla \mathcal{P}_j^{u_k} \, \det\big(\boldsymbol{J}\big) \, \mathrm{d}\xi \, \mathrm{d}\eta, \tag{3.11b}$$

$$\underline{\boldsymbol{G}}_{k_{i,j}} = \iint_{[0,1]^2} \mathcal{P}_i^{p} \, \boldsymbol{e}_k^T \, \boldsymbol{J}^{-T} \, \nabla \mathcal{P}_j^{u_k} \, \det\big(\boldsymbol{J}\big) \, \mathrm{d}\xi \, \mathrm{d}\eta, \tag{3.11c}$$

$$\boldsymbol{f}_{k_i} = \iint_{[0,1]^2} \mathcal{P}_i^{u_k} \, \boldsymbol{e}_k^T \, \boldsymbol{f} \, \det\big(\boldsymbol{J}\big) \, \mathrm{d}\xi \, \mathrm{d}\eta, \tag{3.11d}$$

$$\underline{\boldsymbol{K}}_k = \begin{bmatrix} \boldsymbol{K}_k & \boldsymbol{K}_k^\star \end{bmatrix} \quad \left(N_{\text{dof}}^{u_k} \times (N_{\text{dof}}^{u_k} + N_{\text{fix}}^{u_k})\right), \tag{3.11e}$$

$$\underline{\boldsymbol{C}}_k = \begin{bmatrix} \boldsymbol{C}_k & \boldsymbol{C}_k^\star \end{bmatrix} \quad \left(N_{\text{dof}}^{u_k} \times (N_{\text{dof}}^{u_k} + N_{\text{fix}}^{u_k})\right), \tag{3.11f}$$

$$\underline{\boldsymbol{G}}_k = \begin{bmatrix} \boldsymbol{G}_k & \boldsymbol{G}_k^\star \end{bmatrix} \quad \left(N_{\text{dof}}^{p} \times (N_{\text{dof}}^{u_k} + N_{\text{fix}}^{u_k})\right), \tag{3.11g}$$

$$\underline{\boldsymbol{u}}_k^T = \begin{bmatrix} \bar{\boldsymbol{u}}_k^T & \bar{\boldsymbol{u}}_k^{\star T} \end{bmatrix} \quad \left(1 \times (N_{\text{dof}}^{u_k} + N_{\text{fix}}^{u_k})\right), \tag{3.11h}$$

where $\boldsymbol{u}(\underline{\boldsymbol{u}})$ is given by Equation (3.5a), and all starred quantities are given by the Dirichlet boundary conditions. $\boldsymbol{K}_k$ is often called viscosity matrix, $\boldsymbol{C}_k$ convective matrix, $\boldsymbol{G}_k$ gradient matrix, and $\boldsymbol{f}_k$ force vector.

Implementation Details

We need to solve $N_{\text{dof}}^{u_1} + N_{\text{dof}}^{u_2} + N_{\text{dof}}^{p}$ equations from (3.10) supplemented by the equation from the condition on the mean pressure from (3.7) in $N_{\text{dof}}^{u_1} + N_{\text{dof}}^{u_2} + N_{\text{dof}}^{p}$ unknowns, and we do this in the least square sense. The problem is non-linear, and an iterative, incremental Newton-Raphson method is used, gradually increasing the Reynolds number, see e.g. [Reddy and Gartling, 2001].

The integrals in Equation (3.11) are evaluated using Gaussian quadrature. The necessary number of quadrature points N_G in each knot span is estimated from the relation $\tilde{q} = 2N_G - 1$, where $\tilde{q}$ is an estimate of the highest polynomial degree of the integrands. Since the integrands are in general rational functions, we simply estimate $\tilde{q}$ as the sum of polynomial degrees of the numerator and the denominator. Using polynomial degree 2 for the geometry and 4 for the velocity and pressure, we estimate a polynomial degree of $\tilde{q} = 12$ for the integrand of $\boldsymbol{C}$, and this dictates that we should use at least $N_G = 7$ quadrature points in each knot span. All results in the following are based on 7 quadrature points per knot span, which is a conservative choice compared to recent studies on more efficient quadrature rules [Hughes et al., 2010].

3.3 Stability for Stokes Problem: Wall-Driven Anullar Cavity

In the following section, we deal with the stability of the isogeometric method when applied to Stokes flow, which is the problem that arises when we neglect the non-linear inertial term in Navier-Stokes equation (3.1a). Some discretizations of the mixed formulation of Stokes problem are stable while others are unstable. Unstable discretizations can leave the system matrix $\boldsymbol{\mathcal{K}}$ in Equation (3.10) singular or badly scaled, which in turn leads to spurious, unphysical oscillations for the pressure field, while the velocity field may still look quite reasonable. Figure 3.3 below shows an example of this. Furthermore, it deteriorates the convergence properties of the method and thus prohibits iterative solutions for the full Navier-Stokes problem. In order for a given discretization to be stable, it needs to satisfy the so-called inf-sup condition, also known as the BB or LBB condition:

$$\inf_p \sup_{\boldsymbol{u}} \frac{\iint_\Omega p \nabla \cdot \boldsymbol{u} \, \mathrm{d}A}{\|p\| \, \|\boldsymbol{u}\|} \geq \beta > 0, \tag{3.12}$$

	Name	Knot Vector 1	Knot Vector 2	inf-sup
a	$\mathbf{u}4_1^1\mathrm{p}4_0^1$			√
b	$\mathbf{u}4_0^2\mathrm{p}4_0^1$	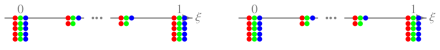		√
c	$\mathbf{u}4_1^1\mathrm{p}3_0^1$	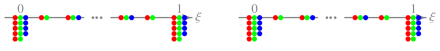		√
d	$\mathbf{u}4_0^2\mathrm{p}3_0^1$	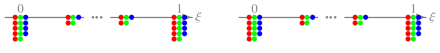		√
e	$\mathbf{u}4_1^1\mathrm{p}2_0^1$			√
f	$\mathbf{u}4_0^2\mathrm{p}2_0^1$	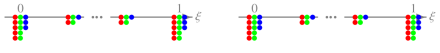		√
g	$\mathbf{u}4_0^1\mathrm{p}2_0^1$	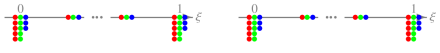		÷
h	Nédélec	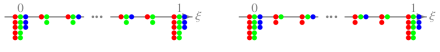		√
i	Raviart-Thomas	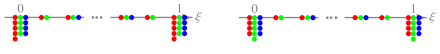		√

Table 3.1: *Discretization names, knot vectors and inf-sup-stability. Velocity knot vectors are shown in red and green, the pressure knot vector is shown in blue.*

where the norm of the pressure p is the L^2-norm, while the norm of the velocity $\boldsymbol{u}$ is the H^1-norm. The positive constant β is independent of the mesh.

In the following, we study how stable discretizations may be constructed by using different basis functions for the velocity and pressure fields. More specifically, we will establish suitable choices of polynomial degrees and knot vectors for the velocity and pressure such that the discretizations are stable. This idea follows the approach in a recent work [Buffa et al., 2011], in which three families of stable discretizations were presented, but contrasts to the stabilized method in which identical basis functions for the velocity and pressure may be used on the cost that stabilizing terms must be added to the Stokes equation, see e.g. [Bazilevs et al., 2006b].

We report the stability of the isogeometric discretizations listed in table 3.1. The discretizations differ in polynomial degrees, knot refinements and inner knot multiplicities between the velocity and pressure representations. We have adopted a heuristic nomenclature for naming of the individual discretizations. For the $\mathbf{u}4_0^2\mathrm{p}3_0^1$ discretization (d), e.g., both velocity components are approximated using quartic B-splines ($\mathbf{u}4$), and the pressure using cubic B-splines (p3). Superscript indicates the multiplicity of inner knots, and thus also the degree of continuity across the knots, see Theorem 2. Subscript indicates the number

of h-refinements by halving all knot spans. For the strategies a-g, each of the velocity components u_1 and u_2 are represented identically, which reduces the computational expenses since equality of the basis functions $\mathcal{P}_i^{u_1} = \mathcal{P}_i^{u_2}$ implies equality of the matrices $K_1 = K_2$, and in addition all fields are represented identically in both parametric directions. This is not the case for the strategies h and i, which are modified versions of the Nédélec and Raviart-Thomas elements presented in [Buffa et al., 2011]. Compared to the original formulation in [Buffa et al., 2011], the velocity fields have been h-refined once. It should be stressed that with this enlargement of the velocity space, the exact fulfillment of the divergence-free constraint for the Raviart-Thomas discretization is lost. The $\mathbf{u}4_0^2\mathrm{p}3_0^1$ discretization (d) was originally proposed in [Bazilevs et al., 2006b] and subsequently introduced in [Buffa et al., 2011] as the Taylor-Hood element.

To examine the numerical stability, we consider the wall-driven annular cavity problem outlined in Figure 3.2a. This is a slight modification of the standard benchmark *lid*-driven *square* cavity problem (treated in Section 3.5), utilizing the capability of isogeometric analysis to exactly represent circular arcs. The

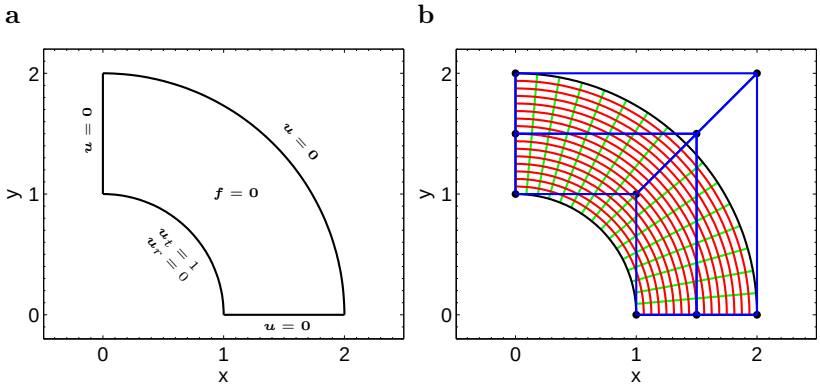

Figure 3.2: *Driven annular cavity.* **a***: Domain and boundary conditions.* **b***: Control net (black dots and blue lines) and image of the computational mesh for velocity and pressure (red and green lines).*

fluid is contained in an annular cavity. The inner circular wall moves with constant tangential speed, while the remaining three walls are at rest. The velocity field is specified along the boundary of the domain, assuming no-slip conditions. No body forces act upon the fluid, and the fluid motion is thus caused—or driven—by the moving wall. We adopt the so-called *leaky-lid* boundary condition, meaning that the corners $(x, y) = (0, 1)$ and $(x, y) = (1, 0)$ belong to the moving wall boundary. We parametrize the domain using quadratic NURBS. The control net is shown in Figure 3.2b. For the velocity and pressure representation, we h-refine the parameter mesh for the geometry by halving the knot spans, leading to a family of parameter meshes ranging from 2×2 to 64×64 knot spans, one of which is also depicted in Figure 3.2b.

Figure 3.3 shows the computed velocity and pressure fields for two different discretizations, namely the $\mathbf{u}4_0^1\mathrm{p}4_0^1$ discretization (top row) and the $\mathbf{u}4_1^1\mathrm{p}4_0^1$ discretization (bottom row). Both of these produce a reasonable, rotational flow field. Clear pressure oscillations, however, are seen for first discretization, whereas the latter nicely approximates the pressure singularities in the inner

corners.

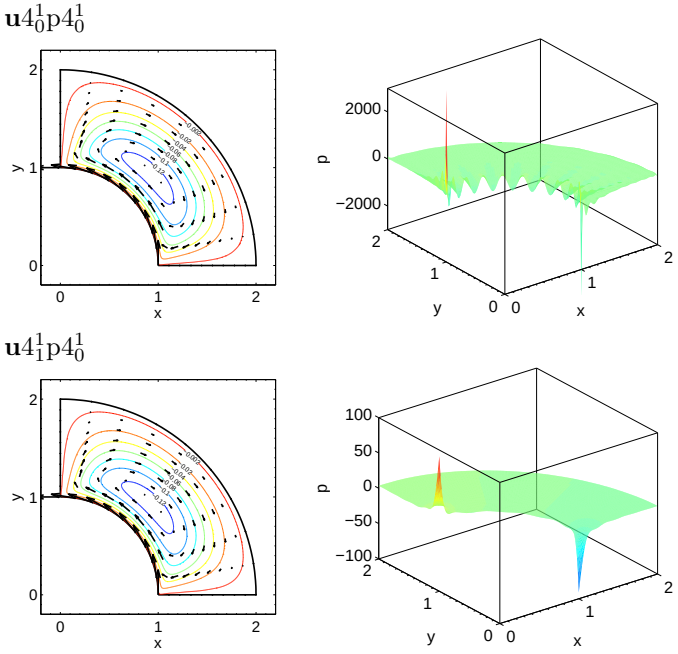

Figure 3.3: *Computed fields for* $\mathbf{u}4_0^1p4_0^1$ *(top) and* $\mathbf{u}4_1^1p4_0^1$ *(bottom) discretizations. Left: stream function contour lines and velocity arrows. Right: pressure (note the different vertical scalings).*

To test the stability of the discretization strategies, we use the approach described in [Chapelle and Bathe, 1993; Bathe, 2001]. For each discretization, we vary the grid size for the velocity and pressure representations, and for each of these meshes we determine a numerical estimate of the inf-sup "constant" β in Equation (3.12). If this value does not change appreciably with varying grid size, it indicates that the discretization is stable. On the other hand, if the value tends to zero as the grid size changes, it indicates that the discretization is *un*stable.

The results of these computations are shown in Figure 3.4. From this we are led to conclude, that the discretization with identical polynomial degree for velocity and pressure is stable if either the velocity knot vector is refined (a) or the inner knot multiplicity for the velocity is increased (b). The same conclusion applies to the discretizations for which the polynomial degree of the velocity is larger than the polynomial degree of the pressure by one (c and d) and two (e and f). The stability of $\mathbf{u}4_0^2\mathrm{p}3_0^1$ (d) was already known from [Buffa et al., 2011]. Both the modified Nédélec (h) and Raviart-Thomas (i) discretizations are seen to be stable, whereas the simple discretization $\mathbf{u}4_0^1\mathrm{p}2_0^1$ (g) with a difference in polynomial degree of two but with identical inner knots does *not* pass the stability test. The stability of each of the discretizations is summarized in the right-most column of Table 3.1.

Several discretizations have been tested in addition to those listed in Table 3.1. It was found that increasing the difference between the polynomial degree

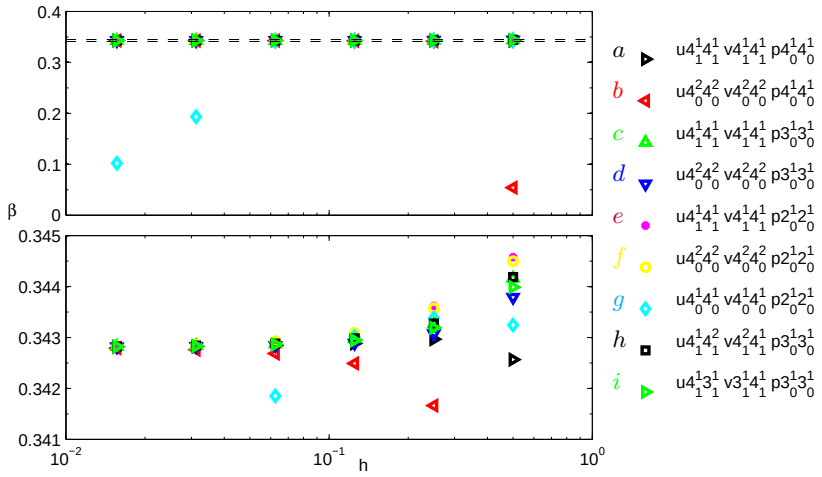

Figure 3.4: *Numerically computed inf-sup "constants" for varying grid size using different discretizations. The bottom plot shows an enlargement of the top plot as marked by the dashed lines.*

of the velocity approximation and the degree of the pressure approximation does influence the inf-sup stability, even without inserting or repeating knots. More specifically, the value of grid size h where the inf-sup "constant" β starts decreasing seemed to decrease with increasing polynomial degrees.

Assuming that the examined discretizations are representative, two simple strategies for choosing stable discretizations for the velocity and pressure approximations can be established by means of induction. Given a simple discretization for the pressure, i.e. open knot vectors, choose the velocity degrees at least equal to the pressure degree and then either take the velocity knot vectors as the refinement of the pressure knot vectors, or use the pressure knot vectors with all inner knots repeated. Or conversely, given simple discretizations for the velocity, i.e. with open knot vectors and single or double inner knots, choose the pressure degree less than or equal to the velocity degree, and take the pressure knot vectors as the velocity knot vectors with every 2^{nd} inner knot removed. The knot refinement strategy is used for the cases a, c and e, and the knot repetition strategy for cases b, d and f. The modified Raviart-Thomas (i) also uses the refinement strategy, while the modified Nédélec (h) combines both strategies.

We conclude by emphasizing firstly that the presented inf-sup method only serves as a numerical test of the stability of the examined discretizations, and secondly that the inductive step, going from the stability of the examined discretizations to the stability of a general discretization strategy, is only motivated by a limited number of tests. None of these should in no way be mistaken for a rigorous mathematical proof.

3.4 Error Convergence: Forced Elliptic Cavity

To asses the validity of the isogeometric method for the full Navier-Stokes problem, we consider a test case for which an analytical solution exists, and examine how well the discretizations listed in table 3.1 are able to reproduce the exact solution.

The problem is outlined in Figure 3.5a. We take the physical domain Ω as the elliptic disk $\{(x,y) \in \mathbb{R}^2 \mid (x/a)^2 + (y/b)^2 \leq 1\}$ with $a = 2$ and $b = 1$. Assuming appropriate units are assigned to all quantities and focussing only on their numerical values, we set $\rho = \mu = 1$, take the body force $\boldsymbol{f} = (f_1, f_2)$ to be

$$\begin{aligned} f_1 = &-\frac{1}{4}\,U^2\,\sin^2\left(\pi\,\tilde{r}^2\right)\,x - \frac{1}{4}\,\frac{\pi}{\tilde{r}}\,\sin\left(\pi\,\tilde{r}\right)\,x + \frac{13}{2}\,\pi\,U\,\cos\left(\pi\,\tilde{r}^2\right)\,y \\ &- 4\,\pi^2\,U\,\sin\left(\pi\,\tilde{r}^2\right)\,y^3 - \frac{1}{4}\,\pi^2\,U\,\sin\left(\pi\,\tilde{r}^2\right)\,x^2\,y \\ f_2 = &-\frac{1}{4}\,U^2\,\sin^2\left(\pi\,\tilde{r}^2\right)\,y - \frac{\pi}{\tilde{r}}\,\sin\left(\pi\,\tilde{r}\right)\,y - \frac{7}{8}\,\pi\,U\,\cos\left(\pi\,\tilde{r}^2\right)\,x \\ &+ \frac{1}{16}\,\pi^2\,U\,\sin\left(\pi\,\tilde{r}^2\right)\,x^3 + \pi^2\,U\,\sin\left(\pi\,\tilde{r}^2\right)\,y^2\,x, \end{aligned}$$

where $\tilde{r} = \tilde{r}(x,y) = \sqrt{(x/2)^2 + y^2}$, and assume homogeneous no-slip boundary conditions: $\boldsymbol{u} = \boldsymbol{0}$ on Γ. The following velocity and pressure fields solve the governing equations and satisfy the boundary conditions:

$$\begin{aligned} u_1^\star &= -U\sin(\pi\tilde{r}^2)\,y, \\ u_2^\star &= \frac{1}{4}\,U\sin(\pi\tilde{r}^2)\,x, \\ p^\star &= \frac{4}{\pi^2} + \cos(\pi\tilde{r}), \end{aligned}$$

where U is a velocity scale which in the following is assumed to be $U = 200/\sqrt{5}$. These fields are depicted in Figure 3.5b–c. Using $L = \sqrt{a^2+b^2} = \sqrt{5}$ as length scale, the Reynolds number for the problem is $\mathrm{Re} = 200$ which makes the problem weakly nonlinear. We parametrize the domain using quadratic NURBS. The control net and the coarsest computational mesh for the velocity and pressure fields are shown in Figure 3.5d.

We examine how well the exact velocity and pressure fields are reproduced by a given discretization as the computational parameter mesh is h-refined by knot insertion. For each discretization, we uniformly vary the computational mesh for velocity and pressure in the range from 4×4 to 64×64 knot spans, and for each of these meshes we compute the L^2-norm and the H^1-seminorm of the velocity residual and the pressure residual as measures of the error:

$$\epsilon_u^2 = \iint_\Omega \|\boldsymbol{u} - \boldsymbol{u}^\star\|^2\,\mathrm{d}x\,\mathrm{d}y, \qquad \epsilon_p^2 = \iint_\Omega (p - p^\star)^2\,\mathrm{d}x\,\mathrm{d}y,$$

$$\epsilon_{\nabla u}^2 = \iint_\Omega \sum_{k=1}^{2} \|\nabla u_k - \nabla u_k^\star\|^2\,\mathrm{d}x\,\mathrm{d}y, \qquad \epsilon_{\nabla p}^2 = \iint_\Omega \|\nabla p - \nabla p^\star\|^2\,\mathrm{d}x\,\mathrm{d}y.$$

The results are shown in Figure 3.6. The figure depicts the velocity error (top) and pressure error (bottom) as function of the total number of variables

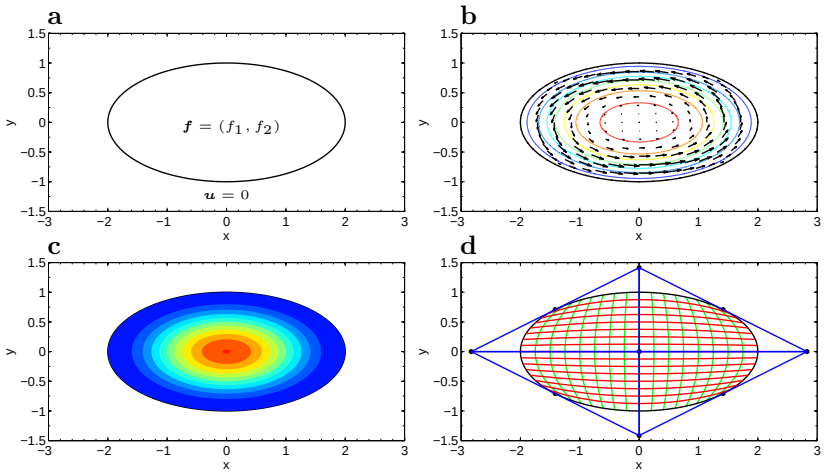

Figure 3.5: *Forced elliptic cavity.* **a***: Domain and boundary conditions.* **b***: Analytical stream function contour lines and velocity arrows.* **c***: Analytical pressure contour lines.* **d***: Control net (black dots and blue lines) and image of the coarsest computational mesh for velocity and pressure (red and green lines).*

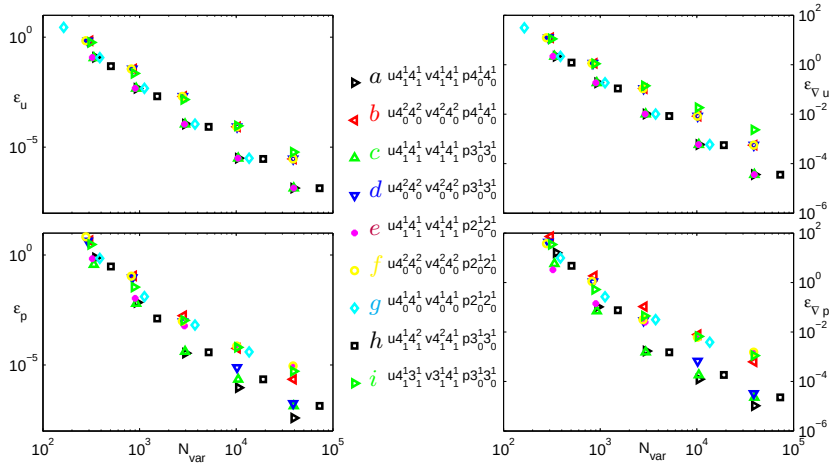

Figure 3.6: *Convergence of error: L^2-norm (left) and H^1-seminorm (right) of velocity residual (top) and pressure residual (bottom) as a function of the total number of variables of the analysis using different discretizations.*

of the analysis, using both the L^2-norm (left) and the H^1-seminorm (right). We note that the discretizations a-f which pairwise have identical polynomial degrees, the knot refinement strategies (a, c, e) have a significantly lower velocity error than the knot repetition strategies (b, d, f). In addition, the difference between the two strategies grows as the number of degrees of freedom increases, as is most evident for the H^1-seminorm. The difference in pressure error between the two strategies varies more, but the error of the knot refinement strategy is never larger than the error of the corresponding knot repetition strategy. This make the knot refinement strategy favorable in a per-degree-of-freedom sense.

The knot refinement strategy, unlike the knot repetition strategy, conserves the degree of continuity for the velocity field. This therefore seems to confirm the high importance of continuity alluded to in [Akkerman et al., 2010]. However, although the increase in number of degrees of freedom for a given refinement is nearly identical for the two strategies, the knot refinement strategy is computationally more expensive than the knot repetition strategy, since it doubles the number of knot spans, and thus quadruples the number of function evaluations needed for the Gaussian quadrature, unless more efficient quadrature rules are employed [Hughes et al., 2010]. It is also worth noting that although the pressure error of the unstable discretization $\mathbf{u}4_0^1\mathrm{p}2_0^1$ (g) flattens out quit quickly as the number of degrees of freedom increases, the velocity error falls off impressively. Lastly, the modified Raviart-Thomas discretization (h) seem to perform somewhat better than the modified Nédélec discretization (i) for both the velocity and the pressure.

3.5 Benchmark: Lid-Driven Square Cavity

As a final validation of the isogeometric method, we compare our results for a standard benchmark flow problem, namely the lid-driven square cavity [Donea and Huerta, 2003; Bazilevs et al., 2006b], against results from other numerical simulations [Ghia et al., 1982; Erturk et al., 2005; Lee, 2010]. We consider a fluid contained in a square cavity with the top wall moving with constant speed, and the other walls kept still as outlined in Figure 3.7a. This prescribes the velocity field along the boundary of the domain, assuming no-slip conditions at the walls and closed-lid conditions ($\boldsymbol{u} = \mathbf{0}$) at the upper corners. No body forces act upon the fluid; the fluid is set in motion from the movement of the lid. We parametrize the domain using linear NURBS, and construct a stretched computational mesh with increased resolution around the corner singularities and boundary regions, see Figure 3.7b. For the analysis, a computational grid of 64×64 regularly spaced knot spans is employed.

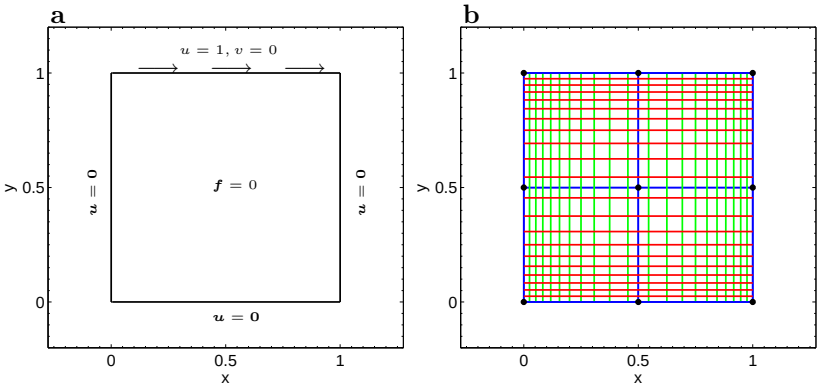

Figure 3.7: *Lid-driven square cavity.* **a***: Domain and boundary conditions.* **b***: Control net (black dots and blue lines) and image of regularly spaced isoparametric lines (red and green lines).*

Using the isogeometric discretizations listed in Table 3.1 we firstly solve the problem for Reynolds number Re = 5,000. We gradually increase Re, and the

number of intermediate steps in Re necessary to achieve convergence for Re = 5,000 is around five, but is in general different for the various discretizations. The total number of basis functions for the analysis ranges from 13,604 for the discretization $\mathbf{u}4_0^1\mathrm{p}2_0^1$ (g) to 72,865 for the Nédélec discretization (h), while the remaining discretizations all have between 38,678 and 39,472 analysis basis functions. Figure 3.8 compares the computed horizontal/vertical velocity profiles through the vertical/horizontal center line of the cavity to the data from [Ghia et al., 1982]. On the left, the velocity profiles for all nine discretizations

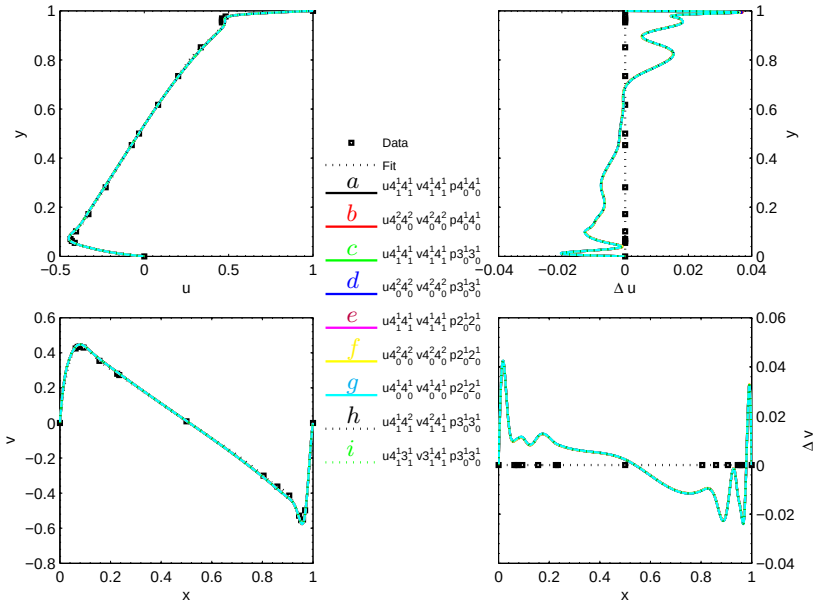

Figure 3.8: *Comparison of velocity profile curves and residual curves (velocity minus fit) for the lid-driven square cavity for* Re = *5,000 using different discretizations, plotted with data from [Ghia et al., 1982] and a fit to the data using a cubic spline. Top: horizontal velocity profiles (left) and residuals (right) through the vertical center line. Bottom: vertical velocity profiles (left) and residuals (right) through the horizontal center line.*

are seen to match very well with the data in [Ghia et al., 1982]. On the right, the velocity residuals reveal that all discretizations yield slightly larger fluid speeds away from the center and towards the boundaries compared to the data. The agreement between the discretizations, however, is very good.

We have in general good experiences with the Taylor-Hood discretization $\mathbf{u}4_0^2\mathrm{p}3_0^1$ (d), since it discretizes both velocity components identically, and the knot spans for the velocity and pressure fields are also the same. In the following, we therefore focus on the discretization $\mathbf{u}4_0^2\mathrm{p}3_0^1$ (d). Figure 3.9 shows velocity vectors and stream function contour lines for Re = 5,000. The general pattern of the stream function matches very well with previous results [Ghia et al., 1982; Erturk et al., 2005; Lee, 2010]. The locations and the extremal values of both the central main eddy as well as the minor eddies in the bottom right, bottom left and top left corners are in overall good agreement. Small discrepancies are

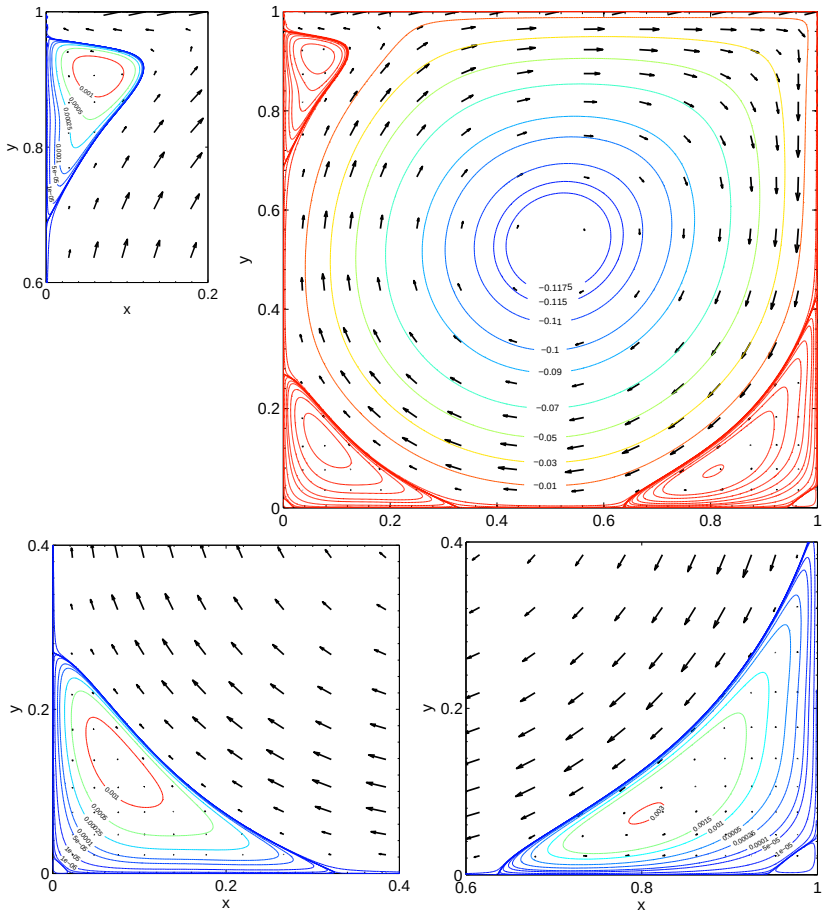

Figure 3.9: *Four views of velocity vectors and stream function contour lines in the lid-driven square cavity for* $\mathrm{Re} = 5{,}000$ *using the* $\mathbf{u}4_0^2p3_0^1$ *discretization (d).*

still seen, e.g. close to the boundary in the top left corner.

Finally, the problem is solved for different values of Re in the range from 100 to 10,000: {*100*; *400*; *1,000*; 2,000; *3,200*; *5,000*; *7,500*; *10,000*}. Figure 3.10**a/b** shows the computed horizontal/vertical velocity profiles through the vertical/horizontal center line of the cavity along with the data from [Ghia et al., 1982] for the values of Re printed in italic. In general, the velocity profiles from the present study match very well with the data in [Ghia et al., 1982]. Once again, however, a closer examination reveals a small difference: for higher Re, we compute slightly larger fluid speeds close to the boundaries than is done in [Ghia et al., 1982], and this difference increases with Re. There is, however, a very nice agreement in the location of the velocity extrema.

Regarding the differences in flow speeds close to the boundaries, several points deserve mentioning. Firstly, the results depend critically on the choice of boundary conditions specified for the upper corners. We emphasize that closed-lid conditions are assumed in the present study. Secondly, the results

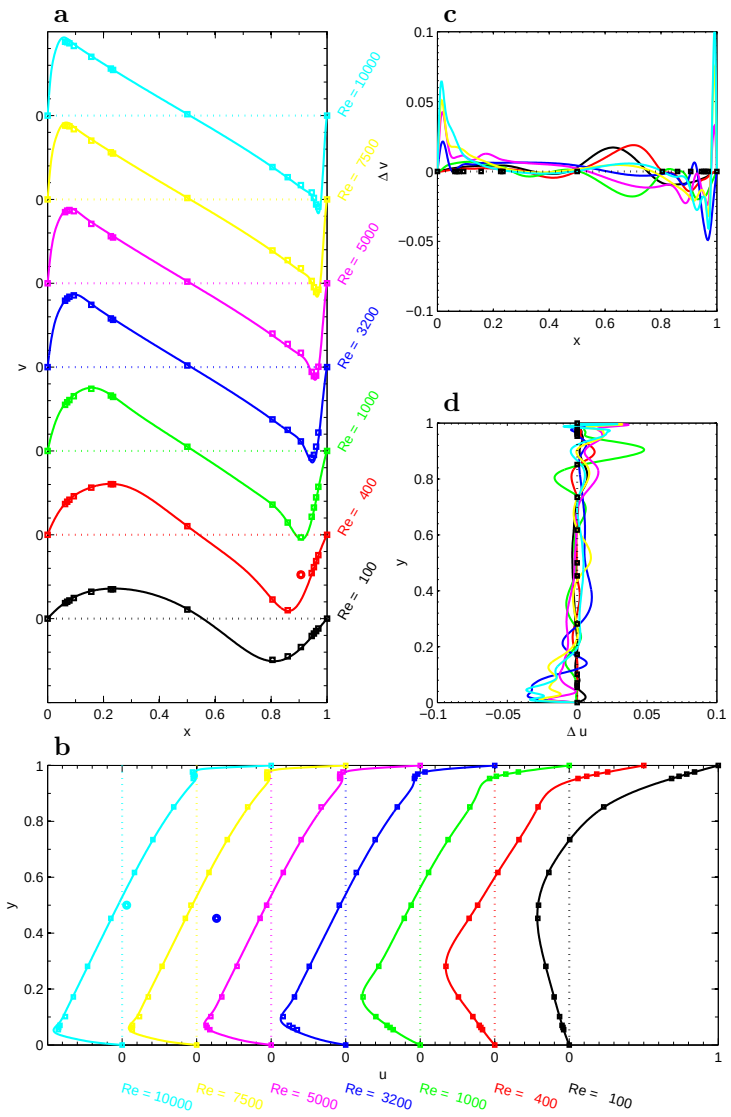

Figure 3.10: *Velocity profile curves for the lid-driven square cavity for seven values of* Re *(solid lines) using the* $\mathbf{u}4_0^2p3_0^1$ *discretization (d) plotted along with data from [Ghia et al., 1982] (points).* **a***: vertical velocity profile through the horizontal center line.* **b***: horizontal velocity profile through the vertical center line.* **c***: vertical velocity residual.* **d***: horizontal velocity residual. The profile curves have been translated to avoid clustering of data. We speculate that three obvious outliers, marked with rings, stem from misprints in the tabulated data in [Ghia et al., 1982]. Cubic splines have been used to fit to the remaining data.*

depend slightly on the formulation of the Navier-Stokes equation for Re $\gtrsim$ 5,000, depending on whether the convective $[(\boldsymbol{u}\cdot\nabla)\boldsymbol{u}]$ or the skew-symmetric $[(\boldsymbol{u}\cdot\nabla)\boldsymbol{u}+1/2\,\nabla\cdot\boldsymbol{u}]$ formulation of the non-linear term is used, see [Nielsen et al., 2011a] in Appendix B for details. Thirdly, the data in [Ghia et al., 1982] are relatively

sparse at the boundaries where the variation in velocity is high. Finally, it should be stressed that the data in [Ghia et al., 1982] stem from another numerical study, and an exact correspondence between that and the present study should not be expected.

3.6 Conclusions

In this chapter, we have applied isogeometric analysis to the 2-dimensional, steady state, incompressible Navier-Stokes equation subjected to Dirichlet boundary conditions, and examined various discretizations of the velocity and pressure spaces. Firstly, a detailed description of the implementation has been given. Secondly, numerical inf-sup stability tests have been presented that confirm the existence of many stable discretizations of the velocity and pressure spaces. In particular it was found that stability may be achieved by means of knot refinement of the velocity space. Thirdly, error convergence studies compared the performance of the various discretizations and indicated optimal convergence, in a per-degree-of-freedom sense, of the discretization with identical polynomial degrees of the velocity and pressure spaces but with the velocity space enriched by knot refinement. Finally, the method has been applied to the lid-driven square cavity for benchmarking purposes, showing that the stable discretizations produce consistent results that match well with existing data and thus confirm the robustness of the method.

Appendix: Data for Geometry Parametrizations

Table 3.2 lists the polynomial degrees, knot vectors and control points for the geometry of the problems analyzed in this chapter.

Wall-Driven Annular Cavity									
Degree	$q = r = 2$								
Knots	$\Xi = \Phi = \{0, 0, 0, 1, 1, 1\}$								
Point	1	2	3	4	5	6	7	8	9
$\bar{x}_1$	0	1	1	0	3/2	3/2	0	2	2
$\bar{x}_2$	1	1	0	3/2	3/2	0	2	2	0
w	1	$1/\sqrt{2}$	1	1	$1/\sqrt{2}$	1	1	$1/\sqrt{2}$	1

Forced Elliptic Cavity									
Degree	$q = r = 2$								
Knots	$\Xi = \Phi = \{0, 0, 0, 1, 1, 1\}$								
Point	1	2	3	4	5	6	7	8	9
$\bar{x}_1$	$-2/\sqrt{2}$	0	$2/\sqrt{2}$	$-4/\sqrt{2}$	0	$4/\sqrt{2}$	$-2/\sqrt{2}$	0	$2/\sqrt{2}$
$\bar{x}_2$	$-1/\sqrt{2}$	$-2/\sqrt{2}$	$-1/\sqrt{2}$	0	0	0	$1/\sqrt{2}$	$2/\sqrt{2}$	$1/\sqrt{2}$
w	1	$1/\sqrt{2}$	1	1	$1/\sqrt{2}$	1	1	$1/\sqrt{2}$	1

Lid-Driven Square Cavity									
Degree	$q = r = 1$								
Knots	$\Xi = \Phi = \{0, 0, 1/2, 1, 1\}$								
Point	1	2	3	4	5	6	7	8	9
$\bar{x}_1$	0	1/2	1	0	1/2	1	0	1/2	1
$\bar{x}_2$	0	0	0	1/2	1/2	1/2	1	1	1
w	1	1/2	1	1/2	1/4	1/2	1	1/2	1

Table 3.2: *Polynomial degrees, knot vectors, control points and weights for the geometry of the analyzed problems.*

Chapter 4

Isogeometric Shape Optimization of Flows

In this chapter, we extend the use of isogeometric analysis to shape optimization of flows. We consider various shape optimization problems for fluids in two dimensions, and use isogeometric analysis both for solving the governing equations, and as tool for designing optimal shapes. The chapter summarizes the findings in [Nielsen and Gravesen, 2012] included in Appendix C.

4.1 Introduction

Numerical shape optimization for fluids is the art of using computers to find "best" shapes in engineering problems involving fluids, based on some notion of goodness [Mohammadi and Pironneau, 2010]. Applications of shape optimization for fluids ranges from, e.g., microfluidic protein-folding devices [Ivorra et al., 2006] to airplane wings [Painchaud-Oullet et al., 2006].

Some of the appealing features of isogeometric analysis from a fluid mechanics point–of–view were presented in Chapter 3. From a shape optimization point–of–view, isogeometric analysis may serve as a natural framework, due to its ability to represent complex shapes in few design variables, and its tight connection between analysis and geometry models. This means that an accurate representation of the geometry can be maintained throughout the optimization, and there is no need of communication between FEA and CAD models.

In recent years, isogeometric analysis has successfully been applied to various shape optimization problems in mechanical engineering. Many studies within structural mechanics have been made, using either NURBS control points [Wall et al., 2008; Cho and Ha, 2009], NURBS control points and weights [Nagy et al., 2010a;b; Qian, 2010; Nagy et al., 2011], or T-splines control points [Ha et al., 2010; Seo et al., 2010a] as design variables. NURBS-based isogeometric shape optimization using a boundary integral method has also been studied [Li and Qian, 2011]. Applications of isogeometric shape optimization also include studies of vibrating membranes [Nguyen et al., 2011], and photonic crystals [Qian and Sigmund, 2011]. Worth mentioning are also recent applications of isogeometric topology optimization within structural mechanics [Seo et al., 2010a;b; Hassani et al., 2012].

An inherent challenge in numerical shape optimization is to maintain a high quality of the computational mesh as the shape of the domain changes during optimization [Mohammadi and Pironneau, 2004; Bletzinger et al., 2010]. In isogeometric analysis, the shape is given by control points. Here, care has to be taken to avoid clustering and folding over of control points during optimization, which in turn may lead to singular parametrizations [Wall et al., 2008; Nagy et al., 2011; Seo et al., 2010a].

The aim of this chapter is twofold. Firstly, we establish isogeometric analysis as a framework for numerical shape optimization in fluid mechanics, using the method both as analysis tool to solve the governing Navier-Stokes equations, and as design tool to guide an optimization procedure through analytically computed gradients of objective and constraint functions. Secondly, to ensure appropriate parametrizations during the optimization, we construct a measure for regularization of the shape optimization problem. Based on a benchmark optimization problem, in which we design a pipe bend to minimize the pressure drop of the flow through it, we examine how this regularization measure influences the optimization process and the optimal design. Finally, to display the robustness of the isogeometric shape optimization methodology, we apply it to two other optimization problems for fluids. First, we design a body at rest in a circular fluid container with rotating boundary to obtain a uniform pressure distribution along its boundary, a design problem which happens to have a known solution, and second, we design a body traveling at constant speed through a fluid to minimize the drag.

4.2 Shape Optimization Problem

In the following, we introduce the generic shape optimization problem for fluids to be studied.

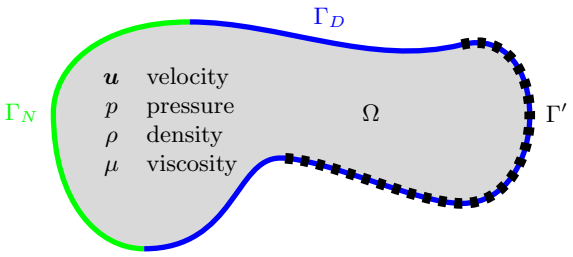

Figure 4.1: *Setup of generic shape optimization problem for fluids.*

As in Chapter 3, we consider a viscous, incompressible, isothermal, steady flow at low to moderate Reynolds numbers in a 2-dimensional domain Ω as depicted in Figure 4.1. The fluid is assumed to be Newtonian with constant density ρ and constant viscosity μ, and the state of the fluid is characterized by its velocity $\boldsymbol{u} = (\, u \; v \,)^T$ and its pressure p. We assume that no external body forces act on the system. For the boundary Γ, we assume that the domain is open along the Neumann part Γ_N, and that the flow field $\boldsymbol{u}$ is given along the Dirichlet part Γ_D, independently of the shape.

The aim in shape optimization is to design the *shape* of some specified part

Γ' of the boundary of the domain to minimize some prescribed *objective*, with some prescribed *constraints* on the problem. The specific form of the objective function will be explained further below. The constraint functions are typically dictated by the geometry and the physics of the problem. Here, we will consider in particular the area of the domain as a constraint. Additional constraints could of course be considered as well.

We formulate the following generic shape optimization problem for fluids:

$$\begin{aligned}
\underset{\Gamma'(\boldsymbol{x})}{\text{minimize}} \quad & C && && && \text{(4.1a)}\\
\text{such that} \quad & A_{\min} && \leq && A_{\max} && \text{(4.1b)}\\
& \boldsymbol{\mathcal{L}}_{\min} && \leq && \boldsymbol{\mathcal{L}}_{\max} && \text{(4.1c)}\\
& \mathbf{0} && = && \rho(\boldsymbol{u}\cdot\nabla)\boldsymbol{u} + \nabla p - \mu\nabla^2\boldsymbol{u} && \text{(4.1d)}\\
& 0 && = && \nabla\cdot\boldsymbol{u} && \text{(4.1e)}\\
& \boldsymbol{u}^* && = && \boldsymbol{u}\,|_{\Gamma_D} && \text{(4.1f)}\\
& 0 && = && (\,\mu\nabla u_i - p\,\boldsymbol{e}_i\,)\cdot\boldsymbol{n}\,|_{\Gamma_N} && \text{(4.1g)}
\end{aligned}$$

Here, the shape of the design boundary Γ' is parametrized through the design variables $\boldsymbol{x}$. Equations (4.1a) and (4.1b) are the objective and the area constraint functions, respectively. Equation (4.1c) establishes bounds on the design variables, as well as linear relations between them. Equations (4.1d) and (4.1e) are the Navier-Stokes equation and the incompressibility condition, respectively, governing the flow in the domain interior Ω. Equations (4.1f) and (4.1g) are the Dirichlet and the Neumann boundary conditions, respectively, where $\boldsymbol{u}^*$ is the given velocity field, $i = 1, 2$ is the component index, and $\boldsymbol{n}$ is the outward unit normal.

We will consider three different quantities as the cost function C in Equation (4.1a): The difference in mean pressure between two boundary segments γ_+ and γ_-, the pressure variation along a boundary segment γ, and the aerodynamic drag on a boundary segment γ. These are given by:

$$C_{\Delta p} = \frac{\int_{\boldsymbol{\gamma}_+} p\,\mathrm{d}s}{L_{\gamma_+}} - \frac{\int_{\boldsymbol{\gamma}_-} p\,\mathrm{d}s}{L_{\gamma_-}}, \tag{4.2a}$$

$$C_{\nabla p} = \int_{\boldsymbol{\gamma}} \big(\nabla p\cdot\boldsymbol{t}\big)^2\,\mathrm{d}s, \tag{4.2b}$$

$$C_d = \int_{\boldsymbol{\gamma}} \Big(-p\boldsymbol{I} + \mu\big(\nabla\boldsymbol{u} + (\nabla\boldsymbol{u})^T\big)\Big)\,\boldsymbol{n}\;\mathrm{d}s\;\cdot\;\boldsymbol{e}_u, \tag{4.2c}$$

respectively, where $L_\gamma = \int_\gamma \mathrm{d}s$ denotes the length of the segment γ, $\boldsymbol{t}$ is the unit tangent vector, $\boldsymbol{e}_u$ the constant unit vector along a specified direction, $\boldsymbol{n}$ the outward unit normal, and $\boldsymbol{I}$ the identity matrix. The context in which these three different cost functions may appear will be exemplified in Sections 4.4, 4.5, and 4.5, respectively.

4.3 Isogeometric Method

In this section, we outline how NURBS/B-spline based isogeometric analysis may be applied to the shape optimization problem (4.1). Many aspects were

already covered in Section 3.2, and we therefore primarily focus on the shape optimization, see also, e.g., [Wall et al., 2008].

Geometry Parametrization

Referring to Figure 4.2, we construct a parametrization of the model domain of the form $\boldsymbol{X} = \sum_i \boldsymbol{x}_i \mathcal{R}_i^g$ for $i = 1, \ldots, N_{\text{var}}^g$, where $\mathcal{R}_i^g$ are tensor product NURBS, $\boldsymbol{x}_i$ are control points, and N_{var}^g is the number of terms. This parametrization serves as foundation for both the flow model and the shape optimization procedure.

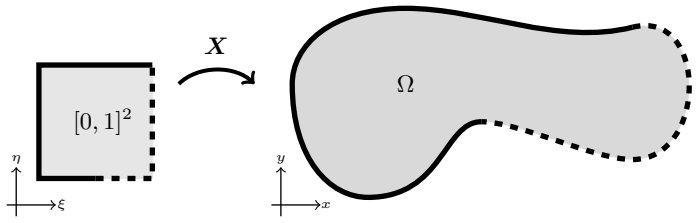

Figure 4.2: *Parametrization of the flow domain.*

Flow Analysis

As in Chapter 3, we construct approximations of the velocity $\boldsymbol{u}$ and pressure p in the form $f = \sum_i \underline{f}_i \mathcal{P}_i^f$ for $i = 1, \ldots, N_{\text{var}}^f$, where, for each of the three state variables $f \in \{u, v, p\}$, $\mathcal{P}_i^f$ are tensor product B-splines, $\underline{f}_i$ are control coefficients, and N_{var}^f is the number of terms. Based on these approximations, we may obtain, from a weak formulation of the governing equations (4.1d)–(4.1e) and the boundary conditions (4.1f)–(4.1g), a system of non-linear equations of the form $\boldsymbol{\mathcal{K}}(\boldsymbol{U})\boldsymbol{U} = \boldsymbol{F}$, where $\boldsymbol{U}$ is the vector of unknown control coefficients for the velocity and pressure, and the system matrix $\boldsymbol{\mathcal{K}}$ and the right hand side vector $\boldsymbol{F}$ are given by Equations (3.10)–(3.11) with $\boldsymbol{f} = \boldsymbol{0}$. This equation may be solved by, e.g., an iterative Newton-Raphson method.

Optimization

To find a minimum in the cost function while fulfilling the constraints, the geometry parametrization is tweaked little by little, and over and over again the governing flow equations are solved, and the objective and constraints evaluated. To guide the optimization process, gradients of the cost function and the constraints are computed analytically.

Design Variables

The control points $\boldsymbol{x}_i$ entering the parametrization of the geometry are the natural geometric "handles" on the flow domain, and these are therefore used as design variables for the shape optimization routine. For simplicity, we neglect weights as design variables. A parametrization and its control net are sketched in Figure 4.3. The design variables of the optimization are the coordinates of

the green control points in Figure 4.3a that determine the shape of the dashed design boundary Γ' in Figure 4.3b. As also shown in Figure 4.3a, control points fall into three categories: The *design* control points (green) are "actively" moved around in the search for the optimal shape, the *linked* control points (yellow) are "passively" following the movement of the design control points, as described below, while the *fixed* control points (red) remain unaltered.

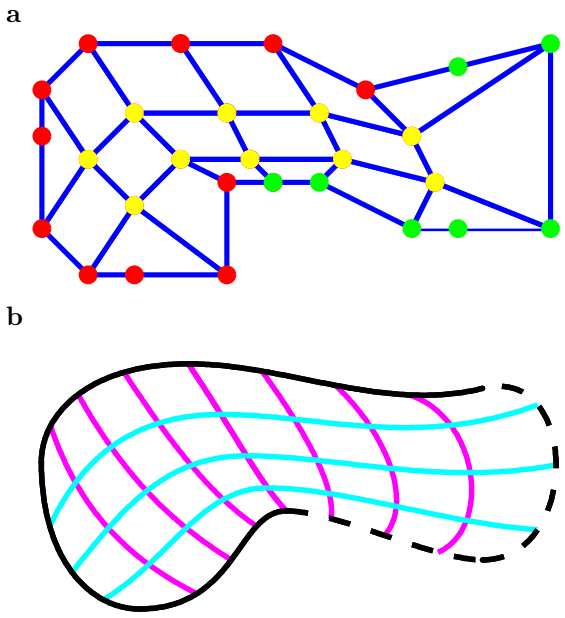

Figure 4.3: **a***: Three types of control points: design (green), linked (yellow), and fixed (red).* **b***: Image of isoparametric lines.*

Interior Parametrization

As the shape of flow domain is changed in the optimization process, the parametrization of its interior must be adequately updated. Referring to Figure 4.3, in the isogeometric framework this amounts to specifying the location of the yellow interior control points as the location of the green design control points are changed through the optimization. This can be seen as the isogeometric equivalent of finite element re-meshing [Mohammadi and Pironneau, 2010], although significantly less work is required, since there are much fewer control points in isogeometric analysis than there are nodes in finite element methods. Parametrization of interiors is a fundamental challenge in isogeometric analysis [Cohen et al., 2010; Xu et al., 2010]. We choose to base the procedure on the Winslow functional, see e.g. [Gravesen et al., 2010; Nguyen et al., 2011]. We defer a description of the methodology to Section 6.1. For now, the following description suffices: The Winslow functional is a measure of conformality. Initially, the interior control points are determined as the ones that minimize the Winslow functional, and thereby make the parametrization as conformal as possible, while keeping the boundary constant and ensuring a valid parametrization $\det(\boldsymbol{J}) > 0$. The latter constraint may be evaluated using B-splines (NURBS),

since the determinant of the Jacobian of a spline (NURBS) surface is itself a spline (NURBS). In each design iteration, the interior control points are then found as those that minimizes the 2^{nd} order Taylor expansion of the Winslow functional based on the initial control net. This procedure leads to a linear problem to be solved in each design iteration. On top of this, the validity of the parametrization is checked in each iteration by checking if $\det(\boldsymbol{J}) > 0$. If this condition is *not* fulfilled, the interior control points are found as the solution to the initial minimization problem as described above. This solution is then subsequently used as linearization point for the Taylor expansion of the Winslow functional, and the optimization is restarted from this configuration.

Function Evaluation

To asses the quality and admissibility of a given design, the objective and constraint functions in Equations (4.2) and (4.1b) are evaluated in each iteration. Using the parametrization of the geometry, and the discretizations of the flow and pressure fields, we collect the control points in two $(N^g_{\text{var}} \times 1)$ vectors $\boldsymbol{x}$ and $\boldsymbol{y}$, and the control coefficients in one $\big((N^u_{\text{var}} + N^v_{\text{var}} + N^p_{\text{var}}) \times 1 \big)$ vector $\boldsymbol{U}$. The mean pressure difference between two boundary segments γ_+ and γ_-, the pressure variation along a boundary segment γ, the aerodynamic drag on a boundary segment γ, and the area of the domain Ω, as defined in Equation (4.2) and (4.1b), may then be computed as:

$$C_{\Delta p} = \boldsymbol{\mathcal{P}}^T \boldsymbol{U}, \tag{4.3a}$$

$$C_{\nabla p} = \boldsymbol{U}^T \boldsymbol{\mathcal{D}} \boldsymbol{U} \tag{4.3b}$$

$$C_d = \boldsymbol{\mathcal{F}}^T \boldsymbol{U}, \tag{4.3c}$$

$$A = \boldsymbol{x}^T \boldsymbol{\mathcal{A}} \boldsymbol{y}, \tag{4.3d}$$

respectively. Here, the following vectors and matrices have been defined:

$$\boldsymbol{\mathcal{P}} = \boldsymbol{\mathcal{P}}_{\gamma_+} - \boldsymbol{\mathcal{P}}_{\gamma_-} \tag{4.4a}$$

$$\boldsymbol{\mathcal{P}}_{\gamma k} = \frac{1}{L_\gamma} \int_0^1 \mathcal{P}^p_k \, \|\dot{\boldsymbol{\gamma}}\| \, \mathrm{d}\xi, \tag{4.4b}$$

$$\boldsymbol{\mathcal{D}}_{k,\ell} = \int_0^1 \big(\boldsymbol{t}^T \boldsymbol{J}^{-T} \nabla \mathcal{P}^p_k \big) \big(\boldsymbol{t}^T \boldsymbol{J}^{-T} \nabla \mathcal{P}^p_\ell \big) \, \|\dot{\boldsymbol{\gamma}}\| \, \mathrm{d}\xi, \tag{4.4c}$$

$$\boldsymbol{\mathcal{F}} = \begin{bmatrix} \boldsymbol{\mathcal{F}}_{11} & \boldsymbol{\mathcal{F}}_{12} \\ \boldsymbol{\mathcal{F}}_{21} & \boldsymbol{\mathcal{F}}_{22} \\ \boldsymbol{\mathcal{F}}_{31} & \boldsymbol{\mathcal{F}}_{32} \end{bmatrix} \boldsymbol{e}_u^T, \tag{4.4d}$$

$$\boldsymbol{\mathcal{F}}_{11k} = \mu \int_0^1 \Big(2 \boldsymbol{e}_1^T \boldsymbol{n} \boldsymbol{e}_1^T + \boldsymbol{e}_2^T \boldsymbol{n} \boldsymbol{e}_2^T \Big) \boldsymbol{J}^{-T} \nabla \mathcal{P}^{u_1}_k \, \|\dot{\boldsymbol{\gamma}}\| \, \mathrm{d}\xi, \tag{4.4e}$$

$$\boldsymbol{\mathcal{F}}_{21k} = \mu \int_0^1 \boldsymbol{e}_2^T \boldsymbol{n} \boldsymbol{e}_1^T \boldsymbol{J}^{-T} \nabla \mathcal{P}^{u_2}_k \, \|\dot{\boldsymbol{\gamma}}\| \, \mathrm{d}\xi, \tag{4.4f}$$

$$\boldsymbol{\mathcal{F}}_{31k} = -\int_0^1 \boldsymbol{e}_1^T \boldsymbol{n} \mathcal{P}_k^p \, \|\dot{\boldsymbol{\gamma}}\| \, \mathrm{d}\xi, \tag{4.4g}$$

$$\boldsymbol{\mathcal{F}}_{12k} = \mu \int_0^1 \boldsymbol{e}_1^T \boldsymbol{n} \boldsymbol{e}_2^T \boldsymbol{J}^{-T} \nabla \mathcal{P}_k^{u_1} \, \|\dot{\boldsymbol{\gamma}}\| \, \mathrm{d}\xi, \tag{4.4h}$$

$$\boldsymbol{\mathcal{F}}_{22k} = \mu \int_0^1 \left(2\boldsymbol{e}_2^T \boldsymbol{n} \boldsymbol{e}_2^T + \boldsymbol{e}_1^T \boldsymbol{n} \boldsymbol{e}_1^T \right) \boldsymbol{J}^{-T} \nabla \mathcal{P}_k^{u_2} \, \|\dot{\boldsymbol{\gamma}}\| \, \mathrm{d}\xi, \tag{4.4i}$$

$$\boldsymbol{\mathcal{F}}_{32k} = -\int_0^1 \boldsymbol{e}_2^T \boldsymbol{n} \mathcal{P}_k^p \, \|\dot{\boldsymbol{\gamma}}\| \, \mathrm{d}\xi, \tag{4.4j}$$

$$\boldsymbol{\mathcal{A}}_{k,\ell} = \iint_{[0,1]^2} \left(\frac{\partial \mathcal{R}_k^g}{\partial u} \frac{\partial \mathcal{R}_\ell^g}{\partial v} - \frac{\partial \mathcal{R}_k^g}{\partial v} \frac{\partial \mathcal{R}_\ell^g}{\partial u} \right) \mathrm{d}\boldsymbol{\xi}, \tag{4.4k}$$

where the length is given by $L_\gamma = \int \|\dot{\boldsymbol{\gamma}}\| \, \mathrm{d}\xi$. The parametric speed $\|\dot{\boldsymbol{\gamma}}\| \equiv \sqrt{\dot{x}^2 + \dot{y}^2}$, the unit tangent vector $\boldsymbol{t} \equiv \dot{\boldsymbol{\gamma}} / \|\dot{\boldsymbol{\gamma}}\|$, and the outward unit normal vector $\boldsymbol{n} \equiv \pm \hat{\boldsymbol{t}}$ are found by differentiating the restriction of the parametrization to the boundary with respect to the parameter ξ. These vectors and matrices are in general sparse, $\boldsymbol{\mathcal{P}}$, $\boldsymbol{\mathcal{D}}$, and $\boldsymbol{\mathcal{F}}$ in particular, since only few of the basis functions have support on the design boundary.

Gradient Evaluation

The optimization is driven by gradients of the objective and constraint functions defining the optimization problem. These sensitivities measure how the design variables affect the objective and constraint functions. We compute these analytically by direct differentiation of the discretized versions of the functions in Equation (4.3) with respect to the coordinates of the control points, that act as our design variables.

We collect the design variables in one vector $\boldsymbol{\chi}$, such that $\boldsymbol{\chi} = (x_1, \ldots, x_N, y_1, \ldots, y_N)$, where (x_k, y_k) are the coordinates of the k^{th} control point, and we let $\bullet' \equiv \partial \bullet / \partial \chi_k$ denote the partial derivative with respect to the k^{th} design variable. For the objectives and the constraint in Equation (4.3) we have:

$$C'_{\Delta p} = \boldsymbol{\mathcal{P}}'^T \boldsymbol{U} + \boldsymbol{\mathcal{P}}^T \boldsymbol{U}', \tag{4.5a}$$

$$C'_{\Delta p} = \boldsymbol{U}^T \boldsymbol{\mathcal{D}}' \boldsymbol{U} + 2\boldsymbol{U}^T \boldsymbol{\mathcal{D}} \boldsymbol{U}', \tag{4.5b}$$

$$C'_d = \boldsymbol{\mathcal{F}}'^T \boldsymbol{U} + \boldsymbol{\mathcal{F}}^T \boldsymbol{U}', \tag{4.5c}$$

$$A' = \boldsymbol{y}^T \boldsymbol{\mathcal{A}} \boldsymbol{x}' + \boldsymbol{x}^T \boldsymbol{\mathcal{A}} \boldsymbol{y}'. \tag{4.5d}$$

The derivatives of $\boldsymbol{x}$ and $\boldsymbol{y}$ in Equation (4.5d) are trivial. The derivatives of the objective matrices/vectors $\boldsymbol{\mathcal{P}}$, $\boldsymbol{\mathcal{D}}$, and $\boldsymbol{\mathcal{F}}$ in Equations (4.5a)—(4.5c) may be found by differentiation of the integrands in Equation (4.4):

$$\begin{aligned} \boldsymbol{\mathcal{P}}'_{\gamma_i} &= \left(\frac{\langle \, \mathcal{P}_i^p \, \|\dot{\boldsymbol{\gamma}}\| \, \rangle}{\langle \, \|\dot{\boldsymbol{\gamma}}\| \, \rangle} \right)' \\ &= \frac{\langle \, \mathcal{P}_i^p \, \|\dot{\boldsymbol{\gamma}}\|' \, \rangle \, \langle \, \|\dot{\boldsymbol{\gamma}}\| \, \rangle + \langle \, \mathcal{P}_i^p \, \|\dot{\boldsymbol{\gamma}}\| \, \rangle \, \langle \, \|\dot{\boldsymbol{\gamma}}\|' \, \rangle}{\langle \, \|\dot{\boldsymbol{\gamma}}\| \, \rangle^2}, \end{aligned} \tag{4.6}$$

where we have defined $\dot{\bullet} \equiv \partial \bullet / \partial \xi$ and $\langle \bullet \rangle \equiv \int \bullet \, \mathrm{d}\xi$, and used that all basis functions $\mathcal{P}$ are independent of the design variables. Here, the derivative of the parametric speed $\|\dot{\boldsymbol{\gamma}}\|$ may be found from the parametrization:

$$\begin{aligned} \|\dot{\boldsymbol{\gamma}}\|' &= \left(\sqrt{\dot{x}^2 + \dot{y}^2}\right)' \\ &= \frac{\dot{x}\,\dot{x}' + \dot{y}\,\dot{y}'}{\|\dot{\boldsymbol{\gamma}}\|} \\ &= \begin{cases} \frac{\dot{x}}{\|\dot{\boldsymbol{\gamma}}\|}\,\dot{\mathcal{R}}^g_k & \text{for } k = 1, \ldots, N \\ \frac{\dot{y}}{\|\dot{\boldsymbol{\gamma}}\|}\,\dot{\mathcal{R}}^g_k & \text{for } k = N+1, \ldots, 2N \end{cases} . \end{aligned} \tag{4.7}$$

Equivalent approaches may be taken for the matrices $\boldsymbol{\mathcal{D}}$ and $\boldsymbol{\mathcal{F}}$ in Equation (4.4).

The derivative of the solution $\boldsymbol{U}$ in Equations (4.5a)—(4.5c) may be found by solving the linear equation system obtained by differentiation of Equation (3.10):

$$(\boldsymbol{M} + \boldsymbol{D})\boldsymbol{U}' = \boldsymbol{F}' - \boldsymbol{M}'\boldsymbol{U}, \tag{4.8}$$

where

$$\boldsymbol{D} = \rho \begin{bmatrix} \boldsymbol{D}_{1,1} & \boldsymbol{D}_{1,2} & \boldsymbol{0} \\ \boldsymbol{D}_{2,1} & \boldsymbol{D}_{2,2} & \boldsymbol{0} \\ \boldsymbol{0} & \boldsymbol{0} & \boldsymbol{0} \end{bmatrix}, \tag{4.9a}$$

$$\boldsymbol{D}_{i,j\,k,\ell} = \iint\limits_{[0,1]^2} \mathcal{P}^{u_i}_k \left(\boldsymbol{e}_j^T \, \boldsymbol{J}^{-T} \, \nabla u_i(\underline{\boldsymbol{u}}) \right) \mathcal{P}^{u_j}_\ell \det\left(\boldsymbol{J}\right) \mathrm{d}\boldsymbol{\xi} \, . \tag{4.9b}$$

We mention that the matrix $\boldsymbol{\mathcal{J}} = \boldsymbol{M} + \boldsymbol{D}$ also appears in the iterative Newton-Raphson method employed for solving the governing equations. The derivative of the system matrix $\boldsymbol{M}$ and vector $\boldsymbol{F}$ in Equation (4.8) may be found by differentiation of the integrands in Equation (3.11):

$$\begin{aligned} \boldsymbol{K}'_{k\,i,j} = & \iint\limits_{[0,1]^2} \nabla^T \mathcal{P}^{u_k}_i \boldsymbol{J}^{-1\prime} \boldsymbol{J}^{-T} \nabla \mathcal{P}^{u_k}_j \det\left(\boldsymbol{J}\right) \mathrm{d}\boldsymbol{\xi} \\ & + \iint\limits_{[0,1]^2} \nabla^T \mathcal{P}^{u_k}_i \boldsymbol{J}^{-1} \boldsymbol{J}^{-T\prime} \nabla \mathcal{P}^{u_k}_j \det\left(\boldsymbol{J}\right) \mathrm{d}\boldsymbol{\xi}. \\ & + \iint\limits_{[0,1]^2} \nabla^T \mathcal{P}^{u_k}_i \boldsymbol{J}^{-1} \boldsymbol{J}^{-T} \nabla \mathcal{P}^{u_k}_j \det\left(\boldsymbol{J}\right)' \mathrm{d}\boldsymbol{\xi}. \end{aligned} \tag{4.10}$$

Here, the derivative of the determinant and of the inverse of the Jacobian matrix may be found by simply writing them out explicitly in terms of x and y and subsequently differentiating this as in Equation (4.7), or alternatively from the relations $\boldsymbol{J}^{-1\prime} = \boldsymbol{J}^{-1}\,\boldsymbol{J}'\,\boldsymbol{J}^{-1}$ and $\det(\boldsymbol{J})' = \det(\boldsymbol{J})\,\mathrm{tr}(\boldsymbol{J}^{-1}\boldsymbol{J}')$, along with differentiation of the parametrization:

$$\boldsymbol{J}' = \begin{cases} \begin{bmatrix} \mathcal{R}^g_{k,\xi} & \mathcal{R}^g_{k,\eta} \\ 0 & 0 \end{bmatrix} & \text{for } k = 1, \ldots, N \\ \\ \begin{bmatrix} 0 & 0 \\ \mathcal{R}^g_{k,\xi} & \mathcal{R}^g_{k,\eta} \end{bmatrix} & \text{for } k = N+1, \ldots, 2N \end{cases}, \tag{4.11}$$

where we have defined $\bullet_{,s} \equiv \partial \bullet / \partial s$. Equivalent approaches may be taken for the matrices $\boldsymbol{C}$ and $\boldsymbol{G}$ in Equation (3.11).

Finally, to account for the induced movement of the linked control points, as a result of the update of the interior parametrization when the design control points are moved, the full sensitivity is computed as $\tilde{\bullet}' = \bullet' + \sum_i \chi_i^{l\prime} \frac{\partial}{\partial \chi_i^l}$, where the summation is over linked design variables, or

$$\widetilde{\nabla}_d = \nabla_d + \mathcal{W} \nabla_l, \tag{4.12}$$

where the subscripts d and l refer to design variables and linked variables, respectively. The matrix $\mathcal{W}_{i,j} = \partial \chi_i^l / \partial \chi_j^d$ relates the linked control points to the design control points.

Implementation Details

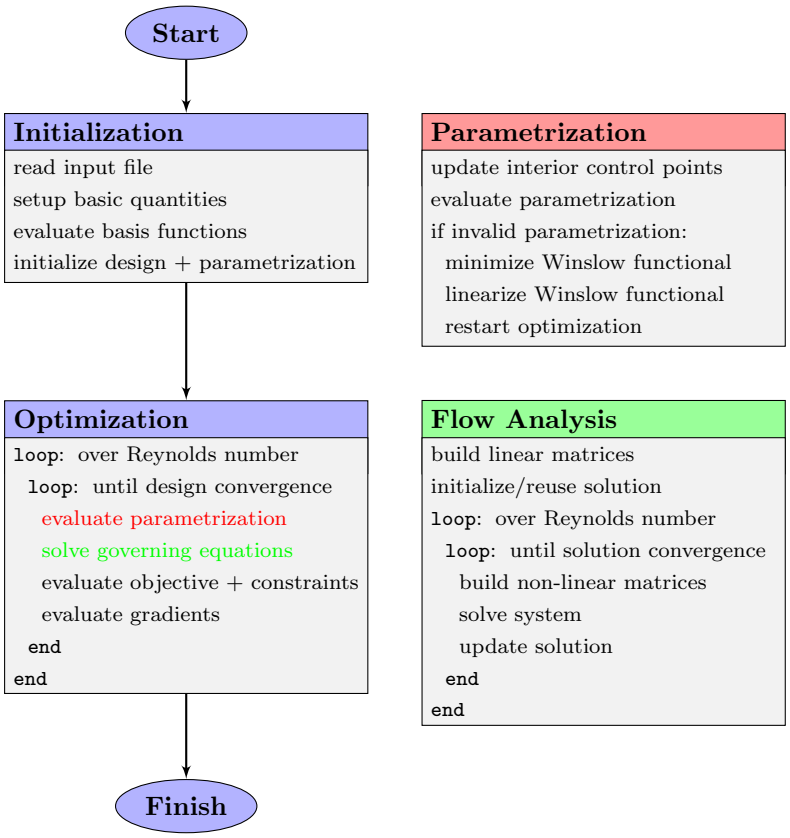

Figure 4.4: *Flow chart for the optimization process (left) with details of the parametrization and analysis procedures (right).*

The flow chart in Figure 4.4 sketches the most significant steps in solving the shape optimization problem in Equation (4.1) based on isogeometric analysis.

In the initialization phase, we perform as many calculations as possible that are independent of the parametrization. In particular, all basis functions and

their derivatives are evaluated in the Gauss quadrature points once and for all. Although more memory demanding, this approach greatly reduces the computational expenses, compared to evaluating the functions on the fly in each optimization iteration. The construction of a good initial parametrization is also vital for the optimization.

The optimization process includes an outer loop over increasing Reynolds number. This is only necessary when designing shapes in higher Reynolds number flows. The entire process outlined in the flow chart may be embedded into a loop over increasing refinement of geometry and/or analysis. The optimization is performed using the SNOPT optimization package, which is based on a sequential quadratic programming algorithm [Gill et al., 2008]. Standard settings for SNOPT are used, except for the step size limit which, when set relatively low, e.g., 5% of the characteristic length scale of the problem, has been found to significantly improve the convergence by avoiding too large jumps in the design space. For validation purposes, the analytically computed gradients are checked initially against finite difference estimates.

On the analysis side, we use an iterative Newton-Raphson method to solve the governing non-linear equation, gradually increasing the Reynolds number when this is high. In the field approximations, bi-quartic tensor product B-splines are used for the velocities and bi-cubic tensor product B-splines for the pressure, both C^2 across knots, corresponding to the Taylor-Hood discretization $\mathbf{u}4_0^2\mathrm{p}3_0^1$ (d) in Table 3.1). Dirichlet boundary conditions are enforced strongly, while homogeneous Neumann boundary conditions are enforced weakly. All integrals are evaluated numerically using Gaussian quadrature.

4.4 Regularization

To strengthen the result of the shape optimization, the design space in which we look for solutions should be as large as possible. A natural way to ensure a large design space is to use many control points as design variables, although the inclusion of weights as design variables could also be considered [Qian, 2010; Nagy et al., 2011]. As the number of design control points go up, more complex shapes can be designed. This comes, however, on the cost of numerical challenges. These challenges, and solution strategies to remedy them, are discussed in this section.

For the purpose of illustration, we consider a concrete example of the shape optimization problem (4.1)-(4.2a), and use this as benchmark for the following tests of the regularization technique. The problem is outlined in Figure 4.5a. The aim is to design the shape Γ' of a pipe bend (dashed) to minimize the pressure drop from the inlet boundary (red) to the outlet boundary (blue), keeping the shape of the inlet and the outlet (solid) fixed, and with an upper bound on the area of the pipe.

We assume a parabolic horizontal velocity profile on the inlet boundary, that the velocity it is zero along the side walls, assuming no-slip conditions, and that its horizontal component is zero along the open outlet boundary. We take the length scale as $r = 1$, the velocity scale as $U = \max(\|\boldsymbol{u}_{\text{inlet}}\|) = 1$, the density as $\rho = 1$, and the viscosity as $\mu = 1$, assuming appropriate units are used, which yields a Reynolds number of $\mathrm{Re} = 1$ for the initial problem.

We parametrize the pipe bend as a bi-cubic tensor product B-spline surface,

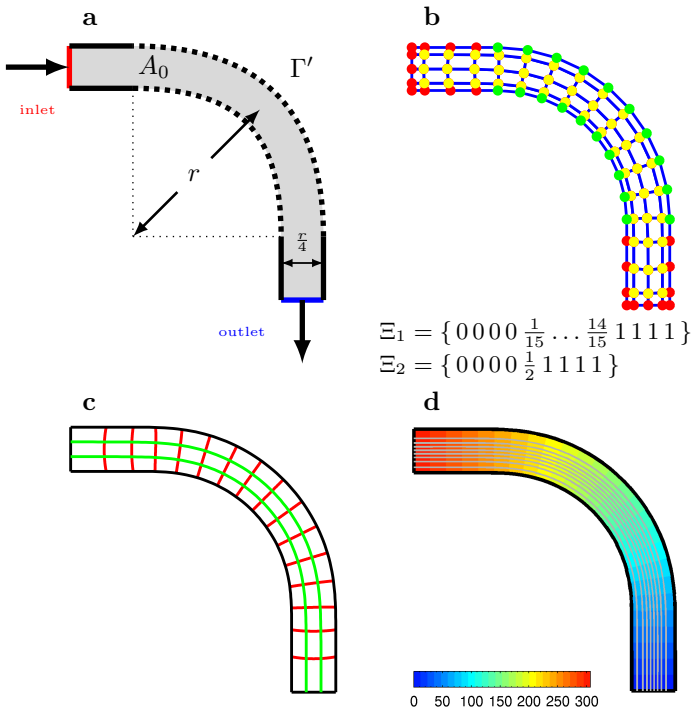

Figure 4.5: *Pipe bend with minimal pressure drop: design problem setup (***a***), initial control net (***b***), initial parametrization (***c***), and initial pressure contours and flow stream lines (***d***).*

and let the initial design connect the inlet and outlet by an approximate quarter annulus. The initial control net, the corresponding parametrization, and the resulting pressure distribution and stream lines of the flow through it are depicted in Figure 4.5b–d. We use 20 control points as design variables, 10 on each of the two boundaries segments to be designed, and we allow these to move freely in both spatial dimensions, except for the four end control points, which are only allowed to move along the direction of the inlet/outlet, in order to keep a handle on these. As upper bound on the area, we use the initial value, i.e., $A_{\max} = A_0$, and we relax the lower bound, i.e., $A_{\min} = -\infty$. Since the lengths of the inlet and outlet boundaries are constant, the sensitivities in Equation (4.6) are greatly simplified.

The Challenge: Clustering of Control Points

Applying the isogeometric machinery from Section 3.2 to the shape optimization problem outlined above results in the optimization history depicted in Figure 4.6. From iteration 0 to 15 (actually *function call* in SNOPT terminology), the design control points firstly align, connecting the inlet and the outlet by a more or less straight segment, thereby decreasing the pressure drop by $\sim 74\%$. This design reduces the length of the pipe in intuitive accordance with the Poiseuille law. At iteration 44, sharper corners at the inlet and outlet are formed, but from iteration 44 and onwards, the shape changes only slightly, and the decrease in

the pressure drop is accordingly small. The location of the control points, however, and the resulting parametrization change *appreciably*, though. The control points cluster and eventually fold over, resulting in an invalid parametrization after 67 iterations from which the method cannot proceed.

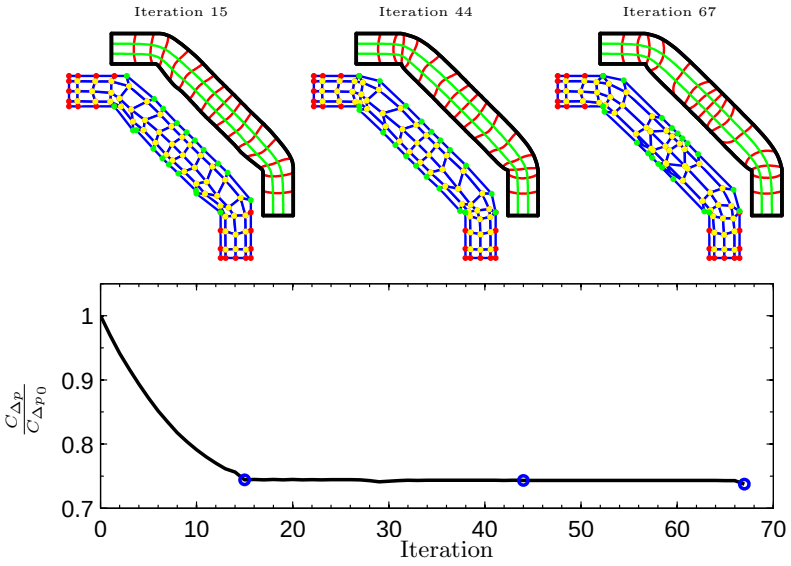

Figure 4.6: *Pipe bend with minimal pressure drop: objective function as a function of optimization iteration (bottom), and three snap shots of the control net and the associated parametrization (top).*

The problem seems to arise in the second of two qualitatively different stages of the optimization: the optimizer finds an "optimal" shape in the first stage, and then tries to find an "optimal" parametrization of it in the second stage. The latter "optimality", however, is a numerical artefact. The optimizer finds the flaws in the numerical procedure, so to say, and tries to align the errors in such a way, that the *numerical estimate* is minimized, although the "actual" value is not. This is the challenge in a nut-shell: when optimizing the location of many control points in sufficiently unconstrained problems, they may cluster, spuriously yielding slightly lower values of the objective function on the cost of significantly worse parametrizations and less accurate analysis, which may eventually lead to a collapse of the method. The clustering of control points is a well-known issue in isogeometric shape optimization [Wall et al., 2008; Nagy et al., 2011; Seo et al., 2010a]. Related numerical problems in finite element based shape optimization, and regularization techniques to address them, are also well-described [Bletzinger et al., 2010]. Below, we firstly give a brief review of some alternative ways out of the current problem, before proposing the regularization approach, in an isogeometric framework.

Some Alternative Solution Strategies

The first natural point of focus, when looking for remedies for the current problem, is on the optimization routine. A quick fix is simply to stop the optimization immediately after the first "shape" stage, and before the onset of the second

"parametrization" stage. This could be achieved by relaxing the existing convergence criterion, or by defining some other relevant measure. However, since this approach only cures the symptoms of the problem, and not the cause of it, and due to the risk of prematurely stopping the optimization, this approach is, in our view, not only quick, but also dirty.

Turning away from the optimization routine, we may focus on the problem formulation instead. An obvious solution to the problem is to reconsider the design degrees of freedom. As the control points align, an ambiguity is introduced, since movements of the control points along the line does not change the shape, but *does* change the parametrization and thus also the numerical estimates of the integrals, and hence the objective function value, making the problem inherently ill-posed. One could then simply argue that for this particular design problem, say, four design control points on each boundary suffice. However, this is an a posteriori type of reasoning that we would like to avoid. More interesting is the idea of making this estimation of the necessary number of design variables dynamic, i.e., inserting and removing design control points on the fly during the optimization [Seo et al., 2010a]. The implementation of a flexible number of design variables in an optimization procedure, however, is less than trivial.

Preserving the *number* of control points, but putting constraints on their movement in the design space, poses yet another alternative. We could, for instance, constrain the design control points to move only along specified directions. In this approach, it is our duty as designers to specify "good" directions along which the control points can move, ensuring both sufficient flexibility in the design while avoiding bad parametrizations. Along the same line of thinking is the concept of putting bounds on the design variables, see e.g. [Cho and Ha, 2009], thus limiting the optimizer to search for a minimum in the vicinity of the initial guess only. In any case, the design space shrinks in these approaches, and the success of the optimization heavily depends on the designers choice in initial condition and constraints on the movement of the control points. A somewhat related, but much more flexible approach, is to introduce a more general constraint on the design variables. A popular choice is to put a lower bound on the distance between control points [Wall et al., 2008]. Although this approach does take care of the tendency of control points to cluster, it still closes the door to parts of the design space. Another choice is to prescribe an upper bound on a single, global measure of the shape change [Nagy et al., 2011] during the optimization, thereby significantly reducing the number of constraints.

Boundary Regularization

To avoid the problem of clustering control points and the associated fatal parametrization, we suggest to regularize the optimization problem [Mohammadi and Pironneau, 2004; 2010]. More specifically, we suggest to add a term to the objective function that, by measuring the quality of the parametrization, prevents the unwanted phenomenon. In this approach, the regularized objective function $\widetilde{C}$ is written as:

$$\widetilde{C} = C + \tilde{\epsilon} R, \tag{4.13}$$

where C is the "actual" physical objective, here expressing the pressure drop in the pipe bend, R is the "artificial" regularization objective, and $\tilde{\epsilon} > 0$ specifies

the weight of the regularization term. The aim of the optimization, when using the regularized objective, is twofold: we are not only searching for the design that minimizes the pressure drop, but also for the shape whose parametrization makes the numerical approximation of it more reliable. Thereby, we embed the construction of a good parametrization into the design optimization, and we are thus targeting the very cause of the problem.

The method poses two challenges: Firstly, it necessitates the construction of a quality measure R of the parametrization, and secondly, it requires the specification of its relative importance $\tilde{\epsilon}$ in the optimization.

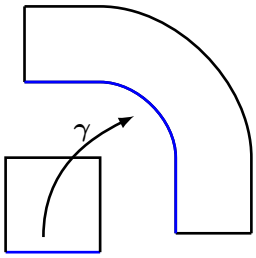

Figure 4.7: *Illustration of the focus of boundary regularization.*

The focus of this study is on boundary regularization, as sketched in Figure 4.7. This addresses the quality of parametrization of the design boundary, which is clearly compromised early on in the fatal optimization history in Figure 4.6. One measure we have found useful is the norm squared of the parametric acceleration along the design boundaries, integrated in parameter domain:

$$R = \int_0^1 \|\ddot{\boldsymbol{\gamma}}\|^2 \,\mathrm{d}\xi, \tag{4.14}$$

where we have defined $\ddot{\bullet} \equiv \partial^2 \bullet / \partial \xi^2$. In discretized form, it reads:

$$R = \boldsymbol{x}^T \boldsymbol{R} \boldsymbol{x} + \boldsymbol{y}^T \boldsymbol{R} \boldsymbol{y}, \tag{4.15a}$$

$$\boldsymbol{R}_{i,j} = \int_0^1 \ddot{\mathcal{R}}_i^g \ddot{\mathcal{R}}_j^g \,\mathrm{d}\xi. \tag{4.15b}$$

By minimizing this measure, we bring the boundary parametrization closer to a constant-speed parametrization, and boundary regularization thus leads the optimizer towards a better boundary parametrization. The measure is computationally cheap to implement, since the matrix $\boldsymbol{R}$ only involves integrals of the second order derivatives of the (univariate) basis functions, and since it is quadratic in the design variables, the sensitivities may be straightforwardly computed.

An important challenge in the methodology is the specification of a suitable weight $\tilde{\epsilon}$ of the regularization. This challenge is similar in nature to the one associated with specifying a suitable minimal distance between control points [Wall et al., 2008], or a maximal shape change norm [Nagy et al., 2011]. The specification may be partly facilitated by estimating the initial ratio between the physical objective C_0 and the regularization objective R_0:

$$\tilde{\epsilon} = \frac{|C_0|}{|R_0|}\epsilon, \tag{4.16}$$

where we assume that $R_0 \neq 0$, and that this ratio does not change too much with the design. Taking $\epsilon = 1$ yields identical initial numerical values for the physical and the regularization terms in Equation (4.13). Usually, a value $\epsilon \ll 1$ is therefore anticipated. The smaller the ϵ, the closer we get to the original optimization problem, but, on the other hand, the more we weaken the regularization and its stabilizing influence on the parametrization and the convergence.

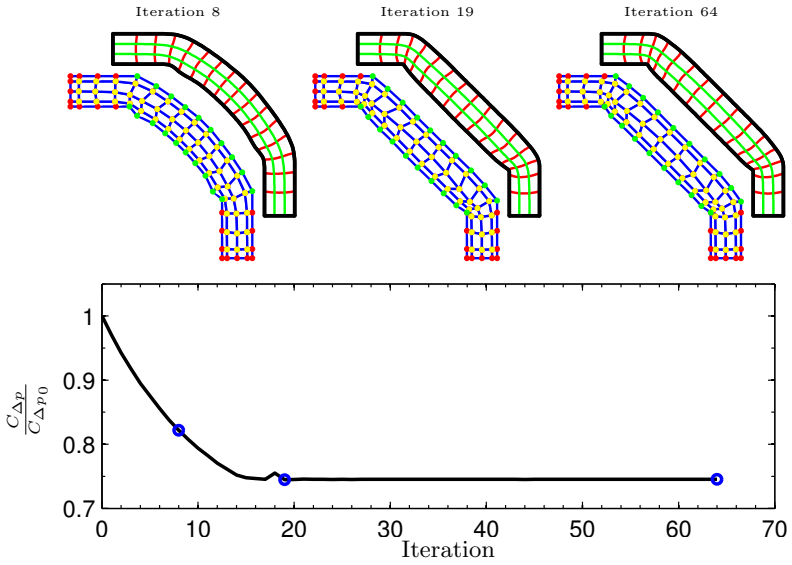

Figure 4.8: *Pipe bend with minimal pressure drop: regularized optimization history (bottom), and snap shots of the control net and the associated parametrization (top).*

We apply the regularized isogeometric shape optimization method to the current design problem, thus minimizing the *regularized* pressure drop (4.13)–(4.14) through the pipe bend using the weight $\epsilon = 10^{-2}$. The optimal design is reached after 64 iterations, at which point the pressure drop is decreased to 74.5%, and the area constraint is active (but fulfilled). The optimization history is shown in Figure 4.8. Here, it is worth noticing that the optimal design is quite close to the design from which the original formulation drifts off, cf. Figure 4.6, that the difference in the minimal pressure drop between the designs is small, and, most importantly, that the parametrization is much better in this regularized formulation, thereby making the analysis more reliable. The effect of the regularization is clearly seen from the intermediate design in iteration 19, to the converged design in iteration 64. The control points spread out along the line, and the concentration of control points is shifted away from the straight central part, towards the curved parts at the inlet and the outlet. This is also where the geometry, and hence the flow analysis, is most challenging, due to the presence of sharp corners that form as a result of coalescing control points. The resulting pressure field is shown in Figure 4.9. The optimized design is similar to the topology optimized design with minimal energy dissipation [Gersborg-Hansen et al., 2005].

To examine the effect of the regularization in greater detail, we solve the problem for a range of regularization weights $\epsilon \in [10^{-3}, 10^{-1}]$. Figure 4.10 shows how the optimized pressure drop, the required number of iterations, and

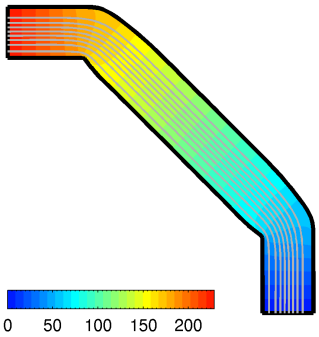

Figure 4.9: *Pipe bend with minimal pressure drop: optimized pressure contours and flow stream lines.*

the optimal design vary with the regularization weight. When the regularization is strong, the optimization converges quickly to a smoother design with a higher pressure drop. As the regularization is decreased, more iterations are required to reach designs with locally higher curvature and smaller pressure drops. A stagnation point in the pressure drop curve is observed, associated with the formation of the sharp corners at the inlet and the outlet, such that the optimized pressure drop only falls off slightly for $\epsilon \leq 3 \cdot 10^{-2}$. In addition, the number of iterations is likewise relatively constant for $3 \cdot 10^{-3} \leq \epsilon \leq 3 \cdot 10^{-2}$. A regularization weight in this range thus seems appropriate in this example. The results, however, are not critically sensitive to the value used.

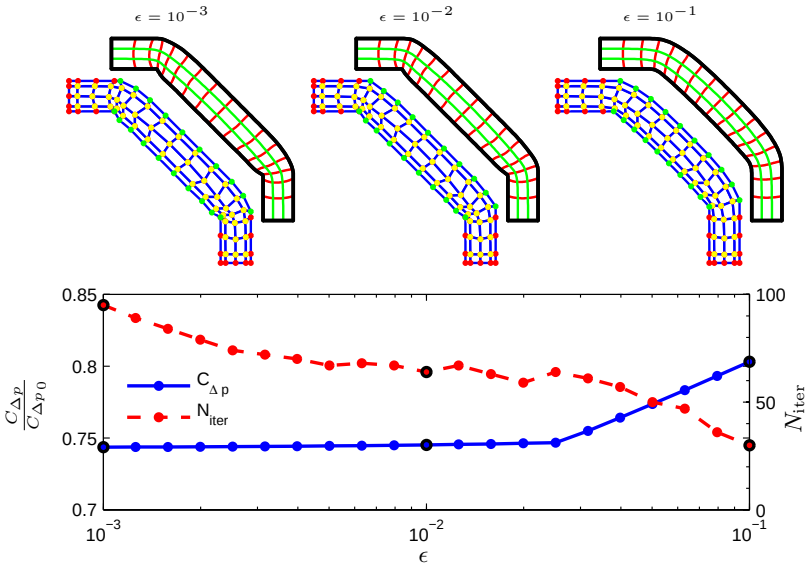

Figure 4.10: *Pipe bend with minimal pressure drop: optimized pressure drop and required number of iterations as a function of regularization weight ϵ (bottom), and optimal design for three values of ϵ (top).*

We conclude this section by mentioning that a range of other regularization measures could be considered. Among these, we have found that similar effects as those presented above may be obtained by minimizing the scalar product of the tangent $\dot{\gamma}$ and the acceleration $\ddot{\gamma}$, the variance of the Jacobian determinant, or the variance of the parametric speed, all evaluated along the design boundary. Minimization of the Winslow functional, however, is found to be more problematic to implement. Furthermore, the regularization measures could alternatively be implemented as constraints, but such investigations have been outside the scope of this study.

4.5 Applications

In this section, we apply the isogeometric shape optimization methodology for fluid design problems to two additional numerical examples.

Body with Uniform Pressure Distribution

We consider the shape optimization problem (4.1)-(4.2b) outlined in Figure 4.11a. The aim is to design the boundary Γ' of a body of given area A_0, placed in a circular fluid container of radius r whose outer boundary rotates, to make the pressure distribution along Γ' as uniform as possible, i.e., to minimize the pressure variation $C_{\nabla p}$ along Γ'. From symmetry considerations, the pressure is constant along the boundary when a disk is placed in the center. Furthermore, analytical solutions to the governing Navier-Stokes equations for this so-called Taylor-Couette flow problem is well-known from the literature. A circle enclosing the specified area and with center in the center of the container is therefore a solution to the shape optimization problem. In the following, we investigate how well the isogeometric shape optimization methodology is able to reproduce this.

To represent the outer perimeter as an exact circle, which is of paramount importance when specifying boundary conditions, we parametrize the geometry using quadratic NURBS. As initial design, we use a square placed in the middle, which is an intentionally bad initial guess. The control net, knot vectors and weights are shown in Figure 4.11b, and the corresponding parametrization is visualized in Figure 4.11c. The patch is attached to itself along the dashed line, resulting in an additional C^0-continuity here. The velocity field is specified as purely tangential along the outer moving perimeter, and as vanishing on the inner steady boundary, assuming no-slip conditions. Since full Dirichlet boundary conditions are prescribed for the velocity field, we set the pressure to zero in an arbitrary point. We take the initial area as $A_0 = 2$, the radius of the outer perimeter as $r = 2$, the velocity scale as $U = 1$, the density as $\rho = 1$, and the viscosity as $\mu = 1$, assuming again appropriate units are used, which again yields a Reynolds number of $\mathrm{Re} = 1$. The initial pressure field is depicted in Figure 4.11d. In this, the C^0-continuities are invisible to the naked eye. We take the constraint on the area as the initial value, i.e., $A_{\max} = A_{\min} = \pi r^2 - A_0$, and a one-step approach is employed for the Reynolds number. To resolve the rotational symmetry, the left-most control point is allowed only to move horizontally. It turns out that this problem is sufficiently constrained to prevent control points from clustering, and we therefore solve it without regularization.

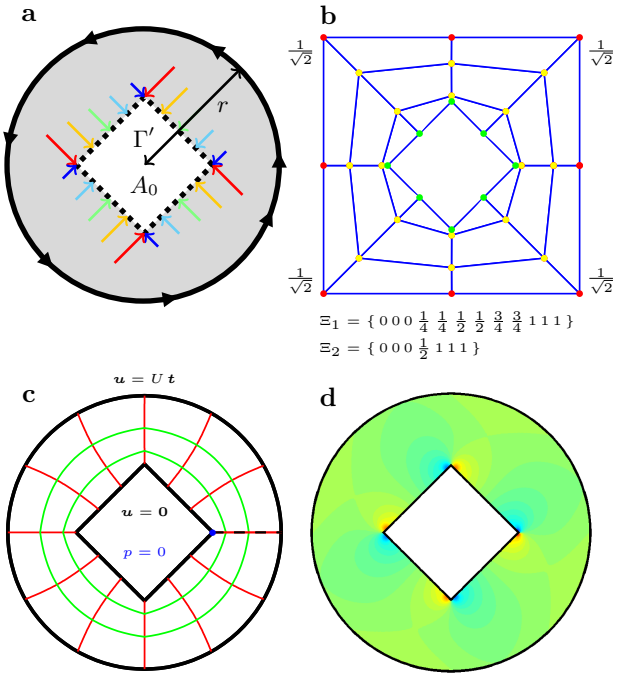

Figure 4.11: *Body with uniform pressure distribution: design problem setup (***a***), initial control net, knot vectors, and non-unitary weights (***b***), initial parametrization (***c***), and initial pressure field (***d***).*

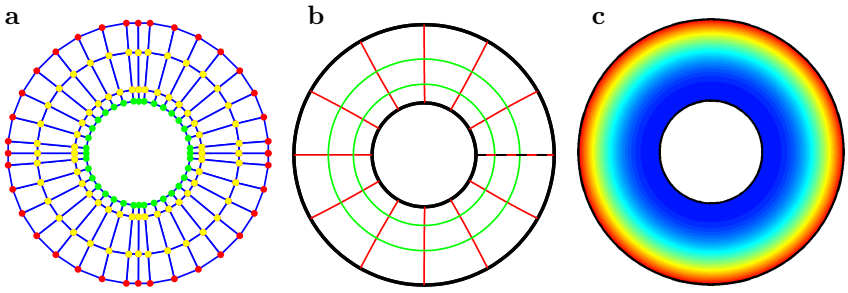

Figure 4.12: *Body with uniform pressure distribution: optimized control net (***a***), parametrization (***b***), and pressure field (***c***) for 36 design control points.*

We consider three consecutive refinements of the coarse geometry described above, obtained by uniform knot refinement along the tangential direction, thereby representing the design boundary Γ' by 8, 12, 20, and 36 control points, respectively. We solve the design problem for each of these four geometric models, using in turn the optimized coarser design as initial guess for the finer optimization. The results for the finest geometric approximation are shown in Figure 4.12. The optimal design is reached in a total of 1032 iterations, and the pressure variation is decreased by a factor of $\sim 10^{-17}$. The optimal control net is shown in (a), and the corresponding optimized parametrization is shown in (b). The inner boundary is seen to approximate a circle very accurately.

N_{design}	$C_{\nabla p}/C_{\nabla p0}$	ϵ_{circle}	N_{iter}
8	$8.1 \cdot 10^{-4}$	$6.3 \cdot 10^{-2}$	131
12	$5.1 \cdot 10^{-5}$	$3.7 \cdot 10^{-3}$	127
20	$3.3 \cdot 10^{-6}$	$2.5 \cdot 10^{-4}$	344
36	$1.4 \cdot 10^{-17}$	$2.1 \cdot 10^{-5}$	430

Table 4.1: *Body with uniform pressure distribution: comparison of objective function, discrepancy from the exact circle, and number of iterations for different numbers of design variables.*

The optimized pressure field shown in (c) is significantly more uniform than the initial one shown in Figure 4.11d.

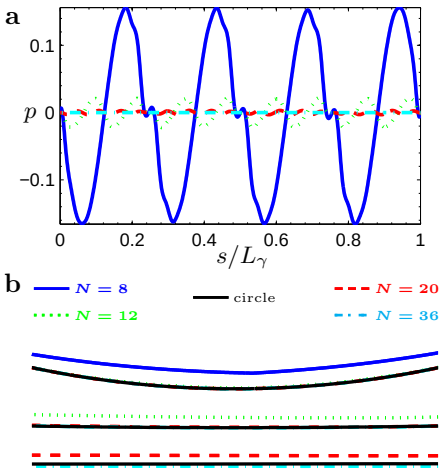

Figure 4.13: *Body with uniform pressure distribution: comparison of pressure distributions along the optimized boundaries (***a***), and comparison of the optimized boundaries to the exact circle in three zooms (***b***).*

To examine more closely the effect of enlarging the design space by the use of more design control points, Figure 4.13a shows the pressure distribution along the optimized boundary when using 8, 16, 20, and 36 design control points. Also shown, in Figure 4.13b, is a comparison of the lower part of the optimized design boundaries to the exact circle. As is evident from the figure, the more control points we use, the more uniform the pressure distribution we obtain, and the better the approximation to the exact circle we find. This is quantitatively supported by the numerical values listed in Table 4.1, showing that both the pressure variation, and the discrepancy of the design boundary from the circle of radius $r_0 = \sqrt{A_0/\pi}$ converge towards zero, as more design control points are used. Here, we have estimated the discrepancy of the design boundary from the circle of radius r_0 by the measure:

$$\epsilon^2_{\text{circle}} = \int_\gamma \left(\frac{x^2 + y^2}{r_0^2} - 1 \right)^2 \, \mathrm{d}s.$$

With 36 design control points, this error is $\sim 2.1 \cdot 10^{-5}$.

Body with Minimal Drag

We consider the classical shape optimization problem (4.1)-(4.2c) outlined in Figure 4.14a, see e.g. [Pironneau, 1973; 1974]. The boundary Γ' of a body with given area A_0 traveling at constant speed U through a fluid is designed to minimize the drag C_d it experiences as the fluid flows past it.

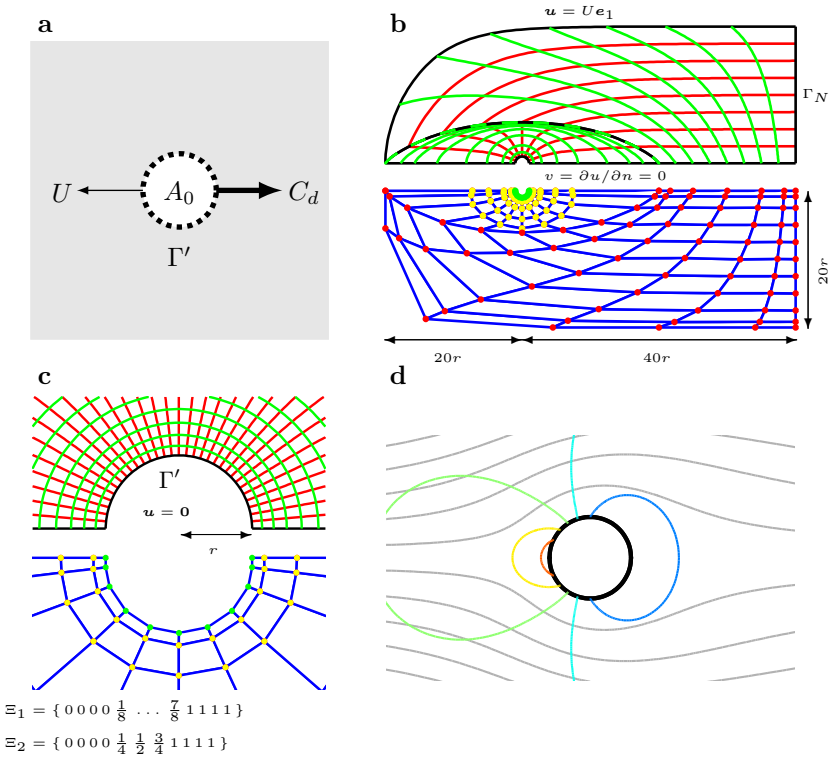

Figure 4.14: *Body with minimal drag: design problem setup (***a***), initial control net, initial parametrization, domain dimensions, boundary conditions, and knot vectors (***b** *and* **c***), and initial pressure contours and flow stream lines for* $U = 1$ *(***d***).*

Symmetry is assumed around the line along which the body travels, and only the upper half of the problem is considered. To facilitate the implementation of boundary conditions, and to achieve local refinement close to the body, this half space is truncated using two patches, as shown by the black lines in Figure 4.14b (top). The design boundary Γ' is initialized as an approximate half circle of radius $r = 1$, as depicted in Figure 4.14c (top), and the computational domain extends $20r$ upstream, $20r$ sidewards, and $40r$ downstream, as depicted in Figure 4.14b (bottom). Cubic B-splines are employed for the geometric parametrization. The initial control net is shown in Figures 4.14b-c (bottom). The governing equations are solved in the co-moving inertial system in which the body is at rest. For the boundary conditions, we assume no-slip along the design boundary Γ', that the flow is undisturbed along the upstream truncation boundary, that the downstream truncation boundary is open, and

that the fields are symmetric around the lower truncation boundary, as sketched in Figures 4.14b-c (top). The density and viscosity are set to $\rho = 1$ and $\mu = 1$, respectively, assuming appropriate units.

We use 11 design control points, and take $A_0 = \pi$ as lower bound on the area of the body, i.e., $A_{\max} = \text{Area}_0 - A_0/2$, and relax the upper bound. The end control points are allowed only to move horizontally and symmetrically, to ensure that the domain is appropriately defined, and to resolve the translational symmetry of the problem. To prevent the control net from folding over at the leading and trailing edges in particular, boundary regularization with weight $\epsilon = 0.01$ is employed.

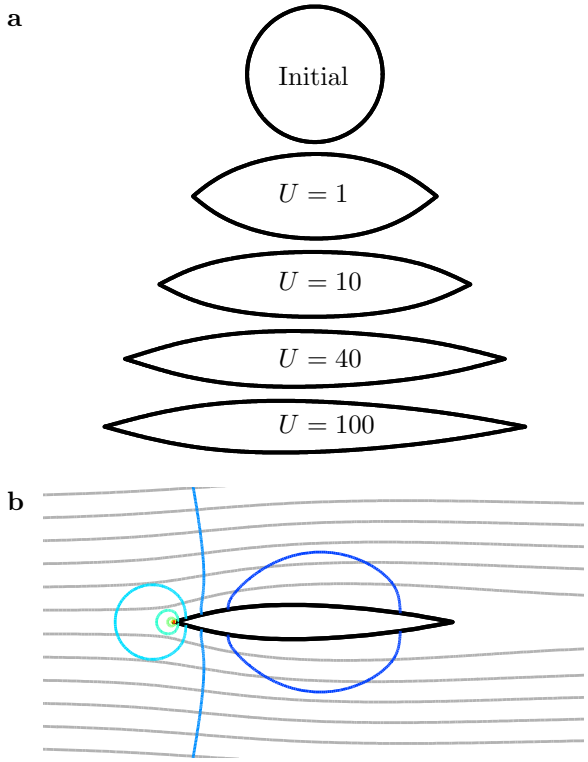

Figure 4.15: *Body with minimal drag: initial and optimized shapes for* $U \in \{1, 10, 40, 100\}$ *(***a***), and optimized pressure contours and flow stream lines for* $U = 100$ *(***b***).*

We solve the shape optimization problem for four consecutive speeds $U \in \{1, 10, 40, 100\}$, using again the lower speed solution as initial guess for the higher speed. These speeds correspond to Reynolds numbers 1, 10, 40, and 100, respectively, based on the initial setup. After $57 + 40 + 67 + 58 = 222$ design iterations, the optimization converges. To illustrate how the design varies with flow speed, the initial and the optimized shapes for each of the four speeds are compared in Figure 4.15a, and the characteristics of the shapes are summarized in Table 4.2. A considerable change in the design is seen as the speed is increased. For low speeds, a football-like shape is optimal. For higher speeds, a more slender shape is optimal, eventually becoming slightly thicker upstream

Design	$L/2$	$H/2$	x_w	C_d^*	r
Initial	1.00	1.00	0.00	4.13	-
$U = 1$	1.80	0.62	0.02	6.12	7.7%
$U = 10$	2.29	0.48	-0.03	1.81	2.4%
$U = 40$	2.80	0.41	-0.32	0.97	1.2%
$U = 100$	3.12	0.38	-0.51	0.64	0.4%

Table 4.2: *Body with minimal drag: length (L), height (H), widest location (x_w), drag coefficient ($C_d^* = C_d/(\frac{1}{2}\rho U^2 H)$), and relative decrease in drag $r = (C_d^{initial} - C_d^{optimal})/C_d^{initial}$ for the initial and optimized shapes.*

than downstream. The long slender design relates well to the increase in the significance of the form drag, and the decrease in the significance of the skin friction drag, as the speed increases. The pressure and flow fields around the optimized shape for the terminal speed $U = 100$ are depicted in Figure 4.15b.

In the present context, minimizing the drag on the body is equivalent to minimizing the energy dissipation in the flow past it [Mohammadi and Pironneau, 2010], and we may compare the results for these two types of problems. Firstly, for Reynolds number $\mathrm{Re} = 1$, the angle of the wedge-shaped upstream part compares well to the theoretically predicted value of 90°, while for higher Reynolds numbers, the shapes are more cusped [Pironneau, 1973; 1974]. For Reynolds number $\mathrm{Re} = 1$, the present optimal shape compare well qualitatively to the numerical results obtained in [Katamine et al., 2005], while for Reynolds numbers $\mathrm{Re} > 1$, the present optimal shapes differ significantly from their ovoid with the upstream part slimmer than the downstream part. Consistently better qualitative correspondence is found with the numerical results in [Kim and Kim, 1995], although the present optimal shapes are slightly longer, thinner, and more ovoid than their elliptic shapes.

4.6 Conclusions

In this chapter, we have applied isogeometric analysis to shape optimization problems for fluids, using NURBS and B-splines from computer aided design both as analysis tool in a finite-element-like manner to solve the governing steady-state, incompressible Navier-Stokes equations, and as design tool to find optimal shapes by moving the control points using a gradient-based numerical optimization package. By adding to the objective function a measure of the quality of the parametrization, we have established a regularization technique to avoid inappropriate parametrizations during optimization, a commonly known problem in isogeometric shape optimization. Based on a benchmark design problem, in which a pipe bend is designed to minimize the pressure drop of the flow through it, the integral of the norm squared parametric acceleration along the design boundary was found to be a cheap, flexible and efficient regularization measure. The method embeds the construction of a good parametrization into the design optimization, allowing the designer to search for shapes in a large design space, with little a priori knowledge on the optimal design. The greatest challenge of the method lies in the choice of the regularization weight.

To emphasize the robustness of the proposed isogeometric shape optimization methodology for fluids, we have used it firstly to design a body at rest in a circular fluid container with rotating boundary to obtain a uniform pressure distribution along its boundary, and secondly to design a body traveling at constant speed through a fluid to minimize the drag from the flow past it. For the former problem, it was found that progressively better approximations of a known solution is achieved when more design control points are used, while the latter problem demonstrated that significantly different shapes of the minimal drag body may be obtained when the speed is varied. In summary, the isogeometric shape optimization methodology facilitates the accurate design of complex shapes in engineering problems within fluid mechanics.

Chapter 5

Isogeometric Analysis of Flow Acoustics

In this chapter, we extend the use of isogeometric analysis to the propagation of sound through moving fluids. We construct and validate a coupled flow-acoustic model based on the methodology, and use it to investigate geometric effects on ultrasound propagation through flows in 2-dimensional ducts. The chapter summarizes the findings in [Nielsen et al., 2011b] included in Appendix D.

5.1 Introduction

It is well known in physics and engineering applications that wave propagation in ducts is sensitive to the duct geometry. In particular, spatial resonances exist at certain frequencies, and it is anticipated that even small disturbances may cause large variations in signal transmission at such frequencies. Motivated by this, we investigate the influence of a background flow on acoustic wave propagation in 2-dimensional ducts of varying width.

Finite element methods within the field of sound propagation through flow in ducts are extensively used, based on, e.g., the convected Helmholtz equation [Becache et al., 2004; Redon et al., 2011], the linearized Euler equations [Astley and Eversman, 1981], or the so-called Galbrun's equation [Peyret and Élias, 2001; Dhia et al., 2007; 2010], and often discretized using Lagrange elements with C^0-continuity of the state variable approximations. Our work contributes to this field in two ways.

Firstly, we analyze the coupled flow-acoustic system by explicitly connecting a flow model to an acoustic model. The procedure we follow is first to compute the background flow based on the steady-state, incompressible Navier-Stokes equations in the laminar regime, i.e., at low Reynolds numbers, and then we adopt a linear, time-harmonic flow-acoustic approach for the sound wave propagation in the low Mach number regime, using the calculated background flow as input. This results in a single equation in the acoustic pressure, linear in both the flow field itself and its gradient.

Secondly, we base our calculations on isogeometric analysis. For the problem at hand, isogeometric analysis is particularly appealing because it allows for

simple descriptions of complex duct geometries, and provides high degrees of smoothness for both flow and acoustic fields. The applicability of the method is well documented within fluid mechanics, as demonstrated in Chapter 3, as well as for wave phenomena and the closely related structural vibrations, see e.g. [Cottrell et al., 2006; Hughes et al., 2008].

The first aim of this chapter is to establish and validate the coupled flow-acoustic model for time-harmonic sound propagation at low Mach numbers through a stationary, incompressible background flow at low Reynolds numbers in 2-dimensional ducts based on isogeometric analysis. The second aim is to use the model to numerically examine how the geometry of the duct influences the sound propagation, and in particular its effect on how the acoustic signal depends on flow speed. We consider a transmitting ultrasonic transducer mounted on the duct wall, as sketched in Figure 5.1, and we examine the difference between the downstream and the upstream acoustic signals for different frequencies and flow speeds. Geometric effects are investigated by considering three different duct geometries.

5.2 Governing Equations and Approximations

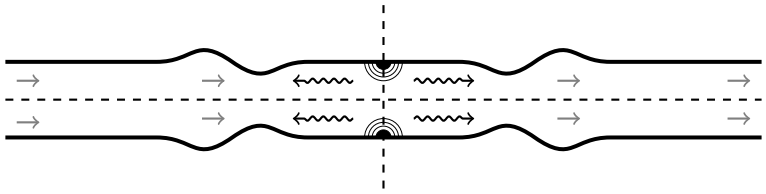

Figure 5.1: *Sound propagates (black arrows) from acoustic sources (black rings) through a moving fluid (gray arrows) in a symmetric (dashed lines) 2-dimensional duct (solid lines).*

In the following, we introduce the governing equations and approximations of the coupled flow-acoustic model.

Referring to Figure 5.1, we consider the propagation of sound through an isothermal moving fluid in a symmetric 2-dimensional duct in the absence of body forces. The fluid is governed by the Navier-Stokes and mass continuity equations (2.1), which we restate here:

$$\rho\frac{\partial \boldsymbol{u}}{\partial t} + \rho(\boldsymbol{u}\cdot\nabla)\boldsymbol{u} + \nabla p - \nabla\cdot\mathbb{T} = 0, \tag{5.1a}$$

$$\frac{\partial \rho}{\partial t} + \nabla\cdot(\rho\boldsymbol{u}) = 0, \tag{5.1b}$$

where p, $\boldsymbol{u}$, ρ, $\mathbb{T}$, and t, denote pressure, velocity, density, deviatoric stress tensor, and time, respectively.

The problem involves two distinct physical phenomena: the flow of the fluid and the propagation of sound in it. We express this separation through the state variables:

$$\boldsymbol{u} = \boldsymbol{u}_0 + \boldsymbol{u}', \quad p = p_0 + p', \quad \rho = \rho_0 + \rho', \tag{5.2}$$

where $\boldsymbol{u}_0$, p_0, ρ_0 relate to the large scale mean flow, and $\boldsymbol{u}'$, p', ρ' relate to the small scale acoustic disturbances. For simplicity, we will assume a one-way coupling of these phenomena, such that flow phenomena ($\boldsymbol{u}_0$, p_0, and ρ_0) influence acoustic phenomena ($\boldsymbol{u}'$, p', and ρ'), but not the other way around. Hence, we may treat the flow model as independent of the acoustic model, and use the output of the flow model as input to the acoustic model.

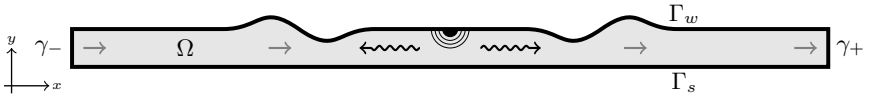

Figure 5.2: *Model domain (gray) and boundaries (black lines).*

In the following, we consider the flow and acoustic equations over a symmetric, finite segment of one half of the symmetric, infinite 2-dimensional duct as depicted in Figure 5.2. The four boundaries of the model domain Ω are: the hard wall boundary Γ_w, the symmetry boundary Γ_s, and the two artificial truncation boundaries γ_- and γ_+.

Flow Equations

For the flow model, we follow closely the approach outlined in the previous chapters. We assume that the fluid is Newtonian and incompressible, and that the flow is stationary. The governing equations (5.1) then simplify to:

$$\rho_0(\boldsymbol{u}_0 \cdot \nabla)\boldsymbol{u}_0 + \nabla p_0 - \mu\nabla^2\boldsymbol{u}_0 = \boldsymbol{0}, \tag{5.3a}$$

$$\nabla \cdot \boldsymbol{u}_0 = 0, \tag{5.3b}$$

where μ is the dynamic viscosity of the fluid, and ρ_0 its density, which are both constants.

The following boundary conditions are prescribed:

$$\boldsymbol{u}_0 = \boldsymbol{u}_0^* \qquad \text{on } \gamma_- \cup \Gamma_w, \tag{5.4a}$$

$$v_0 = 0 \quad \wedge \quad (\,\mu\nabla u_0 - p\,\boldsymbol{e}_1\,) \cdot \boldsymbol{n} = 0 \qquad \text{on } \gamma_+ \cup \Gamma_s, \tag{5.4b}$$

where $\boldsymbol{n}$ is the outward unit normal, and $\boldsymbol{u}_0^*$ prescribes a purely horizontal flow velocity on the flow inlet γ_-, and a vanishing flow velocity along the hard wall Γ_w. On the symmetry edge Γ_s, we note that $\boldsymbol{e}_1 \cdot \boldsymbol{n} = 0$. On the flow outlet γ_-, the enforcement of $v_0 = 0$ has implications on the validity of the acoustic model, as explained below.

We solve the weak, or variational, form of the system (5.3)-(5.4) which reads: given ρ_0 and μ, find $\boldsymbol{u}_0$ and p_0 such that

$$\iint_\Omega \left(\mathcal{U}\rho_0(\boldsymbol{u}_0 \cdot \nabla)u_0 - p_0\frac{\partial \mathcal{U}}{\partial x} + \mu\nabla\mathcal{U} \cdot \nabla u_0\right) \mathrm{d}A = 0, \tag{5.5a}$$

$$\iint_\Omega \left(\mathcal{V}\rho_0(\boldsymbol{u}_0 \cdot \nabla)v_0 - p_0\frac{\partial \mathcal{V}}{\partial y} + \mu\nabla\mathcal{V} \cdot \nabla v_0\right) \mathrm{d}A = 0, \tag{5.5b}$$

$$\iint_\Omega \mathcal{P}\Big(\nabla \cdot \boldsymbol{u}_0\Big) \,\mathrm{d}A = 0, \tag{5.5c}$$

for all test functions $\mathcal{U}, \mathcal{V}, \mathcal{P}$ without support on boundaries where the fields are explicitly prescribed.

Acoustic Equation

Our goal in the following is to derive a single equation that governs the acoustic signal in a known background flow $\boldsymbol{u}_0$. To shorten the notation in the following derivations, we let $\partial_t \equiv \partial/\partial t$ denote differentiation with respect to time, and $\partial_x \equiv \partial/\partial x$ and $\partial_y \equiv \partial/\partial y$ differentiation with respect to spatial dimensions.

We start by assuming that we may neglect viscous effects for the acoustic signal. The governing equations (5.1) then read:

$$\rho\,\partial_t \boldsymbol{u} + \rho\,(\boldsymbol{u}\cdot\nabla)\boldsymbol{u} + \nabla p = \boldsymbol{0}, \tag{5.6a}$$

$$\partial_t \rho + \nabla\cdot(\rho\,\boldsymbol{u}) = 0. \tag{5.6b}$$

Next, we assume that the background flow ($\boldsymbol{u}_0$, p_0, ρ_0) fulfills the governing equations (5.6), that it is incompressible, i.e., $\partial_t\rho_0 = \partial_x\rho_0 = \partial_y\rho_0 = 0$, and hence $\nabla\cdot\boldsymbol{u}_0 = 0$ by Equation (5.6b), and that it is stationary, i.e. $\partial_t\boldsymbol{u}_0 = \boldsymbol{0}$, as in the flow model above. Inserting the conventions (5.2) into the governing equations (5.6), while using the above, and neglecting second orders terms in the acoustic disturbances ($\boldsymbol{u}'$, p', ρ'), we find:

$$\rho_0\partial_t\boldsymbol{u}' + \rho_0(\boldsymbol{u}_0\cdot\nabla)\boldsymbol{u}' + \rho_0(\boldsymbol{u}'\cdot\nabla)\boldsymbol{u}_0 + \nabla p' + \rho'(\boldsymbol{u}_0\cdot\nabla)\boldsymbol{u}_0 = \boldsymbol{0}, \tag{5.7a}$$

$$\partial_t\rho' + \boldsymbol{u}_0\cdot\nabla\rho' + \rho_0\nabla\cdot\boldsymbol{u}' = 0. \tag{5.7b}$$

Dividing Equation (5.7a) by ρ_0, multiplying Equation (5.7b) by c^2, and utilizing the isentropic condition $p' = c^2\rho'$, where c is the speed of sound in the fluid, we obtain:

$$\partial_t\boldsymbol{u}' + (\boldsymbol{u}_0\cdot\nabla)\boldsymbol{u}' + (\boldsymbol{u}'\cdot\nabla)\boldsymbol{u}_0 + \frac{1}{\rho_0}\nabla p' + \frac{\rho'}{\rho_0}(\boldsymbol{u}_0\cdot\nabla)\boldsymbol{u}_0 = \boldsymbol{0}, \tag{5.8a}$$

$$\partial_t p' + \boldsymbol{u}_0\cdot\nabla p' + \rho_0 c^2\nabla\cdot\boldsymbol{u}' = 0. \tag{5.8b}$$

Assuming small acoustic disturbances, i.e., $\rho' \ll \rho_0$, we may neglect the second order term in the background flow $\boldsymbol{u}_0$ in Equation (5.8a).

Next, we apply separation-of-variables and assume time-harmonic conditions. We seek acoustic solutions $\boldsymbol{u}'$ and p' to Equations (5.8) of the following form:

$$\boldsymbol{u}'(t,x,y) = e^{-i\omega t}\tilde{\boldsymbol{u}}(x,y), \qquad p'(t,x,y) = e^{-i\omega t}\tilde{p}(x,y). \tag{5.9}$$

where ω denotes the acoustic angular frequency. Inserting these relations into Equations (5.8), ignoring the second order term in the background flow $\boldsymbol{u}_0$ in Equation (5.8a), and dividing by the common temporal part $e^{-i\omega t}$, we obtain the following equations in the spatial parts of the acoustic fields:

$$-i\omega\tilde{\mathbf{u}} + (\boldsymbol{u}_0\cdot\nabla)\tilde{\mathbf{u}} + (\tilde{\mathbf{u}}\cdot\nabla)\boldsymbol{u}_0 + \frac{1}{\rho_0}\nabla\tilde{p} = \boldsymbol{0}, \tag{5.10a}$$

$$-i\omega\tilde{p} + \boldsymbol{u}_0\cdot\nabla\tilde{p} + \rho_0 c^2\nabla\cdot\tilde{\mathbf{u}} = 0. \tag{5.10b}$$

To reduce this system, Equation (5.10a) gives us:

$$\tilde{\mathbf{u}} = -\frac{i}{\omega}\left(\frac{1}{\rho_0}\nabla\tilde{p} + (\tilde{\mathbf{u}}\cdot\nabla)\boldsymbol{u}_0 + (\boldsymbol{u}_0\cdot\nabla)\tilde{\mathbf{u}}\right) = -\frac{i}{\omega\rho_0}\nabla\tilde{p} + \mathcal{O}(\boldsymbol{u}_0), \tag{5.11}$$

and by inserting this into Equation (5.10b), we find:

$$-i\omega\tilde{p} + \boldsymbol{u}_0 \cdot \nabla\tilde{p} - \frac{i\rho_0 c^2}{\omega}\nabla \cdot \left(\frac{1}{\rho_0}\nabla\tilde{p} + (\tilde{\mathbf{u}} \cdot \nabla)\boldsymbol{u}_0 + (\boldsymbol{u}_0 \cdot \nabla)\tilde{\mathbf{u}}\right) = 0. \quad (5.12)$$

Next, we will neglect all second order terms in the background flow $\boldsymbol{u}_0$, assuming low Mach numbers, i.e. $\|\boldsymbol{u}_0\| \ll c$. Exploiting again Equation (5.11) in the above, we then obtain the following equation in the spatial part of acoustic pressure only:

$$-i\omega\tilde{p} + \boldsymbol{u}_0 \cdot \nabla\tilde{p} - \frac{ic^2}{\omega}\nabla^2\tilde{p} - \frac{c^2}{\omega^2}\nabla \cdot \Big((\nabla\tilde{p} \cdot \nabla)\boldsymbol{u}_0 + (\boldsymbol{u}_0 \cdot \nabla)\nabla\tilde{p}\Big) = 0. \quad (5.13)$$

To simplify Equation (5.13), we use the following identity for two arbitrary vector functions $\boldsymbol{a} = (a_1, a_2)$ and $\boldsymbol{b} = (b_1, b_2)$:

$$\nabla \cdot \Big((\boldsymbol{b} \cdot \nabla)\boldsymbol{a} + (\boldsymbol{a} \cdot \nabla)\boldsymbol{b}\Big) = 2\big(\partial_x\boldsymbol{a} \cdot \nabla b_1 + \partial_y\boldsymbol{a} \cdot \nabla b_2\big) + (\boldsymbol{a} \cdot \nabla)(\nabla \cdot \boldsymbol{b}) + (\boldsymbol{b} \cdot \nabla)(\nabla \cdot \boldsymbol{a}), \quad (5.14)$$

which may be verified by straightforward calculations. Taking $\boldsymbol{a} = \boldsymbol{u}_0$ and $\boldsymbol{b} = \nabla\tilde{p}$ in the above yields:

$$\nabla \cdot \Big((\nabla\tilde{p} \cdot \nabla)\boldsymbol{u}_0 + (\boldsymbol{u}_0 \cdot \nabla)\nabla\tilde{p}\Big) = 2\big(\partial_x\boldsymbol{u}_0 \cdot \nabla\partial_x\tilde{p} + \partial_y\boldsymbol{u}_0 \cdot \nabla\partial_y\tilde{p}\big) + (\boldsymbol{u}_0 \cdot \nabla)(\nabla^2\tilde{p}) + (\nabla\tilde{p} \cdot \nabla)(\nabla \cdot \boldsymbol{u}_0). \quad (5.15)$$

Now, taking the divergence of (5.11), and inserting this into (5.10b), we find:

$$\nabla^2\tilde{p} = -\frac{w^2}{c^2}p + \mathcal{O}(\boldsymbol{u}_0). \quad (5.16)$$

Next, we may insert Equation (5.15) into Equation (5.13), using the above relation, neglecting again higher order terms in the background flow $\boldsymbol{u}_0$, and exploiting the incompressibility of the background flow $\nabla \cdot \boldsymbol{u}_0 = 0$. After some manipulations we find:

$$\nabla^2\tilde{p} + \frac{\omega^2}{c^2}\tilde{p} + \frac{2i}{\omega}\Big(\frac{\omega^2}{c^2}\boldsymbol{u}_0 \cdot \nabla\tilde{p} - \partial_x\boldsymbol{u}_0 \cdot \nabla\partial_x\tilde{p} - \partial_y\boldsymbol{u}_0 \cdot \nabla\partial_y\tilde{p}\Big) = 0. \quad (5.17)$$

Finally, we may define the wave number $k \equiv \omega/c$, and introduce an acoustic source f on the right hand side. This gives us:

$$\nabla^2\tilde{p} + k^2\tilde{p} + \frac{2i}{\omega}\Big(k^2\boldsymbol{u}_0 \cdot \nabla\tilde{p} - \frac{\partial\boldsymbol{u}_0}{\partial x} \cdot \nabla\frac{\partial\tilde{p}}{\partial x} - \frac{\partial\boldsymbol{u}_0}{\partial y} \cdot \nabla\frac{\partial\tilde{p}}{\partial y}\Big) = f. \quad (5.18)$$

Equation (5.18) is a second order partial differential equation for the spatial part $\tilde{p}$ of the acoustic pressure disturbance, with given angular frequency ω and speed of sound c, and based on a given background flow $\boldsymbol{u}_0$. We note that the terms in the parenthesis relate to the background flow $\boldsymbol{u}_0$ and its gradient $\nabla\boldsymbol{u}_0$. When the background flow vanishes, the equation reduces to the usual inhomogeneous Helmholtz equation. We emphasize in particular, that its derivation relies on a linearization of the governing equations, that time-harmonic conditions are assumed, and that second order effects in the background flow have been neglected, i.e., low Mach numbers $M \equiv \|\boldsymbol{u}\|/c$ are assumed.

The associated boundary conditions on the hard wall and the symmetry edge are:

$$\nabla\tilde{p}\cdot\boldsymbol{n}=0 \qquad \text{on } \Gamma_w\cup\Gamma_s. \tag{5.19}$$

The treatment of the artificial truncation boundaries $\gamma_\pm$, however, is less trivial [Givoli, 2008; Becache et al., 2004; Redon et al., 2011]. Here, waves must be allowed to propagate out of the domain, and, at the same time, reflections back into the domain must be avoided. We treat the truncation boundaries using the mode matching formulation [Astley, 1996], based on a modal decomposition, a method closely related to the so-called Dirichlet-to-Neumann map [Redon et al., 2011].

The crux of the mode matching method is to assume that the acoustic pressure on the truncation boundaries $\gamma_\pm$ may be expressed as linear combinations of so-called acoustic duct modes, giving the following relations for the acoustic pressure and its normal derivative:

$$\tilde{p}(x,y)=\sum_{n=1}^{N_m^\pm} b_n^\pm\phi_n^\pm(y)\equiv\tilde{p}_\pm \qquad \text{on } \gamma_\pm, \tag{5.20a}$$

$$\nabla\tilde{p}(x,y)\cdot\boldsymbol{n}=\pm\frac{\partial\tilde{p}}{\partial x}(x,y)=\pm\sum_{n=1}^{N_m^\pm} b_n^\pm\lambda_n\phi_n^\pm(y) \qquad \text{on } \gamma_\pm, \tag{5.20b}$$

where ϕ_n are the acoustic duct modes, λ_n are the associated (complex and signed) wave numbers, b_n are the expansion coefficients, and N_m is the finite (and small) number of modes. The subscript indicates direction of propagation, such that forward propagating modes are specified on the boundary γ_+, and backward propagating modes on the boundary γ_-. This will be explained further in Section 5.5 below.

The mode matching method involves two steps: In the first step, the acoustic duct modes, i.e., the functions ϕ_n and the wave numbers λ_n, are determined. In the second step, the weights b_n of the modes on $\gamma_\pm$, as well as the acoustic pressure $\tilde{p}$ over the entire domain Ω are determined.

For the first step, we assume that the truncation boundaries $\gamma_\pm$ are placed far away from acoustic sources and geometric undulations, such that the background flow $\mathbf{u}_0$ is independent of x and normal to $\gamma_\pm$. With these assumptions, Equation (5.18) evaluated on the truncation boundaries simplifies to:

$$\frac{\partial^2\tilde{p}}{\partial x^2}+\frac{\partial^2\tilde{p}}{\partial y^2}+k^2\tilde{p}+\frac{2i}{\omega}\Big(k^2u_0\frac{\partial\tilde{p}}{\partial x}-u_0'\frac{\partial^2\tilde{p}}{\partial x\partial y}\Big)=0, \tag{5.21}$$

where $u_0=u_0(y)$ is the horizontal background flow velocity, and $u_0'=du_0/dy$ its derivative. From Equation (5.19), the boundary conditions are:

$$u_0'=0 \qquad \text{for } y=0,R, \tag{5.22}$$

where R is the height of the duct. We are interested in the weak form of Equation (5.21) which reads: given ω, k, and u_0, find $\tilde{p}$ such that

$$\int_{\gamma_\pm}\widetilde{\mathcal{P}}\Big[\frac{\partial^2\tilde{p}}{\partial x^2}+\frac{\partial^2\tilde{p}}{\partial y^2}+k^2\tilde{p}+\frac{2i}{\omega}\Big(k^2u_0\frac{\partial\tilde{p}}{\partial x}-u_0'\frac{\partial^2\tilde{p}}{\partial x\partial y}\Big)\Big]\,\mathrm{d}y=0, \tag{5.23}$$

for all test functions $\widetilde{\mathcal{P}}$. The modes are then determined by solving an eigenvalue problem based on Equation (5.23) while using the homogeneous Neumann boundary conditions in Equation (5.22).

For the second step, we consider the weak forms of the system (5.18)-(5.19) for the acoustic pressure over the domain Ω, and of the modal relation (5.20a) on the truncation boundaries $\gamma_\pm$. These read: given ω, k, f, and $\boldsymbol{u}_0$, find $\tilde{p}$ and $\tilde{p}_\pm$ such that

$$\int_{\gamma_\pm} \widetilde{\mathcal{P}}(\nabla\tilde{p}\cdot\boldsymbol{n})\,\mathrm{d}s - \iint_\Omega \nabla\widetilde{\mathcal{P}}\cdot\nabla\tilde{p}\,\mathrm{d}A + \iint_\Omega \widetilde{\mathcal{P}}\Big[k^2\tilde{p} - f + \frac{2i}{\omega}\Big(k^2\boldsymbol{u}_0\cdot\nabla\tilde{p} - \frac{\partial\boldsymbol{u}_0}{\partial x}\cdot\nabla\frac{\partial\tilde{p}}{\partial x} - \frac{\partial\boldsymbol{u}_0}{\partial y}\cdot\nabla\frac{\partial\tilde{p}}{\partial y}\Big)\Big]\,\mathrm{d}A = 0, \tag{5.24a}$$

$$\int_{\gamma_\pm} \widetilde{\mathcal{F}}^\pm(\tilde{p}-\tilde{p}_\pm)\,\mathrm{d}s = 0, \tag{5.24b}$$

for all test functions $\widetilde{\mathcal{P}}, \widetilde{\mathcal{F}}^\pm$. These equations are then solved using the Neumann boundary conditions (5.20b) on the truncation boundaries.

5.3 Isogeometric Method

We solve the coupled flow-acoustic problem numerically using B-spline based isogeometric analysis. We follow closely the approach in Chapter 3, from where only the central parts are repeated in the following, and we primarily focus on the acoustic model.

Geometry Model

Referring to Figure 5.3, we construct a parametrization of the model domain of the form $\boldsymbol{X} = \sum_i \boldsymbol{x}_i \mathcal{P}_i^g$ for $i = 1, \ldots, N_{\text{var}}^g$, where $\mathcal{P}_i^g$ are tensor product B-splines, $\boldsymbol{x}_i$ are control points, and N_{var}^g is the number of terms. The geometry parametrization serves as foundation for both the flow model and the acoustic model.

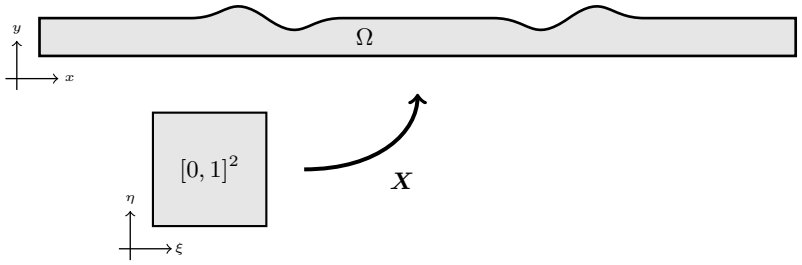

Figure 5.3: *Parametrization of the model domain.*

Flow Model

As for the geometry, approximations of the background flow velocity $\boldsymbol{u}_0$ and pressure p_0 are constructed in the form $f = \sum_i \underline{f}_i \mathcal{P}_i^f$ for $i = 1, \ldots, N_{\text{var}}^f$, where, for each of the three state variables $f \in \{u_0, v_0, p_0\}$, $\mathcal{P}_i^f$ are tensor product B-splines, $\underline{f}_i$ are control coefficients, and N_{var}^f is the number of terms. From these approximations, we may obtain a system of non-linear equations of the form

$$\boldsymbol{\mathcal{K}}(\boldsymbol{U})\boldsymbol{U} = \boldsymbol{F}, \tag{5.25}$$

where $\boldsymbol{U}$ is the vector of unknown control coefficients for the background flow velocity and pressure, and the system matrix $\boldsymbol{\mathcal{K}}$ and the right hand side vector $\boldsymbol{F}$ are given by Equations (3.10)–(3.11) with $\boldsymbol{f} = \boldsymbol{0}$.

Acoustic Model

The acoustic model involves two steps: The first step determines the acoustic duct modes on the truncation boundaries $\gamma_\pm$, i.e., the functions ϕ_n and the wave numbers λ_n. The second step determines the weights b_n of the modes on $\gamma_\pm$ as well as the acoustic pressure $\tilde{p}$ over the entire domain Ω.

Acoustic Duct Modes

To determine the acoustic duct modes, we approximate the pressure in the regions far upstream and far downstream by the following expression:

$$\tilde{p}(x, y) = \sum_{\ell=1}^{n} a_\ell(x)\, \overline{\mathcal{M}}_\ell(y)\,, \tag{5.26}$$

where $\mathcal{M}_\ell$ are univariate B-splines defined over the parameter domain $\xi \in [0, 1]$, $\overline{\mathcal{M}}_\ell$ are their image in physical space, and thus functions of y, c_ℓ are expansion coefficients that are functions of x, and n is the number of terms in the expansion.

Due to the properties of B-splines, the boundary condition (5.22) for the acoustic pressure on the straight parts of the hard wall Γ_w and the symmetry edge Γ_s may be fulfilled a priori by choosing $a_1 = a_2$ and $a_n = a_{n-1}$, or, equivalently, by replacing the approximation (5.26) by

$$\tilde{p}(x, y) = \sum_{\ell=1}^{n-2} b_\ell(x)\, \overline{\mathcal{N}}_\ell(y)\,, \tag{5.27}$$

where

$$\begin{aligned}
\mathcal{N}_1 &= \mathcal{M}_1 + \mathcal{M}_2, & b_1 &= a_1 + a_2,\\
\mathcal{N}_2 &= \mathcal{M}_3, & b_2 &= a_3,\\
&\vdots & &\vdots\\
\mathcal{N}_{n-3} &= \mathcal{M}_{n-2}, & b_{n-3} &= a_{n-2},\\
\mathcal{N}_{n-2} &= \mathcal{M}_{n-1} + \mathcal{M}_n, & b_{n-2} &= a_{n-1} + a_n.
\end{aligned}$$

By inserting the approximation (5.27) into the Equation (5.23) on the truncation boundaries, using $\overline{\mathcal{N}}_k(y)$ as test functions, and pulling the integrals back to parameter domain $[0,1]$, the following system of ordinary differential equations is obtained:

$$\mathbf{R}\,\ddot{\mathbf{b}} + \frac{2i}{\omega}\,\mathbf{S}\,\dot{\mathbf{b}} + \mathbf{T}\,\mathbf{b} = \mathbf{0}\,, \tag{5.28}$$

where dot denotes differentiation with respect to x, and

$$\mathbf{R}_{k,\ell} = \int_0^1 \mathcal{N}_k\,\mathcal{N}_\ell\,y'\,\mathrm{d}\xi\,, \tag{5.29a}$$

$$\mathbf{S}_{k,\ell} = \int_0^1 \mathcal{N}_k\Big(k^2\,u_0\,\mathcal{N}_\ell - u_0'\,y'^{-1}\,\mathcal{N}_\ell'\Big)y'\,\mathrm{d}\xi\,, \tag{5.29b}$$

$$\mathbf{T}_{k,\ell} = \int_0^1 \mathcal{N}_k\Big(y'^{-2}\,\mathcal{N}_\ell'' - y''\,y'^{-3}\,\mathcal{N}_\ell' + k^2\,\mathcal{N}_\ell\Big)y'\,\mathrm{d}\xi\,, \tag{5.29c}$$

$$\mathbf{b} = \begin{pmatrix} b_1(x) & \dots & b_{n-2}(x) \end{pmatrix}^T, \tag{5.29d}$$

for $k,\ell = 1,\dots,n-2$, where prime denotes differentiation with respect to ξ. The second order system (5.28) can be rewritten as the first order system

$$\begin{bmatrix} \mathbf{I} & \mathbf{0} \\ \mathbf{0} & \mathbf{R} \end{bmatrix} \begin{bmatrix} \dot{\mathbf{b}} \\ \dot{\mathbf{c}} \end{bmatrix} = \begin{bmatrix} \mathbf{0} & \mathbf{I} \\ -\mathbf{T} & -\frac{2i}{\omega}\mathbf{S} \end{bmatrix} \begin{bmatrix} \mathbf{b} \\ \mathbf{c} \end{bmatrix}. \tag{5.30}$$

By solving the generalized eigenvalue problem

$$\begin{bmatrix} \mathbf{0} & \mathbf{I} \\ -\mathbf{T} & -\frac{2i}{\omega}\mathbf{S} \end{bmatrix} \begin{bmatrix} \mathbf{b} \\ \mathbf{c} \end{bmatrix} = \lambda \begin{bmatrix} \mathbf{I} & \mathbf{0} \\ \mathbf{0} & \mathbf{R} \end{bmatrix} \begin{bmatrix} \mathbf{b} \\ \mathbf{c} \end{bmatrix}, \tag{5.31}$$

we obtain $2n-4$ pairs of eigenvalues, λ_k, and eigenvectors, $(\mathbf{b}_k\ \mathbf{c}_k)^T$. Each eigenvalue represents a (complex and signed) wave number, and each eigenvector corresponds to a (complex) acoustic duct mode

$$\phi_k(y) = \sum_{\ell=1}^{n-2} b_{\ell,k}\overline{\mathcal{N}}_\ell(y)\,. \tag{5.32}$$

As demonstrated in section 5.5 below, a finite and small number of modes N^m with purely imaginary propagation constant λ are found in practice, while the number of modes with propagation constant with non-vanishing real part is bounded only by the numerical discretization. We base the mode matching formulation on the former *propagative* modes, while the latter *evanescent* modes are neglected.

Acoustic Pressure

To compute the acoustic pressure $\tilde{p}$ over the entire domain, and the weights b_n of the modes on the truncation boundaries, we will, as for the geometry and the background flow variables, seek solutions of the following form:

$$\tilde{p} = \sum_{i=1}^{N_{\mathrm{var}}^{\tilde{p}}} \tilde{p}_i R_i^{\tilde{p}}\,, \tag{5.33}$$

where the basis functions $\mathcal{P}^{\tilde{p}}$ are tensor product B-splines, $\tilde{p}_i$ are the unknown control variables to be determined, and $N^{\tilde{p}}_{\text{var}}$ is the number of terms.

As test functions in the weak formulation of the governing equations (5.24), we use the basis functions $\mathcal{P}^{\tilde{p}}$ and the (B-spline approximations from above of the) propagative acoustic duct modes $\phi^{\pm}$. By inserting the acoustic field approximation (5.33) and the acoustic duct mode approximation (5.32) into these equations, exploiting the Neumann boundary condition (5.20b), rearranging terms and interchanging order of integration and summation, we arrive at the following system of linear equations:

$$\begin{bmatrix} -\boldsymbol{D} + k^2\boldsymbol{M} + \frac{2i}{\omega}\left(k^2\boldsymbol{L} - \boldsymbol{Q}\right) & \mathbf{H}\mathbf{B}\boldsymbol{\Lambda} \\ \mathbf{B}^T\mathbf{H} & -\mathbf{B}^T\mathbf{H}\mathbf{B} \end{bmatrix} \begin{bmatrix} \tilde{\boldsymbol{p}} \\ \mathbf{b} \end{bmatrix} = \begin{bmatrix} \boldsymbol{f} \\ \mathbf{0} \end{bmatrix} \tag{5.34}$$

where

$$\boldsymbol{D}_{i,j} = \iint_{[0,1]^2} \overline{\nabla}\mathcal{P}^{\tilde{p}}_i \cdot \overline{\nabla}\mathcal{P}^{\tilde{p}}_j \det\left(\boldsymbol{J}\right) \mathrm{d}\Xi, \tag{5.35a}$$

$$\boldsymbol{M}_{i,j} = \iint_{[0,1]^2} \mathcal{P}^{\tilde{p}}_i \mathcal{P}^{\tilde{p}}_j \det(\boldsymbol{J}) \,\mathrm{d}\Xi, \tag{5.35b}$$

$$\boldsymbol{L}_{i,j} = \iint_{[0,1]^2} \mathcal{P}^{\tilde{p}}_i \left(\mathbf{u}_0 \cdot \overline{\nabla}\mathcal{P}^{\tilde{p}}_j\right) \det(\boldsymbol{J}) \,\mathrm{d}\Xi, \tag{5.35c}$$

$$\boldsymbol{Q}_{i,j} = \iint_{[0,1]^2} \mathcal{P}^{\tilde{p}}_i \sum_{m=1}^{2} (\mathbf{e}_m^T \overline{\nabla})\mathbf{u}_0 \cdot (\overline{\mathbf{H}\mathcal{P}}^{\tilde{p}}_j \mathbf{e}_m) \det(\boldsymbol{J}) \,\mathrm{d}\Xi, \tag{5.35d}$$

$$\boldsymbol{H}_{i,j} = \int_{[0,1]} \mathcal{P}^{\tilde{p}}_i \mathcal{P}^{\tilde{p}}_j \|\gamma'\| \,\mathrm{d}\xi, \tag{5.35e}$$

$$\boldsymbol{B}_{i,k} = \begin{cases} b_{\ell,k} & \text{if } \operatorname{supp}(\mathcal{P}^{\tilde{p}}_i) \cap \gamma_{\pm} \neq \emptyset \\ 0 & \text{otherwise} \end{cases}, \tag{5.35f}$$

$$\boldsymbol{\Lambda}_{k,\ell} = \delta_{k,l}\lambda_k, \tag{5.35g}$$

$$\boldsymbol{f}_i = \iint_{[0,1]^2} \mathcal{P}^{\tilde{p}}_i f \det\left(\boldsymbol{J}\right) \mathrm{d}\Xi, \tag{5.35h}$$

for $i, j = 1, \ldots, N^{\tilde{p}}_{\text{var}}$ and $k, \ell = 1, \ldots, N^m$, where $\delta_{k,l}$ is the Kronecker delta. Gradients and Hessians may be found from Equation (3.3). Here, the "stiffness" matrix $\boldsymbol{D}$ and the "mass" matrix $\boldsymbol{M}$ appear independently of the background flow, whereas $\boldsymbol{L}$ is due to the flow field $\boldsymbol{u}_0$, and $\boldsymbol{Q}$ is due to the gradient of the flow field $\nabla\boldsymbol{u}_0$.

Implementation

For the geometry parametrization, we take $\mathcal{P}^g_i$ as bi-quadratic tensor product B-splines. For the flow approximations, we take $\mathcal{P}^u_i$ and $\mathcal{P}^v_i$ as bi-quartic and $\mathcal{P}^p_i$ as bi-cubic, respectively, all C^2 across knots, which corresponds to the Taylor-Hood discretization $\mathbf{u}4^2_0\mathrm{p}3^1_0$ (d) in Table 3.1. For the acoustic approximation, $\mathcal{P}^{\tilde{p}}_i$ are taken as bi-quartic, unless otherwise stated.

Dirichlet boundary conditions, for which state variables are explicitly prescribed, are enforced strongly by choosing the corresponding control variables

appropriately. Neumann boundary conditions, for which normal derivatives of state variables must vanish, are enforced weakly by equating the corresponding boundary integrals to zero in the derivation of the weak form of the governing equations.

5.4 Validation: Acoustic Duct Modes

In the following, we consider the propagation of sound waves in a straight duct with uniform background flow, for which analytical solutions are readily available. We validate the coupled flow-acoustic model numerically by examining how well the method is able to reproduce these analytical solutions.

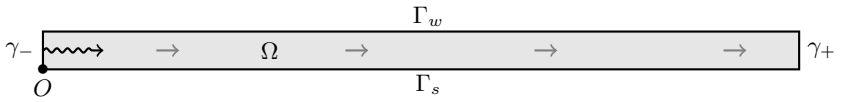

Figure 5.4: *The modal problem.*

The problem is outlined in Figure 5.4. It differs from the one described in Figure 5.2 by the fact that a uniform background flow $\mathbf{u}_0 = (U_0, 0)$ is explicitly prescribed, the interior acoustic source f has been removed, and the mode matching boundary condition on the left boundary γ_- has been replaced by an explicit prescription of the acoustic pressure:

$$\tilde{p} = \tilde{p}_n^* \qquad \text{on } \gamma_-. \tag{5.36}$$

Here, $\tilde{p}_n^*$ is an analytical solution of Equation (5.18) for the acoustic pressure field in a straight duct of height R with uniform background flow $\mathbf{u}_0 = (U_0, 0)$:

$$\tilde{p}_n^* = \exp\left(i\beta_n x\right)\cos\left(\alpha_n y\right), \tag{5.37}$$

where

$$\alpha_n = n\pi/R, \tag{5.38a}$$

$$\beta_n = -kM \pm \sqrt{k^2(1+M^2) - (n\pi/R)^2}\,, \tag{5.38b}$$

where $M \equiv U_0/c$ is the Mach number. This corresponds to the n^{th} propagative acoustic duct mode

$$\phi_n(y) = \cos\left(n\pi\frac{y}{R}\right), \tag{5.39}$$

such that $n \leq \sqrt{1+M^2}\,k\,R\,/\pi$, travelling towards $\pm\infty$.

To assess the quality of the method, we will use the normalized L_2-norm of the modulus of the pressure residual as error measure:

$$\epsilon^2 = \frac{\iint_\Omega |\tilde{p} - \tilde{p}^*|^2 \,\mathrm{d}A}{\iint_\Omega |\tilde{p}^*|^2 \,\mathrm{d}A}\,. \tag{5.40}$$

We investigate how this varies as the analysis mesh is refined by knot insertion, and the number of degrees-of-freedom thereby increased. We use the parameter

values for the duct size, sound frequency and flow speed as described in Table 5.1 in the following section, leading to two propagative modes $n \in \{0, 1\}$.

We firstly examine how different approximations of the acoustic pressure influence the error convergence. Here, we consider the background flow $U_0 = 1$ $\mathrm{m\,s^{-1}}$, the sound frequency $f = 25$ kHz, and the highest propagative mode $n = 1$. For polynomial degrees $q \in \{2, \ldots, 6\}$, we solve the problem for a range of meshes, and evaluate the error using (5.40). The results are shown in

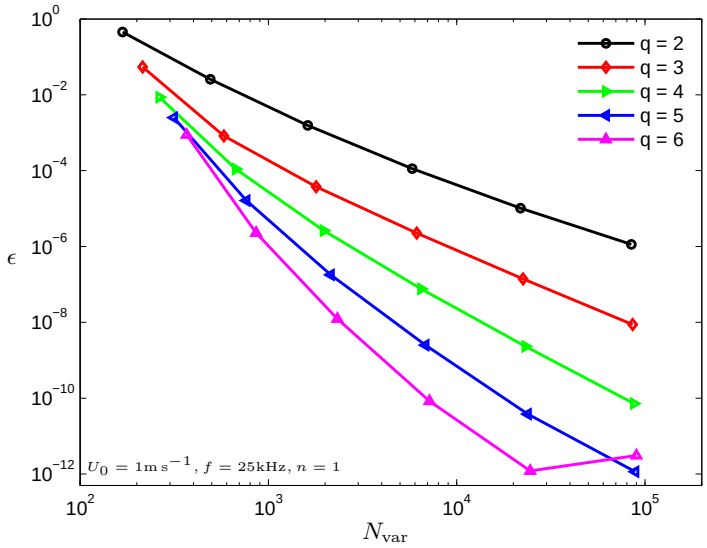

Figure 5.5: *Relative error ϵ as a function of number of basis function N_{var} for different polynomial degrees q.*

Figure 5.5. By inspection of the slope of the curves, we note that the higher the polynomial degree is, the higher the convergence rate also is. For polynomial degrees $q \geq 5$, this holds only for sufficiently few degrees of freedom, presumably because of rounding errors for more degrees of freedom. All following results are based on a polynomial degree of $q = 4$.

Secondly, to illustrate the effect of the background flow on the acoustic wave propagation, Figure 5.6 depicts the real part of the acoustic pressure in the duct without flow (a), with flow $U_0 = 1$ $\mathrm{m\,s^{-1}}$ (b), and the difference between these (c), for the mode $n = 1$ and frequency $f = 25$ kHz. As expected, the effect of background flow is to stretch the wavelength of the sound waves in the downstream region.

Finally, we investigate the error convergence for different background flows, sound frequencies, and modes. For each combination of background flow $U_0 \in \{0, 1\}$ $\mathrm{m\,s^{-1}}$, frequency $f \in \{20, 30\}$ kHz, and mode $n \in \{0, 1\}$, we solve the problem for a range of meshes, and compute the error using (5.40). The results are shown in Figure 5.7. We note that practically identical rates of convergence are found independently of background flow, frequency, and mode.

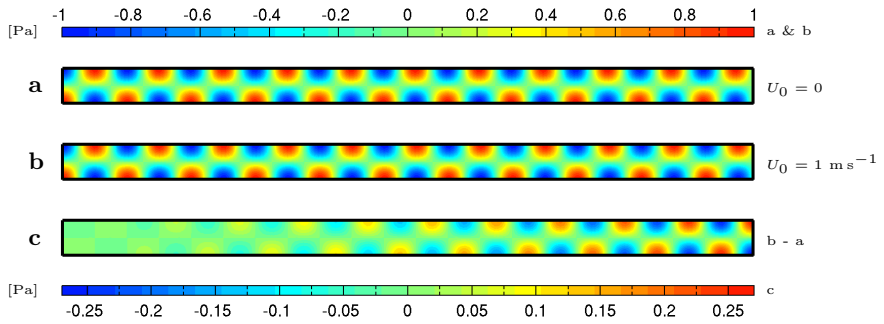

Figure 5.6: *Real part of the acoustic pressure $\tilde{p}$ using the background flow $U_0 = 0$ (**a**), $U_0 = 1\ ms^{-1}$ (**b**), and the difference between these (**c**), for the mode $n = 1$ and frequency $f = 25\ kHz$.*

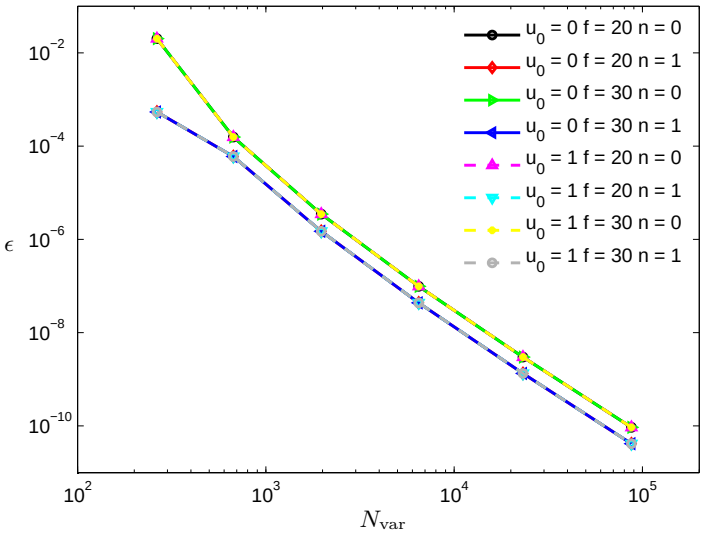

Figure 5.7: *Relative error ϵ as a function of number of basis functions N_{var} for different background flows U_0, frequencies f and modes n.*

5.5 Results

In the following, we use the coupled flow-acoustic model to examine how the duct geometry affects how the acoustic signal depends on sound frequency and flow speed.

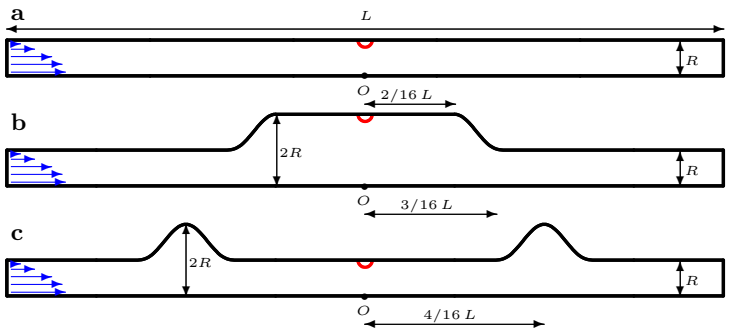

Figure 5.8: *Design of the numerical experiment: We investigate 3 geometries (***a***, ***b***, and ***c***), and prescribe the flow at the inlet (blue arrows) and the sound excitation in the middle (red circles).*

Setup of Numerical Experiment

The numerical experiment is sketched in Figure 5.8. To assess the geometric effects, three different geometries are investigated: a straight duct (a), a duct with a single bulge (b), and a corrugated duct (c). The flow is varied by prescribing, for different mean flow speeds U_0, a parabolic velocity profile at the inlet boundary:

$$u_0 = \frac{3}{2} U_0 \left(1 - \left(\frac{y}{R}\right)^2\right), \qquad v_0 = 0, \qquad \text{on } \gamma_- \,. \tag{5.41}$$

The sound excitation is varied by assuming, for different angular frequencies ω, a smooth, compactly supported acoustic source, centered at $(0, r_0)$, where r_0 is the height of the duct in $x = 0$, with the following form:

$$f(x, y) = f_0 \, \Psi(x; 0, L_x) \, \Psi(y; r_0, L_y), \tag{5.42}$$

where f_0 denotes the strength of the source, $\boldsymbol{L}$ its spatial extent, and the footprint function Ψ is given by:

$$\Psi(x; a, b) = \begin{cases} e^{-\frac{1}{1-\chi^2}} & \text{for } |\chi| \equiv |\frac{x-a}{b}| < 1 \\ 0 & \text{otherwise} \end{cases} . \tag{5.43}$$

The parameter values used in the numerical experiment for the geometry, the fluid, and the sound excitation are summarized in Table 5.1. With R as characteristic length scale, and U_0 as flow speed, this corresponds to Reynolds numbers up to $\mathrm{Re} \simeq 1 \cdot 10^3$ and Mach numbers up to $M \simeq 3 \cdot 10^{-3}$.

Flow Field and Acoustic Modes

We firstly investigate the background flow. Figure 5.9 depicts the flow fields in the three different duct geometries using the flow speed $U_0 = 1 \ \mathrm{m\,s^{-1}}$. In the straight duct (a), the parabolic velocity profile is naturally conserved down the duct. In the bulged duct (b) and the corrugated duct (c), we notice that the flow profile is only slightly perturbed in the vicinity of undulations. In addition, a weak recirculation flow is seen in the bulges.

Parameter	Description	Value	Unit
μ	Dynamic viscosity	$1 \cdot 10^{-5}$	$\mathrm{kg\,m^{-1}s^{-1}}$
ρ	Background density	1	$\mathrm{kg\,m^{-3}}$
c	Speed of sound	340	$\mathrm{m\,s^{-1}}$
R	Duct height	1	cm
L	Duct length	20	cm
f	Source strength	$1 \cdot 10^{6}$	
$\boldsymbol{L} = (L_x, L_y)$	Source size	$(2, 2)$	mm
$f = \omega/2\pi$	Sound frequency	20–30	kHz
U_0	Flow speed	0–1	$\mathrm{m\,s^{-1}}$

Table 5.1: *Parameter values corresponding to propagation of ultrasound in air-filled narrow ducts are used.*

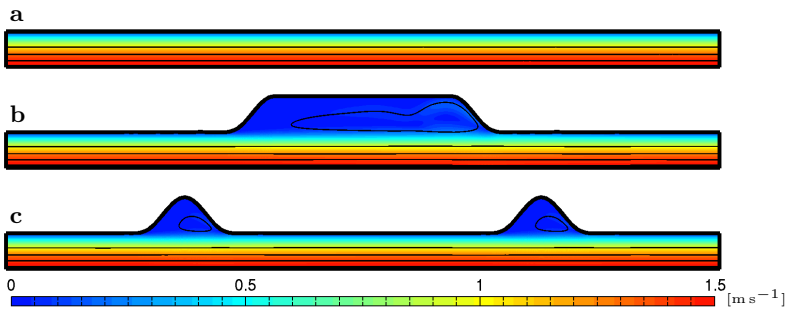

Figure 5.9: *Flow speeds (colors) and stream lines (solid lines) using the mean speed $U_0 = 1\ m\,s^{-1}$ in the straight duct (**a**), the bulged duct (**b**), and the corrugated duct (**c**).*

Next, we investigate how the acoustic duct modes vary with flow speed and sound frequency. This is depicted in Figure 5.10. In **a**, a typical configuration of computed propagation constants λ (scaled by k) is shown in the complex plane, here with vanishing background flow $U_0 = 0$, and frequency $f = 25$ kHz. The propagation constants can be categorized as propagative/evanescent (on/off the imaginary axis), and as positive/negative (positive/negative imaginary part, or vanishing imaginary part and strictly positive/negative real part). Four propagative modes are found, two in each direction, in agreement with the analytical values in Equation (5.38) with $M = 0$. The number of evanescent modes is bounded only by the number of degrees of freedom of the discretization, and only the first eight are shown here. We note that in the presence of a background flow, the symmetry of the propagative modes with respect to the real axis vanishes, whereas the symmetry of the evanescent modes with respect to the imaginary axis is maintained. In **b**, the modal functions ϕ corresponding to the propagation constants in **a** are shown, with propagative modes drawn in solid, and evanescent modes in dashed. These agree with the analytical modes in Equation (5.39). In **c**, the imaginary parts of the propagation constants (scaled

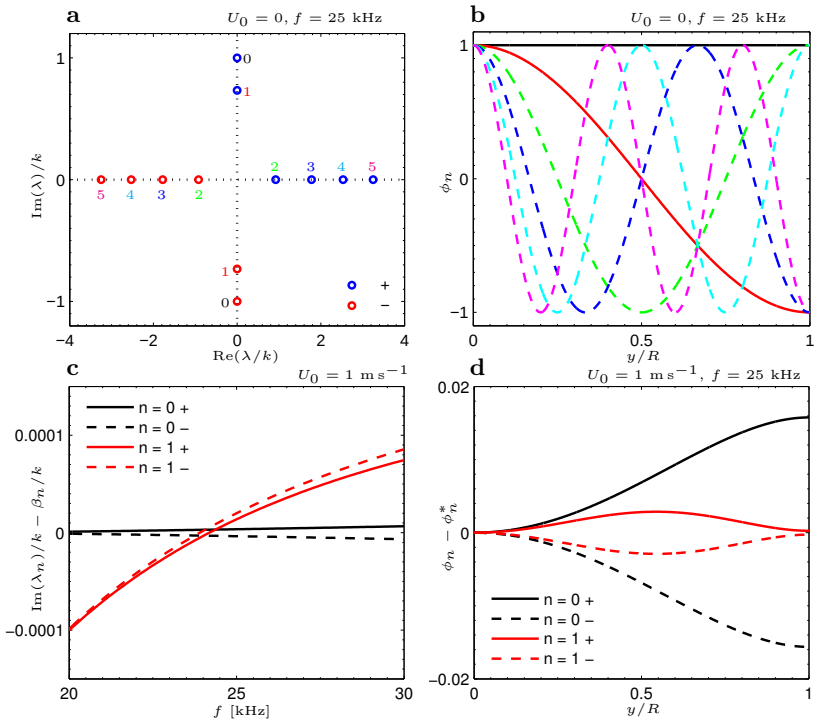

Figure 5.10: *Acoustic duct modes for different frequencies f and flow speeds U_0.* **a***: propagation constants λ for $f = 25$ kHz and $U_0 = 0$.* **b***: mode functions ϕ for $f = 25$ kHz and $U_0 = 0$.* **c***: imaginary part of propagation constants λ for $U_0 = 1$ m s^{-1} and $f \in [20, 30]$ kHz.* **d***: mode function ϕ residuals for $U_0 = 1$ m s^{-1} compared to $U_0 = 0$ for $f = 25$ kHz.*

by k) corresponding to the four propagative modes for mean speed $U_0 = 1\,\mathrm{m\,s^{-1}}$ are shown as a function of frequency in the range $f \in [20, 30]$ kHz, plotted as the residual compared to the case without flow as given by Equation (5.38) with $M = 0$. The perturbations in the propagation constants due to the flow are largest for the second mode $n = 1$, but are in general small and $\lesssim 0.1‰$. Finally in **d**, the four propagative modal functions for mean speed $U_0 = 1\,\mathrm{m\,s^{-1}}$ and frequency $f = 25$ kHz are depicted. The plot shows the modal function residuals compared to the corresponding modal functions without flow, as shown in **a** and given in Equation (5.39). Perturbations are of opposite sign for positive and negative modes, and the perturbations are again in general small, with the largest perturbations $\sim 2\%$ found for the first mode $n = 0$.

Acoustic Field Sensitivity

To quantify the acoustic response by a single entity when examining how it changes with sound frequency and flow speed, we consider the relative modulus of the symmetry deviation of the acoustic pressure:

$$\langle \delta\tilde{p} \rangle = \frac{\iint_\Omega |\tilde{p}(\boldsymbol{x}) - \tilde{p}(-\boldsymbol{x})|\,\mathrm{d}A}{\iint_\Omega |\tilde{p}(\boldsymbol{x})|\,\mathrm{d}A}. \tag{5.44}$$

Since the geometries and the acoustic excitation are all symmetric around $x = 0$, any asymmetry in the acoustic pressure field arises due to the background flow. As such, this quantity is a measure of how strongly the sound signal is coupled to the flow field. For reference, we also examine the mean modulus of the acoustic pressure:

$$\langle \tilde{p} \rangle = \frac{\iint_\Omega |\tilde{p}(\boldsymbol{x})| \, \mathrm{d}A}{\iint_\Omega \mathrm{d}A}. \tag{5.45}$$

To investigate the sensitivity of the sound signal to the frequency for a given flow speed, we compute the mean acoustic pressure $\langle \tilde{p} \rangle$ and the relative symmetry deviation in the acoustic pressure $\langle \delta\tilde{p} \rangle$ for frequencies in the range $f \in [20, 30]$ kHz with fixed flow speed $U_0 = 1 \ \mathrm{m\,s^{-1}}$. The results are shown in Figure 5.11 for each of the three duct geometries. On the top plot, no significant

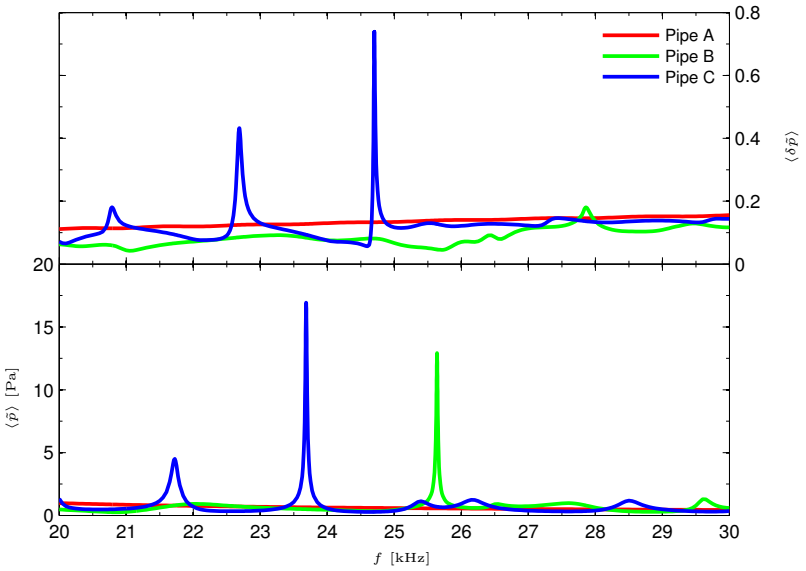

Figure 5.11: *Mean acoustic pressure $\langle \tilde{p} \rangle$ using the flow speed $U_0 = 0$ $m\,s^{-1}$ (bottom), and relative symmetry deviation $\langle \delta\tilde{p} \rangle$ using the flow speed $U_0 = 1$ $m\,s^{-1}$ (top) as a function of frequency f for the three duct geometries.*

changes in the degree of asymmetry are found for the straight duct (a), while the bulged duct (b) shows minor changes with frequency. For the corrugated duct (c), however, strong peaks are seen in the $\langle \delta\tilde{p} \rangle$ response. The strongest peak occurs for frequencies close to $f = 24.7$ kHz, where the signal experiences an increase by a factor of up to ~ 10. From the bottom plot, the peaks in $\langle \delta\tilde{p} \rangle$ for the corrugated duct (c) are seen to occur close to local minima in the mean acoustic pressure $\langle \tilde{p} \rangle$ that fall between strong peaks in the $\langle \tilde{p} \rangle$ response associated with resonances in the duct.

To further illustrate the phenomenon observed in the frequency sweeps above, Figure 5.12 depicts the modulus of the acoustic pressure field using the frequency $f = 24.7$ kHz and the flow speed $U_0 = 1 \ \mathrm{m\,s^{-1}}$ in each of the three duct geometries. Both the straight duct (a) and the bulged duct (b) exhibit a high degree of symmetry in the acoustic pressure field. In the corrugated duct (c), however,

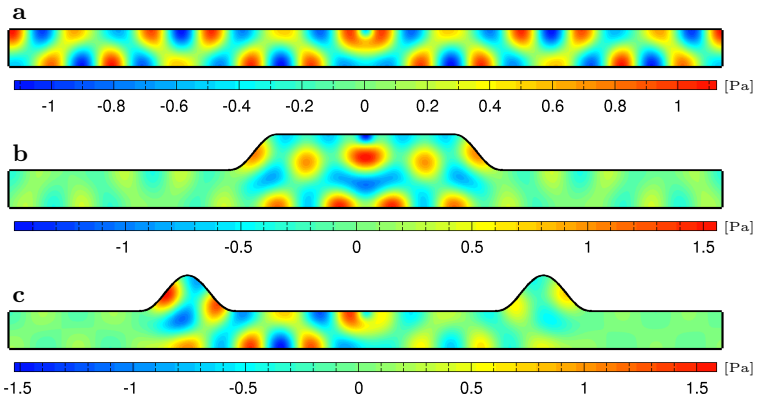

Figure 5.12: *Modulus of the acoustic pressure field $\tilde{p}$ using the frequency $f = 24.7$ kHz and flow speed $U_0 = 1\ m\,s^{-1}$ in the straight duct (**a**), the bulged duct (**b**), and the corrugated duct (**c**).*

there is a clear difference between the upstream and the downstream acoustic fields.

To investigate the sensitivity of the sound signal to the flow speed for a given frequency, we compute the relative symmetry deviation in the acoustic pressure $\langle \delta\tilde{p} \rangle$ for flow speeds in the range $U_0 \in [0, 1]\ \mathrm{m\,s^{-1}}$ with fixed frequency $f = 24.7$ kHz. The results are shown in Figure 5.13 for each of the three duct geometries. For all three ducts, a close-to-linear dependency upon flow speed is

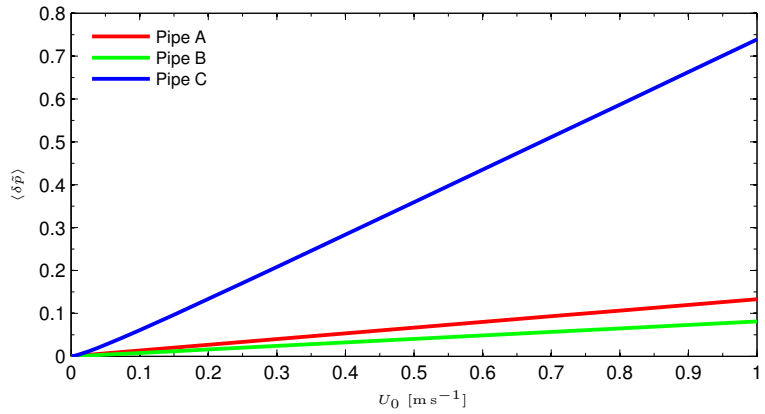

Figure 5.13: *Relative symmetry deviation in the acoustic pressure $\langle \delta\tilde{p} \rangle$ as a function of flow speed U_0 using the frequency $f = 24.7$ kHz for the three duct geometries.*

observed. We note in particular that the slope of the curve for the corrugated duct (c) is significantly larger than the slope of the curve for the straight duct (a) as well as for the duct with a single bulge (b).

The results clearly show that we have identified a combination of duct geometry and sound frequency where the acoustic signal is particularly sensitive to

the background flow. The coupling seems to be related to the parabolic velocity profile in the duct interior. Similar results are found when explicitly prescribing a parabolic velocity profile in the entire domain, whereas the effect is diminished when prescribing a constant velocity profile.

We conclude by noting that if more (evanescent) modes are used in the mode matching formulation for the acoustic truncation boundary conditions, by increasing N_m, practically identical results are found. If the mode matching formulation is replaced by a suitably scaled perfectly matched layer (PML) formulation [Becache et al., 2004; 2006; Givoli, 2008; Bermúdez et al., 2008], using, e.g., a linear absorbing function in a PML of width 10%, equivalent results to within $\sim 2\%$ are found, although the improved error convergence rates for higher order polynomial approximations of the acoustic pressure have been found to be somewhat compromised in this formulation. If different footprints of the acoustic source are used, by changing $\boldsymbol{L}$, qualitatively similar results are found. Still, the phenomenon so far only exists in a numerical model and lacks experimental validation. Nevertheless, it points towards the potential importance of the geometry on flow sensitivity for acoustic wave propagation, and shape optimization could likely enhance the effect.

5.6 Conclusions

In this chapter, we have presented a coupled flow-acoustic model of the propagation of sound through a moving fluid in a 2-dimensional duct based on isogeometric analysis. The model explicitly couples the non-linear, steady state, incompressible Navier-Stokes equation in the laminar regime to a linear, time-harmonic acoustic equation in the low Mach number regime, using both the background flow and its gradient as input. Acoustic boundary conditions along artificial truncation boundaries were dealt with using a mode matching formulation. The model has been validated against known acoustic modes in 2-dimensional ducts. These tests clearly supported the robustness of the method. In particular, desirable error convergence properties were observed for higher order polynomial approximations of the acoustic pressure, and these are naturally embedded in isogeometric analysis. Using the model, acoustic signal changes vs. duct geometry have been examined as a function of frequency and background flow values. A combination of duct geometry and sound frequency was identified for which the acoustic signal is particularly sensitive to the background flow. This enhanced sensitivity deserves closer examination in future studies.

Chapter 6

Extensions and Outlook

This chapter presents, in a somewhat fragmented manner, a short collection of additional investigations made within isogeometric analysis and shape optimization in fluid mechanics. Strategies for construction of parametrizations of domains interiors, and applications of isogeometric shape optimization to design of idealized airfoils are discussed. The chapter is concluded by a summary of future research directions within the field.

6.1 Parametrizations of Domain Interiors

One challenge in isogeometric analysis is to construct a parametrization of the interior of a domain from a parametrization of its boundary, assuming the latter is given, or equivalently, to specify the interior control points from the boundary control points [Xu et al., 2010; Cohen et al., 2010; Gravesen et al., 2010]. This is sketched in Figure 6.1. The challenge is greatly enhanced in isogeometric shape optimization: as described in Section 4.3, when the parametrization of the boundary is changed in each optimization step by moving the boundary control points, the parametrization of the interior must be updated as well by moving the interior control points. Below, we describe two strategies for tackling this challenge.

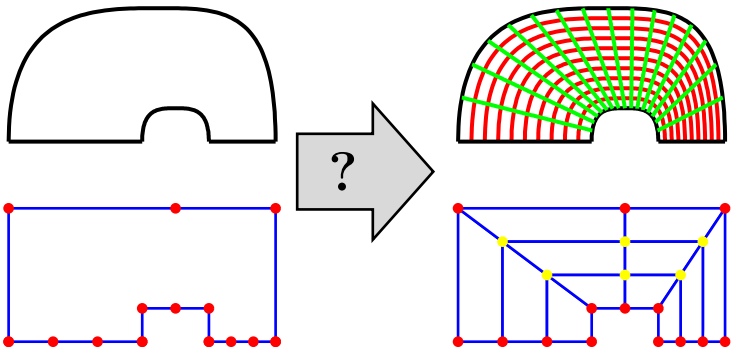

Figure 6.1: *Challenge: How do we go from a parametrization of the boundary of a domain to a parametrization that includes the interior of the domain?*

Conformality: the Winslow functional

In this methodology, the goal is to construct as conformal a parametrization as possible [Gravesen et al., 2010; Nguyen et al., 2011]. For a conformal parametrization, isoparametric lines intersect at right angles, and the mesh therefore consists of "nice" quadrilaterals.

To construct a measure of conformality, we consider a parametrization $\boldsymbol{X}$, its Jacobian $\boldsymbol{J}$, and its first fundamental form $\boldsymbol{g}$:

$$\boldsymbol{X}(\xi,\eta) = \begin{pmatrix} x(\xi,\eta) & y(\xi,\eta) \end{pmatrix}, \tag{6.1a}$$

$$\boldsymbol{J}(\xi,\eta) = \begin{pmatrix} \frac{\partial x}{\partial \xi} & \frac{\partial x}{\partial \eta} \\ \frac{\partial y}{\partial \xi} & \frac{\partial y}{\partial \eta} \end{pmatrix}, \tag{6.1b}$$

$$\boldsymbol{g}(\xi,\eta) = \boldsymbol{J}^T\boldsymbol{T}. \tag{6.1c}$$

Conformality of the parametrization $\boldsymbol{X}$ implies that the Jacobian $\boldsymbol{J}$ is the product of a scaling and a rotation, or equivalently that the first fundamental form $\boldsymbol{g}$ is diagonal with identical diagonal elements. If we let λ_1 and λ_2 denote the eigenvalues of $\boldsymbol{g}$, we want $\lambda_1 = \lambda_2$ to have conformality. We easily find that:

$$\frac{\left(\sqrt{\lambda_1} - \sqrt{\lambda_2}\right)^2}{\sqrt{\lambda_1\lambda_2}} = \frac{\lambda_1 + \lambda_2 - 2\sqrt{\lambda_1\lambda_2}}{\sqrt{\lambda_1\lambda_2}} = \frac{\lambda_1 + \lambda_2}{\sqrt{\lambda_1\lambda_2}} - 2$$

From this, we may define the function W:

$$W = \frac{\lambda_1 + \lambda_2}{\sqrt{\lambda_1\lambda_2}} = \frac{\operatorname{tr}(\boldsymbol{g})}{\sqrt{\det(\boldsymbol{g})}} = \frac{(\frac{\partial x}{\partial \xi})^2 + (\frac{\partial x}{\partial \eta})^2 + (\frac{\partial y}{\partial \xi})^2 + (\frac{\partial y}{\partial \eta})^2}{\frac{\partial x}{\partial \xi}\frac{\partial y}{\partial \eta} - \frac{\partial y}{\partial \xi}\frac{\partial x}{\partial \eta}}, \tag{6.2}$$

where $\sqrt{\det(\boldsymbol{g})} = \det(\boldsymbol{J})$. As such, W is a pointwise measure of conformality. From the function W, we may define the *Winslow functional* $\mathcal{W}$ as the integral of W. This is thus a global measure of conformality.

Now, we may seek a parametrization of the domain that minimizes the Winslow functional $\mathcal{W}$, and has γ as its boundary. To ensure a valid parametrization, we must have $\det(\boldsymbol{J}) > 0$ in the interior. We therefore seek a parametrization $\boldsymbol{X}$ as the argument of the following constrained optimization problem:

$$\underset{\boldsymbol{X}}{\text{minimize}} \qquad \mathcal{W} = \iint_{[0,1]^2} W \,\mathrm{d}\xi \,\mathrm{d}\eta\,, \tag{6.3a}$$

$$\text{such that} \qquad \boldsymbol{X}|_{\partial\Omega} = \gamma\,, \tag{6.3b}$$

$$\det(\boldsymbol{J}) > 0\,. \tag{6.3c}$$

In the framework of B-spline based isogeometric analysis, the optimization problem (6.3) is discretized using the B-spline parametrization in Equation (2.12). The design variables are then the coordinates of the interior control points. The Winslow functional (6.3a) may be evaluated directly from the parametrization. The boundary constraint (6.3b) is easily fulfilled by fixing the boundary control points. The constraint on the determinant of the Jacobian (6.3c) may be evaluated by writing it as a new spline (with increased polynomial degrees and knot multiplicities), and then using the control variables of this spline as constraints, using the convex hull property of splines.

Analysis Consistency: Multimesh Residual

In this methodology, the goal is to construct a parametrization that makes the analysis as consistent as possible. By a consistent analysis, we mean a numerical solution of the governing equations that does not depend (strongly) on the numerical discretization used. We may term this an *analysis-aware* parametrization [Xu et al., 2010; Cohen et al., 2010].

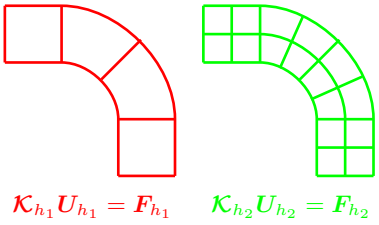

Figure 6.2: *Illustration of the focus of an analysis-aware parametrization based on the multimesh residual.*

To construct a measure of analysis consistency, we consider the discrete form of the governing equations at two different discretizations, or mesh resolutions:

$$\boldsymbol{\mathcal{K}}_{h_i}\boldsymbol{U}_{h_i} = \boldsymbol{F}_{h_i}, \tag{6.4}$$

for $i = 1, 2$. Here, h_1 corresponds to a coarse mesh, and $h_2 < h_1$ corresponds to a fine mesh. An obvious choice is to take $h_1 = 2h_2$, i.e., to construct the h_2-mesh by uniform knot insertion in the h_1-mesh, as sketched in Figure 6.2. We may consider the norm squared difference between the two solutions of Equation (6.4) as a measure of analysis consistency:

$$R = \left\| \overline{\boldsymbol{U}}_{h_2} - \overline{\boldsymbol{T}_{h_1 \to h_2}\boldsymbol{U}}_{h_1} \right\|^2, \tag{6.5}$$

where $\boldsymbol{U}_{h_1}$ and $\boldsymbol{U}_{h_2}$ are the solution vectors on the coarse and the fine mesh, respectively, and $\boldsymbol{T}_{h_1 \to h_2}$ is the matrix that puts the coarse mesh solution $\boldsymbol{U}_{h_1}$ in the basis of the fine mesh solution $\boldsymbol{U}_{h_2}$, cf. Theorem 3. To ensure a proper balancing between velocity and pressure control variables contained in $\boldsymbol{U}_{h_i}$, both the fine solution vector and the mapped coarse solution vector are normalized with respect to the fine solution vector:

$$\overline{\boldsymbol{U}}_{h_i} = \left(\frac{\underline{\boldsymbol{u}}_{h_i}}{\|(\underline{\boldsymbol{u}}_{h_2}, \underline{\boldsymbol{v}}_{h_2})\|}, \frac{\underline{\boldsymbol{v}}_{h_i}}{\|(\underline{\boldsymbol{u}}_{h_2}, \underline{\boldsymbol{v}}_{h_2})\|}, \frac{\underline{\boldsymbol{p}}_{h_i}}{\|\underline{\boldsymbol{p}}_{h_2}\|} \right)^T. \tag{6.6}$$

The measure (6.5) was originally suggested by [Hogan, 2010, Personal communication], and we refer to it here as a multimesh residual.

Based on this measure, we may seek a parametrization $\boldsymbol{X}$ of the computational domain as the argument of the following optimization problem:

$$\begin{aligned}
\underset{\boldsymbol{X}}{\text{minimize}} \quad & R = \left\| \overline{\boldsymbol{U}}_{h_2} - \overline{\boldsymbol{T}_{h_1 \to h_2}\boldsymbol{U}_{h_1}} \right\|^2, && \text{(6.7a)} \\
\text{such that} \quad & \boldsymbol{X}|_{\partial\Omega} = \gamma, && \text{(6.7b)} \\
& \boldsymbol{\mathcal{K}}_{h_i}\boldsymbol{U}_{h_i} = \boldsymbol{F}_{h_i} \quad \text{for } i = 1, 2, && \text{(6.7c)}
\end{aligned}$$

By minimizing the multimesh residual (6.5), we bring the solutions of the governing equations at two different meshes as close to each other as possible, and we expect, all other things being equal, to have a more reliable analysis.

We mention that the multimesh residual approach in principle may serve as error estimator based on any quantity $c(h_i)$, by minimizing, e.g., $(\, c(h_2) - c(h_1)\,)^2$.

A Numerical Example

To illustrate the above procedures at work, we consider the initial parametrization in Figure 6.3a. From this, we may find alternative parametrizations by solving the optimization problems (6.3) and (6.7) using the isogeometric optimization approach outlined in Chapter 4.

Both procedures require the specification of an initial parametrization, i.e., an initial control net, from which the optimizations may proceed. This may be done manually, or by, e.g., a simple linear spring model [Nguyen et al., 2011]. For simplicity, we base the multimesh residual on the linear Stokes problem, using a parabolic horizontal velocity profile specified along the upper left (inlet) boundary, no-slip along the side (wall) boundaries, and outflow boundary conditions on the lower right (outlet) boundary.

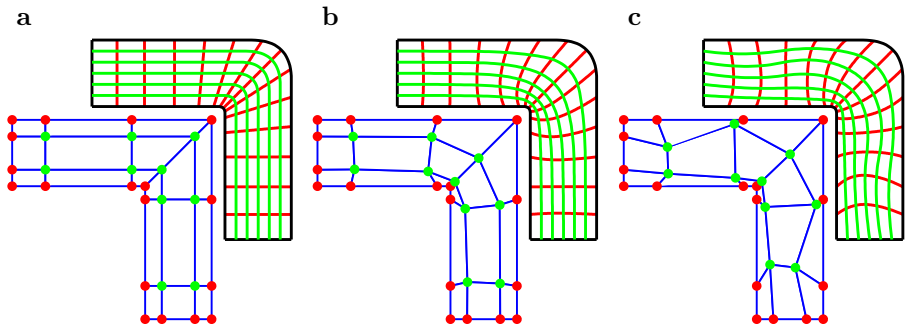

Figure 6.3: *Parametrization of a pipe bend: initial (***a***), Winslow functional (***b***), and multimesh residual (***c***).*

The results for the Winslow functional and the multimesh residual based methods are shown in Figures 6.3a and 6.3b, respectively. The methods agree on the fine resolution of the sharp inner corner. Some differences are seen in the curved outer corner and along the straight parts. We speculate that the multimesh residual method may be too influenced by parts of the domain where the fields taken on high values. A more appropriate normalization of the field variables could possibly resolve the issue. In terms of implementation, the Winslow functional approach is cheaper to calculate, compared to the multimesh residual, where the governing equations must solved in each step. In addition, the Winslow optimization converged in fewer iterations, compared to the multimesh residual optimization.

Linearization

In a shape optimization framework, solving the interior optimization problem (6.3) or (6.7) in each boundary optimization iteration is not only expensive, it also deteriorates the differentiability of the objective and constraint functions, and hence prohibits the use of gradient-based optimization. This problem may be circumvented by the following approach: first we find a good parametrization by minimizing the given measure $\mathcal{M}$ using (6.3) or (6.7). Using these control points $\boldsymbol{x}_0$, we subsequently approximate the measure by its 2^{nd} order Taylor expansion:

$$\mathcal{M}(\boldsymbol{x}_0 + \Delta\boldsymbol{x}) \approx \mathcal{M}_0 + (\nabla_0\mathcal{M})^T\Delta\boldsymbol{x} + \frac{1}{2}(\Delta\boldsymbol{x})^T H_0(\mathcal{M})\Delta\boldsymbol{x}, \tag{6.8}$$

where $\mathcal{M}_0$, $\nabla_0\mathcal{M}$, and $H_0(\mathcal{M})$ denote the measure, its gradient and its Hessian evaluated in $\boldsymbol{x}_0$, respectively. Now we may minimize the 2^{nd} order Taylor expansion of the measure, which then leads to a linear problem. To increase the reliability of the method, the linearization must be updated now and then. Using the Winslow functional, the linearization may be used, e.g., until the parametrization becomes (close to) singular, at which point the procedure is repeated. The optimization results presented in Chapter 4 all rests on this procedure for parametrizing the interior, and it has been found to be quite robust and efficient. More details may be found in [Gravesen et al., 2010; Nguyen et al., 2011].

Conclusions

The construction of an interior parametrization is important, since it affects the analysis results, and hence also the shape optimization results. Two optimization methodologies for parametrizing a given domain from parametrization of its boundaries have been examined. The Winslow functional based method focuses on conformality, whereas the multimesh residual based method focuses on analysis consistency. In a shape optimization framework, we have good experience with the linearization of the former. Further investigations are recommended for the latter.

6.2 Design of Idealized Airfoils

Design of airfoils is a classical engineering task within aerodynamics [Mohammadi and Pironneau, 2010; Painchaud-Oullet et al., 2006]. Within the last decades, the concept of micro air vehicles (MAVs) has emerged, see e.g. [Mueller, 2009; Tanaka and Wood, 2010]. MAVs are interesting in the present context, because the assumptions of incompressibility, steady state, and moderate Reynolds numbers, may be partly justified. The aim in the following is to set up an isogeometric framework for optimal designs of airfoils under such highly idealized flow conditions. We aim at designing a fixed-wing airfoil to minimize the drag of the flow past it, subjected to a constraint on its lift, as well as constraints on its area and thickness, and we present some preliminary results. This is a natural extension of the minimal drag body optimization problem considered in Section 4.5.

Optimization Problem

As above, we consider the exterior flow in 2 dimensions around the airfoil depicted in Figure 6.4. We assume the fluid to be Newtonian, isothermal and incompressible, and the flow is assumed to be stationary. With the dynamic viscosity μ and the density ρ of the fluid given, the velocity $\boldsymbol{u}$ and pressure p of the flow past the airfoil are then governed by the steady-state Navier-Stokes equation and the incompressibility condition, supplemented by suitable boundary conditions, cf. Equations (2.4)–(2.5).

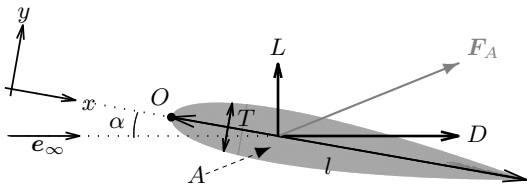

Figure 6.4: *Physical and geometrical quantities for the airfoil.*

The aerodynamic quantities of interest are the drag (D) and the lift (L) of the airfoil. These are the flow-wise parallel and perpendicular components, respectively, of the aerodynamic force $\boldsymbol{F}_A$ on the airfoil, see Figure 6.4. We write the aerodynamic force as:

$$\boldsymbol{F}_A = \int_\gamma \boldsymbol{\sigma}\boldsymbol{n}\,\mathrm{d}s = \int_\gamma \Big(-p\boldsymbol{I} + \mu\big(\nabla\boldsymbol{u} + (\nabla\boldsymbol{u})^T\big)\Big)\boldsymbol{n}\,\mathrm{d}s, \tag{6.9}$$

where $\boldsymbol{\sigma}$ is the shear stress tensor, $\boldsymbol{I}$ the identity matrix, and $\boldsymbol{n}$ is the airfoil-wise outward unit normal. We design the airfoil to minimize the drag *coefficient* C_D and prescribe a minimal lift *coefficient* C_L

$$C_D = \frac{D}{\frac{1}{2}\rho u_\infty^2 l} = \frac{\boldsymbol{F}\cdot\boldsymbol{e}_\infty}{\frac{1}{2}\rho u_\infty^2 l}, \tag{6.10a}$$

$$C_L = \frac{L}{\frac{1}{2}\rho u_\infty^2 l} = \frac{\boldsymbol{F}\cdot\hat{\boldsymbol{e}}_\infty}{\frac{1}{2}\rho u_\infty^2 l}, \tag{6.10b}$$

where u_∞ is the undisturbed far field flow speed, l is the chord length, $\boldsymbol{e}_\infty$ is the unit vector along the undisturbed far field flow direction and $\hat{\boldsymbol{e}}_\infty$ its normal vector.

The geometric quantities of interest are the airfoil cross-sectional area A, and the thickness T, e.g. at points close the leading and trailing edges, see Figure 6.4. The area may be determined by the line integral along the closed airfoil curve:

$$A = \frac{1}{2}\Big(\int_\gamma x\,\mathrm{d}y - \int_\gamma y\,\mathrm{d}x\Big), \tag{6.11}$$

The thickness at a given point x^* along the chord is given by:

$$T(x) = y(\xi^{\mathrm{u}}) - y(\xi^{\mathrm{l}}) \quad \text{s.t.} \quad x(\xi^{\mathrm{u}}) = x(\xi^{\mathrm{l}}) = x^*, \tag{6.12}$$

where $\boldsymbol{\gamma}(\xi) = (x(\xi), y(\xi))$, and the superscripts u and l refer to the upper and lower part of the closed airfoil curve, respectively. We constrain the area and the thicknesses by prescribing minimal allowed values.

The optimization problem reads:

$$
\begin{aligned}
\underset{\boldsymbol{\gamma}(\boldsymbol{x})}{\text{minimize}} \quad & \widetilde{C}_D = C_D + \epsilon\, R && && \text{(6.13a)}\\
\text{such that} \quad & C_L \geq C_{L\min} && && \text{(6.13b)}\\
& A \geq A_{\min} && && \text{(6.13c)}\\
& T_i \geq T_i^{\min} && && \text{(6.13d)}\\
& \mathbf{0} = \rho(\boldsymbol{u}\cdot\nabla)\boldsymbol{u} + \nabla p - \mu\nabla^2\boldsymbol{u} && \text{in } \Omega && \text{(6.13e)}\\
& 0 = \nabla\cdot\boldsymbol{u} && \text{in } \Omega && \text{(6.13f)}\\
& \boldsymbol{u} = \boldsymbol{u}_\infty && \text{on } \Gamma_D && \text{(6.13g)}\\
& 0 = (\mu\nabla u_i - \boldsymbol{e}_i p)\cdot\boldsymbol{n} && \text{on } \Gamma_N && \text{(6.13h)}\\
& \boldsymbol{x}_l \leq \boldsymbol{x} \leq \boldsymbol{x}_u && && \text{(6.13i)}\\
& \boldsymbol{A}\boldsymbol{x} = \boldsymbol{b}. && && \text{(6.13j)}
\end{aligned}
$$

Here, Equations (6.13a)–(6.13d) express the objective and constraint functions, (6.13e)–(6.13h) are the governing equations and boundary conditions, and (6.13i)–(6.13j) establish bounds on and linear relations between the design variables $\boldsymbol{x}$ that parametrize the airfoil γ. The last term in the objective function $\tilde{C}_D$ in Equation (6.13a) is included for regularization purposes.

Isogeometric Implementation

To solve the optimization problem (6.13), we follow the approach outlined in Chapters 3–4.

To construct the geometry, we consider Figure 6.5. The airfoil is embedded in a computational flow domain whose exterior boundary extends 15 chord lengths upstream and sidewards, and 30 chord lengths downstream. A parametrization of the flow domain is constructed from bi-quadratic tensor product B-splines, and we choose to parametrize the flow domain using 6 patches. The airfoil curve is represented as one of the patch boundary segments. This configuration of patches facilitates implementation of different boundary conditions, as well as local refinement around the airfoil and downstream of it (by fixing the airfoil and rotating the surrounding geometry by a prescribed angle of attack), although more efficient local refinement techniques could be used with advantage (see below).

The design variables $\boldsymbol{x}_i$ are the coordinates of the control points corresponding to the patch boundary in Figure 6.5 that define the shape of the airfoil. These control points are shown in Figure 6.6. For simplicity we keep the chord length l and orientation constant throughout the optimization. This is done by fixing the rightmost control point in both directions $\boldsymbol{x}_0 = (l, 0)$, fixing the leftmost control points in the horizontal direction such that $x_6 = x_7 = 0$, while demanding that $y_6 = -y_7$, and finally choosing $x_i \geq x_l = 0$, $x_i \leq x_u = l$ for $i = 1, \ldots, 12$. Additionally, we prescribe $y_i \leq y_u = 0$ for $i = 1, \ldots, 6$ and $y_i \geq y_l = 0$ for $i = 7, \ldots, 12$ to avoid self-intersection of the curve.

For the analysis, we take the density and viscosity as $\rho = 1\,\mathrm{kg\,m^{-3}}$ and $\mu = 1 \cdot 10^{-5}\,\mathrm{kg\,m^{-1}\,s^{-1}}$, approximately corresponding to normal room condi-

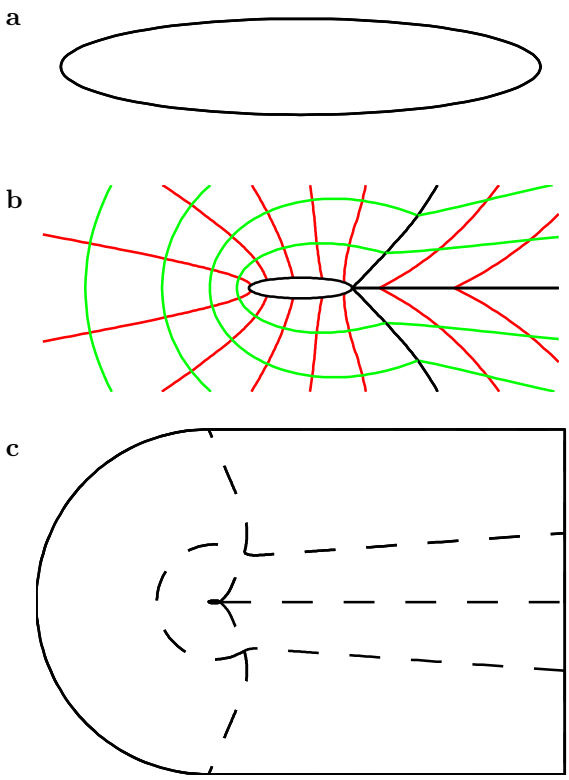

Figure 6.5: **a**: *An approximate ellipse serves as first approximation of the airfoil.* **b**: *A parametrization is constructed of the flow domain around the airfoil. Green and red lines are isoparametric lines.* **c**: *The flow domain (solid) is split into six patches (dashed).*

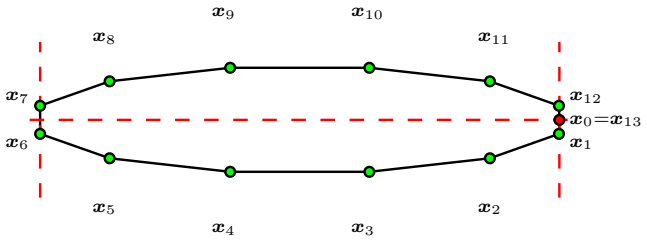

Figure 6.6: *14 control points define the shape of the airfoil.*

tions, and we use a chord length of $l = 1 \cdot 10^{-2}\,\mathrm{m}$, corresponding roughly to an insect wing. Along the upstream exterior boundary Γ_U we prescribe the velocity as $\boldsymbol{u} = u_\infty R_z(\alpha)\boldsymbol{e}_1\,\mathrm{m\,s^{-1}}$, where $R_z(\alpha)$ denotes the matrix that rotates the Cartesian basis vector $\boldsymbol{e}_1$ by the prescribed angle of attack α, and use a (very low) speed of $u_\infty = 10\,\mathrm{cm\,s^{-1}}$, and along the airfoil γ we assume no-slip conditions $\boldsymbol{u} = (0, 0)$. The angle of attack is taken as $\alpha = 5°$, and with this choice of parameters, the Reynolds number is $\mathrm{Re} \sim 100$. The velocity and pressure fields

are approximated using the Taylor-Hood discretization $\mathbf{u}4_0^2\mathrm{p}3_0^1$ (d) in Table 3.1.

For the optimization, we simply use the properties of the initial shape, namely an approximate ellipse with major axis $l/2$ and minor axis $l/20$ as depicted in Figure 6.5 (a), as lower bounds on both the lift, area, and thicknesses at the leading edge $x = 0.15\,l$ and trailing edge $x = 0.85\,l$. The regularization scaling parameter is taken as $\epsilon = 10^{-2}$.

By applying the isogeometric shape optimization machinery to the problem, we find an optimal shape in 29 iterations. Figure 6.7 compares the optimal airfoil shape to the initial shape (a), as well as the location of the control points before and after the optimization (b). The optimized shape is remarkably close to the initial ellipse. A small change, however, is seen near the trailing edge. The decrease in drag is accordingly small, namely only 1‰ (and some of the change in the parametrization may very well be due to the regularization). All constraints are active, except the trailing edge thickness. Larger shape changes may of course be found by slacking the constraints, or equivalently by using a worse initial guess.

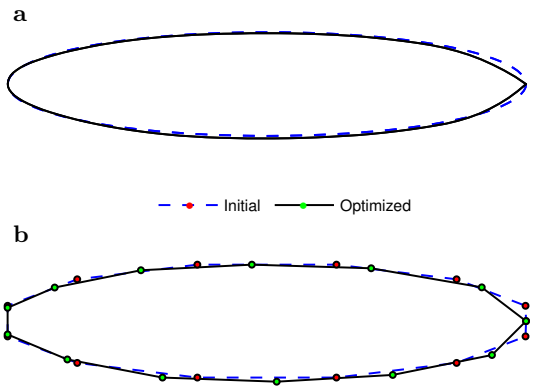

Figure 6.7: *Comparison of initial (dashed blue) and optimized (full black) airfoil shape (***a***) and control net (***b***).*

Conclusions

We have presented a framework for isogeometric shape optimization for design of airfoils in highly idealized flow conditions. Such studies may find their relevance for micro air vehicles (MAVs). The airfoils can be designed to minimize the drag with both constraints on the lift, area, and thickness at specified locations. We have presented some first numerical results, and we emphasize that these are preliminary. On the analysis side, inspection of pressure and skin friction coefficients along the airfoil should be made to validate the results. More reliable results may be obtained, e.g., by the use of more efficient local refinement schemes. This would also facilitate studies at higher Reynolds numbers, where most MAVs operate [Mueller, 2009], as higher Reynolds numbers in the current setup requires too much computer memory. On the optimization side, it could be considered to reformulate the problem slightly and maximize the lift-over-drag ratio instead, and a multipoint optimization with several angles

of attack could also be considered to make the design more robust. Studies of the importance of shape regularization should also be addressed.

6.3 Outlook

This thesis represents but a small step within the field of isogeometric analysis and shape optimization in fluid mechanics. In many aspects, we have merely scratched the surface, and the thesis leaves the field wide open with several challenges for the future.

Firstly, the type of flow problems considered in this thesis are rather simple, compared to most of the real-world flow phenomena we see around us. From the stirring in a coffee cup, to the flow past the wing on an airplane, most flows are inherently turbulent. When turbulent flows are considered, the flow fields become non-stationary, small scale phenomena appear, and in addition, spatial symmetries are broken [Frisch, 1995]. The full time-dependent Navier-Stokes equations in three spatial dimensions must therefore be considered.

In the isogeometric framework, a substantial amount of research has been made within modeling of turbulent flows using the so-called residual-based variational multiscale (RBVM) method, see e.g. [Bazilevs et al., 2007a; Akkerman et al., 2010; Bazilevs and Akkerman, 2010; Bazilevs et al., 2010b; Akkerman et al., 2011; Hsu et al., 2011]. This method has proven very applicable to, e.g., turbulent Taylor-Couette flow, to modelling of wind-turbine aerodynamics, and to free-surface flows. Once again, the high continuity of the method seems to play an important role. In the framework of shape optimization, objective and constraints will dependent on time, which complicates matters [Mohammadi and Pironneau, 2010]. We consider the application of, e.g., the RBVM method to turbulent flow, as an important step towards optimization of shapes in more realistic flow problems.

From a numerical modeling perspective, turbulent flows are much more challenging. Not only does the governing equation involve more terms, the number of degrees of freedom required to do the analysis increases significantly with the Reynolds number [Frisch, 1995]. This put strict requirements on the amount of computer memory. To speed up computations, high-performance parallel computing may be used large scale problems are solved [Hsu et al., 2011]. Implementation of the isogeometric shape optimization methodology in a more efficient computational framework would facilitate the consideration of more advanced problems. This is another interesting challenge.

An important aspect in isogeometric analysis is the concept of *local refinement*, i.e., the ability to have some parts of the parametrization finely resolved in the analysis, and other parts coarsely resolved. In modelling the flow past an airfoil, e.g., we want to have a very fine analysis mesh close to and downstream of it, and a coarse mesh farther away from it. While local refinement may be achieved through the use of multiple patches based on tensor product B-splines, significantly more efficient local refinements may be achieved by other means. We mention here T-splines [Bazilevs et al., 2010a; Dörfel et al., 2010], hierarchical splines [Vuong et al., 2011], and locally refined (LR) B-splines [Dokken, 2011, Personal Communication], that all represent viable ways of achieving local refinement. In the framework of isogeometric shape optimization for fluids, we consider this as a very important next step to achieve higher efficiency and

reliability.

Most real-world problems are coupled problems of different nature. For the airfoil, e.g., the structure itself is actually deformed under the aerodynamic loads from the flow past it, which in turn changes the flow, and so on. Studies of isogeometric analysis to various fluid-structure interaction problems have demonstrated the applicability of the method [Bazilevs et al., 2006a; 2008]. Shape optimization of fluid-structure interaction problems would be a very interesting challenge to take up.

The propagation of sound through flows represents another coupled problem, here between flow and acoustics. The geometric enhancement of the acoustic flow sensitivity for sound propagation through flow in ducts mentioned in Chapter 5 deserves further investigations. Studies in 3 dimensions should be made. Applications of the isogeometric shape optimization methodology to find duct shapes that enhance the effect further are an obvious extension. Here, the formulations of robust objective and constraint functions are the first challenges.

Chapter 7

Conclusions

The aim of this thesis has been to bring together the fields of fluid mechanics, isogeometric analysis, and shape optimization. The flow problems that have been considered are governed by the 2-dimensional, steady-state, incompressible Navier-Stokes equations at low to moderate Reynolds numbers. Studies within flow acoustics have been made as well, where the sound signal is governed by a linear, time-harmonic, background flow-dependent acoustic equation in the low Mach number regime. Isogeometric analysis has been used as numerical method both to solve the governing equations, and as framework for a gradient-based optimization procedure.

Firstly, applications of isogeometric analysis to flows were studied. Splines were used to approximate flow velocity and pressure, and numerical inf-sup stability tests confirmed the existence of many stable discretizations of the velocity and pressure spaces. In particular it was found that stability may be achieved by means of knot refinement of the velocity space. Error convergence studies compared the performance of the various discretizations and indicated optimal convergence, in a per-degree-of-freedom sense, of the discretization with identical polynomial degrees of the velocity and pressure spaces, but with the velocity space enriched by knot refinement. Finally, the method was applied to the lid-driven square cavity for benchmarking purposes, showing that the stable discretizations produce consistent results that match well with previous results and thus confirm the robustness of the method.

Secondly, applications of the isogeometric method to shape optimization problems for fluids were studied. In this formalism, objects in flows were designed by optimizing the location of the control points that define the shape of the body using a gradient-based numerical optimization package. To avoid inappropriate parametrizations during optimization, a regularization technique was established by adding to the objective function a measure of the quality of the parametrization. Based on a benchmark design problem, in which a pipe bend was designed to minimize the pressure drop of the flow through it, the integral of the norm squared parametric acceleration along the design boundary was found to be a cheap, flexible and efficient regularization measure. To emphasize the robustness of the proposed isogeometric shape optimization methodology for fluids, two additional problems were considered. Based on Taylor-Couette flow, we firstly solved a shape optimization problem with a known solution, and we found that the more design variables we use, the better the approximation

to the exact solution we obtain. Secondly, we designed a body to minimize the drag from the flow past it, and we found that the methodology allows for significantly different optimal shapes as the flow speed is increased.

Thirdly, applications of isogeometric analysis to the propagation of sound through flows in ducts were presented. A coupled flow-acoustic model of the phenomenon was described. Acoustic boundary conditions along artificial truncation boundaries were treated based on a mode matching formulation. The model was validated against known acoustic modes in 2-dimensional ducts, and desirable error convergence properties were observed for higher order polynomial approximations of the acoustic pressure. Using the model, acoustic signal changes vs. duct geometry were examined as a function of frequency and background flow values. We identified a combination of duct geometry and sound frequency for which the acoustic signal was particularly sensitive to the background flow, a phenomenon deserving closer examination in future studies.

Finally, miscellaneous studies within the field were presented. Two methods for automated domain parametrizations in isogeometric analysis were studied, supporting the Winslow functional as a robust mesh quality measure, and a preliminary application of isogeometric shape optimization to design of idealized airfoils was presented, demonstrating the potential of the methodology.

The thesis represents but a small step within the field of isogeometric analysis and shape optimization in fluid mechanics. Suggestions for future research directions include, among others, applications within less restrictive flow problems (3-dimensional, time-dependent, and turbulent flows), applications within fluid-structure interactions, implementation in a high-performance computing framework, and implementation of local refinement methods.

References

M. Abromovitz and I. Stegun, editors. *Handbook of mathematical functions with formulas, graphs and mathematical tables*. Dover Publications, ninth edition, 1970. ISBN 0-486-61272-4.

I. Akkerman, Y. Bazilevs, V.M. Calo, T.J.R. Hughes, and S. Hulshoff. The role of continuity in residual-based variational multiscale modeling of turbulence. *Computational Mechanics*, 41:371–378, 2010.

I. Akkerman, Y.Bazilevs, C. E. Kees, and M. W. Farthing. Isogeometric analysis of free-surface flows. *Journal of Computational Physics*, 230:4137–4152, 2011.

R. J. Astley and W. Eversman. Acoustic transmission in non-uniform ducts with mean flow, part II: the finite element method. *Journal of Sound and Vibration*, 74(1):103–121, 1981.

R.J. Astley. FE mode-matching schemes for the exterior Helmholtz problem and their relationship to the FE-DtN approach. *Communications in numerical methods in engineering*, 12:257–267, 1996.

K.J. Bathe. The inf-sup condition and its evaluation for mixed finite element methods. *Computers & Structures*, 79:243–252, 2001.

K.J. Bathe, D. Hendriana, F. Brezzi, and G. Sangalli. In-sup testing of upwind methods. *International Journal for Numerical Methods in Engineering*, 48:745–760, 2000.

Y. Bazilevs and I. Akkerman. Large eddy simulation of turbulent Taylor-Couette flow using isogeometric analysis and the residual-based variational multiscale method. *Journal of Computational Physics*, 229:3402–3414, 2010.

Y. Bazilevs and T.J.R. Hughes. Weak imposition of Dirichlet boundary conditions in fluid mechanics. *Computers & Fluids*, 36:12–26, 2007.

Y. Bazilevs and T.J.R. Hughes. NURBS-based isogeometric analysis for the computation of flows about rotating components. *Computational Mechanics*, 43:143–150, 2008.

Y. Bazilevs, V. M. Calo, Y. Zhang, and T. J. R. Hughes. Isogeometric fluid-structure interaction analysis with applications to arterial blood flow. *Computational Mechanics*, 38:310–322, 2006a.

Y. Bazilevs, L.B. Da Veiga, J.A. Cottrell, T.J.R. Hughes, and G. Sangalli. Isogeometric analysis: Approximation, stability and error estimates for h-refined meshes. *Mathematical Models and Methods in Applied Science*, 16(7):1031–1090, 2006b.

Y. Bazilevs, V.M. Calo, J. A. Cottrell, T.J.R. Hughes, A. Reali, and G. Scovazzi. Variational multiscale residual-based turbulence modeling for large eddy simulation of incompressible flows. *Computer Methods in Applied Mechanics and Engineering*, 197:173–201, 2007a.

Y. Bazilevs, C. Michler, V.M. Calo, and T.J.R. Hughes. Weak Dirichlet boundary conditions for wall-bounded turbulent flows. *Computer Methods in Applied Mechanics and Engineering*, 196:4853–4862, 2007b.

Y. Bazilevs, V. M. Calo, T. J. R. Hughes, and Y. Zhang. Isogeometric fluid-structure interaction: theory, algorithms, and computations. *Computational Mechanics*, 43:3–37, 2008.

Y. Bazilevs, V. M. Calo, J. A. Cottrell, J. A. Evans, T. J. R. Hughes, S. Lipton, M. A. Scott, and T. W. Sederberg. Isogeometric analysis using T-splines. *Computer Methods in Applied Mechanics and Engineering*, 199:229–263, 2010a.

Y. Bazilevs, C. Michler, V.M. Calo, and T.J.R. Hughes. Isogeometric variational multiscale modeling of wall-bounded turbulent flows with weakly enforced boundary conditions on unstretched meshes. *Computer Methods in Applied Mechanics and Engineering*, 199:780–790, 2010b.

E. Becache, A.-S. Bonnet-Ben Dhia, and G. Legendre. Perfectly matched layers for the convected Helmholtz equation. *SIAM Journal on Numerical Analysis*, 42(1):409–433, 2004.

E. Becache, A.-S. Bonnet-Ben Dhia, and G. Legendre. Perfectly matched layers for time-harmonic acoustics in the presence of a uniform flow. *SIAM Journal on Numerical Analysis*, 44(3):1191–1217, 2006.

M. P. Bendsøe and O. Sigmund. *Topology Optimization: Theory, methods and Applications*. Springer, second edition, 2003. ISBN 3-540-42992-0.

A. Bermúdez, L. Hervella-Nieto, A. Prieto, and R. Rodríguez. Perfectly Matched Layers. In S. Marburg and B. Nolte, editors, *Computational Acoustics Of Noise Propagation In Fluids – Finite And Boundary Element Methods*, pages 467–196. Springer, 2008. ISBN 978-3-540-77447-1.

K.-U. Bletzinger, M. Firl, J. Linhard, and R. Wüchner. Optimal shapes of mechanically motivated surfaces. *Computer Methods in Applied Mechanics and Engineering*, 199:324–333, 2010.

A. L. Bowers, B. R. Cousins, A. Linke, and L. G. Rebholz. New connections between finite element formulations of the Navier-Stokes equations. *Journal of Computational Physics*, 229:9020–9025, 2010.

A. Bressan. Isogeometric regular discretization for the Stokes problem. *IMA Journal of Numerical Analysis2*, 2010. doi: 10.1093/imanum/drq014.

A. Bressan, Personal communication.

A. Buffa, C. de Falco, and G. Sangalli. Isogeometric Analysis: Stable elements for the 2D Stokes equation. *International Journal for Numerical Methods in Fluids*, 2011. doi: 10.1002/fld.2337.

D. Chapelle and K.J. Bathe. The inf-sup test. *Computers & Structures*, 47 (4/5):537–545, 1993.

S. Cho and S.-H. Ha. Isogeometric shape design optimization: exact geometry and enhanced sensitivity. *Structural and Multidisciplinary Optimization*, 38:53–70, 2009.

E. Cohen, T. Martin, R. M. Kirby, T. Lyche, and R. F. Riesenfeld. Analysis-aware modeling: understanding quality considerations in modeling for isogeometric analysis. *Computer Methods in Applied Mechanics and Engineering*, 199:334–356, 2010.

R. D. Cook, D. S. Malkus, M. E. Plesha, and R. J. Witt. *Concepts and Applications of Finite Element Analysis*. John Wiley & Sons, fourth edition, 2001. ISBN 978-0-471-35605-9.

J.A. Cottrell, A. Reali, Y. Bazilevs, and T.J.R. Hughes. Isogeometric analysis of structural vibrations. *Computer Methods in Applied Mechanics and Engineering*, 195:5257–5296, 2006.

J.A. Cottrell, T.J.R. Hughes, and Y. Bazilevs. *Isogeometric Analysis: Toward Integration of CAD and FEA*. John Wiley & Sons, 2009. ISBN 978-0-470-78873-2.

A.-S. Bonnet-Ben Dhia, E.-M. Duclairoir, G. Legendre, and J.-F. Mercier. Time-harmonic acoustic propagation in the presence of a shear flow. *Journal of Computational and Applied Mathematics*, 204:428–439, 2007.

A.-S. Bonnet-Ben Dhia, J.-F. Mercier, F. Millot, and S. Pernet. A low-Mach number model for time-harmonic acoustics in arbitrary flows. *Journal of Computational and Applied Mathematics*, 234:1868–1875, 2010.

T. Dokken. Locally refined B-splines, 2011. `http://www.dagstuhl.de/mat/Files/11/11211/11211.DokkenTor.Slides.pdf`.

J. Donea and A. Huerta. *Finite Element Methods for Flow Problems*. John Wiley & Sons, 2003. ISBN 0-471-49666-9.

M. Dörfel, B. J¨uttler, and B. Simeon. Adaptive isogeometric analysis by local h-refinement with T-splines. *Computer Methods in Applied Mechanics and Engineering*, 199:264–275, 2010.

D. R. Durran. *Numerical Methods for Wave Equations in Geophysical Fluid Dynamics*. Springer, 1999. ISBN 0-387-98376-7.

M.S. Engelman, R.L. Sani, and P.M. Gresho. The implementation of normal and/or tangential boundary conditions in finite element codes for incompressible fluid flow. *International Journal for Numerical Methods in Fluids*, Vol. 2:225–238, 1982.

E. Erturk, T.C. Corke, and C. Gokcol. Numerical solutions of 2-d steady incompressible driven cavity flow at high Reynolds numbers. *International Journal for Numerical Methods in Fluids*, **48**:747–774, 2005.

U. Frisch, editor. *Turbulence*. Cambridge University Press, 1995. ISBN 0-521-45713-0.

A. Gersborg-Hansen, O. Sigmund, and R. B. Haber. Topology optimization of channel flow problems. *Structural and Multidisciplinary Optimization*, 30 (3), 2005.

U. Ghia, K.N. Ghia, and C.T. Shin. High-Re Solution for Incompressible Flow Using the Navier-Stokes Equations and a Multigrid Method. *Journal of Computational Physics*, 48:387–411, 1982.

P. E. Gill, W. Murray, and A. Saunders. User's guide for snopt version 7: Software for large-scale nonlinear programming, 2008. `http://www.cam.ucsd.edu/~peg/papers/sndoc7.pdf`.

D. Givoli. Computational absorbing boundaries. In S. Marburg and B. Nolte, editors, *Computational Acoustics Of Noise Propagation In Fluids – Finite And Boundary Element Methods*, pages 145–166. Springer, 2008. ISBN 978-3-540-77447-1.

J. Gravesen. Differential geometry and design of shape and motion, 2002. `http://www2.mat.dtu.dk/people/J.Gravesen/cagd.pdf`.

J. Gravesen, A. Evgrafov, A. R. Gersborg, D. M. Nguyen, and P. N. Nielsen. Isogeometric analysis and shape optimisation. In A. Eriksson and G. Tibert, editors, *Proceedings of NSCM-23: the 23rd Nordic Seminar on Computational Mechanics*, pages 14–17, 2010.

S.-H. Ha, K. K. Choi, and S. Cho. Numerical method for shape optimization using T-spline based isogeometric method. *Structural and Multidisciplinary Optimization*, 42:417–428, 2010.

B. Hassani, M. Khanzadi, and S. M. Tavakkoli. An isogeometrical approach to structural topology optimization by optimality criteria. *Structural and Multidisciplinary Optimization*, 45:223–233, 2012.

T. Hogan. A measure of goodness of a parametrization. 2010.

M.-C. Hsu, I. Akkerman, and Y.Bazilevs. High-performance computing of wind-turbine aerodynamics using isogeometric analysis. *Computer & Fluids*, 49:93–100, 2011.

T. J. R. Hughes, A. Reali, and G. Sangalli. Duality and unified analysis of discrete approximations in structural dynamics and wave propagation: Comparison of p-method finite elements with k-method NURBS. *Computer Methods in Applied Mechanics and Engineering*, 197:4104–4124, 2008.

T.J.R. Hughes, J.A. Cottrell, and Y. Bazilevs. Isogeometric analysis: CAD, finite elements, NURBS, exact geometry and mesh refinement. *Computer Methods in Applied Mechanics and Engineering*, 194:4135–4195, 2005.

T.J.R. Hughes, A. Reali, and G. Sangalli. Efficient quadrature for NURBS-based isogeometric analysis. *Computer Methods in Applied Mechanics and Engineering*, 199:301–313, 2010.

B. Ivorra, D. E. Hertzog, B. Mohammadi, and J. S. Santiago. Semi-deterministic and genetic algorithms for global optimization of microfluidic protein-folding devices. *International Journal for Numerical Methods in Engineering*, 66:319–333, 2006.

E. Katamine, H. Azegami, T. Tsubata, and S. Itoh. Solution to shape optimization problems of viscous flow fields. *International Journal of Computational Fluid Dynamics*, 19(1):45–51, 2005.

D. W. Kim and M.-U. Kim. Minimum drag shape in two-dimensional viscous flow. *International Journal for Numerical Methods in Fluids*, 21:93–111, 1995.

W. Layton, C.C. Manica, M. Neda, M. Olshanskii, and L.G. Rebholz. On the accuracy of the rotation form in simulations of the Navier-Stokes-equations. *Journal of Computational Physics*, 228:3433–3447, 2009.

L. Lee. A class of high-resolution algorithms for incompressible flows. *Computers & Fluids*, 39:1022–1032, 2010.

K. Li and X. Qian. Isogeometric analysis and shape optimization via boundary integral. *Computer-Aided Design*, 43:1427–1437, 2011.

B. Mohammadi and O. Pironneau. Shape optimization in fluid mechanics. *Annual Review of Fluid Mechanics*, 36:255–279, 2004.

B. Mohammadi and O. Pironneau. *Applied Shape Optimization for Fluids*. Oxford Science Publications, second edition, 2010.

T. J. Mueller. On the birth of micro air vehicles. *International Journal of Micro Air Vehicles*, 1(1):1–12, 2009.

A. Nagy, M. Abdalla, and Z. Gürdal. Isogeometric sizing and shape optimization of beam structures. *Computer Methods in Applied Mechanics and Engineering*, 199:1216–1230, 2010a.

A. Nagy, M. Abdalla, and Z. Gürdal. On the variational formulation of stress constraints in isogeometric design. *Computer Methods in Applied Mechanics and Engineering*, 199:2687–2696, 2010b.

A. Nagy, M. Abdalla, and Z. Gürdal. Isogeometric design of elastic arches for maximum fundamental frequency. *Structural and Multidisciplinary Optimization*, 43:135–149, 2011.

D. M. Nguyen, A. Evgrafov, A. R. Gersborg, and J. Gravesen. Isogeometric shape optimization of vibrating membranes. *Computer Methods in Applied Mechanics and Engineering*, 200:1343–1353, 2011.

P. N. Nielsen and J. Gravesen. Isogeometric shape optimization for fluids, 2012. To be submitted to *Structural and Multidisciplinary Optimization*.

P. N. Nielsen, A. R. Gersborg, J. Gravesen, and N. L. Pedersen. Discretizations in isogeometric analysis of Navier-Stokes flow. *Computer Methods in Applied Mechanics and Engineering*, 200:3242–3253, 2011a.

P. N. Nielsen, J. Gravesen, and M. Willatzen. Isogeometric analysis of sound propagation through flow in 2-dimensional ducts, 2011b. Submitted to *Journal of Sound and Vibration*.

S. Painchaud-Oullet, C. Tribes, J.-Y. Trepanier, and D. Pelletier. Airfoil shape optimization using a nonuniform rational B-spline parametrization under thickness constraint. *IAAA Journal*, 44(10):2170–2178, 2006.

C. Peyret and G. Élias. Finite-element method to study harmonic aeroacoustics problems. *Journal of the Acoustical Society of America*, 110(2):661–668, 2001.

L. Piegl and W. Tiller. *The NURBS Book*. Springer, 1995. ISBN 3-540-55069-0.

O. Pironneau. On optimum profiles in Stokes flow. *Journal of Fluid Mechanics*, 59:117–128, 1973.

O. Pironneau. On optimum design in fluid mechanics. *Journal of Fluid Mechanics*, 64:97–110, 1974.

A. Pressley. *Elementary Differential Geometry*. Springer, 2001. ISBN 1-85233-152-6.

X. Qian. Full analytical sensitivities in NURBS based isogeometric shape optimization. *Computer Methods in Applied Mechanics and Engineering*, 199:2059–2071, 2010.

X. Qian and O. Sigmund. Isogeometric shape optimization of photonic crystals via Coons patches. *Computer Methods in Applied Mechanics and Engineering*, 200:2237–2255, 2011.

R. Rannacher. Finite element methods for the incompressible Navier-Stokes equations, 1995. `http://numerik.iwr.uni-heidelberg.de/Oberwolfach-Seminar/CFD-Course.pdf`. Accessed 1 February, 2012.

J.N. Reddy and D.K. Gartling. *The finite element method in heat transfer and fluid dynamics*. CRC Press, 2nd edition, 2001. ISBN 0-8493-2355-X.

E. Redon, A.-S. Bonnet-Ben Dhia, J.-F. Mercier, and S. Poernomo Pari. Non-reflecting boundary conditions for acoustic propagation in ducts with acoustic treatment and mean flow. *International Journal for Numerical Methods in Engineering*, 2011. doi: 10.1002/nme.3108.

Y.-D. Seo, H.-J. Kim, and S.-K. Youn. Shape optimization and its extension to topological design based on isogeometric analysis. *International Journal of Solids and Structures*, 47:1618–1640, 2010a.

Y.-D. Seo, H.-J. Kim, and S.-K. Youn. Isogeometric topology optimization using trimmed spline surfaces. *Computer Methods in Applied Mechanics and Engineering*, 199:3270–3296, 2010b.

H. Tanaka and R. J. Wood. Fabrication of corrugated artificial insect wings using laser micromachined molds. *Journal of Micromechanics and Microengineering*, 20:075008, 2010.

A.-V. Vuong, C. Giannelli, B. Jüttler, and B. Simeon. A hierarchical approach to adaptive local refinement in isogeometric analysis. *Computer Methods in Applied Mechanics and Engineering*, 200:3554–3567, 2011.

W.A. Wall, M.A. Frenzel, and C. Cyron. Isogeometric structural shape optimization. *Computer Methods in Applied Mechanics and Engineering*, 197: 2976–2988, 2008.

F. M. White. *Viscous Fluid Flow.* McGraw-Hill, 1974. ISBN 0-07-069710-8.

G. Xu, B. Mourrain, R. Duvigneau, and A. Galligo. Optimal analysis-aware parametrization of computational domain in isogeometric analysis. In B. Mourrain, S. Schaeffer, and G. Xu, editors, *Advances in Geometric Modeling and Processing*, pages 236–254. Springer, 2010.

Appendix A

Nomenclature

Symbol/Abbreviation	Description
NURBS	Non-uniform Rational B-spline
B-spline	Basis-spline
q, r	Polynomial degree
Ξ, Ψ	Knot vector
$\mathcal{N}, \mathcal{M}$	Univariate B-spline
$\mathcal{B}$	Univariate NURBS
$\mathcal{P}$	Bivariate B-spline
$\mathcal{R}$	Bivariate NURBS
$\boldsymbol{e}$	Unit basis vector
$\boldsymbol{X} = (x, y)$	Geometry/Parametrization
$\boldsymbol{x} = (x_1, \ldots, x_N)$	Control points
Re	Reynolds number
ρ	Fluid density
μ	Fluid viscosity
σ	Fluid shear stress tensor
$\boldsymbol{u} = (u_1, u_2) = (u, v)$	Fluid velocity
p	Fluid pressure
$\boldsymbol{f}$	Fluid body force
c	Speed of sound
f	Acoustic source
λ	Acoustic propagation constant

Appendix B

Paper I: Discretizations in Isogeometric Analysis of Navier-Stokes Flow

This chapter contains a preprint of: P. N. Nielsen, A. R. Gersborg, J. Gravesen, and N. L. Pedersen. Discretizations in isogeometric analysis of Navier-Stokes flow. *Computer Methods in Applied Mechanics and Engineering*, 200:3242–3253, 2011a.

Discretizations in Isogeometric Analysis of Navier-Stokes Flow

Peter Nørtoft Nielsen[a,b,*], Allan Roulund Gersborg[b,1], Jens Gravesen[a], Niels Leergaard Pedersen[b]

[a] *DTU Mathematics, Technical University of Denmark, Matematiktorvet 303S, DK-2800 Kgs. Lyngby, Denmark*
[b] *DTU Mechanical Engineering, Technical University of Denmark, Nils Koppels All 404, DK-2800 Kgs. Lyngby, Denmark*

Abstract

This paper deals with isogeometric analysis of the 2-dimensional, steady state, incompressible Navier-Stokes equation subjected to Dirichlet boundary conditions. We present a detailed description of the numerical method used to solve the boundary value problem. Numerical inf-sup stability tests for the simplified Stokes problem confirm the existence of many stable discretizations of the velocity and pressure spaces, and in particular show that stability may be achieved by means of knot refinement of the velocity space. Error convergence studies for the full Navier-Stokes problem show optimal convergence rates for this type of discretizations. Finally, a comparison of the results of the method to data from the literature for the the lid-driven square cavity for Reynolds numbers up to 10,000 serves as benchmarking of the discretizations and confirms the robustness of the method.

Keywords:
isogeometric analysis, fluid mechanics, Navier-Stokes flow, inf-sup stability, lid-driven square cavity

1. Introduction

Isogeometric analysis unites the power to solve complex engineering problems from finite element analysis (FEA) with the ability to smoothly represent complicated shapes in very few degrees of freedom from computer aided design (CAD) [1, 2]. Within recent years, isogeometric analysis has been applied to various flow problems and proved its value within the field of fluid mechanics. Some of the first studies were on steady-state incompressible Stokes flow in the benchmarking lid-driven square cavity [3]. Subsequent analysis of the full time dependent Navier-Stokes equations using the isogeometric method has shown its advantages both in terms of continuity of state variables [4] and the ability to accurately represent complicated dynamic flow domains [5]. Benchmarking of the method for the turbulent Taylor-Couette flow shows very nice performance of the method [6].

An important issue in the analysis of the mixed formulation of the governing equations for fluids is the stability of the element, or discretization, used to approximate the state variables. The first stable B-spline discretization for the Stokes problem was proposed in [3]. Recently, two more families of stable B-spline discretizations were identified in [7], thereby further emphasizing how easily high degrees of continuity may be achieved in isogeometric analysis. Mathematical proofs of the stability of a range of discretizations have very recently been made [8, 9].

The aim of this paper is threefold. Firstly, we wish to extend the list of stable B-spline discretizations for the 2D steady state, incompressible Stokes problem. Secondly, we wish apply the method to the non-linear 2D steady state, incompressible Navier-Stokes problem and examine how these discretizations perform in terms of error convergence based on a flow problem with an analytical solution. Finally, the benchmarking lid-driven square cavity will be analysed and the results of the discretizations compared to data from the literature.

The outline of the paper is as follows. Section 2 presents the equations that govern problems in fluid mechanics, and section 3 outlines how the problem is solved using isogeometric analysis. In section 4 we perform a numerically test of different isogeometric discretizations in terms of stability, and an error convergence study for these discretizations is presented in section 5. Finally in section 6, a comparison of the dis-

*Corresponding author.
Email addresses: p.n.nielsen@mat.dtu.dk (Peter Nørtoft Nielsen), agersborg.hansen@gmail.com (Allan Roulund Gersborg), j.gravesen@mat.dtu.dk (Jens Gravesen), nlp@mek.dtu.dk (Niels Leergaard Pedersen)
[1] Present address:Burmeister & Wain Energy A/S, Lundtoftegårdsvej 93A, DK-2800 Kgs. Lyngby, Denmark

cretizations against results from the literature is presented for the benchmarking lid-driven square cavity.

2. Boundary Value Problem

We consider a fluid contained in the domain Ω with boundary $\Gamma \equiv \partial\Omega$, see figure 1. We assume the fluid to be a viscous, incompressible, isothermal, Newtonian fluid, and we furthermore assume it to be stationary. The fluid is then governed by:

$$-\mu\Delta\boldsymbol{u} + \rho\boldsymbol{u}\cdot\nabla\boldsymbol{u} + \nabla p - \rho\boldsymbol{f} = 0 \qquad \text{in } \Omega \tag{1a}$$

$$\nabla\cdot\boldsymbol{u} = 0 \qquad \text{in } \Omega \tag{1b}$$

Equation (1a) is the the steady-state Navier-Stokes equation, expressing conservation of momentum for the fluid and written in the primitive variables p and $\boldsymbol{u}$, where p is pressure and $\boldsymbol{u} = (u_1, u_2)$ is the fluid velocity. The quantities ρ, μ and $\boldsymbol{f}$ denote the density, dynamic viscosity and additional body forces acting on the fluid, respectively. Equation (1b) is the incompressibility condition, and it expresses conservation of mass.

We assume the velocity $\boldsymbol{u}$ to be prescribed along the bondary Γ, and we take the mean pressure to be zero:

$$\boldsymbol{u} = \boldsymbol{u}_D \qquad \text{on } \Gamma \tag{1c}$$

$$\iint_\Omega p \,\mathrm{d}A = 0 \tag{1d}$$

where D in equation (1c) stands for Dirichlet. Other boundary conditions, such as Neumann boundary conditions, could also be considered but have been left out for simplicity.

Numerical methods for solving Navier-Stokes equation (1a) can employ different formulations of the equation. The main results of the present study are based on the *convective* formulation. Comparisons to the *skew-symmetric* formulation are also made, while the *rotational* formulation is left out to avoid the introduction of stabilization [10]. The two formulations differ in their treatment of the non-linear inertial term $\boldsymbol{u}\cdot\nabla\boldsymbol{u}$:

$$(\boldsymbol{u}\cdot\nabla)\boldsymbol{u} \quad \text{or} \quad (\boldsymbol{u}\cdot\nabla)\boldsymbol{u} + \frac{1}{2}\nabla\cdot\boldsymbol{u}. \tag{2}$$

Compared to the convective formulation, the skew-symmetric formulation additionally involves the divergence of the velocity field. Even though these formulations on a continous level are exactly equivalent, due to the incompressibility condition (1b), this is not the case on a discrete level, and therefore the numerical solutions might differ.

3. Isogeometric Method

Equations (1) together comprise the *strong form* of the boundary value problem that governs the state of the fluid. We use NURBS-based isogeometric analysis built on Galerkin's method to solve the problem numerically. This section outlines the procedure. See also [2, 11, 12].

3.1. Geometry Parametrisation

The physical domain Ω is parametrised using NURBS, Non-Uniform Rational B-splines. To make the text self-contained, we very briefly revise the basic concepts of B-splines and NURBS in the following. For a more in-depth treatment of this subject, we refer the reader to e.g. [13].

To define univariate B-splines we choose a polynomial degree $q \in \mathbb{N}$ and a knot vector $\Xi = \{\xi_1, \ldots, \xi_m\}$ with $\xi_i \in \mathbb{R}$ for $i = 1, \ldots, m$. For simplicity, we assume the parametric domain $\xi \in [0, 1]$, and that the knot vector is open such that the boundary knots have multiplicity $q + 1$ with $\xi_1 = \xi_2 = \ldots = \xi_{q+1} = 0$ and $\xi_m = \xi_{m-1} = \ldots = \xi_{m-q} = 1$. The univarite B-splines $\mathcal{N}_i^q : [0; 1] \to \mathbb{R}$ are defined recursively as

$$\mathcal{N}_i^0(\xi) = \begin{cases} 1 & \text{if } \xi_i \le \xi < \xi_{i+1} \\ 0 & \text{otherwise} \end{cases} \tag{3a}$$

for $q = 0$, and

$$\mathcal{N}_i^q(\xi) = \frac{\xi - \xi_i}{\xi_{i+q} - \xi_i}\mathcal{N}_i^{q-1}(\xi) + \frac{\xi_{i+q+1} - \xi}{\xi_{i+q+1} - \xi_{i+1}}\mathcal{N}_{i+1}^{q-1}(\xi) \tag{3b}$$

for $q = 1, 2, \ldots$.

The bivariate tensor product B-splines $\mathcal{P}_{i,j}^{q,r} : [0, 1]^2 \to \mathbb{R}$ are defined from two polynomial degrees q and r and two knot vectors $\Xi = \{\xi_1, \ldots, \xi_m\}$ and $\Phi = \{\phi_1, \ldots, \phi_n\}$:

$$\mathcal{P}_{i,j}^{q,r}(\xi_1, \xi_2) = \mathcal{N}_i^q(\xi_1)\mathcal{M}_j^r(\xi_2), \tag{4}$$

where $\mathcal{N}_i^q$ is the i^{th} univariate B-spline with degree q and knot vector Ξ in the first parametric dimension ξ_1 as defined in equation (3), and $\mathcal{M}_j^r$ is the j^{th} univariate B-spline with degree r and knot vector Φ in the second parametric dimension ξ_2.

The bivariate NURBS $\mathcal{R}_{i,j}^{q,r} : [0, 1]^2 \to \mathbb{R}$ are defined from the NM bivariate B-splines in equation (4) and the weights $W = \{w_{1,1}, \ldots, w_{N,M}\}$ with $w_{i,j} \in \mathbb{R}$ for $i = 1, \ldots, N$ and $j = 1, \ldots, M$:

$$\mathcal{R}_{i,j}^{q,r}(\xi_1, \xi_2) = \frac{w_{i,j}\mathcal{P}_{i,j}^{q,r}}{\sum_{k=1}^{N}\sum_{l=1}^{M} w_{k,l}\mathcal{P}_{k,l}^{q,r}} \tag{5}$$

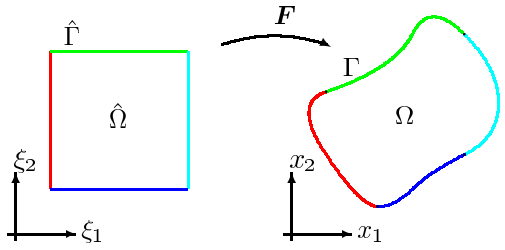

Figure 1: A single patch parametrisation of the fluid domain. Colors indicate how the boundary $\widehat{\Gamma}$ of the parameter domain $\widehat{\Omega}$ is mapped into the boundary Γ of the physical domain Ω.

With the basic concepts of B-splines and NURBS defined, we now make a single patch parametrisation of the fluid domain Ω, see figure 1. We take the parameter domain $\widehat{\Omega}$ as the unit square $(\xi_1, \xi_2) \in [0,1]^2$, and use the bivariate NURBS defined in equation (5). The parametrisation $\boldsymbol{F} : [0,1]^2 \to \mathbb{R}^2$ reads:

$$\begin{aligned}\boldsymbol{F}(\xi_1,\xi_2) &= (\ x_1(\xi_1,\xi_2),\ x_2(\xi_1,\xi_2)\ ) \\ &= \sum_{i=1}^{N}\sum_{j=1}^{M} \boldsymbol{d}_{i,j}\mathcal{R}_{i,j}^{q,r}(\xi_1,\xi_2),\end{aligned} \tag{6}$$

where $\boldsymbol{d}_k \in \mathbb{R}^2$ are the control points. By a simple reordering, we can write the above as

$$\boldsymbol{F}(\xi_1,\xi_2) = \sum_{i=1}^{N_{\text{var}}^g} \bar{\boldsymbol{x}}_i \mathcal{R}_i^g(\xi_1,\xi_2), \tag{7}$$

where $N_{\text{var}}^g = NM$ is the number of NURBS, $\bar{\boldsymbol{x}}_i$ are the reordered control points, and $\mathcal{R}_i^g$ are the reordered NURBS. The superscript g indicates that the NURBS functions refer to polynomial degrees, knots vectors and weights that are specific for the geometry representation.

3.2. Field Approximations

In a similar fashion as for the geometry representation in equation (7) above, we seek approximations of the velocity $\boldsymbol{u} : [0;1]^2 \to \mathbb{R}^2$ and pressure $p : [0;1]^2 \to \mathbb{R}$ as linear combinations of the basis functions defined above. Since NURBS are only needed to represent the geometry, and not the velocity and pressure, we will for simplicity use B-splines to approximate the state variables:

$$u_k(\xi_1,\xi_2) = \sum_{i=1}^{N_{\text{var}}^{u_k}} \underline{u}_{ki}\mathcal{P}_i^{u_k}(\xi_1,\xi_2), \tag{8a}$$

$$p(\xi_1,\xi_2) = \sum_{i=1}^{N_{\text{var}}^{p}} \underline{p}_i\mathcal{P}_i^{p}(\xi_1,\xi_2), \tag{8b}$$

where $k = 1,2$ in (8a) refers to the two components of the velocity field, $\mathcal{P}_i^{u_k}$ denote the B-spline basis functions for the kth component of the velocity field, while $\mathcal{P}_i^p$ similarly denote the B-spline basis functions for the pressure field, all suitably reordered compared to the definition in equation (4). They refer to separate sets of polynomial degrees and knot vectors that are in general not the same. $N_{\text{var}}^{u_k}$ and N_{var}^p are the number of velocity and pressure basis functions, while $\underline{u}_k$ and $\underline{p}$ are the unknown control variables for the velocity and pressure that are to be determined.

The velocity and pressure fields in equations (8) are defined in parameter space, while the governing equations (1) are formulated in physical space. To evaluate the fields in physical space, the inverse of the geometry parametrisation $\boldsymbol{F}$ is used; the pressure $p : \Omega \to \mathbb{R}$ over the physical domain is computed as $p \circ \boldsymbol{F}^{-1}$, and the velocity $\boldsymbol{u} : \Omega \to \mathbb{R}^2$ over the physical domain as $\boldsymbol{u} \circ \boldsymbol{F}^{-1}$. The Piola mapping could also be used to map the velocity [7], but since none of the examined discretizations are exactly divergent free, we take the simpler approach and map each velocity component as a scalar field. With abuse of notation, we use the same symbol for the state variables both in parameter space and in physical space. Gradients in parameter space, $\widehat{\nabla} p = \left[\frac{\partial p}{\partial \xi_1}\ \frac{\partial p}{\partial \xi_2}\right]^T$, are easily evaluated using the field approximations in equation (8) and the definition of B-splines in equation (4). Gradients in physical space, $\nabla p = \left[\frac{\partial p}{\partial x_1}\ \frac{\partial p}{\partial x_2}\right]^T$, are related to the gradients in parameter space by the formula:

$$\widehat{\nabla} p = \boldsymbol{J}^T \nabla p \iff \nabla p = \boldsymbol{J}^{-T}\widehat{\nabla} p, \tag{9}$$

where $\boldsymbol{J}$ is the Jacobian matrix of the geometry parametrisation:

$$\boldsymbol{J} = \begin{bmatrix} \frac{\partial x_1}{\partial \xi_1} & \frac{\partial x_1}{\partial \xi_2} \\ \frac{\partial x_2}{\partial \xi_1} & \frac{\partial x_2}{\partial \xi_2} \end{bmatrix}, \tag{10}$$

which again is easily evaluated using the mapping in equation (7) and the definitions of NURBS in equation (5).

3.3. Boundary Conditions

For simplicity we impose the Dirichlet boundary conditions in (1c) *strongly* as opposed to the weak enforcement suggested in [14, 15]. Hereby we avoid the need

for definition of penalization parameters which is favorable if a sequence of analysis with different geometries is to performed as in shape optimization problems [16].

In general B-splines have compact support. This means that only a few of the velocity basis functions $\mathcal{P}_i^{u_k}$ in equation (8a) have support on Γ. We can simply arrange the functions $\mathcal{P}^{u_k}$ so that the first $N_{\text{dof}}^{u_k}$ of these do *not* have support on the boundary, and the corresponding control variables of these are thus "degrees of freedom", while the last $N_{\text{fix}}^{u_k} = N_{\text{var}}^{u_k} - N_{\text{dof}}^{u_k}$ *have* support on Γ, and the corresponding control variables are thus "fixed":

$$u_k(\xi_1,\xi_2) = \sum_{i=1}^{N_{\text{dof}}^{u_k}} \underline{u}_{ki}\mathcal{P}_i^{u_k}(\xi_1,\xi_2) + \sum_{i=N_{\text{dof}}^{u_k}+1}^{N_{\text{var}}^{u_k}} \underline{u}_{ki}\mathcal{P}_i^{u_k}(\xi_1,\xi_2). \quad (11)$$

The strong imposition is done by directly specifying suitable values for these last $N_{\text{fix}}^{u_k}$ velocity control variables $\underline{u}_{ki}$, so that the sum in equation (8a) approximates the specified value $\boldsymbol{u}_D$ in (1c). If $\boldsymbol{u}_D$ lies within the function space spanned by $\mathcal{P}_i^{u_k}$, the conditions are satisfied exactly; otherwise they are only satisified in a least square sense.

For the pressure, we note that only the pressure *gradient* appears in the Navier-Stokes equation (1a). The pressure is thus only determined up to an arbitrary constant, which is dealt with by the specification of the mean pressure in equation (1d). Using the approximation in equation (8b), this gives rise to the following equation:

$$\begin{aligned} 0 &= \iint_\Omega p \,\mathrm{d}A = \iint_\Omega \sum_{i=1}^{N_{\text{var}}^p} \underline{p}_i \mathcal{P}_i^p(x_1,x_2)\,\mathrm{d}x_1\,\mathrm{d}x_2 \\ &= \sum_{i=1}^{N_{\text{var}}^p} \underline{p}_i \int_0^1\int_0^1 \mathcal{P}_i^p(\xi_1,\xi_2)\det(\boldsymbol{J})\,\mathrm{d}\xi_1\,\mathrm{d}\xi_2 = \underline{\boldsymbol{p}}\boldsymbol{M}^T, \end{aligned} \quad (12)$$

where $\underline{\boldsymbol{p}}$ is the vector of pressure control variables, $\boldsymbol{M}$ the vector of integrals of pressure basis functions, and $\boldsymbol{J}$ is given by (10). Since no pressure control variables needs to be fixed, we have $N_{\text{dof}}^p = N_{\text{var}}^p$ and $N_{\text{fix}}^p = 0$.

3.4. Weak Form of the Governing Equations

The governing equations (1) are cast into their *weak*, or *variational*, form. For this we use the (image in physical space of the) B-spline introduced above as *weight functions* for the governing equations. We will use only the first $N_{\text{dof}}^{u_k}$ velocity basis functions, since these have no support on the fixed boundary. We multiply the kth component of the Navier-Stokes equation (1a) by an arbitrary weight function $\mathcal{P}_i^{u_k}$ among these velocity basis functions, and the incompressibility equation (1b) by an arbitrary weight function $\mathcal{P}_j^p$ among the pressure basis functions, integrate the resulting equations over Ω, and then simplify using integration by parts. After some manipulations we find the following weak form of the governing equations:

$$\begin{aligned} 0 = \iint_\Omega \Big(&(\mu\nabla\mathcal{P}_i^{u_k} + \rho\mathcal{P}_i^{u_k}\boldsymbol{u})\cdot\nabla u_k \\ &- (p\nabla\mathcal{P}_i^{u_k} + \rho\mathcal{P}_i^{u_k}\boldsymbol{f})\cdot\boldsymbol{e}_k\Big)\,\mathrm{d}x_1\,\mathrm{d}x_2 \end{aligned} \quad (13a)$$

$$0 = \iint_\Omega \mathcal{P}_j^p\,(\nabla\cdot\boldsymbol{u})\,\mathrm{d}x_1\,\mathrm{d}x_2 \quad (13b)$$

for $k = 1,2$, $i = 1,\ldots,N_{\text{dof}}^{u_k}$ and $j = 1,\ldots,N_{\text{dof}}^p$, and where $\boldsymbol{e}_k$ is the k^{th} unit vector.

3.5. Matrix Equation

Finally, we insert the (image in physical space of the) approximations of the velocity and pressure fields (8) into the weak form (13) of the governing equations, split the superpositions of $\boldsymbol{u}$ into parts with support on the fixed boundary and parts without as in equation (11), exchange the order of summation and integration, rearrange to get the unknown terms on the LHS and the known terms on the RHS, and pull the integration back to parameter space using standard transformation rules for multiple integrals along with equation (9). This gives:

$$\begin{aligned} &\overbrace{\begin{bmatrix} \boldsymbol{K}_1+\boldsymbol{C}_1(\bar{\boldsymbol{u}}) & \boldsymbol{0} & -\boldsymbol{G}_1^T \\ \boldsymbol{0} & \boldsymbol{K}_2+\boldsymbol{C}_2(\bar{\boldsymbol{u}}) & -\boldsymbol{G}_2^T \\ \boldsymbol{G}_1 & \boldsymbol{G}_2 & \boldsymbol{0} \end{bmatrix}}^{\overline{\boldsymbol{M}}(\overline{U})} \overbrace{\begin{bmatrix} \bar{\boldsymbol{u}}_1 \\ \bar{\boldsymbol{u}}_2 \\ \bar{\boldsymbol{p}} \end{bmatrix}}^{\overline{U}} \\ &= \underbrace{\begin{bmatrix} \boldsymbol{f}_1 \\ \boldsymbol{f}_2 \\ \boldsymbol{0} \end{bmatrix} - \begin{bmatrix} \boldsymbol{K}_1^\star+\boldsymbol{C}_1^\star(\bar{\boldsymbol{u}}) & \boldsymbol{0} \\ \boldsymbol{0} & \boldsymbol{K}_2^\star+\boldsymbol{C}_2^\star(\bar{\boldsymbol{u}}) \\ \boldsymbol{G}_1^\star & \boldsymbol{G}_2^\star \end{bmatrix} \begin{bmatrix} \bar{\boldsymbol{u}}_1^\star \\ \bar{\boldsymbol{u}}_2^\star \end{bmatrix}}_{\overline{\boldsymbol{F}}}, \end{aligned} \quad (14)$$

or simply $\overline{\boldsymbol{M}}(\overline{\boldsymbol{U}})\,\overline{\boldsymbol{U}} = \overline{\boldsymbol{F}}$, with

$$\underline{K}_{ijk} = \mu \int_0^1\int_0^1 \left(\boldsymbol{J}^{-T}\nabla\mathcal{P}_i^{u_k}\right)\cdot\left(\boldsymbol{J}^{-T}\nabla\mathcal{P}_j^{u_k}\right)\det(\boldsymbol{J})\,\mathrm{d}\xi_1\,\mathrm{d}\xi_2, \tag{15a}$$

$$\underline{C}_{ijk}(\underline{\boldsymbol{u}}) = \rho \int_0^1\int_0^1 \mathcal{P}_i^{u_k}\left(\boldsymbol{u}(\underline{\boldsymbol{u}}_l)\cdot(\boldsymbol{J}^{-T}\nabla\mathcal{P}_j^{u_k})\right)\det(\boldsymbol{J})\,\mathrm{d}\xi_1\,\mathrm{d}\xi_2, \tag{15b}$$

$$\underline{G}_{ijk} = \int_0^1\int_0^1 \mathcal{P}_i^{p}\left(\boldsymbol{J}^{-T}\nabla\mathcal{P}_j^{u_k}\right)\cdot\boldsymbol{e}_k\det(\boldsymbol{J})\,\mathrm{d}\xi_1\,\mathrm{d}\xi_2, \tag{15c}$$

$$f_{ik} = \rho \int_0^1\int_0^1 \mathcal{P}_i^{u_k}\left(\boldsymbol{f}\cdot\boldsymbol{e}_k\right)\det(\boldsymbol{J})\,\mathrm{d}\xi_1\,\mathrm{d}\xi_2, \tag{15d}$$

$$\underline{\boldsymbol{K}}_k = \begin{bmatrix} \boldsymbol{K}_k & \boldsymbol{K}_k^{\star} \end{bmatrix} \quad \left(N_{\mathrm{dof}}^{u_k}\times(N_{\mathrm{dof}}^{u_k}+N_{\mathrm{fix}}^{u_k})\right), \tag{15e}$$

$$\underline{\boldsymbol{C}}_k(\underline{\boldsymbol{u}}) = \begin{bmatrix} \boldsymbol{C}_k(\underline{\boldsymbol{u}}) & \boldsymbol{C}_k^{\star}(\underline{\boldsymbol{u}}) \end{bmatrix} \quad \left(N_{\mathrm{dof}}^{u_k}\times(N_{\mathrm{dof}}^{u_k}+N_{\mathrm{fix}}^{u_k})\right), \tag{15f}$$

$$\underline{\boldsymbol{G}}_k = \begin{bmatrix} \boldsymbol{G}_k & \boldsymbol{G}_k^{\star} \end{bmatrix} \quad \left(N_{\mathrm{dof}}^{p}\times(N_{\mathrm{dof}}^{u_k}+N_{\mathrm{fix}}^{u_k})\right), \tag{15g}$$

where $k = 1, 2$, $\boldsymbol{J}$ is the Jacobian matrix in equation (10), $\boldsymbol{u}(\underline{\boldsymbol{u}})$ is given by the approximation in equation (8), $\boldsymbol{e}_k$ is the k^{th} unit vector, $\underline{\boldsymbol{u}}_k^T = [\overline{\boldsymbol{u}}_k^T\,\overline{\boldsymbol{u}}_k^{\star T}]$, and all starred quantities are given by the boundary conditions. $\boldsymbol{K}_k$ is often called viscosity matrix, $\boldsymbol{C}_k$ convective matrix, $\boldsymbol{G}_k$ gradient matrix, and $\boldsymbol{f}_k$ force vector.

The integrals in equation (15) are evaluated using Gaussian quadrature. The necessary number of quadrature points N_G in each knot span is estimated from the relation $\tilde{q} = 2N_G - 1$, where $\tilde{q}$ is an estimate of the highest polynomial degree of the integrands. Since the integrands are in general rational functions, we simply estimate $\tilde{q}$ as the sum of polynomial degrees of the numerator and the denominator. Using polynomial degree 2 for the geometry and 4 for the velocity and pressure, we estimate a polynomial degree of $\tilde{q} = 12$ for the integrand of $\boldsymbol{C}$, and this dictates that we should use at least $N_G = 7$ quadrature points in each knot span. All results in the following are based on 7 quadrature points per knot span, which is a conservative choice compared to recent studies on more efficient quadrature rules [17].

We need to solve $N_{\mathrm{dof}}^{u_1} + N_{\mathrm{dof}}^{u_2} + N_{\mathrm{dof}}^{p}$ equations from (14) supplemented by the equation from the condition on the mean pressure from (12) in $N_{\mathrm{dof}}^{u_1} + N_{\mathrm{dof}}^{u_2} + N_{\mathrm{dof}}^{p}$ unknowns, and we do this in the least square sense. The problem is non-linear, and an incremental Newton-Raphson method is used by gradually increasing Re, see e.g. [11].

4. Stability for Stokes Problem:Wall-Driven Anullar Cavity

In the following section, we deal with the stability of the isogeometric method when applied to Stokes flow, which is the problem that arises when we neglect the non-linear inertial term in Navier-Stokes equation (1a). Some discretizations of the mixed formulation of Stokes problem are stable while others are unstable. Unstable discretizations can leave the system matrix $\overline{\boldsymbol{M}}$ in equation (14) singular or badly scaled, which in turn leads to spurious, unphysical oscillations for the pressure field, while the velocity field may still look quite reasonable. Figure 3 below shows an example of this. Furthermore, it deteriorates the convergence properties of the method and thus prohibits iterative solutions for the full Navier-Stokes problem. In order for a given discretization to be stable, it needs to satisfy the socalled inf-sup condition, also known as the BB or LBB condition:

$$\inf_{p}\sup_{\boldsymbol{u}} \frac{\int\int_{\Omega} p\nabla\cdot\boldsymbol{u}\,\mathrm{d}A}{||p||\;||\boldsymbol{u}||} \geq \beta > 0, \tag{16}$$

where the positive constant β is independent of the mesh. In equation (16), the norm of p is the L^2-norm, while the norm of $\boldsymbol{u}$ is the H^1-norm.

In this section we study how stable discretizations may be constructed by using different basis functions for the velocity and pressure fields. More specifically, we will establish suitable choices of polynomial degrees and knot vectors for the velocity and pressure such that the discretizations are stable. This idea follows the approach in a recent work [7], in which three families of stable discretizations were presented, but contrasts to the stabilized method in which identical basis functions for the velocity and pressure may be used on the cost that stabilizing terms must be added to the Stokes equation, see e.g. [3].

We report the stability of the isogeometric discretizations listed in table 1. The discretizations differ in polynomial degrees, knot refinements and inner knot multiplicities between the velocity and pressure representations. We have adobted a heuristic nomenclature for naming of the individual discretizations. For the $\mathbf{u}4_0^2\mathrm{p}3_0^1$ discretization (d), e.g., both velocity components are approximated using quartic B-splines (**u**4), and the pressure using cubic B-splines (p3). Superscript indicates the multiplicity of inner knots, and thus also the degree of continuity across knots, since this is just the degree minus the multiplicity. Subscript indicates the number of h-refinements by halfing all knot spans. For the strategies a-g, each of the velocity componenents u_1 and

	Name	Knot Vector 1	Knot Vector 2	inf-sup
a	$\mathbf{u}4^1_1\mathrm{p}4^1_0$	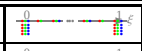	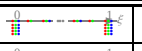	√
b	$\mathbf{u}4^2_0\mathrm{p}4^1_0$	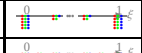	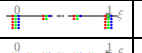	√
c	$\mathbf{u}4^1_1\mathrm{p}3^1_0$	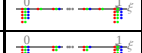	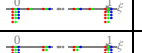	√
d	$\mathbf{u}4^2_0\mathrm{p}3^1_0$	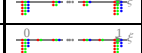	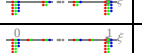	√
e	$\mathbf{u}4^1_1\mathrm{p}2^1_0$	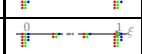	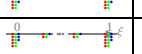	√
f	$\mathbf{u}4^2_0\mathrm{p}2^1_0$	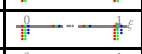	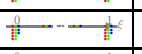	√
g	$\mathbf{u}4^1_0\mathrm{p}2^1_0$	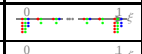	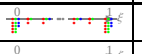	÷
h	Nédélec	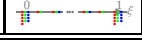	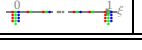	√
i	Raviart-Thomas	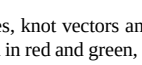	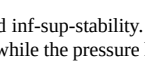	√

Table 1: Discretization names, knot vectors and inf-sup-stability. Velocity knot vectors are shown in red and green, while the pressure knot vector is shown in blue.

u_2 are represented identically, which reduces the computational expenses since equality of the basis functions $\mathcal{R}_i^{u_1} = \mathcal{R}_i^{u_2}$ implies equality of the matrices $K_{ij1} = K_{ij2}$, and in addition all fields are represented identically in both parametric directions. This is not the case for the strategies h and i, which are modified versions of the Nédélec and Raviart-Thomas elements presented in [7]. Compared to the original formulation in [7], the velocity fields have been *h*-refined once. It should be stressed that with this enlargement of the velocity space, the exact fulfillment of the divergence-free constraint for the Raviart-Thomas discretization is lost. The $\mathbf{u}4^2_0\mathrm{p}3^1_0$ discretization (d) was originally proposed in [3] and subsequently introduced in [7] as the Taylor-Hood element.

To examine the numerical stability, we consider the wall-driven annular cavity problem outlined in figure 2**a**. This is a slight modification of the standard benchmark *lid*-driven *square* cavity problem, see the treatment of the problem in Section 6, utilizing the capability of isogeometric analysis to exactly represent circular arcs. The fluid is contained in an annular cavity. The inner circular wall moves with constant tangential speed, while the remaining three walls are at rest. The velocity field is specified along the boundary of the domain, assuming no-slip conditions. No body forces act upon the fluid, and the fluid motion is thus caused—or driven—by the moving wall. We adopt the so-called *leaky-lid* boundary condition, meaning that the corners $(x, y) = (0, 1)$ and $(x, y) = (1, 0)$ belong to the moving wall boundary. We parametrise the domain using quadratic NURBS. The control net is shown in figure 2**b**, and the data for the geometry parametrisation are

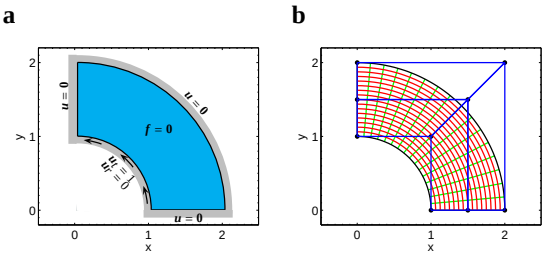

Figure 2: Driven annular cavity. **a**: Domain and boundary conditions. **b**: Control net (black dots and blue lines) and image of the computational mesh for velocity and pressure (red and green lines).

listed in table A.2 in Appendix Appendix A. For the velocity and pressure representation, we *h*-refine the parameter mesh for the geometry by halfing the knot spans, leading to a familiy of parameter meshes ranging from 2×2 to 64×64 knot spans, one of which is also depicted in figure 2**b**.

Figure 3 shows the computed velocity and pressure fields for two different discretizations, namely the $\mathbf{u}4^1_0\mathrm{p}4^1_0$ discretization (top row) and the $\mathbf{u}4^1_1\mathrm{p}4^1_0$ discretization (bottom row). Both of these produce a reasonable, rotational flow field. Clear pressure oscillations, however, are seen for first discretization, whereas the latter nicely approximates the pressure singularitites in the inner corners.

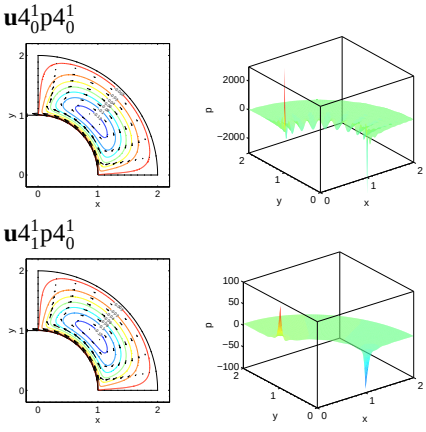

Figure 3: Computed fields for $\mathbf{u}4^1_0\mathrm{p}4^1_0$ (top) and $\mathbf{u}4^1_1\mathrm{p}4^1_0$ (bottom) discretizations. Left: stream function contour lines and velocity arrows. Right: pressure (note the different vertical scalings).

To test the stability of the discretization strategies, we use the approach described in [18, 19]. For each discretization, we vary the grid size for the velocity and

pressure representations, and for each of these meshes we determine a numerical estimate of the inf-sup "constant" β in equation (16). If this value does not change appreciably with varying grid size, it indicates that the discretization is stable. On the other hand, if the value tends to zero as the grid size changes, it indicates that the discretization is *un*stable.

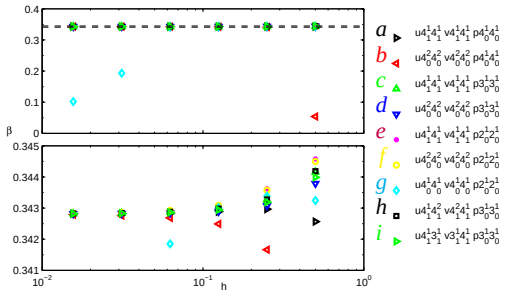

Figure 4: Numerically computed inf-sup "constants" for varying grid size using different discretizations. The bottom plot shows an enlargement of the top plot as marked by the dashed lines.

The results of these computations are shown in figure 4. From this we are led to conclude, that the discretization with identical polynomial degree for velocity and pressure is stable if either the velocity knot vector is refined (a) or the inner knot multiplicity for the velocity is increased (b). The same conclusion applies to the discretizations for which the polynomial degree of the velocity is larger than the polynomial degree of the pressure by one (c and d) and two (e and f). The stability of $\mathbf{u}4_0^2\mathrm{p}3_0^1$ (d) was already known from [7]. Both the modified Nédélec (h) and Raviart-Thomas (i) discretizations are seen to be stable, whereas the simple discretization $\mathbf{u}4_0^1\mathrm{p}2_0^1$ (g) with a difference in polynomial degree of two but with identical inner knots does *not* pass the stability test. The stability of each of the discretizations is summarized in the right-most column of table 1.

Several discretizations have been tested in addition to those listed in table 1. It was found that increasing the difference between the polynomial degree of the velocity approximation and the degree of the pressure approximation does influence the inf-sup stability, even without inserting or repeating knots. More specifically, the value of grid size h where the inf-sup "constant" β starts decreasing seemed to decrease with increasing polynomial degrees.

Assuming that the examined discretizations are representative, two simple strategies for choosing stable discretizations for the velocity and pressure approximations can be established by means of induction. Given a simple discretization for the pressure, i.e. open knot vectors, choose the velocity degrees at least equal to the pressure degree and then either take the velocity knot vectors as the refinement of the pressure knot vectors, or use the pressure knot vectors with all inner knots repeated. Or conversely, given simple discretizations for the velocity, i.e. with open knot vectors and single or double inner knots, choose the pressure degree less than or equal to the velocity degree, and take the pressure knot vectors as the velocity knot vectors with every 2nd inner knot removed. The knot refinement strategy is used for the cases a, c and e, and the knot repetition strategy for cases b, d and f. The modified Raviart-Thomas (i) also uses the refinement strategy, while the modified Nédélec (h) combines both strategies.

We should emphasize firstly that the presented inf-sup method only serves as a numerical test of the stability of the examined discretizations, and secondly that the inductive step, going from the stability of the examined discretizations to the stability of a general discretization strategy, is only motivated by a limited number of tests. None of these should in no way be mistaken for a rigorous mathematical proof.

5. Error Convergence: Forced Elliptic Cavity

To asses the validity of the isogeometric method for the full Navier-Stokes problem, we consider a test case for which an analytical solution exists, and examine how well the discretizations listed in table 1 are able to reproduce the exact solution.

The problem is outlined in figure 5**a**. We take the physical domain Ω as the elliptic disk $\{(x_1, x_2) \in \mathbb{R}^2 \mid (x_1/a)^2 + (x_2/b)^2 \leq 1\}$ with $a = 2$ and $b = 1$. Assuming appropriate units are assigned to all quantities and focussing only on their numerical values, we set $\rho = \mu = 1$, take the body force $\boldsymbol{f} = (f_1, f_2)$ to be

$$
\begin{aligned}
f_1 &= -\frac{1}{4}U^2 \sin^2\left(\pi\tilde{r}^2\right) x - \frac{1}{4}\frac{\pi}{\tilde{r}} \sin\left(\pi\tilde{r}\right) x + \frac{13}{2}\pi U \cos\left(\pi\tilde{r}^2\right) y \\
&\quad - 4\pi^2 U \sin\left(\pi\tilde{r}^2\right) y^3 - \frac{1}{4}\pi^2 U \sin\left(\pi\tilde{r}^2\right) x^2 y \\
f_2 &= -\frac{1}{4}U^2 \sin^2\left(\pi\tilde{r}^2\right) y - \frac{\pi}{\tilde{r}} \sin\left(\pi\tilde{r}\right) y - \frac{7}{8}\pi U \cos\left(\pi\tilde{r}^2\right) x \\
&\quad + \frac{1}{16}\pi^2 U \sin\left(\pi\tilde{r}^2\right) x^3 + \pi^2 U \sin\left(\pi\tilde{r}^2\right) y^2 x,
\end{aligned}
$$

where $\tilde{r} = \tilde{r}(x, y) = \sqrt{(x/2)^2 + y^2}$, and assume no-slip boundary conditions: $\boldsymbol{u} = \boldsymbol{0}$ on Γ. The following velocity and pressure fields solve the governing equations

and satisfy the boundary conditions:

$$u_1^\star = -U \sin(\pi \tilde{r}^2)\, y,$$
$$u_2^\star = \frac{1}{4} U \sin(\pi \tilde{r}^2)\, x,$$
$$p^\star = \frac{4}{\pi^2} + \cos(\pi \tilde{r}),$$

where U is a velocity scale which in the following is assumed to be $U = 200/\sqrt{5}$. These fields are depicted in figure 5**b-c**. Using $L = \sqrt{a^2 + b^2} = \sqrt{5}$ as length scale, the Reynolds number for the problem is $Re = 200$ which makes the problem weakly nonlinear. We parametrise

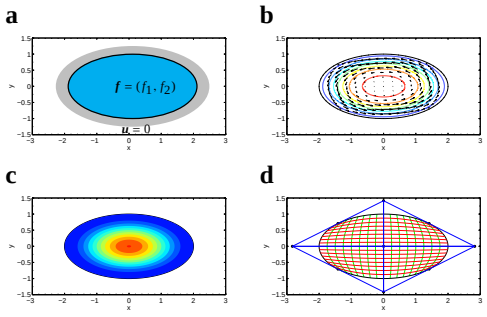

Figure 5: Forced elliptic cavity. **a**: Domain and boundary conditions. **b**: Analytical stream function contour lines and velocity arrows. **c**: Analytical pressure contour lines. **d**: Control net (black dots and blue lines) and image of the coarsest computational mesh for velocity and pressure (red and green lines).

the domain using quadratic NURBS. The control net and the coarsest computational mesh for the velocity and pressure fields are shown in figure 5**d**.

We examine how well the exact velocity and pressure fields are reproduced by a given discretization as the computational parameter mesh is *h*-refined by knot insertion. For each discretization we uniformly vary the computational mesh for velocity and pressure in the range from 4×4 to 64×64 knot spans, and for each of these meshes we compute the L^2-norm and the H^1-seminorm of the velocity residual and the pressure residual as measures of the error:

$$\epsilon_u^2 = \int_\Omega \int \|\boldsymbol{u}(x_1, x_2) - \boldsymbol{u}^\star(x_1, x_2)\|^2 \mathrm{d}x_1 \mathrm{d}x_2,$$
$$\epsilon_p^2 = \int_\Omega \int |p(x_1, x_2) - p^\star(x_1, x_2)|^2 \mathrm{d}x_1 \mathrm{d}x_2,$$
$$\epsilon_{\nabla u}^2 = \int_\Omega \int \sum_{k=1}^{2} \|\nabla u_k(x_1, x_2) - \nabla u_k^\star(x_1, x_2)\|^2 \mathrm{d}x_1 \mathrm{d}x_2,$$
$$\epsilon_{\nabla p}^2 = \int_\Omega \int \|\nabla p(x_1, x_2) - \nabla p^\star(x_1, x_2)\|^2 \mathrm{d}x_1 \mathrm{d}x_2.$$

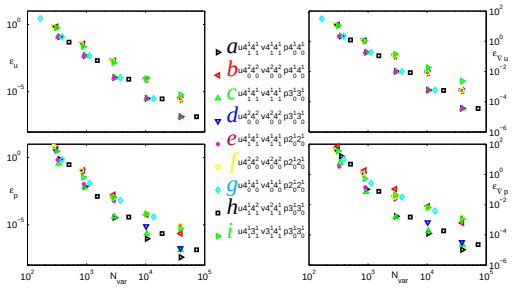

Figure 6: Convergence of error: L^2-norm (left) and H^1-seminorm (right) of velocity residual (top) and pressure residual (bottom) as function of the total number of variables of the analysis using different discretizations.

The results are shown in figure 6. The figure depicts the velocity error (top) and pressure error (bottom) as function of the total number of variables of the analysis, using both the L^2-norm (left) and the H^1-seminorm (right). We note that the discretizations a-f which pairwise have identical polynomial degrees, the knot refinement strategies (a, c, e) have a significantly lower velocity error than the knot repetion strategies (b, d, f). In addition, the difference between the two strategies grows as the number of degrees of fredoom increases, as is most evident for the H^1-seminorm. The difference in pressure error between the two strategies varies more, but the error of the knot refinement strategy is never larger than the error of the corresponding knot repetion strategy. This make the knot refinement strategy favorable in a per-degree-of-freedom sense. The knot refinement strategy, unlike the knot repetition strategy, conserves the degree of continuity for the velocity field. This therefore confirms the high importance of continuity alluded to in [4]. However, although the increase in number of degrees of freedom for a given refinement is nearly identical for the two strategies, the knot refinement strategy is computationally more expensive than

the knot repetition strategy, since it doubles the number of knot spans and thus quadruples the number of function evaluations needed for the Gaussian quadrature, unless more efficient quadrature rules are employed [17]. It is also worth noting that although the pressure error of the unstable discretization $\mathbf{u}4_0^1\mathrm{p}2_0^1$ (g) flattens out quit quickly as the number of degrees of freedom increases, the velocity error falls off impressively. Lastly, the modified Raviart-Thomas discretization (h) seem to perform somewhat better than the modified Nédélec discretization (i) for both the velocity and the pressure.

We have in general good experiences with the Taylor-Hood discretization $\mathbf{u}4_0^2\mathrm{p}3_0^1$ (d), since it discretizes both velocity components identically, and the knot spans for the velocity and pressure fields are also the same. We therefore base the following examination of the influence of the formulations of the Navier-Stokes equation on this discretization. We solve the problem outlined above using both the convective formulation as above and the skew-symmetric formulation, and we do this for two different values of the Reynolds number, namely 200 and 2,000, using {400; 800; 1,000; 1,500} as intermediate values to ensure convergence. Figure 7 compares the convergence of errors for the two formulations. For the low Reynolds number, both the velocity

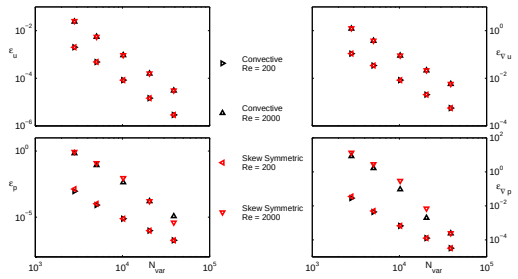

Figure 7: Convergence of error: L^2-norm (left) and H^1-seminorm (right) of velocity residual (top) and pressure residual (bottom) as function of the total number of variables of the analysis for different formulations and Reynolds numbers using the discretization $\mathbf{u}4_0^2\mathrm{p}3_0^1$ (d).

and the pressure errors of the two formulations are practically identical. For the higher Reynolds number, some differences are seen for the pressure error, while the velocity errors remain similar. It should also be mentioned that in our experience, more non-linear solver iterations are needed for the skew-symmetric formulation to converge compared to the convective formulation.

6. Benchmark: Lid-Driven Square Cavity

As a final validation of the isogeometric method, we compare our results for a standard benchmark flow problem, namely the lid-driven square cavity [12, 3], against results from other numerical simulations [20, 21, 22]. We consider a fluid contained in a square cavity with the top wall moving with constant speed, and the other walls kept still as outlined in figure 8**a**. This prescribes the velocity field along the boundary of the domain, assuming no-slip conditions at the walls and closed-lid conditions ($\boldsymbol{u} = \mathbf{0}$) at the upper corners. No body forces act upon the fluid; the fluid is set in motion from the movement of the lid. We parametrise the domain using linear NURBS, and construct a stretched computational mesh with increased resolution around the corner singularities and boundary regions, see figure 8**b**. For the analysis, a computational grid of 64×64 regularly spaced knot spans is employed.

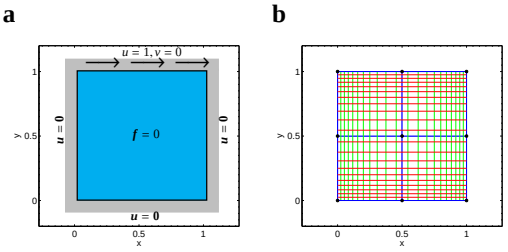

Figure 8: Lid-driven square cavity. **a**: Domain and boundary conditions. **b**: Control net (black dots and blue lines) and image of regularly spaced isoparametric lines (red and green lines).

Using the isogeometric discretizations listed in table 1 we firstly solve the problem for Reynolds number $Re = 5{,}000$. We gradually increase Re, and the number of intermediate steps in Re necessary to achieve convergence for $Re = 5{,}000$ is around five, but is in general different for the various discretizations. The total number of basis functions for the analysis ranges from 13,604 for the discretization $\mathbf{u}4_0^1\mathrm{p}2_0^1$ (g) to 72,865 for the Nédélec discretization (h), while the remaining discretizations all have between 38,678 and 39,472 analysis basis functions. Figure 9 compares the computed horizontal/vertical velocity profiles through the vertical/horizontal center line of the cavity to the data from [20]. On the left, the velocity profiles for all nine discretizations are seen to match very well with the data in [20]. On the right, the velocity residuals reveal that all discretizations yield slightly larger fluid speeds away from the center and towards the boundaries compared

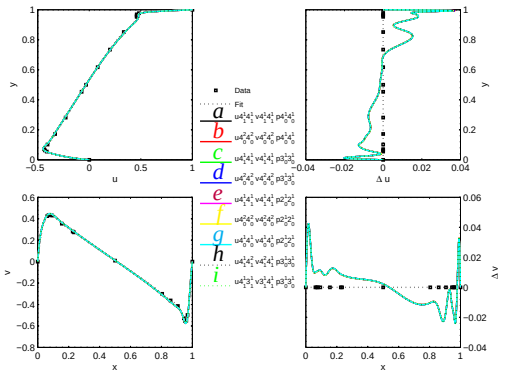

Figure 9: Comparison of velocity profile curves and residual curves (velocity minus fit) for the lid-driven square cavity for Re = 5,000 using different discretizations, plotted with data from [20] and a fit to the data using a cubic spline. Top: horizontal velocity profiles (left) and residuals (right) through the vertical center line. Bottom: vertical velocity profiles (left) and residuals (right) through the horizontal center line.

to the data. The agreement between the discretizations, however, is very good.

In the following, we once again focus on the discretization $\mathbf{u}4_0^2\mathrm{p}3_0^1$ (d). Figure 10 shows velocity vectors and stream function contour lines for Re = 5,000. The

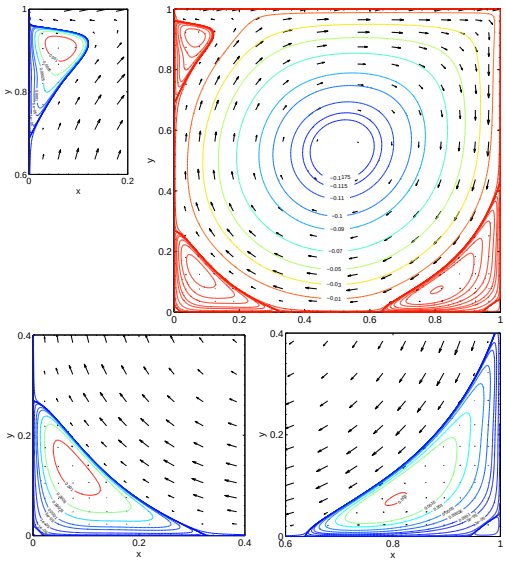

Figure 10: Four views of velocity vectors and stream function contour lines in the lid-driven square cavity for Re = 5,000 using the $\mathbf{u}4_0^2\mathrm{p}3_0^1$ discretization (d).

general pattern of the stream function matches very well with the results of [20], [21] and [22]. The locations and the extremal values of both the central main eddy as well as the minor eddies in the bottom right, bottom left and top left corners are in overall agreement. Small discrepencies are still seen, e.g. close to the boundary in the top left corner.

Finally, the problem is solved for different values of Re in the range from 100 to 10,000: {*100*; *400*; *1,000*; 2,000; *3,200*; *5,000*; *7,500*; *10,000*}. Figure 11**a/b** shows the computed horizontal/vertical velocity profiles through the vertical/horizontal center line of the cavity along with the data from [20] for the values of Re printed in italic. In general, the velocity profiles from

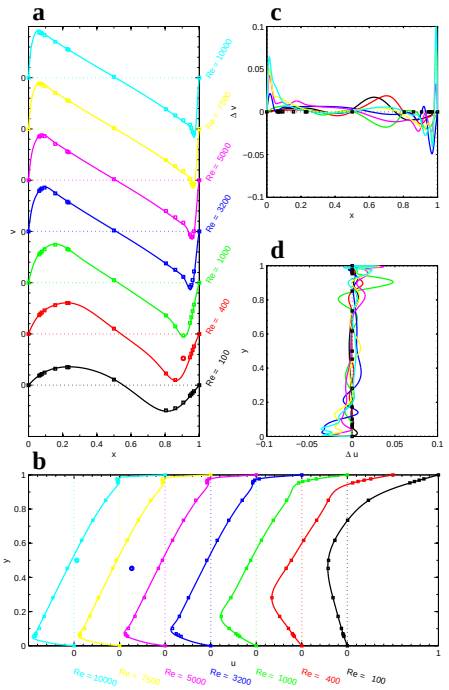

Figure 11: Velocity profile curves for the lid-driven square cavity for seven values of Re (solid lines) using the $\mathbf{u}4_0^2\mathrm{p}3_0^1$ discretization (d) plotted along with data from [20] (points). **a**: vertical velocity profile through the horizontal center line. **b**: horizontal velocity profile through the vertical center line. **c**: vertical velocity residual. **d**: horizontal velocity residual. The profile curves have been translated to avoid clustering of data. We speculate that three obvious outliers, marked with rings, stem from misprints in the tabulated data in [20]. Cubic splines have been fitted to the remaining data.

the present study match very well with the data in [20]. Once again, however, a closer examination reveals a small difference: for higher Re, we compute slightly larger fluid speeds close to the boundaries than is done in [20], and this difference increases with Re. There is, however, a very nice agreement in the location of the

velocity extrema.

Regarding the differences in flow speeds close to the boundaries, several points deserve mentioning. Firstly, the results depend critically on the choice of boundary conditions specified for the upper corners. We emphasize that closed-lid conditions are assumed in the present study. Secondly, the results depend slightly on the formulation of the Navier-Stokes equation (1a) for $Re \gtrsim 5{,}000$, depending on whether the convective or the skew-symmetric formulation is used. This is shown in figure 12, where the computed velocity profiles using each of the two different formulations are compared for $Re = 10{,}000$. The convective and the skew-symmetric

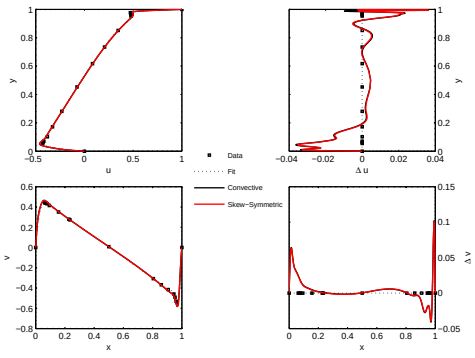

Figure 12: Comparison of velocity profile curves and residual curves (velocity minus fit) for the lid-driven square cavity for $Re = 10{,}000$ with different formulations of the inertial term using the $\mathbf{u}4_0^2\mathrm{p}3_0^1$ discretization (d), plotted with data from [20] and a fit to the data using a cubic spline. Top: horizontal velocity profiles (left) and residuals (right) through the vertical center line. Bottom: vertical velocity profiles (left) and residuals (right) through the horizontal center line.

formulations are found to nearly match each other in the interior, whereas some differences are observed close to the boundaries, in particular at the moving lid. We emphasize that the present study is based on the simpler convective formulation of the Navier-Stokes equation. Thirdly, the data in [20] are relatively sparse at the boundaries where the variation in velocity is high. Finally, it should be stressed that the data in [20] stem from another numerical study, and an exact correspondence between that and the present study should not be expected.

7. Conclusions

This paper has examined various discretizations in isogeometric analysis of 2-dimensional, steady state, incompressible Navier-Stokes equation subjected to Dirichlet boundary conditions. Firstly, a detailed description of the implementation has been given. Secondly, numerical inf-sup stability tests have been presented that confirm the existence of many stable discretizations of the velocity and pressure spaces. In particular it was found that stability may be achieved by means of knot refinement of the velocity space. Thirdly, error convergence studies compared the performance of the various discretizations and indicated optimal convergence, in a per-degree-of-freedom sense, of the discretization with identical polynomial degrees of the velocity and pressure spaces but with the velocity space enriched by knot refinement. Finally, the method has been applied to the lid-driven square cavity for benchmarking purposes, showing that the stable discretizations produce consistent results that match well with existing data and thus confirm the robustness of the method.

Appendix A. Data for Geometry Parametrisations

Table A.2 lists the polynomial degrees, knot vectors and control points for the geometry of the analysed problems.

References

[1] T. Hughes, J. Cottrell, Y. Bazilevs, Isogeometric analysis: CAD, finite elements, NURBS, exact geometry and mesh refinement, Comput. Methods Appl. Mech. Engrg. 194 (2005) 4135–4195.
[2] J. Cottrell, T. Hughes, Y. Bazilevs, Isogeometric Analysis: Toward Integration of CAD and FEA, John Wiley and Sons, 2009.
[3] Y. Bazilevs, L. D. Veiga, J. Cottrell, T. Hughes, G. Sangalli, Isogeometric analysis: Approximation, stability and error estimates for *h*-refined meshes, Mathematical Models and Methods in Applied Science 16 (2006) 1031–1090.
[4] I. Akkerman, Y. Bazilevs, V. Calo, T. Hughes, S. Hulshoff, The role of continuity in residual-based variational multiscale modeling of turbulence., Comput. Mech. 41 (2010) 371–378.
[5] Y. Bazilevs, T. Hughes, NURBS-based isogeometric analysis for the computation of flows about rotating components, Comput. Mech. 43 (2008) 143–150.
[6] Y. Bazilevs, I. Akkerman, Large eddy simulation of turbulent taylor-couette flow using isogeometric analysis and the residual-based variational multiscale method, Journal of Computational Physics 229 (2010) 3402–3414.
[7] A. Buffa, C. de Falco, G. Sangalli, Isogeometric Analysis: Stable elements for the 2D stokes equation, Int. J. Numer. Meth. Fluids (2011).
[8] A. Bressan, Isogeometric regular discretization for the Stokes problem, IMA Journal of Numerical Analysis2 (2010).
[9] A. Bressan, Personal communication.
[10] W. Layton, C. Manica, M. Neda, M. Olshanskii, L. Rebholz, On the accuracy of the rotation form in simulations of the Navier-Stokes-equations, Journal of Computational Physics 228 (2009) 3433–3447.
[11] J. Reddy, D. Gartling, The finite element method in heat transfer and fluid dynamics, CRC Press, 2nd edition, 2001.

[12] J. Donea, A. Huerta, Finite Element Methods for Flow Problems, John Wiley and Sons, 2003.
[13] L. Piegl, W. Tiller, The NURBS Book, Springer, 1995.
[14] Y. Bazilevs, T. Hughes, Weak imposition of Dirichlet boundary conditions in fluid mechanics, Computers & Fluids 36 (2007) 12–26.
[15] Y. Bazilevs, C. Michler, V. Calo, T. Hughes, Weak Dirichlet boundary conditions for wall-bounded turbulent flows, Comput. Methods Appl. Mech. Engrg. 196 (2007) 4853–4862.
[16] W. Wall, M. Frenzel, C. Cyron, Isogeometric structural shape optimization, Comput. Methods Appl. Mech. Engrg. 197 (2008) 2976–2988.
[17] T. Hughes, A. Reali, G. Sangalli, Efficient quadrature for NURBS-based isogeometric analysis, Comput. Methods Appl. Mech. Engrg. 199 (2010) 301–313.
[18] D. Chapelle, K. Bathe, The inf-sup test, Computers & Structures 47 (1993) 537–545.
[19] K. Bathe, The inf-sup condition and its evaluation for mixed finite element methods, Computers & Structures 79 (2001) 243–252.
[20] U. Ghia, K. Ghia, C. Shin, High-Re Solution for Incompressible Flow Using the Navier-Stokes Equations and a Multigrid Method, Journal of Computational Physics 48 (1982) 387–411.
[21] E. Erturk, T. Corke, C. Gokcol, Numerical solutions of 2-d steady incompressible driven cavity flow at high Reynolds numbers, Int. J. Numer. Meth. Fluids **48** (2005) 747–774.
[22] L. Lee, A class of high-resolution algorithms for incompressible flows, Computers & Fluids 39 (2010) 1022–1032.

Wall-Driven Annular Cavity									
Degree	$q = r = 2$								
Knots	$\Xi = \Phi = \{0, 0, 0, 1, 1, 1\}$								
Point	1	2	3	4	5	6	7	8	9
$\bar{x}_1$	0	1	1	0	3/2	3/2	0	2	2
$\bar{x}_2$	1	1	0	3/2	3/2	0	2	2	0
w	1	$1/\sqrt{2}$	1	1	$1/\sqrt{2}$	1	1	$1/\sqrt{2}$	1

Forced Elliptic Cavity									
Degree	$q = r = 2$								
Knots	$\Xi = \Phi = \{0, 0, 0, 1, 1, 1\}$								
Point	1	2	3	4	5	6	7	8	9
$\bar{x}_1$	$-2/\sqrt{2}$	0	$2/\sqrt{2}$	$-4/\sqrt{2}$	0	$4/\sqrt{2}$	$-2/\sqrt{2}$	0	$2/\sqrt{2}$
$\bar{x}_2$	$-1/\sqrt{2}$	$-2/\sqrt{2}$	$-1/\sqrt{2}$	0	0	0	$1/\sqrt{2}$	$2/\sqrt{2}$	$1/\sqrt{2}$
w	1	$1/\sqrt{2}$	1	1	$1/\sqrt{2}$	1	1	$1/\sqrt{2}$	1

Lid-Driven Square Cavity									
Degree	$q = r = 1$								
Knots	$\Xi = \Phi = \{0, 0, 1/2, 1, 1\}$								
Point	1	2	3	4	5	6	7	8	9
$\bar{x}_1$	0	1/2	1	0	1/2	1	0	1/2	1
$\bar{x}_2$	0	0	0	1/2	1/2	1/2	1	1	1
w	1	1/2	1	1/2	1/4	1/2	1	1/2	1

Table A.2: Polynomial degrees, knot vectors, control points and weights for the geometry of the analysed problems.

Appendix C

Paper II: Isogeometric Shape Optimization for Fluids

This chapter contains a preprint of: P. N. Nielsen and J. Gravesen. Isogeometric shape optimization for fluids, 2012. To be submitted to *Structural and Multidisciplinary Optimization*.

Structural and Multidisciplinary Optimization manuscript No.
(will be inserted by the editor)

Isogeometric Shape Optimization for Fluids

Peter N. Nielsen · Jens Gravesen

Abstract We consider various shape optimization problems for fluids in two dimensions. The governing steady-state, incompressible Navier-Stokes equations are solved using isogeometric analysis, and the methodology also serves as framework for the shape optimization procedure. For benchmarking purposes, we design a pipe bend to minimize the pressure drop of the flow through it. To avoid inappropriate parametrizations during optimization, we regularize the problem by adding to the objective function a measure of the quality of the parametrization. We find that minimizing the parametric acceleration along the design boundary is a cheap, flexible and efficient regularization technique. To further test the isogeometric shape optimization methodology, we apply it to two additional design problems for fluids. Based on Taylor-Couette flow, we firstly solve a shape optimization problem with a known solution. We find that the more design variables we use, the better the approximation to the exact solution we obtain. Secondly, we design a body to minimize the drag from the flow past it. We find that the methodology allows for significantly different optimal shapes as the flow speed increases. Both examples emphasize the robustness of the methodology.

Keywords shape optimization · isogeometric analysis · fluid mechanics · regularization · Navier-Stokes equation · Taylor-Couette flow · drag

P. N. Nielsen · J. Gravesen
DTU Mechanical Engineering & DTU Mathematics, Technical University of Denmark, Matematiktorvet 303S, DK-2800 Kgs. Lyngby
Tel.: +45-4525-3031
Fax: +45-4588-1399
E-mail: p.n.nielsen@mat.dtu.dk
E-mail: j.gravesen@mat.dtu.dk

1 Introduction

Numerical shape optimization for fluids is the art of using computers to find "best" shapes in engineering problems involving fluids, based on some notion of "goodness" (Mohammadi and Pironneau 2010). Applications of shape optimization for fluids ranges from, e.g., microfluidic protein-folding devices (Ivorra et al 2006) to airplane wings (Painchaud-Oullet et al 2006).

Isogeometric analysis is a recently proposed computational methodology for solving engineering problems, uniting the analysis powers from finite element analysis (FEA) in terms of solving partial differential equations with the powers from computer aided design (CAD) in terms of geometric modeling (Hughes et al 2005; Cottrell et al 2009). From a fluid mechanics point–of–view, isogeometric analysis is appealing in particular due its ability to represent boundaries exactly (Bazilevs and Hughes 2008), and because of the inherent high regularity of the flow fields (Akkerman et al 2010). From a shape optimization point–of–view, isogeometric analysis serves as a natural framework, due to its ability to represent complex shapes in few design variables, and its tight connection between analysis and geometry models. This means that an acurate representation of the geometry can be maintained throughout the optimization, and there is no need of communcation between FEA and CAD models.

In recent years, isogeometric analysis has succesfully been applied to various shape optimization problems in mechanical engineering. Many studies within structural mechanics have been made, using either NURBS control points (Wall et al 2008; Cho and Ha 2009), NURBS control points and weights (Nagy et al 2010a,b; Qian 2010; Nagy et al 2011), or T-splines control points (Ha et al 2010; Seo et al 2010b) as design variables. NURBS-based isogeometric shape optimization using a bound-

ary integral method has also been studied (Li and Qian 2011). Applications of isogeometric shape optimization also include studies of vibrating membranes (Nguyen et al 2011), and of photonic crystals (Qian and Sigmund 2011). Worth mentioning are also recent applications of isogeometric topology optimization within structural mechanics (Seo et al 2010b,a; Hassani et al 2012).

An inherent challenge in numerical shape optimization is to maintain a high quality of the computational mesh as the shape of the domain changes during optimization (Mohammadi and Pironneau 2004; Bletzinger et al 2010). When using isogeometric analysis, the shape is given by control points. In this setting, care has to be taken to avoid clustering and folding over of control points during optimization, which in turn may lead to singular parametrizations (Wall et al 2008; Nagy et al 2011).

The aim of this work is twofold. Firstly, we establish isogeometric analysis as a framework for numerical shape optimization in fluid mechanics, presenting how the method may be used both as analysis tool to solve the Navier-Stokes equations, and as design tool to guide an optimization procedure through analytically computed gradients of objective and constraint functions. Secondly, to ensure appropriate parametrizations during the optimization, we construct a measure for regularization of the shape optimization problem. Based on a benchmark optimization problem, in which we design a pipe bend to minimize the pressure drop of the flow through it, we examine how this regularization measure influences the optimization process and the optimal design. Finally, to display the robustness of the isogeometric shape optimization methodology, we apply it to two other optimization problems for fluids. First, we design a body at rest in a circular fluid container with rotating boundary to obtain a uniform pressure distribution along its boundary, a design problem which happens to have a known solution, and second, we design a body traveling at constant speed through a fluid to minimize the drag.

The outline of the paper is as follows: Section 2 introduces the generic shape optimization for fluids to be studied, and its isogeometric implementation is accounted for in Section 3. The regularization technique is investigated in Section 4, after which two applications of the methodology are presented in Section 5. Finally, conclusions are drawn in Section 6.

2 Shape Optimization Problem

In this section we introduce the generic shape optimization problem for fluids to be studied.

We consider a viscous, incompressible, isothermal, steady flow at low to moderate Reynolds numbers in a 2-dimensional domain Ω as depicted in Figure 1. The

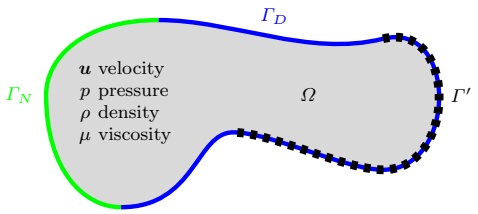

Fig. 1 Setup of generic shape optimization problem for fluids

fluid is assumed to be Newtonian with constant density ρ and constant viscosity μ, and the state of the fluid is characterized by its velocity $\boldsymbol{u} = (\, u \; v \,)^T$ and its pressure p. We assume that no external body forces act on the system (such as gravity). For the boundary Γ, we assume that the domain is open along the Neumann part Γ_N, and that the flow field $\boldsymbol{u}$ is given along the Dirichlet part Γ_D, independently of the shape.

The aim of the optimization is to design the shape of some specified part Γ' of the boundary of the domain to minimize some prescribed objective function, with constraints on the area of the domain. The specific form of the objective function will be explained further below.

All of the above is contained in the following generic shape optimization problem:

$$\underset{\Gamma'(\boldsymbol{x})}{\text{minimize}} \quad C \tag{1a}$$

$$\text{such that} \quad A_{\min} \leq \text{Area} \leq A_{\max} \tag{1b}$$

$$\boldsymbol{\mathcal{L}}_{\min} \leq \mathcal{L}(\boldsymbol{x}) \leq \boldsymbol{\mathcal{L}}_{\max} \tag{1c}$$

$$\boldsymbol{0} = \rho(\boldsymbol{u}\cdot\nabla)\boldsymbol{u} - \nabla p + \mu\nabla^2\boldsymbol{u} \tag{1d}$$

$$0 = \nabla\cdot\boldsymbol{u} \tag{1e}$$

$$\boldsymbol{u}^* = \boldsymbol{u}\,|_{\Gamma_D} \tag{1f}$$

$$0 = (\,\mu\nabla u_i - p\,\boldsymbol{e}_i\,)\cdot\boldsymbol{n}\,|_{\Gamma_N} \tag{1g}$$

Here, the shape of the design boundary Γ' is parametrized through the design variables $\boldsymbol{x}$. Equations (1a) and (1b) are the objective and the area constraint functions, respectively. Equation (1c) establishes bounds on the design variables, as well as linear relations between them, as dictated by the geometry and the physics of the specific problem. Equations (1d) and (1e) are the Navier-Stokes equation and the incompressibility condition, respectively, governing the flow in the domain interior Ω. Equations (1f) and (1g) are the Dirichlet and the Neumann boundary conditions, respectively, where $\boldsymbol{u}^*$ is the given velocity field, $i = 1, 2$ is the component index, and $\boldsymbol{n}$ is the outward unit normal.

We will consider three different quantities as the cost function C in Equation (1a): The difference in mean pressure between two boundary segments γ_+ and γ_-, the pressure variation along a boundary segment γ, and the aerodynamic drag on a boundary segment γ. These are given by:

$$C_{\Delta p} = \frac{\int_{\gamma_+} p \, \mathrm{d}s}{L_{\gamma_+}} - \frac{\int_{\gamma_-} p \, \mathrm{d}s}{L_{\gamma_-}}, \tag{2a}$$

$$C_{\nabla p} = \int_{\boldsymbol{\gamma}} \left(\nabla p \cdot \boldsymbol{t}\right)^2 \mathrm{d}s, \tag{2b}$$

$$C_d = \int_{\boldsymbol{\gamma}} \Big(-p\boldsymbol{I} + \mu\big(\nabla \boldsymbol{u} + (\nabla \boldsymbol{u})^T\big)\Big)\, \boldsymbol{n} \, \mathrm{d}s \cdot \boldsymbol{e}_u, \tag{2c}$$

respectively, where $L_\gamma = \int_\gamma \mathrm{d}s$ denotes the length of the segment γ, $\boldsymbol{t}$ is the unit tangent vector, $\boldsymbol{e}_u$ the constant unit vector along a specified direction, $\boldsymbol{n}$ the outward unit normal, and $\boldsymbol{I}$ the identity matrix. The context in which these three different cost functions may appear will be examplified in Sections 4, 5.1, and 5.2, respectively.

3 Isogeometric Method

In this section, we explain how B-spline based isogeometric analysis may be applied to the shape optimization problem (1). The reader is referred to, e.g., (Piegl and Tiller 1995) for a thorough treatment of B-splines and NURBS (Non-Uniform Rational B-splines), (Cottrell et al 2009) for a thorough treatment of isogeometric analysis, (Nielsen et al 2011) for an introduction to its application to Navier-Stokes flow, and (Wall et al 2008) for an introduction to its application to shape optimization.

3.1 B-splines and NURBS

The building blocks of the method are B-splines and NURBS. To set the scene and for later reference, we briefly revise the basic concepts of these functions.

Univariate B-splines $\mathcal{N}_i^q : [0,1] \to \mathbb{R}$ are piecewise polynomials defined recursively from a polynomial degree $q \in \mathbb{N}$ and a knot vector $\Xi = \{\xi_1, \ldots, \xi_m\} \in \mathbb{R}^m$:

$$\mathcal{N}_i^0(\xi) = \begin{cases} 1 \text{ if } \xi_i \leq \xi < \xi_{i+1} \\ 0 \text{ otherwise} \end{cases} \tag{3a}$$

for $q = 0$, and

$$\mathcal{N}_i^q(\xi) = \frac{\xi - \xi_i}{\xi_{i+q} - \xi_i}\mathcal{N}_i^{q-1}(\xi) + \frac{\xi_{i+q+1} - \xi}{\xi_{i+q+1} - \xi_{i+1}}\mathcal{N}_{i+1}^{q-1}(\xi) \tag{3b}$$

for $q = 1, 2, \ldots$ with $i = 1, \ldots, m-q-1$. We use the unit parametric domain $\xi \in [0,1]$, and we assume open knot vectors, i.e., the boundary knots have multiplicity $q+1$ with $\xi_1 = \xi_2 = \ldots = \xi_{q+1} = 0$ and $\xi_m = \xi_{m-1} = \ldots = \xi_{m-q} = 1$.

Bivariate tensor product B-splines $\mathcal{P}_{i,j}^{q,r} : [0,1]^2 \to \mathbb{R}$ are defined from the univariate B-splines above:

$$\mathcal{P}_{i,j}^{q,r}(\xi,\eta) = \mathcal{N}_i^q(\xi)\, \mathcal{M}_j^r(\eta), \tag{4}$$

where $\mathcal{N}_i^q$ is the i^{th} univariate B-spline with degree q and knot vector $\Xi_1 = \{\xi_1, \ldots, \xi_m\}$ in the parametric dimension ξ, and $\mathcal{M}_j^r$ is the j^{th} univariate B-spline with degree r and knot vector $\Xi_2 = \{\eta_1, \ldots, \eta_n\}$ in the parametric dimension η.

Bivariate NURBS $\mathcal{R}_{i,j}^{q,r} : [0,1]^2 \to \mathbb{R}$ are defined from the bivariate B-splines above, and the weights $W = \{w_{1,1}, \ldots, w_{N,M}\}$ with $w_{i,j} \in \mathbb{R}$ for $i = 1, \ldots, m-q-1$ and $j = 1, \ldots, n-r-1$:

$$\mathcal{R}_{i,j}^{q,r}(\xi,\eta) = \frac{w_{i,j}\, \mathcal{P}_{i,j}^{q,r}(\xi,\eta)}{\sum_{k=1}^{m-q-1}\sum_{l=1}^{n-r-1} w_{k,l}\, \mathcal{P}_{k,l}^{q,r}(\xi,\eta)}. \tag{5}$$

The construction of bivariate B-splines from a set of polynomial degrees and knots vectors is illustrated in Figure 2. This type of function will serve as basis for the subsequent analysis and optimization.

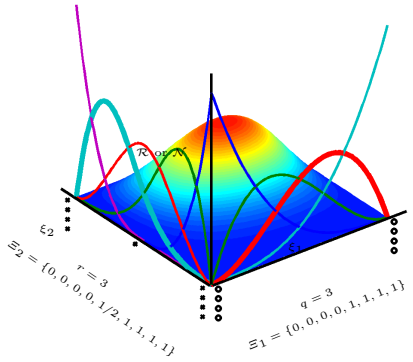

Fig. 2 Construction of a bivariate tensor product B-spline (surface) from two univariate B-splines (lines in bold) of given polynomial degrees and knot vectors (crosses and circles)

3.2 Geometry Parametrization

Using bivariate tensor product NURBS $\mathcal{R}_i$ as defined above, we construct a parametrization of the physical

domain Ω, defined over the parameter domain $[0,1]^2$, cf. figure 3:

$$\boldsymbol{X} = (\, x,\, y\,) = \sum_{i}^{N^g_{\text{var}}} \boldsymbol{x}_i \mathcal{R}^g_i, \tag{6}$$

where $\boldsymbol{x}_i = (\, x_i\,,\, y_i\,)$ are control points, and N^g_{var} is the number of terms in the expansion. The superscript g indicates that the functions refer to given knot vectors, polynomial degrees and control weights specific for the geometry.

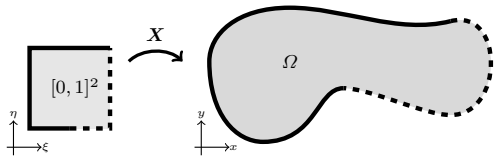

Fig. 3 Parametrization of the flow domain

For any scalar variable, e.g., the pressure p, or one of the velocity components u_1 and u_2, we will consider it both as a function $\overline{f}$ on physical space Ω, and as a function f on parameter space $[0,1]^2$. The gradient $\overline{\nabla} \equiv (\, \partial/\partial x\ \partial/\partial y\,)^T$ in physical space Ω is related to its counterpart $\nabla \equiv (\, \partial/\partial \xi\ \partial/\partial \eta\,)^T$ in parameter space $[0,1]^2$ by the following relation:

$$\nabla f = \boldsymbol{J}^T \overline{\nabla f} \iff \overline{\nabla f} = \boldsymbol{J}^{-T} \nabla f, \tag{7}$$

where $\boldsymbol{J} \equiv \partial x_i / \partial \xi_j$ is the Jacobian matrix of the parametrization.

3.3 Flow Analysis

The governing equations (1d)–(1e) are solved numerically by a standard Galerkin approach based on B-splines as test and weight functions.

Approximations of the velocity and pressure fields are constructed using bivariate tensor product B-splines $\mathcal{R}_i$ as defined above:

$$\boldsymbol{u} = \sum_{i=1}^{N^{\boldsymbol{u}}_{\text{var}}} \boldsymbol{u}_i \mathcal{R}^{\boldsymbol{u}}_i = \sum_{i=1}^{N^{\boldsymbol{u}}_{\text{dof}}} \underline{\boldsymbol{u}}_i \mathcal{R}^{\boldsymbol{u}}_i + \sum_{i=N^{\boldsymbol{u}}_{\text{dof}}+1}^{N^{\boldsymbol{u}}_{\text{var}}} \underline{\boldsymbol{u}}_i \mathcal{R}^{\boldsymbol{u}}_i, \tag{8a}$$

$$p = \sum_{i=1}^{N^p_{\text{var}}} p_i \mathcal{R}^p_i = \sum_{i=1}^{N^p_{\text{dof}}} \underline{p}_i \mathcal{R}^p_i, \tag{8b}$$

where, p_i are control coefficients, and N^p_{var} is the number of terms in the expansions for the pressure. The superscript p now indicates that the functions refer to given knot vectors and polynomial degrees that are specific for the pressure, and quantities for the velocities $\boldsymbol{u}$ are defined similarly. The velocity expansions have been split into terms *with* and terms *without* support on the Dirichlet boundary Γ_D.

The numerical solution of the incompressible Navier-Stokes equations (1d)–(1e) rests on a discretized form of their *weak* or *variational* formulation. This is obtained by multiplying the two equations by the image of each of the velocity basis functions $\mathcal{R}^{\boldsymbol{u}}$ without support on the Dirichlet boundary Γ_D, and the image of each of the pressure basis functions $\mathcal{R}^p$, respectively, and then simplifying the resulting expressions using integration by parts and insertion of the Neumann boundary condition from Equation (1g). By subsequently inserting the image of the discretizations of the state variables in Equation (8) into this, interchanging the order of summation and integration, rearranging terms, and finally pulling all integrals back to parameter space, the following system of non-linear equations in the control coefficients is obtained:

$$\begin{bmatrix} \mu \boldsymbol{K}_1 + \rho \boldsymbol{C}_1(\underline{\boldsymbol{u}}) & \boldsymbol{0} & -\boldsymbol{G}_1^T \\ \boldsymbol{0} & \mu \boldsymbol{K}_2 + \rho \boldsymbol{C}_2(\underline{\boldsymbol{u}}) & -\boldsymbol{G}_2^T \\ \boldsymbol{G}_1 & \boldsymbol{G}_2 & \boldsymbol{0} \end{bmatrix} \begin{bmatrix} \bar{\boldsymbol{u}}_1 \\ \bar{\boldsymbol{u}}_2 \\ \bar{\boldsymbol{p}} \end{bmatrix} = - \begin{bmatrix} \mu \boldsymbol{K}_1^\star + \rho \boldsymbol{C}_1^\star(\underline{\boldsymbol{u}}) & \boldsymbol{0} \\ \boldsymbol{0} & \mu \boldsymbol{K}_2^\star + \rho \boldsymbol{C}_2^\star(\underline{\boldsymbol{u}}) \\ \boldsymbol{G}_1^\star & \boldsymbol{G}_2^\star \end{bmatrix} \begin{bmatrix} \bar{\boldsymbol{u}}_1^\star \\ \bar{\boldsymbol{u}}_2^\star \end{bmatrix}, \tag{9}$$

or simply $\boldsymbol{M}(\boldsymbol{U})\, \boldsymbol{U} = \boldsymbol{F}$, with

$$\underline{\boldsymbol{K}}_{k\,i,j} = \iint\limits_{[0,1]^2} \nabla^T \mathcal{R}^{u_k}_i\, \boldsymbol{J}^{-1}\, \boldsymbol{J}^{-T}\, \nabla \mathcal{R}^{u_k}_j\, \det\big(\boldsymbol{J}\big)\, \mathrm{d}\boldsymbol{\xi}, \tag{10a}$$

$$\underline{\boldsymbol{C}}_{k\,i,j} = \iint\limits_{[0,1]^2} \mathcal{R}^{u_k}_i\, \boldsymbol{u}^T(\underline{\boldsymbol{u}})\, \boldsymbol{J}^{-T}\, \nabla \mathcal{R}^{u_k}_j\, \det\big(\boldsymbol{J}\big)\, \mathrm{d}\boldsymbol{\xi}, \tag{10b}$$

$$\underline{\boldsymbol{G}}_{k\,i,j} = \iint\limits_{[0,1]^2} \mathcal{R}^{p}_i\, \boldsymbol{e}_k^T\, \boldsymbol{J}^{-T}\, \nabla \mathcal{R}^{u_k}_j\, \det\big(\boldsymbol{J}\big)\, \mathrm{d}\boldsymbol{\xi}, \tag{10c}$$

$$\underline{\boldsymbol{K}}_k = \Big[\, \boldsymbol{K}_k\ \boldsymbol{K}_k^\star \,\Big] \quad \Big(N^{u_k}_{\text{dof}} \times (N^{u_k}_{\text{dof}} + N^{u_k}_{\text{fix}})\Big), \tag{10d}$$

$$\underline{\boldsymbol{C}}_k = \Big[\, \boldsymbol{C}_k\ \boldsymbol{C}_k^\star \,\Big] \quad \Big(N^{u_k}_{\text{dof}} \times (N^{u_k}_{\text{dof}} + N^{u_k}_{\text{fix}})\Big), \tag{10e}$$

$$\underline{\boldsymbol{G}}_k = \Big[\, \boldsymbol{G}_k\ \boldsymbol{G}_k^\star \,\Big] \quad \Big(N^{p}_{\text{dof}} \times (N^{u_k}_{\text{dof}} + N^{u_k}_{\text{fix}})\Big), \tag{10f}$$

$$\underline{\boldsymbol{u}}_k^T = \Big[\, \bar{\boldsymbol{u}}_k^T\ \bar{\boldsymbol{u}}_k^{\star T} \,\Big] \quad \Big(1 \times (N^{u_k}_{\text{dof}} + N^{u_k}_{\text{fix}})\Big), \tag{10g}$$

where $\boldsymbol{u}(\underline{\boldsymbol{u}})$ is given by equation (8a), $\boldsymbol{e}_1 = (1\ 0)^T$ and $\boldsymbol{e}_2 = (0\ 1)^T$ are the standard unit vectors, and all starred quantities are given by the Dirichlet boundary conditions. Equation (9) may be solved by, e.g., an iterative Newton-Raphson method.

3.4 Optimization

To find a minimum in the cost function while fulfilling the constraints, the geometry parametrization is tweaked little by little, and over and over again the governing flow equations are solved, and the objective and constraints evaluated. To guide the optimization process, gradients of the cost function and the constraints are computed analytically.

3.4.1 Design Variables

The control points $\boldsymbol{x}_i$ entering the geometry parametrization in Equation (6) are the natural geometric "handles" on the flow domain, and these are therefore used as design variables for the shape optimization routine. A parametrization and its control net are sketched in Figure 4. The design variables of the optimization are the coordinates of the green control points in Figure 4a that determine the shape of the dashed design boundary Γ' in figure 4b. As also shown in figure 4a, control points fall into three categories: The *design* control points (green) are "actively" moved around in the search for the optimal shape, the *linked* control points (yellow) are "passively" following the movement of the design control points, as described below, while the *fixed* control points (red) remain unaltered.

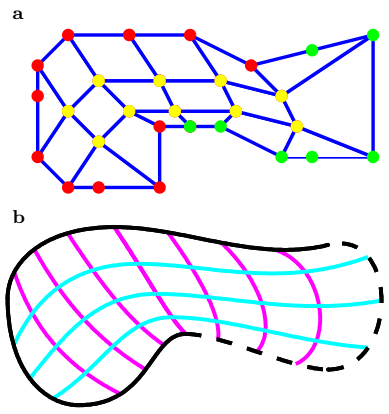

Fig. 4 **a**: Three types of control points: design (green), linked (yellow), and fixed (red). **b**: Image of isoparametric lines

3.4.2 Interior Parametrization

As the shape of flow domain is changed in the optimization process, the parametrization of its interior must be adequately updated. Referring to Figure 4, in the isogeometric framework this amounts to specifying the location of the yellow interior control points as the location of the green design control points are changed through the optimization. This is a fundamental challenge in isogeometric analysis (Cohen et al 2010; Xu et al 2010). We choose to base the parametrization of the interior on the Winslow functional, which is a useful measure when constructing conformal maps (Gravesen et al 2010; Nguyen et al 2011). Initially, the interior control points are determined as the ones that minimize the Winslow functional while keeping the boundary constant and ensuring a valid parametrization $\det(\boldsymbol{J}) > 0$. The latter constraint may be evaluated using B-splines (NURBS), since the determinant of the Jacobian of a spline (NURBS) surface is itself a spline (NURBS). In each design iteration, the interior control points are then found as those that minimizes the 2nd order Taylor expansion of the Winslow functional based on the initial control net. This procedure leads to a linear problem to be solved in each design iteration. On top of this, the validity of the parametrization is checked in each iteration by checking if $\det(\boldsymbol{J}) > 0$. If this condition is *not* fulfilled, the interior control points are found as the solution to the initial minimization problem as described above. This solution is then subsequently used as linearization point for the Taylor expansion of the Winslow functional, and the optimization is restarted from this configuration.

3.4.3 Function Evaluation

To asses the quality and admissibility of a given design, the objective and constraint functions in equations (2) and (1b) are evaluated in each iteration. Using the parametrization of the geometry in Equation (6) and the discretizations of the flow and pressure fields in Equation (8), we collect the control points in two $(N^g_{\text{var}} \times 1)$ vectors $\boldsymbol{x}$ and $\boldsymbol{y}$, and the control coefficients in one $\left((N^u_{\text{var}} + N^v_{\text{var}} + N^p_{\text{var}}) \times 1\right)$ vector $\boldsymbol{U}$. The mean pressure difference between two boundary segments γ_2 and γ_1, the pressure variation along a boundary segment γ, the aerodynamic drag on a boundary segment γ, and the area of the domain Ω, as defined in Equation (2) and (1b), may then be computed as:

$$C_{\Delta p} = \boldsymbol{\mathcal{P}}^T \boldsymbol{U}, \tag{11a}$$

$$C_{\nabla p} = \boldsymbol{U}^T \boldsymbol{\mathcal{D}} \boldsymbol{U} \tag{11b}$$

$$C_d = \boldsymbol{\mathcal{F}}^T \boldsymbol{U}, \tag{11c}$$

$$A = \boldsymbol{x}^T \boldsymbol{\mathcal{A}} \boldsymbol{y}, \tag{11d}$$

respectively. Here, the following vectors and matrices have been defined:

$$\boldsymbol{\mathcal{P}} = \boldsymbol{\mathcal{P}}_{\gamma_+} - \boldsymbol{\mathcal{P}}_{\gamma_-} \tag{12a}$$

$$\boldsymbol{\mathcal{P}}_{\gamma k} = \frac{1}{L_\gamma} \int_0^1 \mathcal{R}_k^p \, \|\dot{\boldsymbol{\gamma}}\| \, \mathrm{d}\xi, \tag{12b}$$

$$\boldsymbol{\mathcal{D}}_{k,\ell} = \int_0^1 \left(\boldsymbol{t}^T \boldsymbol{J}^{-T} \nabla \mathcal{R}_k^p \right) \left(\boldsymbol{t}^T \boldsymbol{J}^{-T} \nabla \mathcal{R}_\ell^p \right) \|\dot{\boldsymbol{\gamma}}\| \, \mathrm{d}\xi, \tag{12c}$$

$$\boldsymbol{\mathcal{F}} = \begin{bmatrix} \boldsymbol{\mathcal{F}}_{11} \, \boldsymbol{\mathcal{F}}_{12} \\ \boldsymbol{\mathcal{F}}_{21} \, \boldsymbol{\mathcal{F}}_{22} \\ \boldsymbol{\mathcal{F}}_{31} \, \boldsymbol{\mathcal{F}}_{32} \end{bmatrix} \boldsymbol{e}_u, \tag{12d}$$

$$\boldsymbol{\mathcal{F}}_{11k} = \mu \int_0^1 \left(2\boldsymbol{e}_1^T \boldsymbol{n} \boldsymbol{e}_1^T + \boldsymbol{e}_2^T \boldsymbol{n} \boldsymbol{e}_2^T \right) \boldsymbol{J}^{-T} \nabla \mathcal{R}_k^u \, \|\dot{\boldsymbol{\gamma}}\| \, \mathrm{d}\xi, \tag{12e}$$

$$\boldsymbol{\mathcal{F}}_{21k} = \mu \int_0^1 \boldsymbol{e}_2^T \boldsymbol{n} \boldsymbol{e}_1^T \boldsymbol{J}^{-T} \nabla \mathcal{R}_k^v \, \|\dot{\boldsymbol{\gamma}}\| \, \mathrm{d}\xi, \tag{12f}$$

$$\boldsymbol{\mathcal{F}}_{31k} = -\int_0^1 \boldsymbol{e}_1^T \boldsymbol{n} \mathcal{R}_k^p \, \|\dot{\boldsymbol{\gamma}}\| \, \mathrm{d}\xi, \tag{12g}$$

$$\boldsymbol{\mathcal{F}}_{12k} = \mu \int_0^1 \boldsymbol{e}_1^T \boldsymbol{n} \boldsymbol{e}_2^T \boldsymbol{J}^{-T} \nabla \mathcal{R}_k^u \, \|\dot{\boldsymbol{\gamma}}\| \, \mathrm{d}\xi, \tag{12h}$$

$$\boldsymbol{\mathcal{F}}_{22k} = \mu \int_0^1 \left(2\boldsymbol{e}_2^T \boldsymbol{n} \boldsymbol{e}_2^T + \boldsymbol{e}_1^T \boldsymbol{n} \boldsymbol{e}_1^T \right) \boldsymbol{J}^{-T} \nabla \mathcal{R}_k^v \, \|\dot{\boldsymbol{\gamma}}\| \, \mathrm{d}\xi, \tag{12i}$$

$$\boldsymbol{\mathcal{F}}_{32k} = -\int_0^1 \boldsymbol{e}_2^T \boldsymbol{n} \mathcal{R}_k^p \, \|\dot{\boldsymbol{\gamma}}\| \, \mathrm{d}\xi, \tag{12j}$$

$$\boldsymbol{\mathcal{A}}_{k,\ell} = \iint_{[0,1]^2} \left(\frac{\partial \mathcal{R}_k^g}{\partial u} \frac{\partial \mathcal{R}_\ell^g}{\partial v} - \frac{\partial \mathcal{R}_k^g}{\partial v} \frac{\partial \mathcal{R}_\ell^g}{\partial u} \right) \mathrm{d}\boldsymbol{\xi}, \tag{12k}$$

where the length is given by $L_\gamma = \int \|\dot{\boldsymbol{\gamma}}\| \, \mathrm{d}\xi$. The parametric speed $\|\dot{\boldsymbol{\gamma}}\| \equiv \sqrt{\dot{x}^2 + \dot{y}^2}$, the unit tangent vector $\boldsymbol{t} \equiv \dot{\boldsymbol{\gamma}} / \|\dot{\boldsymbol{\gamma}}\|$, and the outward unit normal vector $\boldsymbol{n} \equiv \pm \dot{\boldsymbol{t}}$ are found by differentiating the restriction of the geometry parametrization in Equation (6) to the boundary with respect to the parameter ξ. These vectors and matrices are in general sparse, $\boldsymbol{\mathcal{P}}$, $\boldsymbol{\mathcal{D}}$, and $\boldsymbol{\mathcal{F}}$ in particular, since only few of the basis functions have support on the design boundary.

3.4.4 Gradient Evaluation

The optimization is driven by gradients of the objective and constraint functions defining the optimization problem. These sensitivities measure how the design variables affect the objective and constriaint functions. We compute these analytically by direct differentiation of the discretized versions of the functions in Equation (11) with respect to the coordinates of the control points, that act as our design variables.

We collect the design variables in one vector $\boldsymbol{\chi}$, such that $\boldsymbol{\chi} = (x_1 \, \ldots \, x_N \, y_1 \, \ldots \, y_N)$, where $(x_k \; y_k)$ are the coordinates of the kth control point, and we let $\bullet' \equiv \partial \bullet / \partial \chi_k$ denote the partial derivative with respect to the kth design variable. For the objectives and the constraint in Equation (11) we have:

$$C'_{\Delta p} = \boldsymbol{\mathcal{P}}'^T \boldsymbol{U} + \boldsymbol{\mathcal{P}}^T \boldsymbol{U}', \tag{13a}$$

$$C'_{\Delta p} = \boldsymbol{U}^T \boldsymbol{\mathcal{D}}' \boldsymbol{U} + 2 \boldsymbol{U}^T \boldsymbol{\mathcal{D}} \boldsymbol{U}', \tag{13b}$$

$$C'_d = \boldsymbol{\mathcal{F}}'^T \boldsymbol{U} + \boldsymbol{\mathcal{F}}^T \boldsymbol{U}', \tag{13c}$$

$$A' = \boldsymbol{y}^T \boldsymbol{\mathcal{A}} \boldsymbol{x}' + \boldsymbol{x}^T \boldsymbol{\mathcal{A}} \boldsymbol{y}'. \tag{13d}$$

The derivatives of $\boldsymbol{x}$ and $\boldsymbol{y}$ in Equation (13d) are trivial. The derivatives of the objective matrices/vectors $\boldsymbol{\mathcal{P}}$, $\boldsymbol{\mathcal{D}}$, and $\boldsymbol{\mathcal{F}}$ in Equations (13a)—(13c) may be found by differentiation of the integrands in Equation (12):

$$\begin{aligned} \boldsymbol{\mathcal{P}}'_{\gamma i} &= \left(\frac{\langle \, \mathcal{R}_i^p \, \|\dot{\boldsymbol{\gamma}}\| \, \rangle}{\langle \, \|\dot{\boldsymbol{\gamma}}\| \, \rangle} \right)' \\ &= \frac{\langle \, \mathcal{R}_i^p \, \|\dot{\boldsymbol{\gamma}}\|' \, \rangle \, \langle \, \|\dot{\boldsymbol{\gamma}}\| \, \rangle + \langle \, \mathcal{R}_i^p \, \|\dot{\boldsymbol{\gamma}}\| \, \rangle \, \langle \, \|\dot{\boldsymbol{\gamma}}\|' \, \rangle}{\langle \, \|\dot{\boldsymbol{\gamma}}\| \, \rangle^2}, \end{aligned} \tag{14}$$

where we have defined $\dot{\bullet} \equiv \partial \bullet / \partial \xi$ and $\langle \bullet \rangle \equiv \int \bullet \, \mathrm{d}\xi$, and used that all basis functions $\mathcal{R}$ are independent of the design variables. Here, the derivative of the parametric speed $\|\dot{\boldsymbol{\gamma}}\|$ may be found from Equation (6):

$$\begin{aligned} \|\dot{\boldsymbol{\gamma}}\|' &= \left(\sqrt{\dot{x}^2 + \dot{y}^2} \right)' \\ &= \frac{\dot{x} \, \dot{x}' + \dot{y} \, \dot{y}'}{\|\dot{\boldsymbol{\gamma}}\|} \\ &= \begin{cases} \frac{\dot{x}}{\|\dot{\boldsymbol{\gamma}}\|} \, \dot{\mathcal{R}}_k^g \text{ for } k = 1, \ldots, N \\ \frac{\dot{y}}{\|\dot{\boldsymbol{\gamma}}\|} \, \dot{\mathcal{R}}_k^g \text{ for } k = N+1, \ldots, 2N \end{cases}. \end{aligned} \tag{15}$$

Equivalent approaches may be taken for the matrices $\boldsymbol{\mathcal{D}}$ and $\boldsymbol{\mathcal{F}}$ in Equation (12).

The derivative of the solution $\boldsymbol{U}$ in Equations (13a)—(13c) may be found by solving the linear equation system obtained by differentiation of Equation (9):

$$(\boldsymbol{M} + \boldsymbol{D}) \boldsymbol{U}' = \boldsymbol{F}' - \boldsymbol{M}' \boldsymbol{U}, \tag{16}$$

where

$$\boldsymbol{D} = \rho \begin{bmatrix} \boldsymbol{D}_{1,1} \; \boldsymbol{D}_{1,2} \; \boldsymbol{0} \\ \boldsymbol{D}_{2,1} \; \boldsymbol{D}_{2,2} \; \boldsymbol{0} \\ \boldsymbol{0} \quad \boldsymbol{0} \quad \boldsymbol{0} \end{bmatrix}, \tag{17a}$$

$$\boldsymbol{D}_{i,jk,\ell} = \iint_{[0,1]^2} \mathcal{R}_k^{u_i} \left(\boldsymbol{e}_j^T \boldsymbol{J}^{-T} \nabla u_i(\underline{\boldsymbol{u}}) \right) \mathcal{R}_\ell^{u_j} \det(\boldsymbol{J}) \, \mathrm{d}\boldsymbol{\xi} \, . \tag{17b}$$

We mention that the matrix $\boldsymbol{\mathcal{J}} = \boldsymbol{M} + \boldsymbol{D}$ also appears in the iterative Newton-Raphson method employed for solving the governing equations. The derivative of the system matrix $\boldsymbol{M}$ and vector $\boldsymbol{F}$ in Equation (16) may be found by differentiation of the integrands in equation (10):

$$\begin{aligned}\boldsymbol{K}'_{k\,i,j} = & \iint\limits_{[0,1]^2} \nabla^T \mathcal{R}_i^{u_k} \boldsymbol{J}^{-1\prime} \boldsymbol{J}^{-T} \nabla \mathcal{R}_j^{u_k} \det\left(\boldsymbol{J}\right) \mathrm{d}\boldsymbol{\xi} \\ & + \iint\limits_{[0,1]^2} \nabla^T \mathcal{R}_i^{u_k} \boldsymbol{J}^{-1} \boldsymbol{J}^{-T\prime} \nabla \mathcal{R}_j^{u_k} \det\left(\boldsymbol{J}\right) \mathrm{d}\boldsymbol{\xi}. \\ & + \iint\limits_{[0,1]^2} \nabla^T \mathcal{R}_i^{u_k} \boldsymbol{J}^{-1} \boldsymbol{J}^{-T} \nabla \mathcal{R}_j^{u_k} \det\left(\boldsymbol{J}\right)' \mathrm{d}\boldsymbol{\xi}. \quad (18)\end{aligned}$$

Here, the derivative of the determinant and of the inverse of the Jacobian matrix may be found by simply writing them out explicitly in terms of x and y and subsequently differentiating this as in Equation (15), or alternatively from the relations $\boldsymbol{J}^{-1\prime} = \boldsymbol{J}^{-1}\,\boldsymbol{J}'\,\boldsymbol{J}^{-1}$ and $\det(\boldsymbol{J})' = \det(\boldsymbol{J})\,\mathrm{tr}(\boldsymbol{J}^{-1}\boldsymbol{J}')$, along with differentiation of Equation (6):

$$\boldsymbol{J}' = \begin{cases} \begin{bmatrix} \mathcal{R}^g_{k,\xi} & \mathcal{R}^g_{k,\eta} \\ 0 & 0 \end{bmatrix} \text{ for } k = 1, \ldots, N \\ \\ \begin{bmatrix} 0 & 0 \\ \mathcal{R}^g_{k,\xi} & \mathcal{R}^g_{k,\eta} \end{bmatrix} \text{ for } k = N+1, \ldots, 2N \end{cases}, \quad (19)$$

where we have defined $\bullet_{,s} \equiv \partial \bullet / \partial s$. Equivalent approaches may be taken for the matrices $\boldsymbol{C}$ and $\boldsymbol{G}$ in equation (10).

Finally, to account for the induced movement of the linked control points, as a result of the update of the interior parametrization when the design control points are moved, the full sensitivity is computed as $\tilde{\bullet}' = \bullet' + \sum_i \chi_i^{l\prime} \frac{\partial}{\partial \chi_i^l}$, where the summation is over linked design variables, or

$$\widetilde{\nabla}_d = \nabla_d + \mathcal{W} \nabla_l, \quad (20)$$

where the subscripts d and l refer to design variables and linked variables, respectively. The matrix $\mathcal{W}_{i,j} = \partial \chi_i^l / \partial \chi_j^d$ relates the linked control points to the design control points.

3.5 Implementation Details

The flow chart in Figure 5 sketches the most significant steps in solving the shape optimization problem in Equation (1) based on isogeometric analysis.

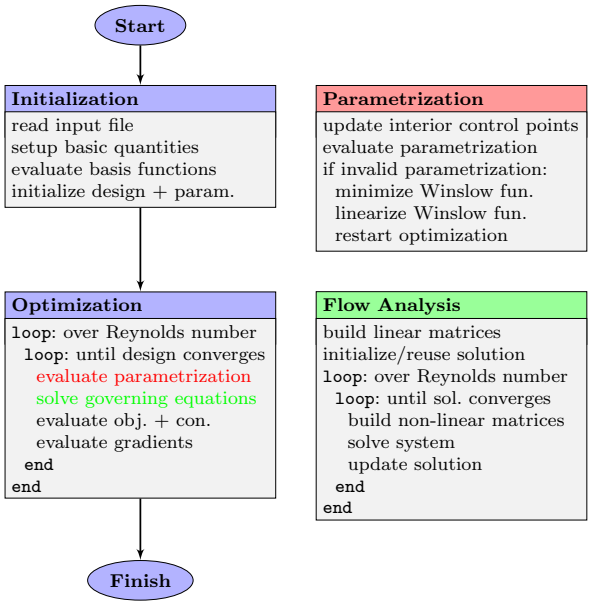

Fig. 5 Flow chart for the optimization process (left) with details of the parametrization and analysis procedures (right)

In the initialization phase, we perform as many calculations as possible that are independent of the parametrization. In particular, all basis functions and their derivatives are evaluated in the Gauss quadrature points once and for all. Although more memory demanding, this approach greatly reduces the computational expenses, compared to evaluating the functions on the fly in each optimization iteration. The construction of a good initial parametrization is also vital for the optimization.

The optimization process includes an outer loop over increasing Reynolds number. This is only neccesary when designing shapes in higher Reynolds number flows. The entire process outlined in the flow chart may be embedded into a loop over increasing refinement of geometry and/or analysis. The optimization is performed using the SNOPT optimization package (Gill et al 2008). Standard settings for SNOPT are used, except for the step size limit which, when set relatively low, e.g., 5% of the characteristic length scale of the problem, has been found to significantly improve the convergence by avoiding too large jumps in the design space. For validation purposes, the analytically computed gradients are checked initially against finite difference estimates.

On the analysis side, we use an iterative Newton-Raphson method to solve the governing non-linear equation (9), gradually increasing the Reynolds number when this is high. In the field approximations, bi-quartic ten-

sor product B-splines are used for the velocities and bi-cubic tensor product B-splines for the pressure, both C^2 across knots. Dirichlet boundary conditions are enforced strongly, while homogenous Neumann boundary conditions are enforced weakly. All integrals are evaluated numerically using Gaussian quadrature.

4 Regularization

To strengthen the result of the shape optimization, the design space in which we look for solutions should be as large as possible. A natural way to ensure a large design space is to use many control points as design variables, although the inclusion of weights as design variables could also be considered (Qian 2010; Nagy et al 2011). As the number of design control points go up, more complex shapes can be designed. This comes, however, on the cost of numerical challenges. These challenges, and solution strategies to remedy them, are discussed in this section.

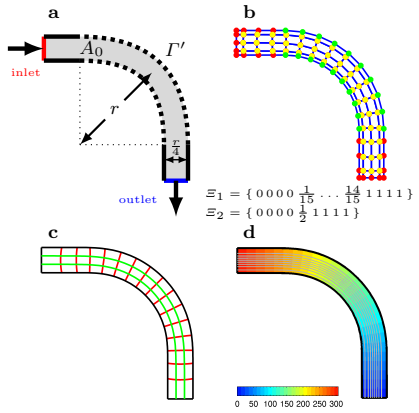

Fig. 6 Pipe bend with minimal pressure drop: design problem setup (**a**), initial control net (**b**), initial parametrization (**c**), and initial pressure contours and flow stream lines (**d**)

For the purpose of illustration, we consider a concrete example of the shape optimization problem (1)-(2a), and use this as benchmark for the following tests of the regularization technique. The problem is outlined in figure 6a. The aim is to design the shape Γ' of a pipe bend (dashed) to minimize the pressure drop from the inlet boundary (red) to the outlet boundary (blue), keeping the shape of the inlet and the outlet (solid) fixed, and with an upper bound on the area of the pipe.

We assume a parabolic horizontal velocity profile on the inlet boundary, that the velocity it is zero along the side walls, assuming no-slip conditions, and that its horizontal component is zero along the open outlet boundary. We take the length scale as $r = 1$, the velocity scale as $U = \max(\|\boldsymbol{u}_{\text{inlet}}\|) = 1$, the density as $\rho = 1$, and the viscosity as $\mu = 1$, assuming appropriate units are used, which yields a Reynolds number of $\text{Re} = 1$ for the initial problem.

We parametrize the pipe bend as a bi-cubic tensor product B-spline surface, and let the initial design connect the inlet and outlet by an approximate quarter annulus. The initial control net, the corresponding parametrization, and the resulting pressure distribution and stream lines of the flow through it are depicted in Figure 6b–d. We use 20 control points as design variables, 10 on each of the two boundaries segments to be designed, and we allow these to move freely in both spatial dimensions, except for the four end control points, which are only allowed to move along the direction of the inlet/outlet, to keep a handle on these. As upper bound on the area, we use the initial value, i.e., $A_{\max} = A_0$, and we relax the lower bound, i.e., $A_{\min} = -\infty$. Since the lengths of the inlet and outlet boundaries are constant, the sensitivities in Equation (14) are greatly simplified.

4.1 The Challenge: Clustering of Control Points

Applying the isogeometric machinery from Section 3 to the shape optimization problem outlined above results in the optimization history depicted in Figure 7. From iteration 0 to 15 (actually *function call* in SNOPT terminology), the design control points firstly align, connecting the inlet and the outlet by a more or less straight segment, thereby decreasing the pressure drop by $\sim 74\%$. This design reduces the length of the pipe in intuitive accordance with the Poiseuille law. At iteration 44, sharper corners at the inlet and outlet are formed, but from iteration 44 and onwards, the shape changes only slightly, and the decrease in the pressure drop is accordingly small. The location of the control points, however, and the resulting parametrization change *appreciably*, though. The control points cluster and eventually fold over, resulting in an invalid parametrization after 67 iterations from which the method cannot proceed.

The problem seems to arise in the second of two qualitatively different stages of the optimization: the optimizer finds an "optimal" shape in the first stage, and then tries to find an "optimal" parametrization of it in the second stage. The latter "optimality", however, is a numerical artefact. The optimizer finds the flaws in the numerical procedure, so to say, and tries to align the errors in such a way, that the *numerical*

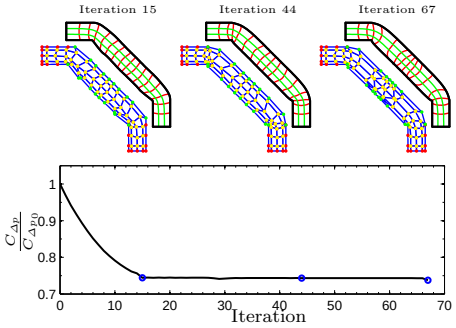

Fig. 7 Pipe bend with minimal pressure drop: objective function as a function of optimization iteration (bottom), and three snap shots of the control net and the associated parametrization (top)

estimate is minimized, although the "actual" value is not. This is the challenge in a nut-shell: when optimizing the location of many control points, they may cluster when the problem is sufficiently unconstrained, spuriously yielding slightly lower values of the objective function on the cost of significantly worse parametrizations and less accurate analysis, which may eventually lead to a collapse of the method. The clustering of control points is a well-known issue in isogeometric shape optimization (Wall et al 2008; Nagy et al 2011). Related numerical problems in finite element based shape optimization, and regulariation techniques to adress them, are also well-described (Bletzinger et al 2010). Below, we firstly give a brief review of some alternative ways out of the current problem, before proposing the regularization approach, in an isogeometric framework.

4.2 Some Alternative Solution Strategies

The first natural point of focus, when looking for remedies for the current problem, is on the optimization routine. A quick fix is simply to stop the optimization immediately after the first "shape" stage, and before the onset of the second "parametrization" stage. This could be achieved by relaxing the existing convergence criterion, or by defining some other relevant measure. However, since this approach only cures the symptoms of the problem, and not the cause of it, and due to the risk of prematurely stopping the optimization, this approach is, in our view, not only quick, but also dirty.

Turning away from the optimization routine, we may focus on the problem formulation instead. An obvious solution to the problem is to reconsider the design degrees of freedom. As the control points align, an ambiguity is introduced, since movements of the control points along the line does not change the shape, but *does* change the parametrization and thus also the numerical estimates of the integrals, and hence the objective function value, making the problem inherently ill-posed. One could then simply argue that for this particular design problem, say, four design control points on each boundary suffice. However, this is an aposteriori type of reasoning that we would like to avoid. More interesting is the idea of making this estimation of the neccesary number of design variables dynamic, i.e., inserting and removing design control points on the fly during the optimization (Seo et al 2010b). The implementation of a flexible number of design variables in an optimization procedure, however, is less than trivial.

Preserving the *number* of control points, but putting constraints on their movement in the design space, poses yet another alternative. We could, for instance, constrain the design control points to move only along specified directions. In this approach, it is our duty as designers to specify "good" directions along which the control points can move, ensuring both sufficient flexibility in the design while avoiding bad parametrizations. Along the same line of thinking is the concept of putting bounds on the design variables, see e.g. (Cho and Ha 2009), thus limiting the optimizer to search for a minimum in the vicinity of the initial guess only. In any case, the design space shrinks in these approaches, and the success of the optimization heavily depends on the designers choice in initial condition and constraints on the movement of the control points. A somewhat related, but much more flexible approach, is to introduce a more general constraint on the design variables. A popular choice is to put a lower bound on the distance between control points (Wall et al 2008). Although this approach does take care of the tendency of control points to cluster, it still closes the door to parts of the design space. Another choice is to prescribe an upper bound on a single, global measure of the shape change (Nagy et al 2011) during the optimization, thereby significantly reducing the number of constraints, but still relying partly on a qualified initial guess.

4.3 Boundary Regularization

To avoid the problem of clustering control points and the associated fatal parametrization, we suggest to regularize the optimization problem (Mohammadi and Pironneau 2004, 2010). More specifically, we suggest to add a term to the objective function that, by measuring the quality of the parametrization, prevents the unwanted phenomenon. In this approach, the regularized objec-

tive function $\widetilde{C}$ is written as:

$$\widetilde{C} = C + \tilde{\epsilon} R, \tag{21}$$

where C is the "actual" physical objective, here expressing the pressure drop in the pipe bend, R is the "artificial" regularization objective, and $\tilde{\epsilon} > 0$ specifies the weight of the regularization term. The aim of the optimization, when using the regularized objective, is twofold: we are not only searching for the design that minimizes the pressure drop, but also for the shape whose parametrization makes the numerical approximation of it more reliable. Thereby, we embed the construction of a good parametrization into the design optimization, and we are thus targeting the very cause of the problem.

The method poses two challenges: Firstly, it neccessitates the construction of a quality measure R of the parametrization, and secondly, it requires the specification of its relative importance $\tilde{\epsilon}$ in the optimization.

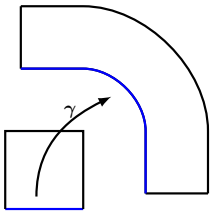

Fig. 8 Illustration of the focus of boundary regularization

The focus of this study is on boundary regularization, as sketched in Figure 8. This adresses the quality of parametrization of the design boundary, which is clearly compromised early on in the fatal optimization history in Figure 7. We define the measure as the norm squared of the parametric acceleration along the design boundaries, integrated in parameter domain:

$$R = \int_0^1 \|\ddot{\boldsymbol{\gamma}}\|^2 \, \mathrm{d}\xi, \tag{22}$$

where we have defined $\ddot{\bullet} \equiv \partial^2 \bullet / \partial \xi^2$. In discretized form, it reads:

$$R = \boldsymbol{x}^T \boldsymbol{R} \boldsymbol{x} + \boldsymbol{y}^T \boldsymbol{R} \boldsymbol{y}, \tag{23a}$$

$$\boldsymbol{R}_{i,j} = \int_0^1 \ddot{\mathcal{R}}_i \ddot{\mathcal{R}}_j \, \mathrm{d}\xi. \tag{23b}$$

By minimizing this measure, we bring the boundary parametrization closer to a constant-speed parametrization, and boundary regularization thus leads the optimizer towards a better boundary parametrization. The measure is computationally cheap to implement, since the matrix $\boldsymbol{R}$ only involves integrals of the second order derivatives of the (univariate) basis functions, and since it is quadratic in the design variables, the sensitivities may be straightforwardly computed.

An important challenge in the methodology is the specification of a suitable weight $\tilde{\epsilon}$ of the regularization. This challenge is similar in nature to the one associated with specifying a suitable minimal distance between control points (Wall et al 2008), or a maximal shape change norm (Nagy et al 2011). The specification may be partly facilitated by estimating the initial ratio between the physical objective C_0 and the regularization objective R_0:

$$\tilde{\epsilon} = \frac{|C_0|}{|R_0|} \epsilon, \tag{24}$$

assuming $R_0 \neq 0$, and that this ratio does not change too much with the design. Taking $\epsilon = 1$ yields identical initial numerical values for the physical and the regularization terms in Equation (21). Usually, a value $\epsilon \ll 1$ is therefore anticipated. The smaller the ϵ, the closer we get to the original optimization problem, but, on the other hand, the more we weaken the regularization and its stabilizing influence on the parametrization and the convergence.

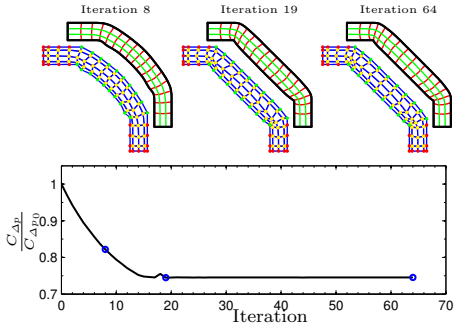

Fig. 9 Pipe bend with minimal pressure drop: regularized optimization history (bottom), and snap shots of the control net and the associated parametrization (top)

We apply the regularized isogeometric shape optimization method to the current design problem, thus minimizing the *regularized* pressure drop (21)–(22) through the pipe bend using the weight $\epsilon = 10^{-2}$. The optimal design is reached after 64 iterations, at which point the pressure drop is decreased to 74.5%. The optimization history is shown in Figure 9. Here, it is worth noticing that the optimal design is quite close to the design from which the original formulation drifts off, cf. Figure 7, that the difference in the minimal pressure drop between the designs is small, and, most importantly, that

the parametrization is much better in this regularized formulation, thereby making the analysis more reliable. The effect of the regularization is clearly seen from the intermediate design in iteration 19, to the converged design in iteration 64. The control points spread out along the line, and the concentration of control points is shifted away from the straight central part, towards the curved parts at the inlet and the outlet. This is also where the geometry, and hence the flow analysis, is most challenging, due to the presence of sharp corners that form as a result of coallescing control points. The resulting pressure field is shown in figure 10. The optimized design is similar to the topology optimized design with minimal energy dissipation (Gersborg-Hansen et al 2005).

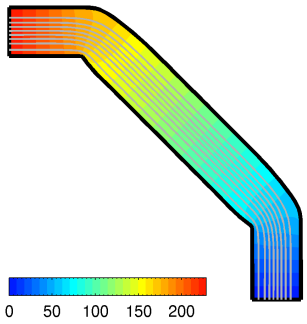

Fig. 10 Pipe bend with minimal pressure drop: optimized pressure contours and flow stream lines

To examine the effect of the regularization in greater detail, we solve the problem for a range of regularization weights $\epsilon \in [10^{-3}, 10^{-1}]$. Figure 11 shows how the optimized pressure drop, the required number of iterations, and the optimal design vary with the regularization weight. When the regularization is strong, the optimization converges quickly to a smoother design with a higher pressure drop. As the regularization is decreased, more iterations are required to reach designs with locally higher curvature and smaller pressure drops. A stagnation point in the pressure drop curve is observed, associated with the formation of the sharp corners at the inlet and the outlet, such that the optimized pressure drop only falls off slightly for $\epsilon \leq 3 \cdot 10^{-2}$. In addition, the number of iterations is likewise relatively constant for $3 \cdot 10^{-3} \leq \epsilon \leq 3 \cdot 10^{-2}$. A regularization weight in this range thus seems appropriate in this example. The results, however, are not critically sensitive to the value used.

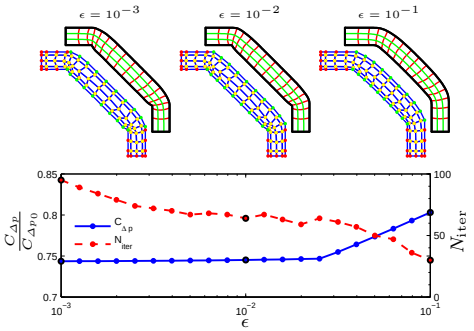

Fig. 11 Pipe bend with minimal pressure drop: optimized pressure drop and required number of iterations as a function of regularization weight ϵ (bottom), and optimal design for three values of ϵ (top)

We conclude this section by mentioning that a range of other regularization measures could be considered. Among these, we have found that similar effects as those presented above may be obtained by minimizing the scalar product of the tangent and the acceleration, the variance of the Jacobian determinant, or the variance of the parametric speed, all evaluated along the design boundary. Minimization of the Winslow functional, however, is found to be more problematic to implement. Furthermore, the regularization measures could alternatively be implemented as contraints, but such investigations have been outside the scope of this study.

5 Applications

In this section, we apply the isogeometric shape optimization methodology for fluid design problems to two additional numerical examples.

5.1 Body with Uniform Pressure Distribution

We consider the shape optimization problem (1)-(2b) outlined in figure 12a. The aim is to design the boundary Γ' of a body of given area A_0, placed in a circular fluid container of radius r whose outer boundary rotates, to make the pressure distribution along Γ' as uniform as possible, i.e., to minimize the pressure variation $C_{\nabla p}$ along Γ'. From symmetry considerations, the pressure is constant along the boundary when a disk is placed in the centre. Furthermore, analytical solutions to the governing Navier-Stokes equations for this so-called Taylor-Couette flow problem is well-known from the literature. A circle enclosing the specified area and with centre in the centre of the container is therefore a

solution to the shape optimization problem. In the following, we investigate how well the isogeometric shape optimization methodology is able to reproduce this.

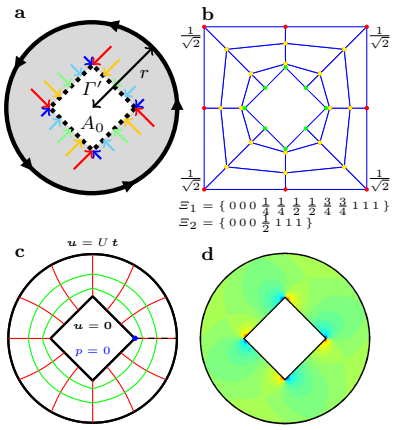

Fig. 12 Body with uniform pressure distribution: design problem setup (**a**), initial control net, knot vectors, and non-unitary weights (**b**), initial parametrization (**c**), and initial pressure field (**d**)

To represent the outer perimeter as an exact circle, which is of paramount importance when specifying boundary conditions, we parametrize the geometry using quadratic NURBS. As initial design, we use a square placed in the middle, which is an intentionally bad initial guess. The control net, knot vectors and weights are shown in Figure 12b, and the corresponding parametrization is visualized in Figure 12c. The patch is attached to itself along the dashed line, resulting in an additional C^0-continuity here. The velocity field is specified as purely tangential along the outer moving perimeter, and as vanishing on the inner steady boundary, assuming no-slip conditions. Since full Dirichlet boundary conditions are prescribed for the velocity field, we set the pressure to zero in an arbitrary point. We take the initial area as $A_0 = 2$, the radius of the outer perimeter as $r = 2$, the velocity scale as $U = 1$, the density as $\rho = 1$, and the viscosity as $\mu = 1$, assuming again appropriate units are used, which again yields a Reynolds number of $\mathrm{Re} = 1$. The initial pressure field is depicted in Figure 12d. In this, the C^0-continuities are invisible to the naked eye. We take the constraint on the area as the initial value, i.e., $A_{\max} = A_{\min} = \pi r^2 - A_0$, and a one-step approach is employed for the Reynolds number. To resolve the rotational symmetry, the left-most control point is allowed only to move horizontally. It turns out that this problem is sufficiently constrained to prevent control points from clustering, and we may solve it without regularization.

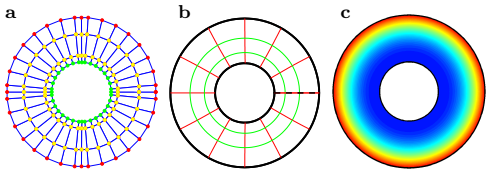

Fig. 13 Body with uniform pressure distribution: optimized control net (**a**), parametrization (**b**), and pressure field (**c**) for 36 design control points

We consider three consecutive refinements of the coarse geometry described above, obtained by uniform knot refinement along the tangential direction, thereby representing the design boundary Γ' by 8, 12, 20, and 36 control points, respectively. We solve the design problem for each of these four geometric models, using in turn the optimized coarser design as initial guess for the finer optimization. The results for the finest geometric approximation are shown in figure 13. The optimal design is reached in a total of 1032 iterations, and the pressure variation is decreased by a factor of $\sim 10^{-17}$. The optimal control net is shown in (a), and the corresponding optimized parametrization is shown in (b). The inner boundary is seen to approximate a circle very accurately. The optimized pressure field shown in (c) is significantly more uniform than the initial one shown in Figure 12d.

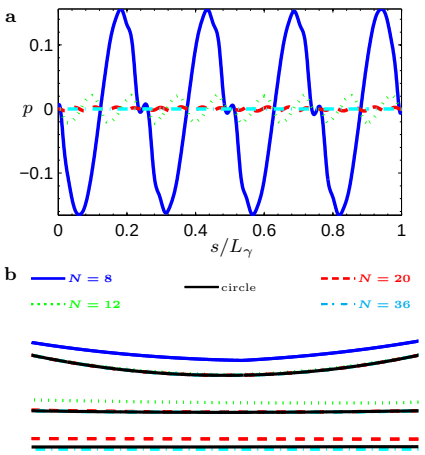

Fig. 14 Body with uniform pressure distribution: comparison of pressure distributions along the optimized boundaries (**a**), and comparison of the optimized boundaries to the exact circle in three zooms (**b**)

Table 1 Body with uniform pressure distribution: comparison of objective function, discrepancy from the exact circle, and number of iterations for different numbers of design variables

N_{design}	$C_{\nabla p}/C_{\nabla p0}$	ϵ_{circle}	N_{iter}
8	$8.1 \cdot 10^{-4}$	$6.3 \cdot 10^{-2}$	131
12	$5.1 \cdot 10^{-5}$	$3.7 \cdot 10^{-3}$	127
20	$3.3 \cdot 10^{-6}$	$2.5 \cdot 10^{-4}$	344
36	$1.4 \cdot 10^{-17}$	$2.1 \cdot 10^{-5}$	430

To examine more closely the effect of enlarging the design space by the use of more design control points, Figure 14a shows the pressure distribution along the optimized boundary when using 8, 16, 20, and 36 design control points. Also shown, in figure 14b, is a comparison of the lower part of the optimized design boundaries to the exact circle. As is evident from the figure, the more control points we use, the more uniform the pressure distribution we obtain, and the better the approximation to the exact circle we find. This is quantitatively supported by the numerical values listed in Table 1, showing that both the pressure variation, and the discrepancy of the design boundary from the circle of radius $r_0 = \sqrt{A_0/\pi}$ converge towards zero, as more design control points are used. Here, we have estimated the discrepancy of the design boundary from the circle of radius r_0 by the measure:

$$\epsilon^2_{\text{circle}} = \int_\gamma \left(\frac{x^2 + y^2}{r_0^2} - 1 \right)^2 \, \mathrm{d}s.$$

With 36 design control points, this error is $\sim 2.1 \cdot 10^{-5}$.

5.2 Body with Minimal Drag

We consider the shape optimization problem (1)-(2c) outlined in figure 15a. The boundary Γ' of a body with given minimal area A_0 traveling at constant speed U through a fluid is designed to minimize the drag C_d it experiences as the fluid flows past it.

Symmetry is assumed around the line along which the body travels, and only the upper half of the problem is considered. To facilitate the implementation of boundary conditions, and to achieve local refinement close to the body, this half space is truncated using two patches, as shown by the black lines in figure 15b (top). The design boundary Γ' is initialized as an approximate half circle of radius $r = 1$, as depicted in Figure 15c (top), and the computational domain extends $20r$ upstream, $20r$ sidewards, and $40r$ downstream, as depicted in Figure 15b (bottom). Cubic B-splines are employed for the geometric parametrization. The initial control net is shown in Figures 15b-c (bottom). The

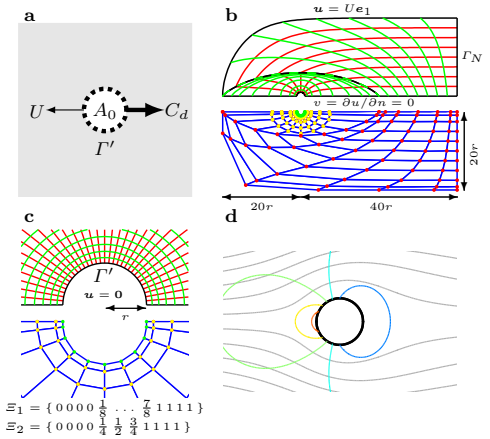

Fig. 15 Body with minimal drag: design problem setup (**a**), initial control net, initial parametrization, domain dimensions, boundary conditions, and knot vectors (**b** and **c**), and initial pressure contours and flow stream lines for $U = 1$ (**d**)

governing equations are solved in the co-moving inertial system in which the body is at rest. For the boundary conditions, we assume no-slip along the design boundary Γ', that the flow is undisturbed along the upstream truncation boundary, that the downstream truncation boundary is open, and that the fields are symmetric around the lower truncation boundary, as sketched in Figures 15b-c (top). The density and viscosity are set to $\rho = 1$ and $\mu = 1$, respectively, assuming appropriate units.

We use 11 design control points, and take $A_0 = \pi$ as lower bound on the area of the body, i.e., $A_{\max} = \text{Area}_0 - A_0/2$. The end control points are allowed only to move horizontally and symmetrically, to ensure that the domain is appropriately defined, and to resolve the translational symmetry of the problem. To prevent the control net from folding over at the leading and trailing edges in particular, boundary regularization with weight $\epsilon = 0.01$ is employed.

Table 2 Body with minimal drag: length (L), height (H), widest location (x_w), drag coefficient ($C_d^* = C_d/(\frac{1}{2}\rho U^2 H)$), and relative decrease in drag $r = (C_d^{\text{initial}} - C_d^{\text{optimal}})/C_d^{\text{initial}}$ for the initial and optimized shapes

Design	$L/2$	$H/2$	x_w	C_d^*	r
Initial	1.00	1.00	0.00	4.13	-
$U = 1$	1.80	0.62	0.02	6.12	7.7%
$U = 10$	2.29	0.48	-0.03	1.81	2.4%
$U = 40$	2.80	0.41	-0.32	0.97	1.2%
$U = 100$	3.12	0.38	-0.51	0.64	0.4%

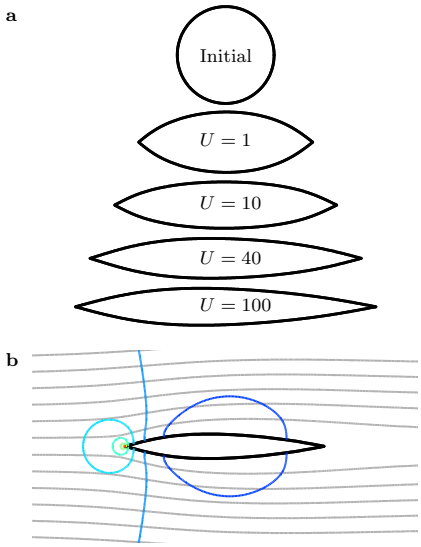

Fig. 16 Body with minimal drag: initial and optimized shapes for $U \in \{1, 10, 40, 100\}$ (**a**), and optimized pressure contours and flow stream lines for $U = 100$ (**b**)

We solve the shape optimization problem for four consecutive speeds $U \in \{1, 10, 40, 100\}$, using again the lower speed solution as initial guess for the higher speed. These speeds correspond to Reynolds numbers 1, 10, 40, and 100, respectively, based on the initial setup. After $57 + 40 + 67 + 58 = 222$ design iterations, the optimization converges. To illustrate how the design varies with flow speed, the initial and the optimized shapes for each of the four speeds are compared in Figure 16a, and the characteristics of the shapes are summarized in Table 2. A considerable change in the design is seen as the speed is increased. For low speeds, a rugby ball-like shape is optimal. For higher speeds, a more slender shape is optimal, with a slightly thicker upstream part than downstream. The long slender design relates well to the increase in the significance of the form drag, and the decrease in the significance of the skin friction drag, as the speed increases. The pressure and flow fields around the optimized shape for the terminal speed $U = 100$ are depicted in figure 16b.

In the present context, minimizing the drag on the body is equivalent to minimizing the energy dissipation in the flow past it (Mohammadi and Pironneau 2010), and we may compare the results for these two types of problems. Firstly, for Reynolds number $\mathrm{Re} = 1$, the angle of the wedge-shaped upstream part compares well to the theoretically predicted value of 90°, while for higher Reynolds numbers, the shapes are more cusped (Pironneau 1973, 1974). For Reynolds number $\mathrm{Re} = 1$, the present optimal shape compare well qualitatively to the numerical results obtained in (Katamine et al 2005), while for Reynolds numbers $\mathrm{Re} > 1$, the present optimal shapes differ significantly from their ovoid with the upstream part slimmer than the downstream part. Consistently better qualitative correspondance is found with the numerical results in (Kim and Kim 1995), although the present optimal shapes are slightly longer, thinner, and more ovoid than their elliptic shapes.

6 Conclusions

In this work, we have applied isogeometric analysis to shape optimization problems for fluids. The methodology uses NURBS and B-splines from computer aided design both as analysis tool in a finite-element-like maner to solve the governing steady-state, incompressible Navier-Stokes equations, and as design tool to find optimal shapes by moving the control points using a gradient-based numerical optimization package.

By adding to the objective function a measure of the quality of the parametrization, we have established a regularization technique to avoid inappropriate parametrizations during optimization, a commonly known problem in isogeometric shape optimization. Based on a bechmark design problem, in which a pipe bend is designed to minimize the pressure drop of the flow through it, the integral of the norm squared parametric acceleration along the design boundary was found to be a cheap, flexible and efficient regularization measure. The method embeds the construction of a good parametrization into the design optimization, allowing the designer to search for shapes in a large design space, with little apriori knowledge on the optimal design. The greatest challenge of the method lies in the choice of the regularization weight.

To emphasize the robustness of the proposed isogeometric shape optimization methodology for fluids, we have used it firstly to design a body at rest in a circular fluid container with rotating boundary to obtain a uniform pressure distribution along its boundary, and secondly to design a body traveling at constant speed through a fluid to minimize the drag from the flow past it. For the former problem, it was found that progressively better approximations of a known solution is achieved when more design control points are used, while the latter problem demonstrated that significantly different shapes of the minimal drag body may be obtained when the speed is varied.

In summary, the isogometric shape optimization methodology facilitates the accurate design of complex shapes in engineering problems within fluid mechanics.

Aknowledgment

The authors would like to thank Allan Roulund Gersborg, Burmeister & Wain Energy A/S, Denmark, and Thomas A. Grandine and Thomas A. Hogan, The Boeing Company, USA, for their conceptual support to this study.

References

Akkerman I, Bazilevs Y, Calo VM, Hughes TJR, Hulshoff S (2010) The role of continuity in residual-based variational multiscale modeling of turbulence. Comput Mech 41:371–378

Bazilevs Y, Hughes T (2008) NURBS-based isogeometric analysis for the computation of flows about rotating components. Comput Mech 43:143–150

Bletzinger KU, Firl M, Linhard J, Wüchner R (2010) Optimal shapes of mechanically motivated surfaces. Computer Methods in Applied Mechanics and Engineering 199:324–333

Cho S, Ha SH (2009) Isogeometric shape design optimization: exact geometry and enhanced sensitivity. Struct Multidisc Optim 38:53–70

Cohen E, Martin T, Kirby RM, Lyche T, Riesenfeld RF (2010) Analysis-aware modeling: understanding quality considerations in modeling for isogeometric analysis. Computer Methods in Applied Mechanics and Engineering 199:334–356

Cottrell JA, Hughes TJR, Bazilevs Y (2009) Isogeometric Analysis: Toward Integration of CAD and FEA. John Wiley and Sons

Gersborg-Hansen A, Sigmund O, Haber RB (2005) Topology optimization of channel flow problems. Structural and Multidisciplinary Optimization 30(3)

Gill PE, Murray W, Saunders A (2008) User's guide for snopt version 7: Software for large-scale nonlinear programming. http://www.cam.ucsd.edu/ peg/papers/sndoc7.pdf. Accessed 25 January, 2012.

Gravesen J, Evgrafov A, Gersborg AR, Nguyen DM, Nielsen PN (2010) Isogeometric analysis and shape optimisation. In: Eriksson A, Tibert G (eds) Proceedings of NSCM-23: the 23rd Nordic Seminar on Computational Mechanics, pp 14–17

Ha SH, Choi KK, Cho S (2010) Numerical method for shape optimization using T-spline based isogeometric method. Structural and Multidisciplinary Optimization 42:417–428

Hassani B, Khanzadi M, Tavakkoli SM (2012) An isogeometrical approach to structural topology optimization by optimality criteria. Struct Multidisc Optim 45:223–233

Hughes TJR, Cottrell JA, Bazilevs Y (2005) Isogeometric analysis: CAD, finite elements, NURBS, exact geometry and mesh refinement. Comput Methods Appl Mech Engrg 194:4135–4195

Ivorra B, Hertzog DE, Mohammadi B, Santiago JS (2006) Semi-deterministic and genetic algorithms for global optimization of microfluidic protein-folding devices. International Journal for Numerical Methods in Engineering 66:319–333

Katamine E, Azegami H, Tsubata T, Itoh S (2005) Solution to shape optimization problems of viscous flow fields. International Journal of Computational Fluid Dynamics 19(1):45–51

Kim DW, Kim MU (1995) Minimum drag shape in two-dimensional viscous flow. International Journal for Numerical Methods in Fluids 21:93–111

Li K, Qian X (2011) Isogeometric analysis and shape optimization via boundary integral. Computer-Aided Design 43:1427–1437

Mohammadi B, Pironneau O (2004) Shape optimization in fluid mechanics. Annu Rev Fluid Mech 36:255–279

Mohammadi B, Pironneau O (2010) Applied Shape Optimization for Fluids, 2nd edn. Oxford Science Publications

Nagy A, Abdalla M, Gürdal Z (2010a) Isogeometric sizing and shape optimization of beam structures. Comput Methods Appl Mech Engrg 199:1216–1230

Nagy A, Abdalla M, Gürdal Z (2010b) On the variational formulation of stress constraints in isogeometric design. Comput Methods Appl Mech Engrg 199:2687–2696

Nagy A, Abdalla M, Gürdal Z (2011) Isogeometric design of elastic arches for maximum fundamental frequency. Structural and Multidisciplinary Optimization 43:135–149

Nguyen DM, Evgrafov A, Gersborg AR, Gravesen J (2011) Isogeometric shape optimization of vibrating membranes. Comput Methods Appl Mech Engrg 200:1343–1353

Nielsen PN, Gersborg AR, Gravesen J, Pedersen NL (2011) Discretizations in isogeometric analysis of navier-stokes flow. Comput Methods Appl Mech Engrg 200:3242–3253

Painchaud-Oullet S, Tribes C, Trepanier JY, Pelletier D (2006) Airfoil shape optimization using a nonuniform rational b-spline parametrization under thickness constraint. IAAA Journal 44(10):2170–2178

Piegl L, Tiller W (1995) The NURBS Book. Springer

Pironneau O (1973) On optimum profiles in Stokes flow. Journal of Fluid Mechanics 59:117–128

Pironneau O (1974) On optimum design in fluid mechanics. Journal of Fluid Mechanics 64:97–110

Qian X (2010) Full analytical sensitivities in NURBS based isogeometric shape optimization. Computer Methods in Applied Mechanics and Engineering 199:2059–2071

Qian X, Sigmund O (2011) Isogeometric shape optimization of photonic crystals via Coons patches. Computer Methods in Applied Mechanics and Engineering 200:2237–2255

Seo YD, Kim HJ, Youn SK (2010a) Isogeometric topology optimization using trimmed spline surfaces. Computer Methods in Applied Mechanics and Engineering 199:3270–3296

Seo YD, Kim HJ, Youn SK (2010b) Shape optimization and its extension to topological design based on isogeometric analysis. International Journal of Solids and Structures 47:1618–1640

Wall WA, Frenzel MA, Cyron C (2008) Isogeometric structural shape optimization. Comput Methods Appl Mech Engrg 197:2976–2988

Xu G, Mourrain B, Duvigneau R, Galligo A (2010) Optimal analysis-aware parametrization of computational domain in isogeometric analysis. In: Mourrain B, Schaeffer S, Xu G (eds) Advances in Geometric Modeling and Processing, Springer, pp 236–254

Appendix D

Paper III: Isogeometric Analysis of Sound Propagation through Flow in 2-Dimensional Ducts

This chapter contains a preprint of: P. N. Nielsen, J. Gravesen, and M. Willatzen. Isogeometric analysis of sound propagation through flow in 2-dimensional ducts, 2011b. Submitted to *Journal of Sound and Vibration*.

Isogeometric Analysis of Sound Propagation through Flow in 2-Dimensional Ducts

Peter Nørtoft Nielsen[a,b,*], Jens Gravesen[a], Morten Willatzen[c]

[a] *DTU Mathematics, Technical University of Denmark, Matematiktorvet 303S, DK-2800 Kgs. Lyngby, Denmark*
[b] *DTU Mechanical Engineering, Technical University of Denmark, Nils Koppels All 404, DK-2800 Kgs. Lyngby, Denmark*
[c] *The Mads Clausen Institute, University of Southern Denmark, Alsion 2, DK-6400 Sønderborg, Denmark*

Abstract

We consider the propagation of sound through a moving fluid in a 2-dimensional duct. A detailed description of a coupled flow-acoustic model of the problem based on isogeometric analysis is given. The model couples the non-linear, steady-state, incompressible Navier-Stokes equation in the laminar regime for the flow field to a linear, time-harmonic acoustic equation in the low Mach number regime for the sound signal. Acoustic boundary conditions on artificial truncation boundaries are treated using a mode matching formulation. We validate the model against known acoustic modes in 2-dimensional ducts. Improved error convergence rates are found when the acoustic pressure is approximated by higher order polynomials. Based on the model, we examine effects of the duct geometry on how the acoustic signal depends on sound frequency and flow speed. A combination of duct geometry and sound frequency is identified for which the acoustic signal is particularly sensitive to the background flow.

Keywords:
flow acoustics, isogeometric analysis, duct, ultrasound, mode matching

1. Introduction

It is well known in physics and engineering applications that wave propagation in ducts is sensitive to the duct geometry [1, 2, 3]. In particular, spatial resonances exist at certain frequencies [4, 5, 6], and it is anticipated that disturbances may cause large variations in signal transmission at such frequencies. While these effects have been explored in quantum mechanics, solid state physics, and optics, in particular for quasi-periodic and periodic structures [7, 8, 9, 10, 11], we here investigate the influence of a background flow on acoustic wave propagation in 2-dimensional ducts of varying height.

Finite element methods within the field of sound propagation through flow in ducts are extensively used, based on, e.g., the convected Helmholtz equation [12, 13], the linearized Euler equations [14], or the so-called Galbrun's equation [15, 16, 17], and often discretized using Lagrange elements with C^0-continuity of the state variable approximations. Our work contributes to this field in two ways.

Firstly, we analyse the coupled flow-acoustic system by explicitly connecting a flow model to an acoustic model. The procedure we follow is first to compute the background flow based on the steady-state, incompressible Navier-Stokes equations in the laminar regime, i.e., at low Reynolds numbers, and then we adobt a linear, time-harmonic flow-acoustic approach for the sound wave propagation in the low Mach number regime, using the calculated background flow as input. This results in a single equation in the acoustic pressure, linear in both the flow field itself and its gradient.

Secondly, we base our calculations on isogeometric analysis, a recently proposed numerical method that unites the powers of finite element methods to solve partial differential equations with the powers of computer aided design to represent complex shapes [18, 19]. For the problem at hand, isogeometric analysis is particularly appealing because it allows for simple descriptions of complex duct geometries, and provides high degrees of smoothness for both flow and acoustic fields. The applicability of the method is well documented within fluid mechanics, see, e.g., [20, 21, 22, 23], as well as

*Corresponding author.
Email addresses: p.n.nielsen@mat.dtu.dk (Peter Nørtoft Nielsen), j.gravesen@mat.dtu.dk (Jens Gravesen), willatzen@mci.sdu.dk (Morten Willatzen)

for wave phenomena and the closely related structural vibrations [24, 25].

The first aim of the paper is to establish and validate the coupled flow-acoustic model for time-harmonic sound propagation at low Mach numbers through a stationary, incompressible background flow at low Reynolds numbers in 2-dimensional ducts based on isogeometric analysis.

The second aim of the paper is to use the model to numerically examine how the geometry of the duct influences the sound propagation, and in particular its effect on how the acoustic signal depends on flow speed. We consider a transmitting ultrasonic transducer mounted on the duct wall, as sketched in Figure 1, and we examine the difference between the downstream and the upstream acoustic signals for different frequencies and flow speeds. Geometric effects are investigated by considering three different duct geometries: a straight duct, a duct with a single bulge, and a corrugated duct with two bulges.

The outline of the paper is as follows: section 2 introduces the governing equations and approximations leading to the coupled flow-acoustic model. The isogeometric method is presented in section 3, after which the method is validated in section 4. Numerical results are presented in section 5, and finally conclusions are summarized in section 6.

2. Governing Equations and Approximations

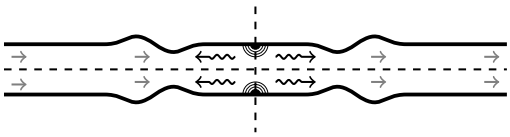

Figure 1: Sound propagates (black arrows) from acoustic sources (black rings) through a moving fluid (gray arrows) in a symmetric (dashed lines) 2-dimensional duct (solid lines).

We consider the propagation of sound through a moving fluid in a symmetric 2-dimensional duct as depicted in Figure 1. The state of the fluid is characterised by the velocity $\mathbf{u} = (u, v)$, the pressure p, and the density ρ, assuming the fluid is isothermal, i.e., at constant temperature. These state variables are governed by the Navier-Stokes and mass continuity equations:

$$\rho\frac{\partial \mathbf{u}}{\partial t} + \rho(\mathbf{u}\cdot\nabla)\mathbf{u} + \nabla p - \nabla\cdot\mathbb{T} = \mathbf{0}, \tag{1a}$$

$$\frac{\partial \rho}{\partial t} + \nabla\cdot(\rho\mathbf{u}) = 0, \tag{1b}$$

where t denotes time, and $\mathbb{T}$ is the deviatoric stress tensor.

The problem involves two distinct physical phenomena: the flow of the fluid and the propagation of sound in it. We express this separation through the state variables:

$$\mathbf{u} = \mathbf{u}_0 + \mathbf{u}', \quad p = p_0 + p', \quad \rho = \rho_0 + \rho', \tag{2}$$

where $\mathbf{u}_0$, p_0, and ρ_0 relates to the large scale mean flow, and $\mathbf{u}'$, p', and ρ' relates to the small scale acoustic disturbances. For simplicity, we will assume a one-way coupling of these phenomena, such that flow phenomena ($\mathbf{u}_0$, p_0, and ρ_0) influence acoustic phenomena ($\mathbf{u}'$, p', and ρ'), but not the other way around. Hence, we may treat the flow model as independent of the acoustic model, and use the output of the flow model as input to the acoustic model.

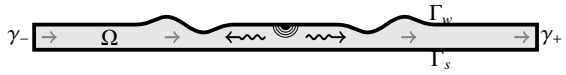

Figure 2: Model domain (light gray) and boundaries (black lines).

In the following, we consider the flow and acoustic equations over a symmetric, finite segment of one half of the symmetric, infinite 2-dimensional duct as depicted in Figure 2. The four boundaries of the model domain Ω are: the hard wall boundary Γ_w, the symmetry boundary Γ_s, and the two artificial truncation boundaries γ_- and γ_+.

2.1. Flow Equations

For the flow model, we assume that the fluid is Newtonian and incompressible, and that the flow is stationary. The governing equations (1) over Ω then simplify to:

$$\rho_0(\mathbf{u}_0\cdot\nabla)u_0 + \frac{\partial p_0}{\partial x} - \mu\nabla^2 u_0 = 0, \tag{3a}$$

$$\rho_0(\mathbf{u}_0\cdot\nabla)v_0 + \frac{\partial p_0}{\partial y} - \mu\nabla^2 v_0 = 0, \tag{3b}$$

$$\nabla\cdot\mathbf{u}_0 = 0, \tag{3c}$$

where μ is the dynamic viscosity of the fluid, and ρ_0 its constant density.

The boundary conditions are:

$$\mathbf{u}_0 = \mathbf{u}_0^* \quad \text{on } \gamma_-\cup\Gamma_w, \tag{4a}$$

$$v_0 = 0 \quad \wedge \quad (\,\mu\nabla u_0 - p\,\mathbf{e}_1\,)\cdot\mathbf{n} = 0 \quad \text{on } \gamma_+\cup\Gamma_s, \tag{4b}$$

where $\mathbf{n}$ is the outward unit normal, and $\mathbf{u}_0^*$ prescribes a purely horizontal flow velocity on the flow inlet γ_-, and a vanishing flow velocity along the hard wall Γ_w. On the symmetry edge Γ_s, we note that $\mathbf{e}_1 \cdot \mathbf{n} = 0$. On the flow outlet γ_-, the enforcement of $v_0 = 0$ has implications on the validity of the acoustic model, as explained.

We solve the weak, or variational, form of the system (3)-(4) which reads: given ρ_0 and μ, find $\mathbf{u}_0$ and p_0 such that

$$\iint_\Omega \Big(\mathcal{U}\rho_0(\mathbf{u}_0\cdot\nabla)u_0 - p_0\frac{\partial \mathcal{U}}{\partial x} + \mu\nabla\mathcal{U}\cdot\nabla u_0\Big)\,\mathrm{d}A = 0, \tag{5a}$$

$$\iint_\Omega \Big(\mathcal{V}\rho_0(\mathbf{u}_0\cdot\nabla)v_0 - p_0\frac{\partial \mathcal{V}}{\partial y} + \mu\nabla\mathcal{V}\cdot\nabla v_0\Big)\,\mathrm{d}A = 0, \tag{5b}$$

$$\iint_\Omega \mathcal{P}\Big(\nabla\cdot\mathbf{u}_0\Big)\,\mathrm{d}A = 0, \tag{5c}$$

for all test functions $\mathcal{U}, \mathcal{V}, \mathcal{P}$ without support on boundaries where the fields are explicitly prescribed.

2.2. Acoustic Equations

The acoustic model sets out from the Navier-Stokes and mass conservation equations (1). Inserting the conventions (2) in this, neglecting all higher orders terms in the acoustic variables, neglecting viscous effects, and using the isentropic relation $p' = c^2\rho'$, where c is the speed of sound in the fluid, we arrive at the following linearized acoustic equations:

$$\frac{\partial u'}{\partial t} + (\mathbf{u}'\cdot\nabla)u_0 + (\mathbf{u}_0\cdot\nabla)u' + \frac{1}{\rho_0}\frac{\partial p'}{\partial x} = 0, \tag{6a}$$

$$\frac{\partial v'}{\partial t} + (\mathbf{u}'\cdot\nabla)v_0 + (\mathbf{u}_0\cdot\nabla)v' + \frac{1}{\rho_0}\frac{\partial p'}{\partial y} = 0, \tag{6b}$$

$$\frac{\partial p'}{\partial t} + \nabla p'\cdot\mathbf{u}_0 + c^2\rho_0\nabla\cdot\mathbf{u}' = 0. \tag{6c}$$

Applying separation-of-variables and assuming time-harmonic conditions, we seek acoustic solutions $\mathbf{u}'$ and p' to equations (6) of the following form:

$$\mathbf{u}'(t,\mathbf{x}) = e^{-i\omega t}\tilde{\mathbf{u}}(\mathbf{x}), \qquad p'(t,\mathbf{x}) = e^{-i\omega t}\tilde{p}(\mathbf{x}). \tag{7}$$

where ω denotes the acoustic angular frequency. Using the above assumptions, neglecting higher order terms in the background flow $\mathbf{u}_0$, and introducing an acoustic source f, the following single equation in the spatial part of the acoustic pressure $\tilde{p}$ can be derived:

$$\nabla^2\tilde{p} + k^2\tilde{p} + \frac{2i}{\omega}\Big(k^2\mathbf{u}_0\cdot\nabla\tilde{p} - \frac{\partial\mathbf{u}_0}{\partial x}\cdot\nabla\frac{\partial\tilde{p}}{\partial x} - \frac{\partial\mathbf{u}_0}{\partial y}\cdot\nabla\frac{\partial\tilde{p}}{\partial y}\Big) = f, \tag{8}$$

where $k \equiv \omega/c$ is the wave number. This equation is valid for low background flow speeds only. We note that the terms in the paranthesis all relate to the background flow $\mathbf{u}_0$. When this vanishes, the equation reduces to the usual inhomogenous Helmholtz equation.

The boundary conditions on the hard wall and the symmetry edge are:

$$\nabla\tilde{p}\cdot\mathbf{n} = 0 \qquad \text{on } \Gamma_w \cup \Gamma_s. \tag{9}$$

The treatment of the artificial truncation boundaries $\gamma_\pm$, however, is less trivial [26, 12, 13]. Here, waves must be allowed to propagate out of the domain, and, at the same time, reflections back into the domain must be avoided. We treat the truncation boundaries using the mode matching formulation [27], based on a modal decomposition, a method closely related to the so-called Dirichlet-to-Neumann map [13].

The crux of the mode matching method is to assume that the acoustic pressure on the truncation boundaries $\gamma_\pm$ may be expressed as linear combinations of so-called acoustic duct modes, giving the following relations for the acoustic pressure and its normal derivative:

$$\tilde{p}(x,y) = \sum_{n=1}^{N_m^\pm} b_n^\pm\phi_n^\pm(y) \equiv \tilde{p}_\pm \qquad \text{on } \gamma_\pm, \tag{10a}$$

$$\nabla\tilde{p}(x,y)\cdot\mathbf{n} = \pm\frac{\partial\tilde{p}}{\partial x}(x,y) = \pm\sum_{n=1}^{N_m^\pm} b_n^\pm\lambda_n\phi_n^\pm(y) \quad \text{on } \gamma_\pm, \tag{10b}$$

where ϕ_n are the acoustic duct modes, λ_n are the associated (complex and signed) wave numbers, b_n are the expansion coefficients, and N_m is the finite (and small) number of modes.

The mode matching method involves two steps: In the first step, the acoustic duct modes, i.e., the functions ϕ_n and the wave numbers λ_n, are determined. In the second step, the weights b_n of the modes on $\gamma_\pm$, as well as the acoustic pressure $\tilde{p}$ over the entire domain Ω are determined.

For the first step, we assume that the truncation boundaries $\gamma_\pm$ are placed far away from acoustic sources and geometric ondulations, such that the background flow $\mathbf{u}_0$ is independent of x and normal to $\gamma_\pm$. With these assumptions, equation (8) evaluated on the truncation boundaries simplifies to:

$$\frac{\partial^2\tilde{p}}{\partial x^2} + \frac{\partial^2\tilde{p}}{\partial y^2} + k^2\tilde{p} + \frac{2i}{\omega}\Big(k^2u_0\frac{\partial\tilde{p}}{\partial x} - u_0'\frac{\partial^2\tilde{p}}{\partial x\partial y}\Big) = 0, \tag{11}$$

where $u_0 = u_0(y)$ is the horizontal background flow velocity, and $u_0' = du_0/dy$ its derivative. From equation

(9), the boundary conditions are:

$$u_0' = 0 \qquad \text{for } y = 0, R, \tag{12}$$

where R is the height of the duct. We are interested in the weak form of equation (11) which reads: given ω, k, and u_0, find $\tilde{p}$ such that

$$\int_{\gamma_\pm} \widetilde{\mathcal{P}}\Big[\frac{\partial^2 \tilde{p}}{\partial x^2} + \frac{\partial^2 \tilde{p}}{\partial y^2} + k^2 \tilde{p} + \frac{2i}{\omega}\Big(k^2 u_0 \frac{\partial \tilde{p}}{\partial x} - u_0' \frac{\partial^2 \tilde{p}}{\partial x \partial y}\Big)\Big] \,\mathrm{d}y = 0, \tag{13}$$

for all test functions $\widetilde{\mathcal{P}}$. The modes are then determined by solving an eigenvalue problem based on equation (13) while using the homogenous Neumann boundary conditions in equation (12).

For the second step, we consider the weak forms of the system (8)-(9) for the acoustic pressure over the domain Ω, and of the modal relation (10a) on the truncation boundaries $\gamma_\pm$. These read: given ω, k, f, and $\mathbf{u}_0$, find $\tilde{p}$ and $\tilde{p}_\pm$ such that

$$\int_{\gamma_\pm} \widetilde{\mathcal{P}}(\nabla \tilde{p} \cdot \mathbf{n}) \,\mathrm{d}s - \iint_\Omega \nabla \widetilde{\mathcal{P}} \cdot \nabla \tilde{p} \,\mathrm{d}A + \iint_\Omega \widetilde{\mathcal{P}}\Big[k^2 \tilde{p} - f + \frac{2i}{\omega}\Big(k^2 \mathbf{u}_0 \cdot \nabla \tilde{p} - \frac{\partial \mathbf{u}_0}{\partial x} \cdot \nabla \frac{\partial \tilde{p}}{\partial x} - \frac{\partial \mathbf{u}_0}{\partial y} \cdot \nabla \frac{\partial \tilde{p}}{\partial y}\Big)\Big] \,\mathrm{d}A = 0 \tag{14a}$$

$$\int_{\gamma_\pm} \widetilde{\mathcal{F}}^\pm (\tilde{p} - \tilde{p}_\pm) \,\mathrm{d}s = 0, \tag{14b}$$

for all test functions $\widetilde{\mathcal{P}}, \widetilde{\mathcal{F}}^\pm$. These equations are then solved using the Neumann boundary conditions (10b) on the truncation boundaries.

3. Isogeometric Analysis

We solve the coupled flow-acoustic problem numerically using B-spline based isogeometric analysis, building on the Galerkin method. This section gives an account of the numerical procedure. The reader is referred to, e.g., [28] for treatment of B-splines, and to, e.g., [19] for an extensive introduction to isogeometric analysis.

3.1. Geometry Parametrization

A parametrization $\mathbf{X} : [0,1]^2 \to \mathbb{R}^2$ of the computational domain is constructed, see Figure 3:

$$\mathbf{X}(\xi, \eta) = (\, x(\xi, \eta),\, y(\xi, \eta)\,) = \sum_{i=1}^{N^g_{\text{fun}}} \mathbf{x}_i \mathcal{R}^g_i(\xi, \eta), \tag{15}$$

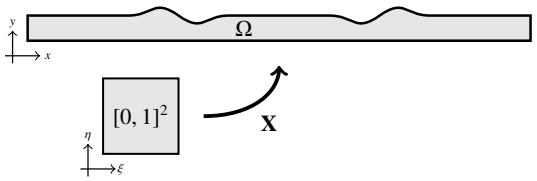

Figure 3: Parametrization of the model domain.

where $\mathcal{R}^g_i$ are tensor product B-splines with given knot vectors and polynomial degrees, $\mathbf{x}_i$ are the associated control points, and N^g_{fun} is the number of terms in the expansion.

The geometry parametrization serves as foundation for both the flow model and the acoustic model. Rather than solving the equations over the physical domain Ω, we pull them back to the parameter domain $[0,1]^2$ and solve them there.

For later reference, the gradient $\overline{\nabla}$ and the Hessian matrix $\overline{\mathbf{H}}$ in physical space Ω of any scalar quantity $\overline{h}$ are related to their counterparts ∇, $\mathbf{H}$, and h in parameter space $[0,1]^2$ by the following relations:

$$\nabla h = \mathbf{J}^T \overline{\nabla h} \tag{16a}$$

$$\mathbf{H}(h) = \mathbf{J}^T \overline{\mathbf{H}}(\overline{h}) \mathbf{J} + \sum_{m=1}^{2} \mathbf{H}(x_m) \mathbf{e}_m^T \overline{\nabla h}, \tag{16b}$$

where $\mathbf{J}$ is the Jacobian matrix of the parametrization, and $\mathbf{e}_1 = (1\ 0)^T$ and $\mathbf{e}_2 = (0\ 1)^T$ are the standard unit vectors. These relations are easily solved for the quantities $\overline{\nabla h}$ and $\overline{\mathbf{H}}(\overline{h})$ in physical space whose elements appear in the governing equations, and expressed through the quantities ∇h, $\mathbf{H}(h)$, $\mathbf{J}$, $\mathbf{H}(x)$, and $\mathbf{H}(y)$ in parameter space where we solve the equations.

3.2. Flow Model

Approximations of the background flow velocity and pressure fields are constructed in a similar fashion as for the geometry (15):

$$u = \sum_{i=1}^{N^u_{\text{fun}}} u_i \mathcal{R}^u_i = \sum_{i=1}^{N^u_{\text{dof}}} \underline{u}_i \mathcal{R}^u_i + \sum_{i=N^u_{\text{dof}}+1}^{N^u_{\text{fun}}} \underline{u}_i \mathcal{R}^u_i, \tag{17a}$$

$$v = \sum_{i=1}^{N^v_{\text{fun}}} u_i \mathcal{R}^v_i = \sum_{i=1}^{N^v_{\text{dof}}} \underline{v}_i \mathcal{R}^v_i + \sum_{i=N^v_{\text{dof}}+1}^{N^v_{\text{fun}}} \underline{v}_i \mathcal{R}^v_i, \tag{17b}$$

$$p = \sum_{i=1}^{N^p_{\text{fun}}} p_i \mathcal{R}^p_i = \sum_{i=1}^{N^p_{\text{dof}}} \underline{p}_i \mathcal{R}^p_i, \tag{17c}$$

where, for the u-field, the basis functions $\mathcal{R}^u$ are tensor product B-splines with given knot vectors and polynomial degree, the expansions coefficients $\underline{\mathbf{u}}$ are the unknown control variables to be determined, and N^u is the number of terms in the expansion, and similarly for the v-field and p-field. Also, for book keeping purposes, the velocity expansion has been split into terms with and terms without support on the Dirichlet boundary.

Using suitable functions $\mathcal{R}^u$, $\mathcal{R}^v$ and $\mathcal{R}^p$ as test functions in the weak formulation of the governing equations (5), inserting the discretizations of the state variables (17) into it, interchanging order of summation and integration, and rearranging terms, the following system of non-linear equations can be derived:

$$\begin{bmatrix} \mu\mathbf{K}_1 + \rho_0\mathbf{C}_1(\underline{\mathbf{u}}) & \mathbf{0} & -\mathbf{G}_1^T \\ \mathbf{0} & \mu\mathbf{K}_2 + \rho_0\mathbf{C}_2(\underline{\mathbf{u}}) & -\mathbf{G}_2^T \\ \mathbf{G}_1 & \mathbf{G}_2 & \mathbf{0} \end{bmatrix} \begin{bmatrix} \bar{\mathbf{u}}_1 \\ \bar{\mathbf{u}}_2 \\ \bar{\mathbf{p}} \end{bmatrix} = -\begin{bmatrix} \mu\mathbf{K}_1^\star + \rho_0\mathbf{C}_1^\star(\underline{\mathbf{u}}) & \mathbf{0} \\ \mathbf{0} & \mu\mathbf{K}_2^\star + \rho_0\mathbf{C}_2^\star(\underline{\mathbf{u}}) \\ \mathbf{G}_1^\star & \mathbf{G}_2^\star \end{bmatrix} \begin{bmatrix} \bar{\mathbf{u}}_1^\star \\ \bar{\mathbf{u}}_2^\star \end{bmatrix} \tag{18}$$

or simply $\mathbf{M}(\mathbf{U})\,\mathbf{U} = \mathbf{F}$, with

$$\underline{\mathbf{K}}_{i,j,k} = \iint_{[0,1]^2} \overline{\nabla\mathcal{R}}_i^{u_k} \cdot \overline{\nabla\mathcal{R}}_j^{u_k} \det(\mathbf{J})\,\mathrm{d}\Xi, \tag{19a}$$

$$\underline{\mathbf{C}}_{i,j,k} = \iint_{[0,1]^2} \mathcal{R}_i^{u_k}(\mathbf{u}(\underline{\mathbf{u}}) \cdot \overline{\nabla\mathcal{R}}_j^{u_k}) \det(\mathbf{J})\,\mathrm{d}\Xi, \tag{19b}$$

$$\underline{\mathbf{G}}_{i,j,k} = \iint_{[0,1]^2} \mathcal{R}_i^{p}(\mathbf{e}_k \cdot \overline{\nabla\mathcal{R}}_j^{u_k}) \det(\mathbf{J})\,\mathrm{d}\Xi, \tag{19c}$$

$$\underline{\mathbf{K}}_k = \begin{bmatrix} \mathbf{K}_k & \mathbf{K}_k^\star \end{bmatrix} \quad \left(N_{\text{dof}}^{u_k} \times (N_{\text{dof}}^{u_k} + N_{\text{fix}}^{u_k})\right), \tag{19d}$$

$$\underline{\mathbf{C}}_k = \begin{bmatrix} \mathbf{C}_k & \mathbf{C}_k^\star \end{bmatrix} \quad \left(N_{\text{dof}}^{u_k} \times (N_{\text{dof}}^{u_k} + N_{\text{fix}}^{u_k})\right), \tag{19e}$$

$$\underline{\mathbf{G}}_k = \begin{bmatrix} \mathbf{G}_k & \mathbf{G}_k^\star \end{bmatrix} \quad \left(N_{\text{dof}}^{p} \times (N_{\text{dof}}^{u_k} + N_{\text{fix}}^{u_k})\right), \tag{19f}$$

$$\underline{\mathbf{u}}_k^T = \begin{bmatrix} \bar{\mathbf{u}}_k^T & \bar{\mathbf{u}}_k^{\star T} \end{bmatrix} \quad \left(1 \times (N_{\text{dof}}^{u_k} + N_{\text{fix}}^{u_k})\right), \tag{19g}$$

where all starred quantities are given by the Dirichlet boundary conditions.

3.3. Acoustic Model

The acoustic model involves two steps: The first step determines the acoustic duct modes on the truncation boundaries $\gamma_\pm$, i.e., the functions ϕ_n and the wave numbers λ_n. The second step determines the weights b_n of the modes on $\gamma_\pm$ as well as the acoustic pressure $\tilde{p}$ over the entire domain Ω.

3.3.1. Acoustic Duct Modes

To determine the acoustic duct modes, we approximate the pressure in the regions far upstream and far downstream by the following expression:

$$\tilde{p}(x,y) = \sum_{\ell=1}^{n} a_\ell(x)\,\overline{\mathcal{M}}_\ell(y)\,, \tag{20}$$

where $\mathcal{M}_\ell$ are univariate B-splines defined over the parameter domain $\xi \in [0,1]$, $\overline{\mathcal{M}}_\ell$ are their image in physical space, and thus functions of y, c_ℓ are expansion coefficients that are functions of x, and n is the number of terms in the expansion.

Due to the properties of B-splines, the boundary condition (12) for the acoustic pressure on the straight parts of the hard wall Γ_w and the symmetry edge Γ_s may be fulfilled a priori by choosing $a_1 = a_2$ and $a_n = a_{n-1}$, or, equivalently, by replacing the approximation (20) by

$$\tilde{p}(x,y) = \sum_{\ell=1}^{n-2} b_\ell(x)\,\overline{\mathcal{N}}_\ell(y)\,, \tag{21}$$

where

$$\begin{aligned} \mathcal{N}_1 &= \mathcal{M}_1 + \mathcal{M}_2, & b_1 &= a_1 + a_2, \\ \mathcal{N}_2 &= \mathcal{M}_3, & b_2 &= a_3, \\ &\vdots & &\vdots \\ \mathcal{N}_{n-3} &= \mathcal{M}_{n-2}, & b_{n-3} &= a_{n-2}, \\ \mathcal{N}_{n-2} &= \mathcal{M}_{n-1} + \mathcal{M}_n, & b_{n-2} &= a_{n-1} + a_n. \end{aligned}$$

By inserting the approximation (21) into the equation (13) on the truncation boundaries, using $\overline{\mathcal{N}}_k(y)$ as test functions, and pulling the integrals back to parameter domain $[0,1]$, the following system of ordinary differential equations is obtained:

$$\mathbf{R}\,\ddot{\mathbf{b}} + \frac{2i}{\omega}\,\mathbf{S}\,\dot{\mathbf{b}} + \mathbf{T}\,\mathbf{b} = \mathbf{0}\,, \tag{22}$$

where dot denotes differentiation with respect to x, and

$$\mathbf{R}_{k,\ell} = \int_0^1 \mathcal{N}_k\,\mathcal{N}_\ell\,y'\,\mathrm{d}\xi\,, \tag{23a}$$

$$\mathbf{S}_{k,\ell} = \int_0^1 \mathcal{N}_k\Big(k^2\,u_0\,\mathcal{N}_\ell - u_0'\,y'^{-1}\,\mathcal{N}_\ell'\Big)y'\,\mathrm{d}\xi\,, \tag{23b}$$

$$\mathbf{T}_{k,\ell} = \int_0^1 \mathcal{N}_k\Big(y'^{-2}\,\mathcal{N}_\ell'' - y''\,y'^{-3}\,\mathcal{N}_\ell' + k^2\,\mathcal{N}_\ell\Big)y'\,\mathrm{d}\xi\,, \tag{23c}$$

$$\mathbf{b} = \begin{pmatrix} b_1(x) & \dots & b_{n-2}(x) \end{pmatrix}^T, \tag{23d}$$

for $k, \ell = 1, \ldots, n-2$, where prime denotes differentiation with respect to ξ. The second order system (22) can be rewritten as the first order system

$$\begin{bmatrix} \mathbf{I} & \mathbf{0} \\ \mathbf{0} & \mathbf{R} \end{bmatrix} \begin{bmatrix} \dot{\mathbf{b}} \\ \dot{\mathbf{c}} \end{bmatrix} = \begin{bmatrix} \mathbf{0} & \mathbf{I} \\ -\mathbf{T} & -\frac{2i}{\omega}\mathbf{S} \end{bmatrix} \begin{bmatrix} \mathbf{b} \\ \mathbf{c} \end{bmatrix}. \tag{24}$$

By solving the generalised eigenvalue problem

$$\begin{bmatrix} \mathbf{0} & \mathbf{I} \\ -\mathbf{T} & -\frac{2i}{\omega}\mathbf{S} \end{bmatrix} \begin{bmatrix} \mathbf{b} \\ \mathbf{c} \end{bmatrix} = \lambda \begin{bmatrix} \mathbf{I} & \mathbf{0} \\ \mathbf{0} & \mathbf{R} \end{bmatrix} \begin{bmatrix} \mathbf{b} \\ \mathbf{c} \end{bmatrix}, \tag{25}$$

we obtain $2n-4$ pairs of eigenvalues, λ_k, and eigenvectors, $(\mathbf{b}_k \ \mathbf{c}_k)^T$. Each eigenvalue represents a (complex and signed) wave number, and each eigenvector corresponds to a (complex) acoustic duct mode

$$\phi_k(y) = \sum_{\ell=1}^{n-2} b_{\ell,k} \overline{\mathcal{N}}_\ell(y). \tag{26}$$

As demonstrated in section 5 below, a finite and small number of modes N^m with purely imaginary propagation constant λ are found in practice, while the number of modes with propagation constant with non-vanishing real part is bounded only by the numerical discretization. We base the mode matching formulation on the former propagative modes, while the latter evanescent modes are neglected.

3.3.2. Acoustic Pressure

To compute the acoustic pressure $\tilde{p}$ over the entire domain, and the weights b_n of the modes on the truncation boundaries, we will, as for the geometry and the background flow variables, seek solutions of the following form:

$$\tilde{p} = \sum_{i=1}^{N^{\tilde{p}}_{\text{fun}}} \tilde{p}_i R_i^{\tilde{p}}, \tag{27}$$

where the basis functions $\mathcal{R}^{\tilde{p}}$ are tensor product B-splines with given knot vectors and polynomial degrees, the expansions coefficients $\tilde{\mathbf{p}}$ are the unknown control variables to be determined, and $N^{\tilde{p}}_{\text{fun}}$ is the number of terms in the expansion.

As test functions in the weak formulation of the governing equations (14), we use the basis functions $\mathcal{R}^{\tilde{p}}$ and the (B-spline approximations from above of the) propagative acoustic duct modes $\phi^{\pm}$. By inserting the acoustic field approximation (27) and the acoustic duct mode approximation (26) into these equations, exploiting the Neumann boundary condition (10b), rearranging terms and interchanging order of integration and summation, we arrive at the following system of linear equations:

$$\begin{bmatrix} -\mathbf{D} + k^2\mathbf{M} + \frac{2i}{\omega}\left(k^2\mathbf{L} - \mathbf{Q}\right) & \mathbf{H}\mathbf{B}\mathbf{\Lambda} \\ \mathbf{B}^T\mathbf{H} & -\mathbf{B}^T\mathbf{H}\mathbf{B} \end{bmatrix} \begin{bmatrix} \tilde{\mathbf{p}} \\ \mathbf{b} \end{bmatrix} = \begin{bmatrix} \mathbf{f} \\ \mathbf{0} \end{bmatrix} \tag{28}$$

where

$$\mathbf{D}_{i,j} = \iint_{[0,1]^2} \overline{\nabla\mathcal{R}}_i^{\tilde{p}} \cdot \overline{\nabla\mathcal{R}}_j^{\tilde{p}} \det(\mathbf{J}) \, \mathrm{d}\Xi, \tag{29a}$$

$$\mathbf{M}_{i,j} = \iint_{[0,1]^2} \mathcal{R}_i^{\tilde{p}} \mathcal{R}_j^{\tilde{p}} \det(\mathbf{J}) \, \mathrm{d}\Xi, \tag{29b}$$

$$\mathbf{L}_{i,j} = \iint_{[0,1]^2} \mathcal{R}_i^{\tilde{p}} (\mathbf{u}_0 \cdot \overline{\nabla\mathcal{R}}_j^{\tilde{p}}) \det(\mathbf{J}) \, \mathrm{d}\Xi, \tag{29c}$$

$$\mathbf{Q}_{i,j} = \iint_{[0,1]^2} \mathcal{R}_i^{\tilde{p}} \sum_{m=1}^{2} (\mathbf{e}_m^T \overline{\nabla}) \mathbf{u}_0 \cdot (\overline{\mathbf{H}\mathcal{R}}_j^{\tilde{p}} \mathbf{e}_m) \det(\mathbf{J}) \, \mathrm{d}\Xi, \tag{29d}$$

$$\mathbf{H}_{i,j} = \int_{[0,1]} \mathcal{R}_i^{\tilde{p}} \mathcal{R}_j^{\tilde{p}} \|\gamma'\| \, \mathrm{d}\xi, \tag{29e}$$

$$\mathbf{B}_{i,k} = \begin{cases} b_{\ell,k} & \text{if } \operatorname{supp}(\mathcal{R}_i^{\tilde{p}}) \cap \gamma_{\pm} \neq \emptyset \\ 0 & \text{otherwise} \end{cases}, \tag{29f}$$

$$\mathbf{\Lambda}_{k,\ell} = \delta_{k,l} \lambda_k, \tag{29g}$$

$$\mathbf{f}_i = \iint_{[0,1]^2} \mathcal{R}_i^{\tilde{p}} f \det(\mathbf{J}) \, \mathrm{d}\Xi, \tag{29h}$$

for $i, j = 1, \ldots, N^{\tilde{p}}_{\text{fun}}$ and $k, \ell = 1, \ldots, N^m$, where $\delta_{k,l}$ is the Kronecker delta. Here, the matrices $\mathbf{M}$ and $\mathbf{D}$ appears independently of the background flow, whereas $\mathbf{L}$ is due to the flow field $\mathbf{u}_0$, and $\mathbf{Q}$ is due to the gradient of the flow field $\nabla\mathbf{u}_0$.

3.4. Implementation

For the geometry parametrization, we take $\mathcal{R}_i^g$ as bi-quadratic tensor product B-splines. For the flow approximations, we take $\mathcal{R}_i^u$ and $\mathcal{R}_i^v$ as bi-quartic and $\mathcal{R}_i^p$ as bi-cubic, respectively, all C^2 across knots cf. [23]. For the acoustic approximation, $\mathcal{R}_i^{\tilde{p}}$ are taken as bi-quartic, unless otherwise stated.

The Dirichlet boundary conditions, for which the background flow is explicitly prescribed, are enforced strongly. This is done by specifying suitable control variables $\underline{\mathbf{u}}^*$ corresponding to basis functions for which the relevant basis functions have support on the relevant boundary. The Neumann boundary conditions, for which the normal component of the background flow velocity gradient or the acoustic pressure gradient are prescribed, are enforced weakly by equating the corresponding parts of the boundary integrals to their respective values.

All integrals are evaluated numerically using Gaussian quadrature based on 7 points in each knot span, which is a conservative choice compared to more efficient quadrature rules [29].

4. Validation: Acoustic Duct Modes

In this section we consider the propagation of sound waves in a straight duct with uniform background flow, for which analytical solutions are readily available. We validate the coupled flow-acoustic model numerically by examining how well the method is able to reproduce these analytical solutions.

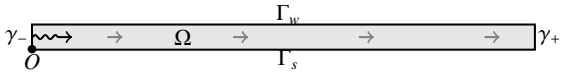

Figure 4: The modal problem.

The problem is outlined in Figure 4. It differs from the one described in Figure 2 by the fact that a uniform background flow $\mathbf{u}_0 = (U_0, 0)$ is explicitly prescribed, the interior acoustic source f has been removed, and the mode matching boundary condition on the left boundary γ_- has been replaced by an explicit prescription of the acoustic pressure:

$$\tilde{p} = \tilde{p}_n^* \qquad \text{on } \gamma_-. \tag{30}$$

Here, $\tilde{p}_n^*$ is an analytical solution of equation (8) for the acoustic pressure field in a straight duct of height R with uniform background flow $\mathbf{u}_0 = (U_0, 0)$:

$$\tilde{p}_n^* = \exp(i\beta_n x)\cos(\alpha_n y), \tag{31}$$

where

$$\alpha_n = n\pi/R, \tag{32a}$$

$$\beta_n = -kM \pm \sqrt{k^2(1+M^2) - (n\pi/R)^2}, \tag{32b}$$

where $M \equiv U_0/c$ is the Mach number. This corresponds to the n^{th} propagative acoustic duct mode

$$\phi_n(y) = \cos\left(n\pi\frac{y}{R}\right), \tag{33}$$

such that $n \leq \sqrt{1+M^2}\, kR/\pi$, travelling towards $\pm\infty$.

To assess the quality of the method, we will use the normalised L_2-norm of the modulus of the pressure residual as error measure:

$$\epsilon^2 = \frac{\iint_\Omega |\tilde{p} - \tilde{p}^*|^2 \,\mathrm{d}A}{\iint_\Omega |\tilde{p}^*|^2 \,\mathrm{d}A}. \tag{34}$$

We investigate how this varies as the analysis mesh is refined by knot insertion, and the number of degrees-of-freedom thereby increased. We use the parameter values for the duct size, sound frequency and flow speed as described in Table 1 in the following section, leading to two propagative modes $n \in \{0, 1\}$.

We firstly examine how different approximations of the acoustic pressure influence the error convergence. Here, we consider the background flow $U_0 = 1\ \mathrm{m\,s^{-1}}$, the sound frequency $f = 25$ kHz, and the highest propagative mode $n = 1$. For polynomial degrees $q \in \{2, \ldots, 6\}$, we solve the problem for a range of meshes, and evaluate the error using (34). The results

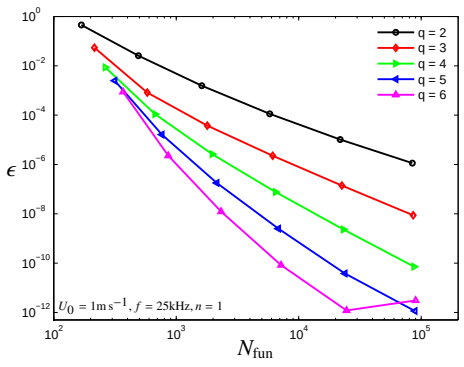

Figure 5: Relative error ϵ as function of number of basis function N_{fun} for different polynomial degrees q.

are shown in Figure 5. By inspection of the slope of the curves, we note that the higher the polynomial degree is, the higher the convergence rate also is. For polynomial degrees $q \geq 5$, this holds only for sufficiently few degrees of freedom, presumably because of rounding errors for more degrees of freedom. All following results are based on a polynomial degree of $q = 4$.

Secondly, to illustrate the effect of the background flow on the acoustic wave propagation, Figure 6 depicts the real part of the acoustic pressure in the duct without flow (a), with flow $U_0 = 1\ \mathrm{m\,s^{-1}}$ (b), and the difference between these (c), for the mode $n = 1$ and frequency $f = 25$ kHz. As expected, the effect of background flow is to strech the wavelength of the sound waves in the downstream region.

Finally, we investigate the error convergence for different background flows, sound frequencies, and modes. For each combination of background flow $U_0 \in \{0, 1\}$ $\mathrm{m\,s^{-1}}$, frequency $f \in \{20, 30\}$ kHz, and mode $n \in \{0, 1\}$, we solve the problem for a range of meshes, and compute the error using (34). The results are shown in Fig-

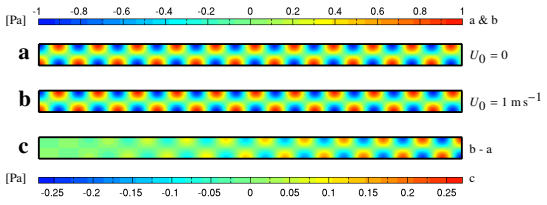

Figure 6: Real part of the acoustic pressure $\tilde{p}$ using the background flow $U_0 = 0$ (**a**), $U_0 = 1\ \mathrm{m\,s^{-1}}$ (**b**), and the difference between these (**c**), for the mode $n = 1$ and frequency $f = 25$ kHz.

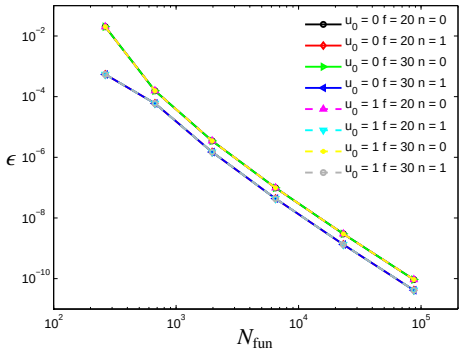

Figure 7: Relative error ϵ as function of number of basis functions N_{fun} for different background flows U_0, frequencies f and modes n.

ure 7. We note that practically identical rates of convergence are found independently of background flow, frequency, and mode.

5. Results

In this section we use the coupled flow-acoustic model to examine how the duct geometry affects how the acoustic signal depends on sound frequency and flow speed.

5.1. Setup of Numerical Experiment

The numerical experiment is sketched in Figure 8. To assess the geometric effects, three different geometries are investigated: a straight duct (a), a duct with a single bulge (b), and a corrugated duct (c). The flow is varied by prescribing, for different mean flow speeds U_0, a parabolic velocity profile at the inlet boundary:

$$u_0 = \frac{3}{2} U_0 \left(1 - \left(\frac{y}{R}\right)^2\right), \qquad v_0 = 0, \qquad \text{on } \gamma_- . \quad (35)$$

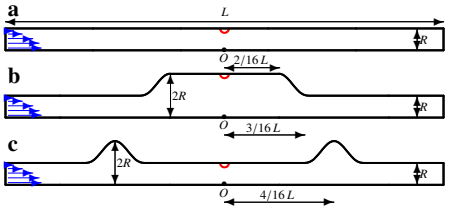

Figure 8: Design of the numerical experiment: We investigate 3 geometries (**a**, **b**, and **c**), and prescribe the flow at the inlet (blue arrows) and the sound excitation in the middle (red circles).

The sound excitation is varied by assuming, for different angular frequencies ω, a smooth, compactly supported acoustic source, centered at $(0, r_0)$, where r_0 is the height of the duct in $x = 0$, with the following form:

$$f(x, y) = f_0\, \Psi(x; 0, L_x)\, \Psi(y; r_0, L_y), \quad (36)$$

where f_0 denotes the strength of the source, $\mathbf{L}$ its spatial extent, and the footprint function Ψ is given by:

$$\Psi(x; a, b) = \begin{cases} e^{-\frac{1}{1-\chi^2}} & \text{for } |\chi| \equiv |\frac{x-a}{b}| < 1 \\ 0 & \text{otherwise} \end{cases} . \quad (37)$$

The parameter values used in the numerical experiment for the geometry, the fluid, and the sound excitation are summarised in Table 1. With R as characteristic length scale, and U_0 as flow speed, this corresponds to Reynolds numbers up to $\mathrm{Re} \simeq 1 \cdot 10^3$ and Mach numbers up to $M \simeq 3 \cdot 10^{-3}$.

Parameter	Description	Value	Unit
μ	Dynamic viscosity	$1 \cdot 10^{-5}$	$\mathrm{kg\,m^{-1}s^{-1}}$
ρ	Background density	1	$\mathrm{kg\,m^{-3}}$
c	Speed of sound	340	$\mathrm{m\,s^{-1}}$
R	Duct height	1	cm
L	Duct length	20	cm
f	Source strength	$1 \cdot 10^6$	
$\mathbf{L} = (L_x, L_y)$	Source size	$(2, 2)$	mm
$f = \omega/2\pi$	Sound frequency	20–30	kHz
U_0	Flow speed	0–1	$\mathrm{m\,s^{-1}}$

Table 1: Parameter values corresponding to propagation of ultrasound in air-filled narrow ducts are used.

5.2. Flow Field and Acoustic Modes

We firstly investigate the background flow. Figure 9 depicts the flow fields in the three different duct geometries using the flow speed $U_0 = 1\ \mathrm{m\,s^{-1}}$. In the straight

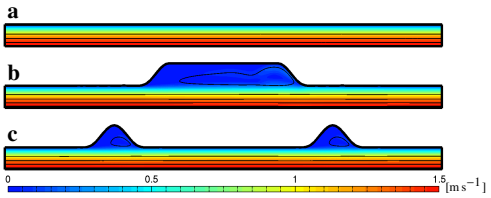

Figure 9: Flow speeds (colours) and stream lines (solid lines) using the mean speed $U_0 = 1$ m s^{-1} in the straight duct (**a**), the bulged duct (**b**), and the corrugated duct (**c**).

duct (a), the parabolic velocity profile is naturally conserved down the duct. In the bulged duct (b) and the corrugated duct (c), we notice that the flow profile is only slightly perturbed in the vicinity of ondulations. In addition, a weak recirculation flow is seen in the bulges.

Next, we investigate how the acoustic duct modes vary with flow speed and sound frequency. This is depicted in Figure 10. In **a**, a typical configuration

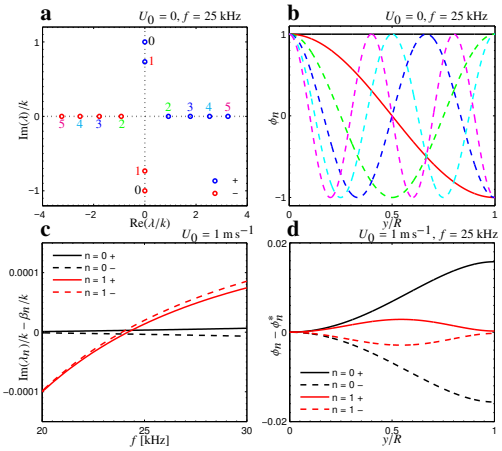

Figure 10: Acoustic duct modes for different frequencies f and flow speeds U_0. **a**: propagation constants λ for $f = 25$ kHz and $U_0 = 0$. **b**: mode functions ϕ for $f = 25$ kHz and $U_0 = 0$. **c**: imaginary part of propagation constants λ for $U_0 = 1$ m s^{-1} and $f \in [20, 30]$ kHz. **d**: mode function ϕ residuals for $U_0 = 1$ m s^{-1} compared to $U_0 = 0$ for $f = 25$ kHz.

of computed propagation constants λ (scaled by k) is shown in the complex plane, here with vanishing background flow $U_0 = 0$, and frequency $f = 25$ kHz. The propagation constants can be categorized as propagative/evanescent (on/off the imaginary axis), and as positive/negative (positive/negative imaginary part, or vanishing imaginary part and strictly positive/negative real part). Four propagative modes are found, two in each direction, in agreement with the analytical values in equation (32) with $M = 0$. The number of evanescent modes is bounded only by the number of degrees of freedom of the discretization, and only the first eight are shown here. In **b**, the modal functions ϕ corresponding to the propagation constants in **a** are shown, with propagative modes drawn in solid, and evanescent modes in dashed. These agree with the analytical modes in equation (33). In **c**, the imaginary parts of the propagation constants (scaled by k) corresponding to the four propagative modes for mean speed $U_0 = 1$ m s^{-1} are shown as a function of frequency in the range $f \in [20, 30]$ kHz, plotted as the residual compared to the case without flow as given by equation (32) with $M = 0$. The perturbations in the propagation constants due to the flow are largest for the second mode $n = 1$, but are in general small and $\lesssim 0.1‰$. Finally in **d**, the four propagative modal functions for mean speed $U_0 = 1$ m s^{-1} and frequency $f = 25$ kHz are depicted. The plot shows the modal function residuals compared to the corresponding modal functions without flow, as shown in **a** and given in equation (33). Perturbations are of opposite sign for positive and negative modes, and the perturbations are again in general small, with the largest perturbations $\sim 2\%$ found for the first mode $n = 0$.

5.3. Acoustic Field Sensitivity

To quantify the acoustic response by a single entity when examining how it changes with sound frequency and flow speed, we consider the relative modulus of the symmetry deviation of the acoustic pressure:

$$\langle \delta\tilde{p} \rangle = \frac{\iint_\Omega |\tilde{p}(\mathbf{x}) - \tilde{p}(-\mathbf{x})| \, \mathrm{d}A}{\iint_\Omega |\tilde{p}(\mathbf{x})| \, \mathrm{d}A}. \tag{38}$$

Since the geometries and the acoustic excitation are all symmetric around $x = 0$, any asymmetry in the acoustic pressure field arises due to the background flow (acoustic reciprocity in the absence of flow). As such, this quantity is a measure of how strongly the sound signal is coupled to the flow field. For reference, we also examine the mean (modulus of the) acoustic pressure:

$$\langle \tilde{p} \rangle = \frac{\iint_\Omega |\tilde{p}(\mathbf{x})| \, \mathrm{d}A}{\iint_\Omega \mathrm{d}A}. \tag{39}$$

To investigate the sensitivity of the sound signal to the frequency for a given flow speed, we compute the mean acoustic pressure $\langle \tilde{p} \rangle$ and the relative symmetry deviation in the acoustic pressure $\langle \delta\tilde{p} \rangle$ for frequencies in the range $f \in [20, 30]$ kHz with fixed flow speed $U_0 = 1$ m s^{-1}. The results are shown in Figure 11 for each of the three duct geometries. On the top plot,

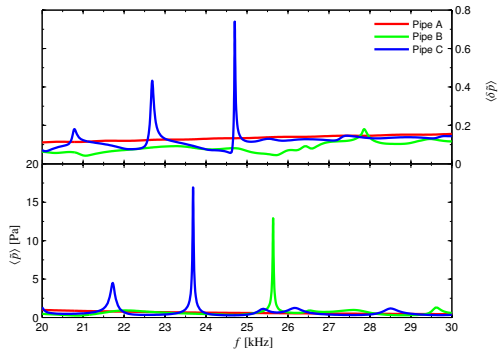

Figure 11: Mean acoustic pressure $\langle\tilde{p}\rangle$ using the flow speed $U_0 = 0\,\mathrm{m\,s^{-1}}$ (bottom), and relative symmetry deviation $\langle\delta\tilde{p}\rangle$ using the flow speed $U_0 = 1\,\mathrm{m\,s^{-1}}$ (top) as function of frequency f for the three duct geometries.

no significant changes in the degree of asymmetry are found for the straight duct (a), while the bulged duct (b) shows minor changes with frequency. For the corrugated duct (c), however, strong peaks are seen in the $\langle\delta\tilde{p}\rangle$ response. The strongest peak occurs for frequencies close to $f = 24.7$ kHz, where the signal experiences an increase by a factor of up to ~ 10. From the bottom plot, the peaks in $\langle\delta\tilde{p}\rangle$ for the corrugated duct (c) are seen to occur close to local minima in the mean acoustic pressure $\langle\tilde{p}\rangle$ that fall between strong peaks in the $\langle\tilde{p}\rangle$ response associated with resonances in the duct.

To further illustrate the phenomenon observed in the frequency sweeps above, Figure 12 depicts the modulus of the acoustic pressure field using the frequency $f = 24.7$ kHz and the flow speed $U_0 = 1\,\mathrm{m\,s^{-1}}$ in each of the three duct geometries. Both the straight duct (a)

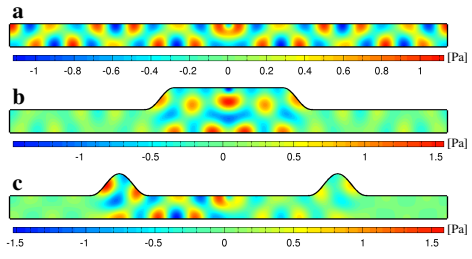

Figure 12: Modulus of the acoustic pressure field $\tilde{p}$ using the frequency $f = 24.7$ kHz and flow speed $U_0 = 1\,\mathrm{m\,s^{-1}}$ in the straight duct (**a**), the bulged duct (**b**), and the corrugated duct (**c**).

and the bulged duct (b) exhibit a high degree of symmetry in the acoustic pressure field. In the corrugated duct (c), however, there is a clear difference between the upstream and the downstream acoustic fields.

To investigate the sensitivity of the sound signal to the flow speed for a given frequency, we compute the relative symmetry deviation in the acoustic pressure $\langle\delta\tilde{p}\rangle$ for flow speeds in the range $U_0 \in [0, 1]\,\mathrm{m\,s^{-1}}$ with fixed frequency $f = 24.7$ kHz. The results are shown in Figure 13 for each of the three duct geometries. For

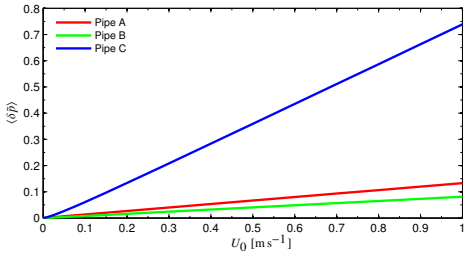

Figure 13: Relative symmetry deviation in the acoustic pressure $\langle\delta\tilde{p}\rangle$ as function of flow speed U_0 using the frequency $f = 24.7$ kHz for the three duct geometries.

all three ducts, a close-to-linear dependency upon flow speed is observed. We note in particular that the slope of the curve for the corrugated duct (c) is significantly larger than the slope of the curve for the straight duct (a) as well as for the duct with a single bulge (b).

The results clearly show that we have identified a combination of duct geometry and sound frequency where the acoustic signal is particularly sensitive to the background flow. The coupling seems to be related to the parabolic velocity profile in the duct interior. Similar results are found when explicitly prescribing a parabolic velocity profile in the entire domain, whereas the effect is diminished when prescribing a constant velocity profile.

We conclude by noting that if more (evanescent) modes are used in the mode matching formulation for the acoustic truncation boundary conditions, by increasing N_m, practically identical results are found. If the mode matching formulation is replaced by a suitably scaled perfectly matched layer (PML) formulation [12, 30, 26, 31], using, e.g., a linear absorbing function in a PML of width 10%, equivalent results to within $\sim 2\%$ are found. If different footprints of the acoustic source are used, by changing $\mathbf{L}$, qualitatively similar results are found. In addition, unpublished numerical investigations by the authors based on the Stevenson method [32] have also shown that strong resonance couplings between flow speed and duct radius variations can occur. Still, the phenomenon so far only exists in numerical models and lacks experimental vali-

dation. Nevertheless, it points towards the potential importance of the geometry on flow sensitivity for acoustic wave propagation, and shape optimization could likely enhance the effect.

6. Conclusions

We have presented a coupled flow-acoustic model of the propagation of sound through a moving fluid in a 2-dimensional duct based on isogeometric analysis. The model explicitly couples the non-linear, steady state, incompressible Navier-Stokes equation in the laminar regime to a linear, time-harmonic acoustic equation in the low Mach number regime, using both the background flow and its gradient as input. Acoustic boundary conditions along artificial truncation boundaries are dealt with using a mode matching formulation. The model has been validated against known acoustic modes in 2-dimensional ducts. These tests clearly supported the robustness of the method. In particular, desireable error convergence properties were observed for higher order polynomial approximations of the acoustic pressure, and these are naturally embedded in isogeometric analysis. Using the model, acoustic signal changes vs. duct geometry have been examined as a function of frequency and background flow values. A combination of duct geometry and sound frequency was identified for which the acoustic signal is particularly sensitive to the background flow. This enhanced sensitivity deserves closer examination in future studies.

References

[1] P. Exner, P. Seba, Bound states in curved quantum waveguides, Journal of Mathematical Physics 30 (1989) 2574–2580.

[2] F. H. Borgnis, C. H. Papas, Electromagnetic waveguides and resonators, in: S. Flugge (Ed.), Encyclopedia of Physics, volume 16, Springer-Verlag, 1958, p. 326.

[3] J. Goldstone, R. L. Jaffe, Bound states in twisting tubes, Physical Review B 45 (1992) 14100–14107.

[4] P. W. Anderson, Absence of diffusion in certain random lattices, Physical Review 109 (1958) 1492–1505.

[5] N. E. Hurt, Mathematical Physics of Quantum Wires and Devices. From Spectral Resonances to Anderson Localization, Mathematics and Its Applications, Kluwer Academic Publisher, 2000.

[6] V. I. Grinchenko, Wave motion localization effects in elastic waveguides, International Applied Mechanics 41 (2005) 988–994.

[7] J. D. Joannopoulos, R. D. Meade, J. N. Winn, Photonic Crystals: Molding the flow of light, Princeton University Press, 1995.

[8] M. M. Sigalas, E. N. Economou, Band structure of elastic waves in two dimensional systems, Solid State Communications 86 (1993) 141–143.

[9] M. S. Kushwaha, G. Martinez, Photonic bandgaps in two-dimensional semiconductor-dielectric composite crystals, Journal of the Optical Society of America B 23 (2006) pp. 1460–1470.

[10] A. A. Krokhin, J. Arriaga, L. N. Gumen, Speed of sound in periodic elastic composites, Physical Review Letters 91 (2003) 264302 (4 pages).

[11] L. C. L. Y. Voon, M. Willatzen, Electron states in modulated nanowires, Journal of Applied Physics 93 (2003). Also published in virtual Journal of Nanoscale Science & Technology, June 9, 2003, Volume 7, Issue 23.

[12] E. Becache, A.-S. B.-B. Dhia, G. Legendre, Perfectly matched layers for the convected Helmholtz equation, SIAM Journal on Numerical Analysis 42 (2004) 409–433.

[13] E. Redon, A.-S. B.-B. Dhia, J.-F. Mercier, S. P. Pari, Non-reflecting boundary conditions for acoustic propagation in ducts with acoustic treatment and mean flow, International Journal for Numerical Methods in Engineering (2011).

[14] R. J. Astley, W. Eversman, Acoustic transmission in non-uniform ducts with mean flow, part II: the finite element method, Journal of Sound and Vibration 74 (1981) 103–121.

[15] C. Peyret, G. Élias, Finite-element method to study harmonic aeroacoustics problems, Journal of the Acoustical Society of America 110 (2001) 661–668.

[16] A.-S. B.-B. Dhia, E.-M. Duclairoir, G. Legendre, J.-F. Mercier, Time-harmonic acoustic propagation in the presence of a shear flow, Journal of Computational and Applied Mathematics 204 (2007) 428–439.

[17] A.-S. B.-B. Dhia, J.-F. Mercier, F. Millot, S. Pernet, A low-Mach number model for time-harmonic acoustics in arbitrary flows, Journal of Computational and Applied Mathematics 234 (2010) 1868–1875.

[18] T. J. R. Hughes, J. A. Cottrell, Y. Bazilevs, Isogeometric analysis: CAD, finite elements, NURBS, exact geometry and mesh refinement, Computer methods in applied mechanics and engineering 194 (2005) 4135–4195.

[19] J. A. Cottrell, T. J. R. Hughes, Y. Bazilevs, Isogeometric Analysis: Toward Integration of CAD and FEA, John Wiley and Sons, 2009.

[20] Y. Bazilevs, T. J. R. Hughes, NURBS-based isogeometric analysis for the computation of flows about rotating components, Computational Mechanics 43 (2008) 143–150.

[21] Y. Bazilevs, I. Akkerman, Large eddy simulation of turbulent taylor-couette flow using isogeometric analysis and the residual-based variational multiscale method, Journal of Computational Physics 229 (2010) 3402–3414.

[22] A. Buffa, C. de Falco, G. Sangalli, Isogeometric Analysis: Stable elements for the 2D Stokes equation, International Journal for Numerical Methods in Fluids (2011).

[23] P. N. Nielsen, A. R. Gersborg, J. Gravesen, N. L. Pedersen, Discretizations in isogeometric analysis of Navier-Stokes flow, Computer methods in applied mechanics and engineering 200 (2011) 3242–3253.

[24] J. A. Cottrell, A. Reali, Y. Bazilevs, T. J. R. Hughes, Isogeometric analysis of structural vibrations, Computer methods in applied mechanics and engineering 195 (2006) 5257–5296.

[25] T. J. R. Hughes, A. Reali, G. Sangalli, Duality and unified analysis of discrete approximations in structural dynamics and wave propagation: Comparison of p-method finite elements with k-method NURBS, Computer methods in applied mechanics and engineering 197 (2008) 4104–4124.

[26] D. Givoli, Computational absorbing boundaries, in: S. Marburg, B. Nolte (Eds.), Computational Acoustics Of Noise Propagation In Fluids – Finite And Boundary Element Methods, Springer, 2008, pp. 145–166.

[27] R. Astley, FE mode-matching schemes for the exterior Helmholtz problem and their relationship to the FE-DtN approach, Communications in numerical methods in engineering 12 (1996) 257–267.
[28] L. Piegl, W. Tiller, The NURBS Book, Springer, 1995.
[29] T. J. R. Hughes, A. Reali, G. Sangalli, Efficient quadrature for NURBS-based isogeometric analysis, Computer methods in applied mechanics and engineering 199 (2010) 301–313.
[30] E. Becache, A.-S. B.-B. Dhia, G. Legendre, Perfectly matched layers for time-harmonic acoustics in the presence of a uniform flow, SIAM Journal on Numerical Analysis 44 (2006) 1191–1217.
[31] A. Bermúdez, L. Hervella-Nieto, A. Prieto, R. Rodríguez, Perfectly Matched Layers, in: S. Marburg, B. Nolte (Eds.), Computational Acoustics Of Noise Propagation In Fluids – Finite And Boundary Element Methods, Springer, 2008, pp. 467–196.
[32] A. F. Stevenson, Exact and approximate equations for wave propagation in acoustic horns, Journal of Applied Physics 22 (1951) 1461–1463.